University of Bradford eThesis

COMPUTER SIMULATION STUDIES OF
DENSE SUSPENSION RHEOLOGY

Computational studies of model sheared fluids; elucidation, interpretation and description of the observed rheological behaviour of simple colloidal suspensions in the granulo-viscous domain by Non-Equilibrium Particulate Dynamics.

A Thesis submitted to the

University of Bradford

in fulfilment of the requirements for the degree of

Doctor of Philosophy

by

Alan John HOPKINS

Department of Chemical Engineering,
University of Bradford,
BRADFORD,
West Yorkshire,
BD7 1DP

February 1989

Alan John HOPKINS

COMPUTER SIMULATION STUDIES OF DENSE SUSPENSION RHEOLOGY

Key Words:- computer-simulation; particulate-dynamics; hard-sphere; dense-suspension; rheology; polydispersity.

ABSTRACT

Rheological properties of idealised models which exhibit all the non-Newtonian flow phenomenology commonly seen in dense suspensions are investigated by particulate-dynamics computer-simulations.

The objectives of these investigations are:

(i) to establish the origins of various aspects of dense suspension rheology such as shear-thinning, shear thickening and dilatancy;

(ii) to elucidate the different regions of a typical dense suspension rheogram by examining underlying structures and shear induced anisotropies in kinetic energy, diffusivity and pressure;

(iii) to investigate the scaling of the simplest idealised model suspension; i.e. the hard-sphere model in Newtonian media and its relationship to the isokinetic flow curves obtained through non-equilibrium molecular dynamics (NEMD) simulations;

(iv) to preliminarily determine the effect of perturbations present in all real colloidal suspensions, namely particle size polydispersity and a slight 'softness' of the interparticle potential.

Non-equilibrium isokinetic simulations have been performed upon systems of particles interacting through the classical hard-sphere potential and a perturbation thereof, in which the hard-core is surrounded by a 'slightly soft' repulsive skin. The decision to base the present work upon isokinetic studies was made in order to obtain a better understanding of suspension rheology by making a direct connection with previous NEMD studies of thermal systems(93). These studies have shown that the non-linear behaviour exhibited by these systems under shear is atttributable to a shear-induced perturbation of the equilibrium phase behaviour. The present study shows this behaviour to correspond to the high shear region of the generalised suspension flow curve.

ACKNOWLEDGEMENTS

Completion of the work described herein would not have been possible without the generous assistance of many individuals. It is with great pleasure that I am able to extend my gratitude to these people here.

Particular thanks must go to my parents, and my wife, Mandy, for their support and encouragement throughout the duration of my research.

I am also deeply indebted to my research supervisor, Dr. L. V. Woodcock, for the many hours of painstaking and patient guidance devoted to me during the last three years. His vast knowledge and understanding have proved to be inspirational throughout.

Receipt of a Science and Engineering Research Council Studentship, and further financial assistance from Unilever Research are both gratefully acknowledged.

Miss Judith A. Squires deserves a special mention for her diligent typing of this thesis and Dr. Ahmad I. Jomha for his assistance in the final stages of preparation of this thesis.

Alan J. Hopkins
February 1989

TABLE OF CONTENTS

TABLE OF CONTENTS continued ......

CHAPTER 1

INTRODUCTION AND LITERATURE SURVEY

CHAPTER 1

INTRODUCTION AND LITERATURE SURVEY

1.1 General Background

The interest in dense suspension rheology is one that has been shared by industrialists and academics alike for many years. The industrial interest becomes self-evident when one considers the vast range of materials falling into this category encountered during the manufacture of a wide selection of everyday materials. In addition to the need for optimum, reproducible behaviour during the manufacturing processes (e.g. pumping, mixing, coating), the ultimate product performance is often dependent on its rheological characteristics.

The need for a fundamental understanding of the parameters responsible for the observed rheological behaviour of both suspensions and pure liquids has long been recognised, and is exemplified by the magnitude of the rheological literature, which stretches as far back as the seventeenth century(1). Despite this substantial research effort, there still remains a considerable amount of uncertainty, both in the reproducibility and interpretation of rheological measurements(2). A review of the relevant rheological literature appears later in this chapter.

Following the advent of electronic computers, two scientists working in the Los Alamos National Laboratory in America developed a simulation technique, with which, theoretically each of the 3 states of matter could be studied(3). These original simulations, whose foundations lay in the foundations of classical statistical mechanics were aimed at the Atomic/Molecular level, and were consequently referred to as Molecular Dynamics (MD) simulations.

The essential ingredients of a MD simulation are an effective pair potential describing the force-distance relationship between particles, and the equations of motion, which describe the motion of particles comprising the model system. The simulation then proceeds via the integration of the equations of motion, enabling us to monitor the individual trajectories of the model particles. The effects of interparticle and any external forces are taken into account.

From a knowledge of the particle positions and velocities at discrete points in time throughout the simulation, we are able to calculate various thermodynamic properties of the system. A review of the development of these types of simulations is given in the latter part of this chapter, and a fuller description of the techniques will be given in the relevant section.

More recently it has been realised that the statistical mechanical foundations of MD simulations may be equally applicable to solid/liquid suspensions of macroscopic particles(4). Furthermore, experimental investigations upon well-characterised, nearly monodisperse, polymer latices at equilibrium have shown that these systems undergo order-disorder transitions analogous to the melting transitions exhibited by atomic/molecular systems(5).

The objective of the present work is to take the established techniques of MD simulations, and incorporate effective pair potentials more relevant to dense suspensions. Consequently, a more appropriate description for the simulations described herein, would be 'Particulate Dynamics' (PD) simulations. The value of these PD simulations is threefold:

(i) qualitatively reproduce observed experimental behaviour, and thereby elucidate the underlying mechanisms responsible for that behaviour;

(ii) provide reliable data for simple model suspensions, which can be used as a basis on which to express the properties of experimental systems;

(iii) to enable progression towards the ultimate objective: a quantitative description of experimental systems through the introduction of perturbations to the model system that reflect the discrepancies between model and experimental systems.

1.2 A Historical Review of the Development of Rheology

The following section, which has been incorporated for completeness is intended to represent a brief historical account of the development of rheology. It is by no means intended to represent an exhaustive review, but merely aims to 'set the scene' for the bulk of the thesis to follow.

The word 'rheology' (from the Greek - 'rheo' - to flow, 'logos' - science) to describe the study of deformation and flow of matter was first used by an American scientist, Professor Eugene C. Bingham. The word was officially accepted in 1929, when the American Society of Rheology was founded(6).

Scientists had been studying the science of deformation and flow long before this, however. The first generally accepted rheological law was put forward by Hooke in 1676(7), when after studying the elongation of metal wires due to the suspension of weights wrote in Latin, 'ut tensio sic vis', which translates into modern day English as, 'the deformation is proportional to the applied force', or:

$$\tau = E\gamma \qquad (1.2.1)$$

where τ is the stress, γ is the strain, and E is the constant of proportionality, known as Young's modulus.

Shortly after this, in 1685, Sir Isaac Newton(8) noted that (again translated from the Latin), 'the resistance which arises from the lack of slipperiness of the points of the liquid, other things being equal, is proportional to the velocity with which the parts of the liquid are separated from one another', from which we obtain the usual definition of shear viscosity:

$$\eta = \frac{\tau}{\dot{\gamma}} \qquad (1.2.2)$$

where η is the shear viscosity, τ is the shear stress, and $\dot{\gamma}$ is the shear rate.

These early descriptions by Hooke and Newton of the response of matter to an applied stress have become accepted descriptions of the classical solid and fluid respectively.

Among the first experimental studies of fluid flow were those carried out almost simultaneously by J. L. Poiseuille and G.H.L. Hagen. Working independently on the flow of fluids through tubes, the two workers arrived at the same conclusions(9,10), which are embodied in the Hagen-Poiseuille equation:

$$\frac{Q}{t} = \frac{\pi\ r^4\ \Delta P}{8\ \eta\ L} \qquad (1.2.3)$$

where Q/t is the volumetric flow rate, η is the fluid viscosity, r is the tube radius, and $\Delta P/L$ denotes the pressure drop per unit length.

A significant advance was made in 1888, by an English scientist, A. Mallock(11), who performed the first experimental investigation of flow in the absence of a pressure gradient, i.e. in a concentric cylinder geometry. Mallock's work was followed shortly afterwards, in 1890, by a thorough investigation of flow between concentric cylinders by a French worker, Couette(12), who obtained good agreement between the results of tube and concentric cylinder flow.

Time dependent effects were observed early in rheology's history. These effects appeared to be inexplicable in terms of the classical models available, i.e. the Newtonian fluid and the Hookean solid. The first serious study of viscoelasticity was carried out in 1835 by Willhelm Weber(13), who observed that, when subjected to longitudinal loads, silk threads undergo an immediate extension, followed by a further lengthening with time. On removal of the load an immediate contraction to a length equal to the immediate extension takes place, followed by a gradual further decrease in length until the original length is reached.

The first experimental description of viscoelasticity was proposed in 1867 by James Clerk Maxwell(14) in the form of his famous first order differential equation:

$$\tau + \lambda \dot{\tau} = \dot{\gamma} \eta \qquad (1.2.4)$$

where λ is a characteristic time, and $\dot{\tau}$ represents the time derivative of stress τ.

Incorporated into his description of viscoelasticity, Maxwell introduced the concept of a relaxation time, defined as the time required for the stress to relax to 1/e of its original value.

Solid/liquid suspensions have been the subject of much research, and that these systems exhibit non-Newtonian behaviour has long been recognised. As far back as 1885, Osborne Reynolds(15), more noted for his work on turbulence, observed that a suspension of rigid particles in water simultaneously exhibited a viscosity increase and volumetric expansion under shear.

A theoretical treatment of very dilute suspensions of non-interacting, rigid spheres was put forward by Albert Einstein(16) in 1906.

Einstein's approach was purely hydrodynamic, and his model comprised an isolated sphere, situated in a simple shear flow field in an infinite fluid. The increase in the viscosity of the suspension due to the suspended particles is taken to be due to the relative increase of energy dissipation owing to the presence of the sphere. The resultant equation, relating suspension viscosity to volumetric packing fraction is given as:

$$\frac{\eta}{\eta_o} = 1 + \frac{5}{2}\, \emptyset \qquad (1.2.5)$$

where η is the suspension viscosity, η_o is the suspension medium viscosity and $\emptyset$ is the volumetric packing fraction. This relationship is generally found to be accurate for very low packing fractions, but fails for packing fractions greater than approximately 0.10(17).

The early part of the twentieth century saw a great deal of work carried out on solid/liquid suspensions, and many empirical models were postulated to describe the observed experimental behaviour. Although it would not be practicable to mention all the models that have been proposed, a brief description of those in more common use follows.

Probably the most widely used model is one proposed by Ostwald(18) around 1925, after observing that the non-Newtonian regions of experimental flow curves often follow a power relationship between stress and shear rate, put forward the following relationship, which has subsequently come to be known as the Power Law:

$$\tau = K\,\dot{\gamma}^{n} \qquad (1.2.6)$$

it may be noted that when:

$n < 1$ we have shear thinning behaviour

$n = 1$ we have Newtonian behaviour

$n > 1$ we have shear thickening behaviour.

Soon afterwards, Bingham$^{(19)}$ noted that some materials, particularly pastes, exhibit yield values, i.e. that these materials remained solid like below a critical stress. Such systems are known as Bingham Plastics, and are defined as follows:

$$\left.\begin{array}{lll} \dot{\gamma} = 0 & & \text{for } \tau < \tau_o \\ \tau = \tau_o + \eta_B \dot{\gamma} & & \text{for } \tau > \tau_o \end{array}\right\} \quad (1.2.7)$$

where τ_o is the yield stress, and η_B is the Bingham viscosity.

A contemporary research group led by Freundlich were simultaneously conducting an investigation into solid/liquid suspension rheology, particularly time-dependent, non-Newtonian behaviour. It was this research group who introduced the words thixotropy and rheopexy to describe the time-dependent decrease/increase in viscosity respectively of a fluid under shear$^{(20)}$.

Following a study on the rheology of filled varnishes, Casson$^{(21)}$ proposed a semi-empirical relationship to describe experimental flow curves. Casson was able to explain the form of his flow curve through the alignment of the suspended particles into 'rods'. The Casson equation, which appears below has been used extensively in industry:

$$\sqrt{\tau} = \sqrt{\tau_y} + \eta_c \sqrt{\dot{\gamma}} \quad (1.2.8)$$

where τ_y is the Casson yield value, and η_c is the Casson viscosity.

1.3 More Recent Developments in the Understanding of Suspension Rheology

Despite the considerable effort expended by experimental rheologists, from the pioneers described previously, to the present day, there still remains the lack of a consistent theory to explain the wide range of experimental behaviour.

The applicability of Einstein's equation (Equation (1.2.5)) was extended to slightly higher concentrations by Batchelor(22), who proposed:

$$\frac{\eta}{\eta_o} = 1 + \frac{5}{2}\,\phi + 6.2\phi^2 + 0\,\phi^3 \qquad (1.3.1)$$

Batchelor's extension to Einstein's equation is only applicable in the limit that the random particle distribution found at zero shear rate is not perturbed by the shear field, and is not found to hold at all for packing fractions greater than 0.15(23).

The majority of systems of interest to experimental rheologists, however, fall outside the bounds of applicability of the Einstein-Batchelor equation. The observation that many of these systems of interest exhibit strongly non-Newtonian behaviour at typical laboratory shear rates has led to their classification according to this behaviour. Diagrams of the type presented in Figure 1.3.1, summarising the observed rheological behaviour of suspensions can frequently be found in rheology text books.

The lack of a consistent theory to explain the wealth of observed behaviour is in no small part due to the great difficulty in even reproducing consistent data for identical systems in different viscometer geometries. This difficulty was reported by Cheng(2), who proposed that the steady shear properties of a dense suspension are not characterised by a unique flow curve, but rather one described by a shear stress-shear rate band.

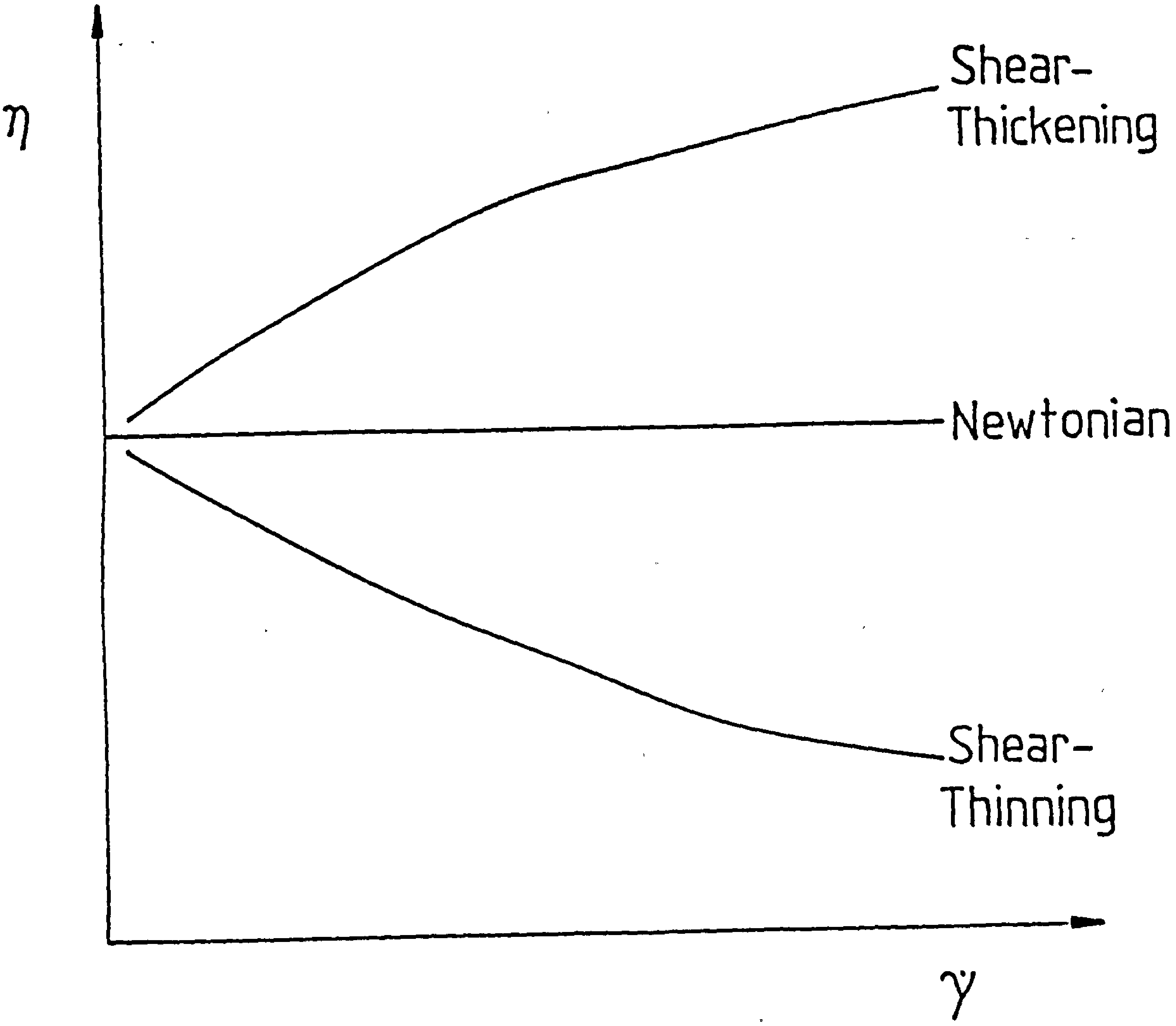

FIGURE 1.3.1: Typical Text Book Representation of Rheological Behaviour

Additionally, Leighton and Acrivos(24,25) have described experiments designed to investigate the assymptotic decrease in the viscosity of a suspension of polystyrene beads, as measured in a concentric cylinder viscometer. From the results of these experiments it was concluded that the viscosity decrease could be explained in terms of a shear induced particle migration from high to low shear rate regions within the concentric cylinder geometry. The authors attributed this particle migration to irreversible particle interactions.

Woodcock(26) had previously predicted such a shear induced particle migration from the results of his computer simulation studies, which established the importance of osmotic pressure effects in dense suspension rheology.

The fact that the shear history of a dense suspension can significantly affect the observed rheological properties of that system is well known amongst experimental rheologists. This presumably contributes significantly to the difficulties encountered in the accurate characterisation of these systems. This difficulty can be explained in terms of the very long relaxation times of particles comprising dense suspensions. The characteristic relaxation time in this context may be visualised as the average time taken for a particle to diffuse over a length comparable to its diameter. Consequently, it can be taken as an indication of the time required for structural rearrangement, and hence determines the time scale necessary for the achievement of steady state conditions(27).

More recently, developments in emulsion polymerisation have made possible the production of nearly monodisperse, spherical particles in the colloidal size range(28), which can be suspended in Newtonian liquids to form well characterised, dense suspensions. The study of these suspensions enables the elimination of 3 experimental variables immediately, namely particle shape, size and size distribution. As a result of the study of these simplified systems, significant advances are now being made towards the understanding of the rheological and equilibrium properties of dense suspensions.

Experiments carried out by Pusey and Van Megen(5) on stabilised poly-methylmethacrylate particles suspended in a mixture of carbon disulphide and decalin showed that these systems display a variety of phase behaviour resembling that of simple atomic or molecular systems. Nearly monodisperse colloidal suspensions have been shown to crystallise into face centre cubic arrangements(29).

An investigation into the mechanisms underlying the observed shear thinning and thickening behaviour of polyvinyl chloride and polystyrene acrylonitrile particles was conducted by Hoffman(30). Particle arrangements within various shear rate regimes were examined by light diffraction techniques. Hoffman concluded that the shear thinning of his suspensions could be explained in terms of the formation of layers of hexagonally packed 2-dimensional layers passing over one another in the direction of flow. The subsequent shear thickening is explained in terms of the disruption of this 2-dimensional order.

Using a dimensional analysis approach, Krieger(31) proposed a 'corresponding rheological states' basis for the comparison of rheological data. This approach predicts that two hard sphere suspensions at equivalent volume fractions would exhibit the same relative viscosity, if compared at equivalent values of reduced shear stress. The form of the reduced stress value, which is defined below aims to express the relative importance of the flow field to Brownian motion:

$$\tau_r = \frac{\tau a^3}{KT} \qquad \eta_r = \frac{\eta}{\eta_o} \qquad (1.3.2)$$

where τ_r = reduced stress, a = particle diameter, K is Boltzmann's constant and T is absolute temperature.

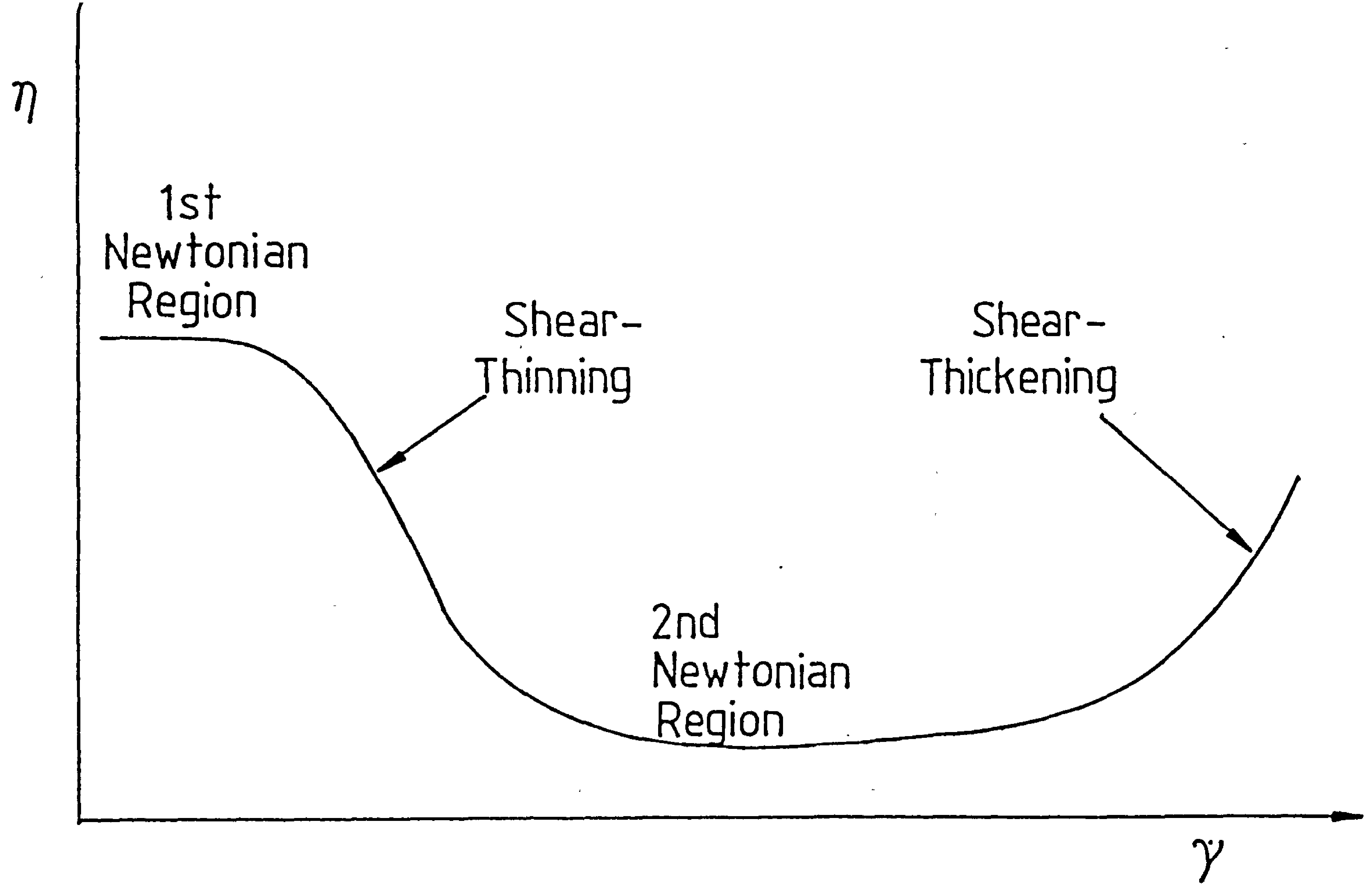

FIGURE 1.3.2: The Generalised Flow Curve

For his theory to hold, Krieger pointed out that suspended particles must be uniform, spherical, rigid and interact through hard sphere repulsions. Despite these limitations, Krieger's approach has enjoyed some success, and is frequently used for the presentation of rheological data.

In his survey of 'Industrial Problems and Academic Progress', Barnes(32) introduced the 'generalised flow curve', which embodies all the commonly observed aspects of dense suspension rheology. The features of this generalised flow curve are reproduced in Figure 1.3.2. Barnes went on to suggest that all dense suspensions would exhibit the broad features of this flow curve if it was possible to examine them over a sufficiently wide shear rate range. The hitherto accepted view that different suspensions exhibit different types of rheological behaviour as summarised in Figure 1.3.1, therefore, is merely a consequence of the limited stress-shear rate 'windows' of laboratory rheometers.

1.4 Computer Simulation Studies

Of the 3 classical states of matter, the state which, to date has presented the greatest problems to the scientist wishing to probe microstructure and its relation to macroscopic properties, is undoubtedly the liquid state.

The most important experimental techniques used to probe liquid microstructure are based on the scattering of radiation. Technical difficulties, coupled with the relatively small amount of information one can actually derive from these radiation scattering experiments limit their usefulness(33).

A complementary and quasi-experimental means of probing any of the states of matter is that of computer simulation. The very first computer simulation of the liquid state was performed by Metropolis et al.(34) at the Los Alamos National Laboratory in the United States.

These initial studies focussed upon a system of particles interacting through a discontinuous inter-particle potential, the so called 'Hard Sphere' potential, defined below:

$$\phi = 0 \quad \text{when} \quad r > \sigma$$

$$\phi = \infty \quad \text{when} \quad r < \sigma$$

where ϕ = inter-particle potential, r = separation of particle centres and σ = particle diameter. These initial simulations laid the foundations of a computational technique which has subsequently grown considerably in importance. Monte Carlo is the name given in mathematics to the numerical integration of difficult, often multidimensional integrals, by random sampling techniques. The Monte Carlo method of Metropolis et al. involves the generation of a series of particulate configurations in such a way that the configurations are distributed according to some pre-selected probability distribution. The averaged value of any configurational property then converges onto the statistical mechanical ensemble mean value providing a large enough number of configurations have been considered. Shortly after this initial work the properties of a system of particles interacting through the continuous Lennard-Jones potential were determined from a Monte Carlo simulation(35).
The Lennard-Jones potential, defined below has since frequently been used to describe the interactions between particles in computer simulation studies:

$$\phi = 4\varepsilon \left[\left(\frac{\sigma}{r}\right)^m - \left(\frac{\sigma}{r}\right)^n \right] \tag{1.4.1}$$

where m is usually given a value of 12, and n a value of 6. The first term in the square brackets represents the repulsive component, and the second term is the attractive component of the potential.

Despite being of considerable value in the study of the liquid state, Monte Carlo simulations are only able to provide information on equilibrium properties. In order to probe the dynamic behaviour of model systems, an alternative approach, namely Molecular Dynamics (MD) simulation is used.

Alder and Wainwright first succeeded in performing a MD simulation of the previously described hard sphere system in 1957(3). The discontinuous nature of the hard sphere potential simplifies the situation considerably. Hard particles travel in straight lines at constant velocity between collisions. The problem is therefore reduced to that of calculating potential collision times for each particle, followed by the solution of consecutive binary collisions. Despite its relative simplicity, the hard-sphere system has been shown to exhibit many properties characteristic of real systems(36), and to the present day remains an actively researched area(37-40).

Some years later Rahman(41) extended the MD simulation technique to study a system of atoms in liquid argon interacting through the more realistic Lennard-Jones potential. MD simulations of systems interacting through continuous potentials require a step-wise approach to the integration of the equations of motion, inevitably introducing a degree of approximation. Rahman's pioneering work utilized a predictor-corrector algorithm, however in order to yield an accurate prediction of particle trajectories, 2 or 3 predictor-corrector iterations were required, and hence the algorithm was computationally inefficient.

A few years later, Verlet(42) described a method for integrating the equations of motion based upon a direct solution of the second order differential equation. The Verlet algorithm is easy to program, time reversible, conserves linear momentum, and has been shown to have excellent energy conservation properties(43). For these reasons the Verlet algorithm and its various modifications are probably the most widely used method for the integration of the equations of motion in MD simulations.

As computational resources subsequently became more widely available, the use of dynamical simulations by scientists, to probe a wide range of experimentally inaccessible phenomena increased dramatically. A review of the diverse areas studied was given recently by Abraham(44).

Although Molecular Dynamics simulations can be used to examine systems of particles interacting through any effective pair potential, the bulk of work to date has focussed upon one of 3 model potentials. The Hard Sphere and Lennard-Jones potential have already been described. The remaining well studied pair potential corresponds to the repulsive component of the Lennard-Jones potential, and has been called the Soft Sphere (SS) potential. It may be defined as the following:

$$\phi = \varepsilon \left(\frac{\sigma}{r} \right)^{n} \qquad (1.4.2)$$

where ε is the unit of energy; σ is the unit of length; r is the distance between particle centres; and n is usually given the value of 12. The SS potential's appeal lies in its unique scaling properties(45). These properties stem from the fact that changes in reduced temperature, $T^* = (KT/\varepsilon)$ can be equated in terms of reduced volume $V^* = (V/N\sigma^3)$. As a result, the state of a SS system can be completely defined by one reduced hybrid state variable $(V^{*4}T^*)$.

Surprisingly, little work has been published in the scientific literature concerning the effects of polydispersity upon the properties of solid/liquid suspensions. Along with occasional collaborators, Dickinson has studied the effects of polydispersity upon the equilibrium phase diagram of dense suspensions(46-50). An initial Monte Carlo study(46) led to the prediction that the osmotic pressure of an ordered colloidal suspension would increase with polydispersity. This study was complemented with a MD study that suggested the osmotic pressure of the fluid phase to be virtually independent of polydispersity, whilst supporting the previous prediction concerning the ordered phase. This line of thought has been extended further with the estimation of a 'critical' degree of polydispersity, defined as that beyond which no fluid-crystalline transition could occur. From an extrapolation of volume change associated with the transition, against polydispersity, to zero volume change, a critical degree of polydispersity of 30% was estimated.

Salacuse and Stell(51) investigated the statistical thermodynamics of polydisperse systems of particles. Systems of hard spheres and hard spheres with Kac tails are treated as illustrative examples. Quantitative results using a Schultz distribution of particle diameters are given. It is proposed that for a d-dimensional system of particles, the equation of state may be characterised from m_o through m_d (dth moment of particle size distribution), and the system density.

Hansen et al.(52) examined the effects of polydispersity upon phase equilibria, and particularly the critical packing fraction. Extending conformal solution theory to incorporate polydispersity, the authors conclude that for small degrees of polydispersity, the increase in critical packing fraction is very low.

One particular aspect of liquid behaviour which has attracted the attention of many workers in the area of dynamical simulations is that concerning the response to an applied shear field, i.e. the rheological characteristics of model liquids. A review of the work published to date in this area will form the bulk of the remainder of this section.

Any transport coefficient may be defined as the response of a system to an applied perturbation; shear viscosity, for example, being a measure of the shear stress induced by an applied velocity gradient.

The response of a system to an applied perturbation can be related to fluctuations in the properties of the system at equilibrium. These equilibrium fluctuations may be monitored by the use of time correlation functions. For the case of shear viscosity (η):

$$\eta = \frac{V}{K_B T} \int_0^\infty < P_{\alpha\beta} (t) \, P_{\alpha\beta} (o) > dt \qquad (1.4.3)$$

where V = volume, K_B = Boltzmann's constant, T = temperature, t = time, and $< P_{\alpha\beta} (t) \, P_{\alpha\beta} (o) >$ represents the normalised, ensemble averaged, stress correlation function, where:

$$P_{\alpha\beta} = -\frac{1}{V} \left[\sum_i \frac{p_{i\alpha} \, p_{i\beta}}{m \; i} + \sum_i \sum_{j>i} r_{ij\,\alpha} \, f_{ij\,\beta} \right] \qquad (1.4.4)$$

and $p_{i\alpha}$ is the α momentum component of particle i, m is the mass of particle i, $r_{ij\,\alpha}$ is the relative α-position co-ordinate of particle i, and $f_{ij\,\beta}$ is the β component of force between particles i and j.

The relationships between time correlation functions and transport coefficients are generally termed Green-Kubo formulae(53). These relationships form the basis of the first method used to access the shear viscosity of model systems. A discussion of the role of correlation functions in calculating transport coefficients is given by Hansen and McDonald(33), and Allen and Tildesley(54).

A comprehensive study of the velocity auto correlation function, self diffusion coefficient and shear viscosity of the hard-sphere system has been reported by Alder and co-workers(55). In this work the shear viscosity is not calculated through the Green-Kubo relation, but by the equivalent Einstein expression:

$$\eta = \lim_{t \to \infty} \frac{1}{2VKTt} \left\langle \sum_{i=1}^{N} p_{\alpha i}(t) \, R_{\beta i}(t) - p_{\alpha i} \, R_{\beta i}(o) \Big]^2 \right\rangle \qquad (1.4.5)$$

Levesque et al.(56) pioneered the use of Green-Kubo relations to calculate the shear viscosity of a system of particles interacting through the LJ potential. Many papers have subsequently appeared in this area(51-58). A major disadvantage of the 'equilibrium' approach to the calculation of shear viscosity is the difficulty experienced in the integration of the stress correlation function. The problem lies in the persistence of a finite stress correlation, even at relatively long times. This so called 'long time tail', combined with the decreasing quality of signal/noise ratio poses a major problem with respect to the integration of the stress correlation function(54).

These difficulties lead scientists to consider an alternative approach, more akin to a laboratory investigation of shear viscosity. Essentially, the simulation system is subjected to a perturbation sufficiently large so as to significantly enhance the system response.

One obvious consequence of this large applied perturbation is that the simulation system can no longer be assumed to be at equilibrium, and hence the approach has become to be known as Non Equilibrium Molecular Dynamics (NEMD) simulations.

Among the first reported NEMD studies was that reported by Gosling et al.(60) who applied a sinusoidally varying force to a system of LJ particles with parameters appropriate to liquid argon. The form of the applied force was consistent with conventional periodic boundary conditions (Figure 1.4.1), and the resultant sinusoidally varying drift velocity was related to the shear viscosity. Problems were encountered, owing to the magnitude of force required to achieve the desired signal/noise ratio enhancement leading to a rapid temperature rise. Despite this drawback, the authors report reasonable agreement with experimental data, and the technique represented a substantial saving in computational effort when compared to the time correlation function approach.

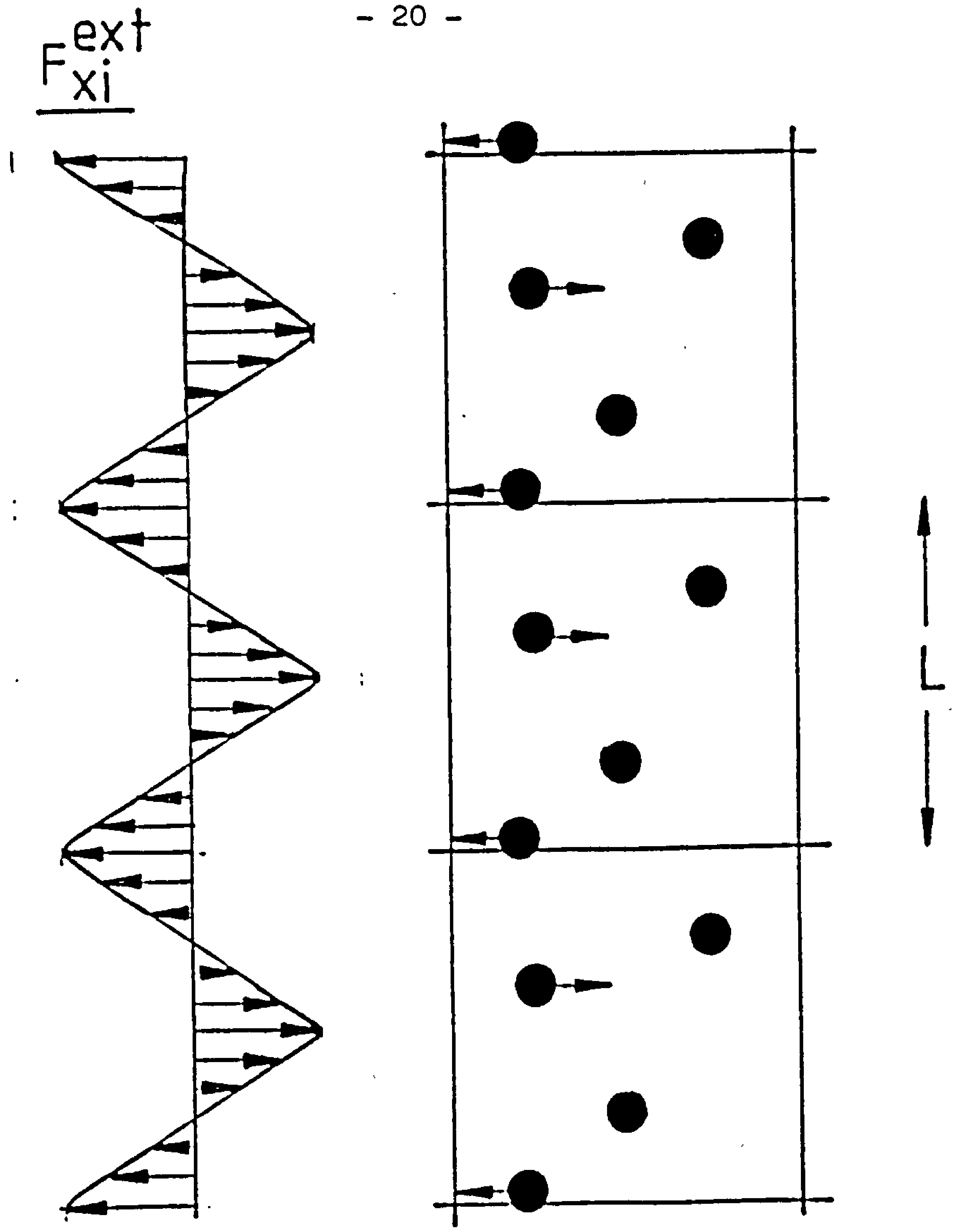

FIGURE 1.4.1: Sinusoidally Varying Velocity Profile

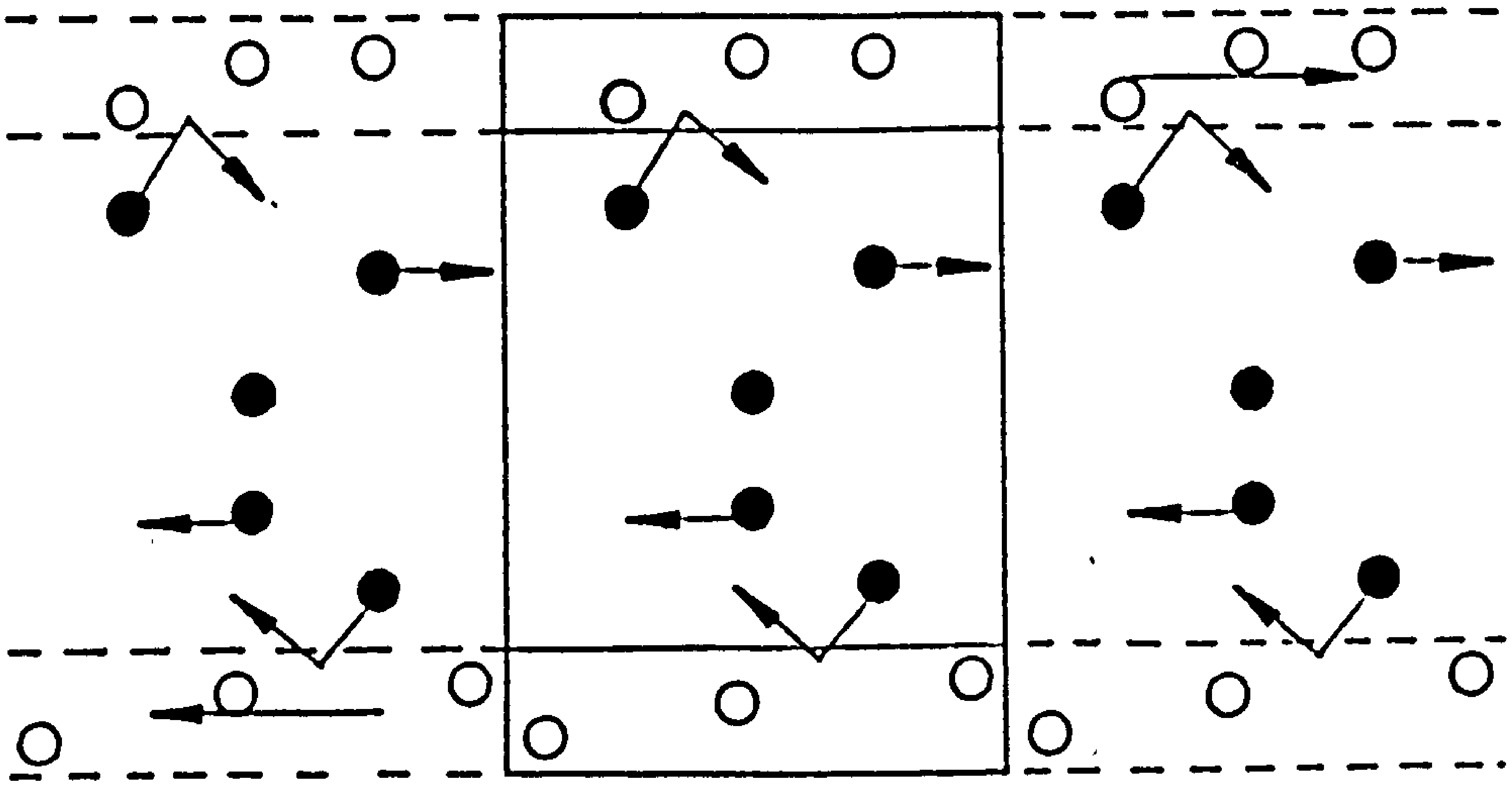

FIGURE 1.4.2: Ashurst and Hoover's 'Fluid Walls' Shearing Boundary Conditions

Around the same time, Ashurst and Hoover(61) devised an alternative procedure aimed at the simulation of planar Couette flow. Their approach involved replacing periodicity in one of 3 cartesian dimensions by a relatively narrow layer of identical particles, at equivalent density to the bulk system (Figure 1.4.2). Particles comprising these 'fluid walls' were given preferential velocities in the direction of flow. This preferential velocity is transferred from the fluid walls to the bulk system via particle interaction across the bulk/wall boundary. As steady state conditions are approached, a linear velocity profile develops in the bulk system. The system is thermostatted by adjusting the kinetic energies of the particles comprising the fluid walls. The removal of periodicity in one dimension leads to a dependence of the results upon system width. Nevertheless, a reasonable agreement with experiment is reported for LJ particles with parameters appropriate to argon.

The majority of NEMD simulations performed subsequently have made use of a modification to the conventional periodic boundary conditions, originally described by Lees and Edwards(62). In this approach the upper and lower periodic image cells are deemed to be translating in the direction of flow relative to the static central simulation cell. A velocity profile which effectively extends to infinity is created by these translating periodic image cells. A fuller description of the Lees-Edwards shearing boundary conditions can be found in the next chapter.

Ashurst and Hoover(63,64) studied the shear viscosity of both the LJ and SS fluids, and parametrised the results to obtain a 'best-fit' expression for the shear viscosities over the whole temperature-density range. The authors also compared the results with experimental data for hydrogen and deuterium, and reported excellent agreement.

More recently Woodcock(65) has evaluated this expression for the shear viscosity prediction of molecular liquids. Even for highly non-spherical molecules, predicted viscosity values were found to deviate by no more than 50% of the experimental values, whereas viscosities of the liquids scrutinised span many orders of magnitude. These encouraging results clearly demonstrate the importance of using scaling laws to describe the volume-temperature dependent viscosity/rheology of complex fluids.

The shear viscosity of the HS fluid was examined by Naitoh and Ono(66,67) using the Lees-Edwards shearing boundary conditions. In the absence of any thermostatting procedure, the temperature of the simulation system was allowed to continuously increase. The rate of temperature increase was used as a basis for viscosity calculation to complement the more usual method involving shear stress evaluation. Excellent agreement between viscosity values calculated from the 2 alternate approaches was found.

Naitoh and Ono's NEMD studies at low shear rates were later supplemented by Erpenbeck(68,69), who examined the response of the hard sphere system to higher shear rates. In order to limit the rapid temperature rise at these higher shear rates, particle peculiar velocities were intermittently rescaled so as to return the system total kinetic energy to the desired value. Erpenbeck reports a shear induced phase transition at higher shear rates, characterised by a 2-dimensional ordering with a corresponding sharp decrease in viscosity.

A modification of the Lees-Edwards shearing method was proposed by Evans(70), aimed at the elimination of spontaneous shear rate fluctuations. In his method, Evans adjusts individual particle velocities in such a manner that a least squares fit of the actual linear velocity profile leads to the desired shear rate.

Heyes et al.(71) made use of Evans' modification to study the effect of high shear rates upon a system of Lennard-Jones particles. Structural anisotropy was observed in the sheared fluid, and resolution of the diffusion coefficient showed differences between the 3 cartesian components.

A short time later, Evans and Morriss(72) introduced a method of incorporating the velocity profile imposition directly into the equations of motion. In practice, for an x-velocity profile in the y-direction, the method involves incrementing individual particle x-co-ordinates by an amount depending on that particle's y-co-ordinate. Lees-Edwards shearing boundary conditions are still utilised to maintain continuity of the velocity profile in the positive and negative y-direction. This method with its variations(73) now forms the basis of a great deal of NEMD simulations.

Originally motivated by an interest in the behaviour of lubricants under conditions of high temperature, pressure, and shear rate, Heyes and co-workers(74-81) have examined the non-equilibrium properties of the Lennard-Jones system in great detail. The earliest studies made use of the Lees-Edwards shearing boundary conditions to superimpose a velocity profile. The shear rigidity modulus was obtained from the system relaxation following an instantaneously imposed shear. Comparisons of shear viscosity obtained from NEMD studies at low shear rates were made with values obtained from the integration of time correlation functions, and good agreement was reported. In an attempt to improve the signal/noise ratio of the system response at low rates of shear, the 'segmented MD' approach, first proposed by Ciccotti et al.(82) was used. In this approach, statistical noise is eliminated by allowing the simultaneous evolution of 2 systems, originating from 2 identical points in phase space. One of the concurrent simulation systems is subjected to a perturbation, whilst the remaining system is left unperturbed. By subtracting the random fluctuation in the system response, as exhibited by the unperturbed system, from the perturbed system response, an improvement in signal/noise ratio is achieved. The assumption here, that statistical noise is correlated in the 2 systems, evidently breaks down after a fairly short time. For this reason it is necessary to regularly halt the progress of the perturbed system and originate a 'new' perturbed system from a point in phase space arrived at by the equilibrium trajectory.

Later work(75) proposed the method of Modified Homogeneous Shear (MHS) for the imposition of a flow field. More recently Heyes has used the SLLOD equations of motion, as proposed by Evans and Morriss, to impose a velocity profile upon his Lennard-Jones systems. The form of the Lennard-Jones flow curve was tested at various densities against several macroscopic rheological equations(79). The Carreau and Cross models were found to fit the shear thinning curves for densities slightly below the freezing density, whilst a Herschel-Buckley equation was found to be more suitable at higher densities.

A study of the tensile viscosity of the Lennard-Jones system has been performed by gradually elongating the central simulation cell in one dimension(76). Owing to the non-regenerative nature of elongational flow, difficulty was experienced in reaching steady state conditions. For this reason the standard route to viscosity calculation in NEMD simulations, i.e. a calculation of the steady state stress reponse was not practicable, and consequently a viscoelastic response was monitored.

A substantial amount of effort has been recorded in the scientific literature regarding the development of methods for performing isokinetic MD simulations. Equilibrium MD simulations can be maintained at constant temperature in a number of ways. Andersen(83) proposed a technique in which a randomly chosen particle is deemed to undergo a collision with a particle from an imaginary heat bath at a pre-selected frequency. In practice the velocity of the chosen particle is replaced by one sampled from the Maxwell-Boltzmann distribution.

Instead of altering the velocity of a randomly selected particle from time to time, Andrea et al.(84) proposed a method in which all particle velocities are resampled simultaneously, but correspondingly less frequently. These two methods are part of a group of methods which have been categorised as 'Stochastic Methods'(54).

Clearly, any method which replaces particle velocities by pseudo-randomly sampled velocities, represents an inappropriate choice to maintain isokinetic conditions in any system where correlations in particle velocities might exist.

An alternative approach involves the simulation of a thermal reservoir in contact with the bulk system, between which energy is allowed to flow. Nosé has presented the details of this type of simulation(85), in which a pre-selected parameter controls the rate of heat flow. Ashurst and Hoover's pioneering use of 'fluid walls'(61) to simultaneously impose a velocity profile upon, and subsequently control the temperature rise of, a model system falls into this category of 'Extended System' methods.

The easiest way to maintain isokinetic conditions is simply to rescale individual particle velocities by a factor $(To/T)^{\frac{1}{2}}$ where To is the desired, and T is the actual temperature, as often as is required. This procedure was originally suggested by Woodcock(86).

Evans et al.(87) later derived a velocity rescaling method based upon Gauss's principle of minimum constraint. The method, referred to as 'Gaussian Isokinetic Dynamics' has been put to use by some workers(78).

Other methods have been proposed and discussed at length by other workers(87,89). A review of the various methods of 'Isothermal Constraint Dynamics' has been published recently by Woodcock(90), in which he concludes that the methods of simple continuous renormalization and Gaussian Isokinetic Dynamics are essentially equivalent. A further relevant point contained therein is that the difference between results obtained using the various methods is negligible for systems of sufficient size, i.e. several hundred particles or more.

A recently published paper(91) describes the simulation of a fluid confined between narrow walls, resembling a capillary. When subjected to an external force, akin to gravity, a parabolic velocity profile reminiscent of Poiseuille flow is observed to develop.

Woodcock(4) has pointed out that NEMD simulations more closely resemble planar Couette flow in colloidal suspensions than atomic or molecular liquids as previously proposed. In this context, the suspension medium plays a dual role, that of transmitting the shearing force, coupled with the damping of particle velocities to maintain an effectively constant particle kinetic energy. In addition, the pressure trace evaluated throughout a simulation corresponds to a suspension osmotic pressure, rather than the hydrostatic pressure relevant to an atomic or molecular simulation. With the help of his particle dynamics simulations Woodcock elucidated the osmotic pressure dependence upon shear rate(26). The serious implications of this relationship upon the experimentally observed rheology of dense suspensions were also discussed. Further simulations of the soft sphere model enabled the observed form of an experimental flow curve to be explained in terms of a shear induced perturbation of the equilibrium phase behaviour(92).

A review article describing the progress made to date towards the fundamental understanding of dense suspension rheology through the use of dynamical simulations has been written by Barnes et al.(93). The review discusses the shortcomings of currently adopted engineering approaches in light of this recent progress.

Very recently, Woodcock(94) has devised an algorithm to incorporate a simplified form of hydrodynamics into the hard-sphere equations of motion. In this 'Mean Field Stokesian Dynamics' (MFSD) approach particle velocities may be damped by an amount which can be related to the viscosity of the suspension medium. When the hard-sphere system is sheared, the MFSD method can be implemented in one of two ways:

(i) Particle velocities can be damped by a differing, shear rate dependent amount such that isokinetic conditions are maintained.

(ii) Particle velocities can be damped by a constant, shear rate dependent amount, leading to the hard sphere system equilibrating at a different kinetic energy for each shear rate point studied.

This latter procedure is more akin to experiment, where particle kinetic energies are unknown functions of suspension medium viscosity and shear rate. Woodcock progresses to point out the consequences of the physically unrealistic approach of maintaining isokinetic conditions irrespective of shear rate. The main consequence is that isokinetic simulations performed over a wide shear rate range, lead to a flow curve whose form is inverted with respect to experimental flow curves.

The use of NEMD simulations have not been restricted to the study of systems of simple spherical particles. Whittle and Clarke(95) performed NEMD simulations upon a system of diatomic molecules with parameters known to resemble nitrogen at liquid densities. Several papers have appeared describing the study of model molecules resembling n-alkanes(96,97), in which shear induced effects such as molecular alignment, deformation, and rotation are described.

Brown and Clarke(98) have simulated amorphous and crystalline regions of a model polymer fibre. Semi-crystalline polymer fibres are believed to comprise small, oriented crystallites separated by small (100 - 500 segments) amorphous regions. The relatively small number of chain segments simulated, consequently has some justification. The study provides support to previous conclusions that interchain forces have little direct influence upon the stress developed across microstructures. Under tension, however, evidence of significant indirect effects was found.

A procedure for incorporating the effects of Brownian motion into MD simulations has been described by Ermak and McCammon(99). In these 'Brownian Dynamics' simulations, particles are subjected to randomly fluctuating thermal forces deemed to originate from the suspension medium. Despite subsequent improvements(100), at present the methods do not lead to the correct equilibrium properties for colloidal-like spheres. The problem arises from the non-Boltzmann weighted nature of the randomly fluctuating forces.

Other workers(101) have attempted to incorporate the many body hydrodynamic effects in addition to inter-particle and Brownian forces into their computer simulations of colloidal suspensions. The complexity of the non-pairwise additive, hydrodynamic forces has, to date limited these simulations to a relatively small number of particles in 2 dimensions.

CHAPTER 2

DESCRIPTION OF THE SIMULATION METHODS

CHAPTER 2

DESCRIPTION OF THE SIMULATION METHODS

2.1 Introduction

The primary objective of the present work is the investigation of the rheological phenomena exhibited by dense colloidal solid/liquid suspensions. The computational techniques that have been used are based upon simulation methods that have evolved over the last few decades, and which were originally aimed at the study of matter at the atomic or molecular level(3).

There are several important differences between the dynamical simulation of a system of suspended particles and that of a simple liquid that require clarification from the outset. Of central importance in a molecular-dynamics study is the concept of an effective inter-molecular pair potential, defining the force-distance relationship between interacting molecules. The pair-potentials used in the present simulations correspond to an effective 'potential of mean force'(106) embodying contributions from the suspension medium and suspended electrolyte in addition to particle-particle interactions. Calculated pressure values of the model systems arising from a summation of interparticle repulsions correspond to the osmotic pressure of a colloidal solid/liquid suspension.

The motion of suspended colloidal particles will, undoubtedly, be influenced by the presence of the suspension medium. Brownian motion arising from the random collision with solvent molecules is important for small suspended particles of 1 μm or less in diameter. At intermediate concentrations, when the flow of solvent molecules around a suspended particle is perturbed by the presence of neighbouring suspended particles, many-body hydrodynamic effects should be taken into consideration. Many-body hydrodynamic forces are extremely complex, and attempts to incorporate them into dynamical simulations are currently restricted to a relatively small number of particles in two dimensions(101).

Woodcock(65) has recently derived the following expression which may be used to estimate the average distance x to the first neighbour for an amorphous hard-sphere suspension:

$$x = \left[\frac{1}{3\pi y} + \frac{5}{6} \right]^{\frac{1}{2}} - 1 \qquad (2.1.1)$$

A plot of x as a function of packing fraction(y), reproduced from Reference (65) appears in Figure 2.1.1. The present work is concerned with dense colloidal suspensions where the effective packing fraction is typically in excess of 0.4. Figure 2.1.1 shows that typical separations between nearest-neighbour particle surfaces in this high packing fraction regime are very small, and consequently the forces between particles are dominated by geometric packing considerations. For this reason many-body hydrodynamic and Brownian motion effects are not incorporated into these simulations.

Effective pair-potentials used in the present study have been chosen for their simplicity. Full descriptions appear in the subsequent, relevant sections of this chapter. In certain situations these simple effective pair-potentials are shown to exhibit scaling properties, which are of great importance in the application of simulation results to the study of experimental phenomena.

Essentially the simulations involve the prediction of the trajectories of a fixed number N of particles around a central simulation cell. Since Brownian motion and many-body hydrodynamic effects are explicitly omitted here, particle trajectories may be predicted via the step-wise numerical integration of the classical Newtonian equations-of-motion, i.e.

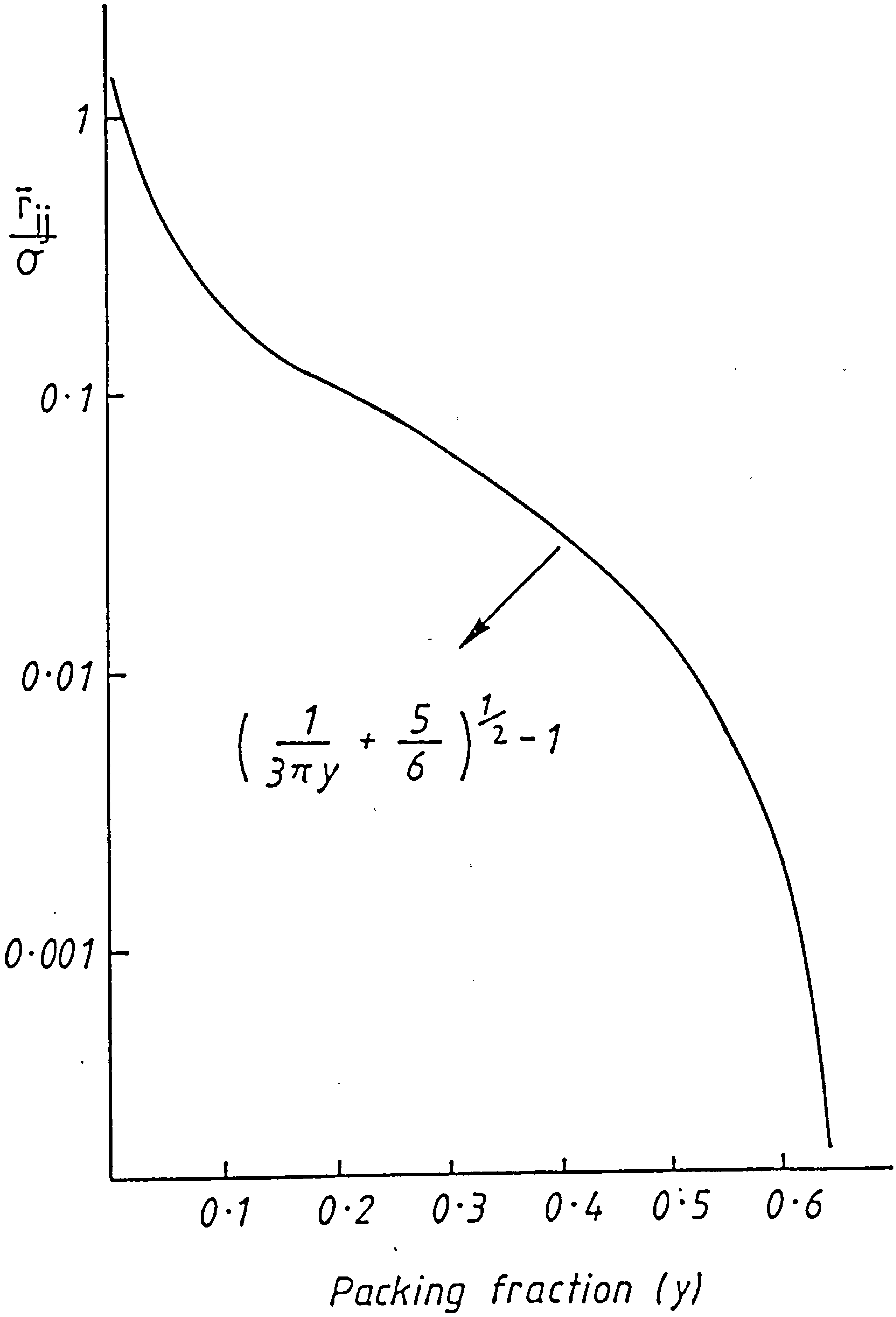

FIGURE 2.1.1: Mean Distance to the Nearest Neighbouring Particle of the Hard-Sphere Model as a Function of Packing Fraction

$$\frac{d\,\underline{r_i}}{dt} = \frac{\underline{p_i}}{mi} \qquad (2.1.2)$$

$$\frac{d^2\,\underline{r_i}}{dt^2} = \frac{\underline{f_i}}{mi} \qquad (2.1.3)$$

where: $\underline{r_i}$ is the particle position, $\underline{p_i}$ is the particle momentum; $\underline{f_i}$ is the particle force; m_i is the particle mass and t is time.

A convenient system of reduced units expressed in terms of parameters fundamental to the simulation system are used during the simulations, as well as for the subsequent presentation of results. The fundamental parameters used are particle mass (m), diameter (σ) and energy (Eo). Definitions of these reduced units (denoted by a superscript dagger †) are given in Table 2.1.1.

Despite an ever-increasing availability, computational resources currently practically restrict the size of a simulation system to a relatively small size, typically less than a thousand particles. In order to remove the effects of the resultant unacceptably high proportion of 'surface' particles, periodic-boundary conditions have been utilised. Here the central simulation cell is deemed to be surrounded by identical replicas of itself in all cartesian dimensions. Particles leaving the central simulation cell through one face are replaced by identical particles re-entering through the opposite face. In addition to the removal of undesirable boundary effects, periodic boundaries also aid the necessary conservation of constant overall system density and zero total momenta. A two-dimensional representation of periodic boundary conditions appears in Figure 2.1.2.

At the very outset of a particulate-dynamics simulation, particle velocities are pseudo-randomly sampled through the use of a suitable

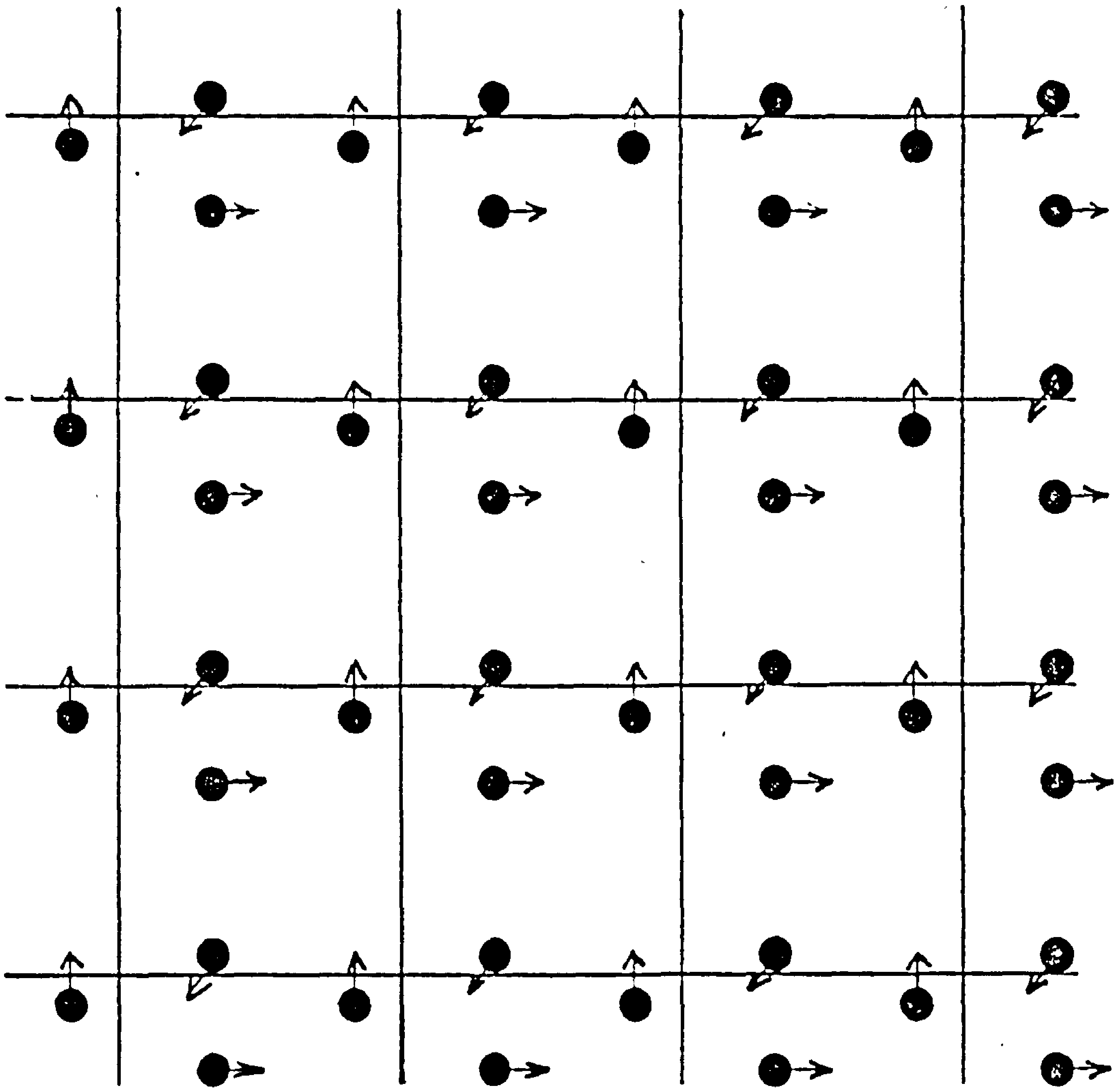

FIGURE 2.1.2: Two-Dimensional Representation of Periodic Boundary Conditions

NAG routine(102). Conditions of zero total momenta in each cartesian dimension, together with a system kinetic energy of the desired value are initially created by the adjustment of particle velocities as necessary. Subsequent conservation of these system properties is taken as an indication of the accuracy of the equations-of-motion integration procedure.

The heart of any particulate-dynamics simulation involves the execution of a computationally expensive 'double loop' during which, all particle pairs are sequentially considered. A considerable saving in execution time required for this double loop is possible through the use of the 'link-cell' method. Here the central simulation cell is sub-divided into a matrix of link-cells (Figure 2.1.3). The dimensions of each link cell are chosen such that, for any particle located in a central link cell, only particles located within the immediate 'skin' of neighbouring link-cells need be considered. Particles contained within each link-cell are imaginarily linked together to form a closed chain. The sequence of particle consideration now proceeds from one link cell to another, and around the particle chain within each link cell. Any particle is freely available to move between link cells, involving the breaking and reforming of particle chains. It must be stressed that this method is purely a time-saving device, and that particle trajectories are unperturbed through its use.

2.2 Hard-Sphere Particulate Dynamics

Conceptually the hard-sphere model constitutes the simplest realistic representation of a system of interacting particles. In recent years this classical model has proved to be of great value to the physical scientist wishing to probe macroscopic experimental phenomena at the microscopic level. As a result of this considerable interest, the hard-sphere model has been the subject of a large number of scientific

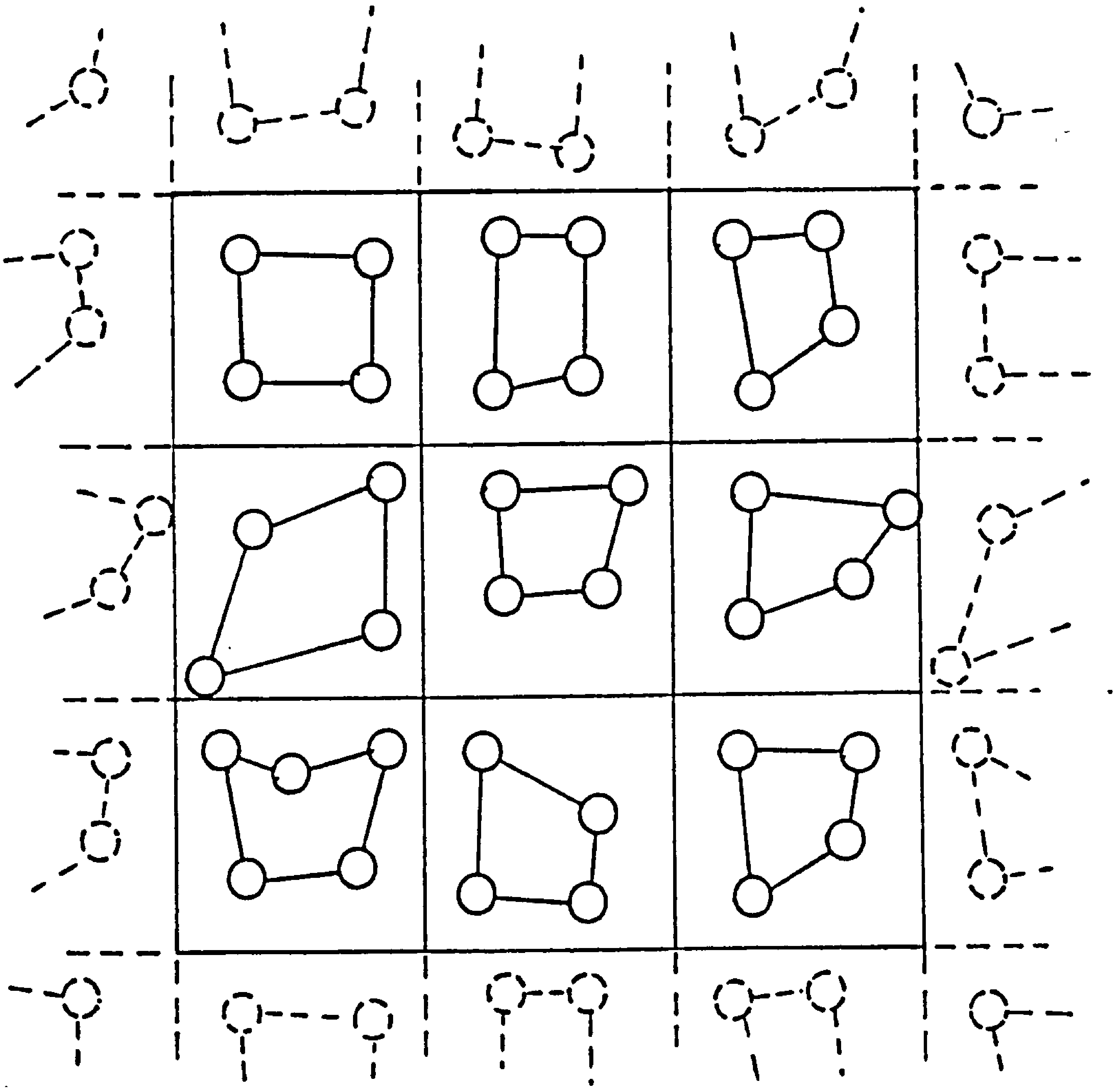

FIGURE 2.1.3: Two-Dimensional Representation of the Link-Cell Method

publications, and consequently its equilibrium phase behaviour is relatively well documented(33). Figure 2.2.1 summarising this equilibrium behaviour is reproduced from Reference (65).

The suitability of the hard-sphere model as a basis for the description of the equilibrium properties of concentrated particle suspensions interacting through fairly short-ranged potentials has been pointed out previously by Van Megen and Snook(103,104). The one-component plasma is suggested as a more appropriate reference model for suspensions interacting through longer range potentials such as an unscreened Coulomb potential(105).

Despite the accepted applicability to the study of both atomic/molecular systems and solid/liquid suspensions, surprisingly little work has been reported in the scientific literature concerning the study of the sheared hard-sphere fluid. One of the objectives of the present work is to perform such a study.

The classical hard-sphere model (illustrated in Figure 2.2.2) may be formally defined by the following:

$$\begin{aligned} \phi &= 0 \qquad \text{when } r > \sigma \\ \phi &= \infty \qquad \text{when } r \leq \sigma \end{aligned} \tag{2.2.1}$$

where the interparticle separation is represented by r, and the particle diameter by σ.

Classical hard-spheres may be visualised as perfectly hard billiard balls, travelling in straight lines at constant velocity between elastic collisions.

When suspended in a liquid however, particle velocities must be damped due to particle-liquid frictional forces. The simplest description of this velocity damping originates from Stokes' Law, and predicts a frictional force proportional to the particle-liquid relative

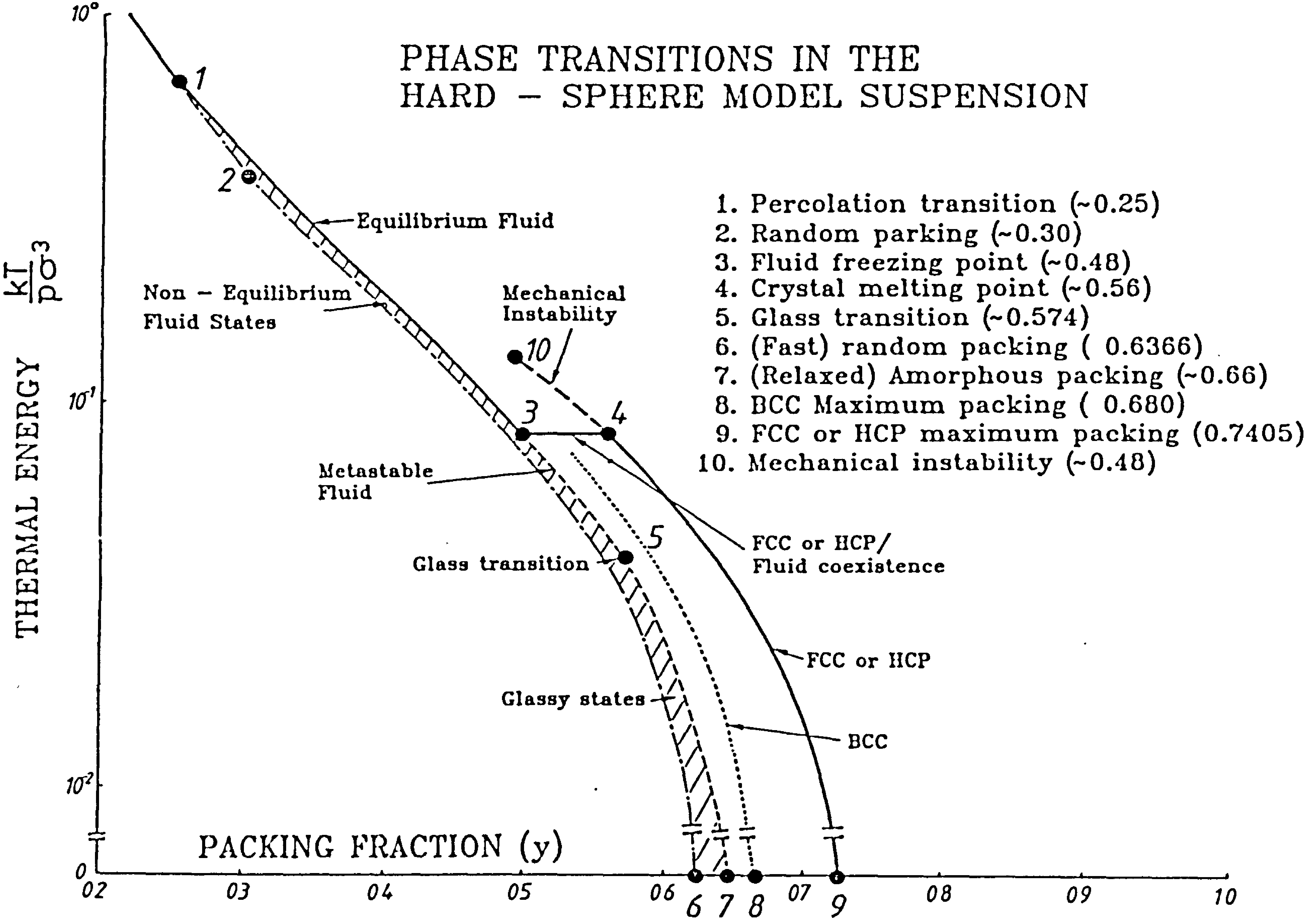

PHASE TRANSITIONS IN THE
HARD – SPHERE MODEL SUSPENSION

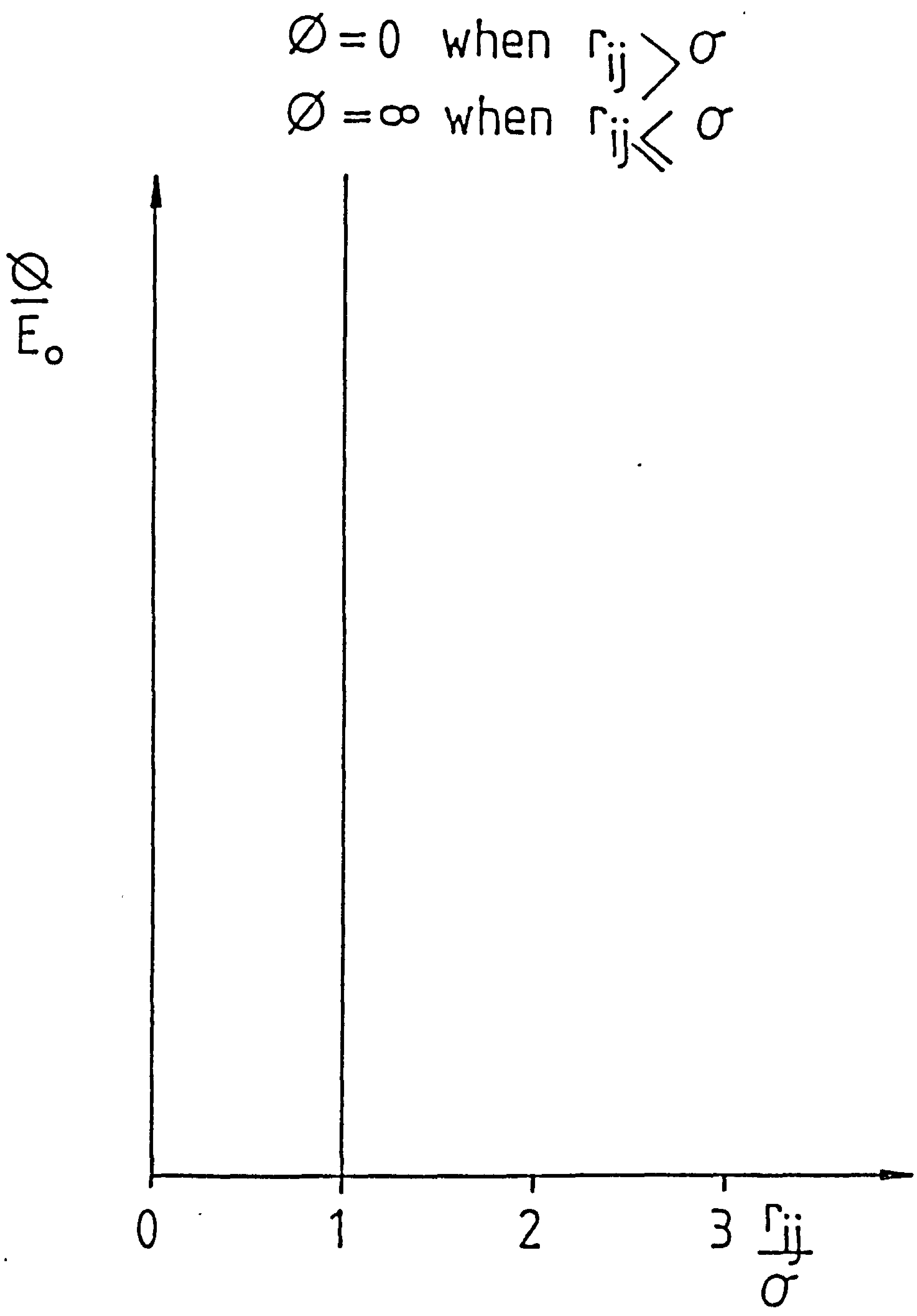

FIGURE 2.2.2: The Hard-Sphere Potential

velocity $\underline{V}_i$. A Stokesian friction constant C can be defined by the following:

$$C = \frac{3 \pi \sigma \eta_m}{m_i} \tag{2.2.2}$$

where η_m refers to the suspension medium viscosity.

The equations-of-motion for the simplest model of a hard-sphere colloidal suspension can thus be rewritten as$^{(65)}$:

$$\frac{d^2 \underline{r}_i}{dt^2} = - C \frac{d\underline{r}_i}{dt} \tag{2.2.3}$$

Implicit in this description of uniform particle retardation is the omission of many-body hydrodynamic effects. Consequently the frictional force experienced by any particle is deemed to be independent of any secondary flow in the suspension medium that might be caused by the presence of neighbouring particles. Woodcock$^{(65)}$ has recently devised a computational method to study the hard-sphere colloidal suspension, in which particles obey the 'mean-field Stokesian' equations of motion given in Equation (2.2.3). The present study utilises the classical Newtonian equations-of-motion given in Equations (2.1.1) and (2.1.2). A scaling relationship between the properties of hard-sphere systems obeying Newtonian and 'mean-field Stokesian' equations-of-motion however, allows the properties of either system to be predicted from a knowledge of the properties of the other. A further description of this scaling will appear in the next chapter.

Owing to the discontinuous nature of its inter-particle potential, the evolution of a hard-sphere system is monitored as a sequence of strictly binary collisions. If we denote particle positions as $\underline{r}_i$ and velocities as $\underline{V}_i$, then relative positions and velocities are defined as:

$$\underline{r}_{ij} = \underline{r}_i - \underline{r}_j \quad (2.2.4)$$

$$\underline{V}_{ij} = \underline{V}_i - \underline{V}_j \quad (2.2.5)$$

Particles are deemed to undergo collision when their particle centres are separated by a distance equivalent to a particle diameter, i.e.

$$r_{ij} = \sigma \quad (2.2.6)$$

Since hard spheres travel at constant velocity between collisions, a particle position at any point forward in time before its next collision may be predicted from:

$$\underline{r}_i\,(t) = \underline{r}_i\,(o) + \underline{V}_i\,(o)t \quad (2.2.7)$$

Moreover, relative positions develop according to:

$$\underline{r}_{ij}\,(t) = \underline{r}_{ij}\,(o) + \underline{V}_{ij}\,(o)t \quad (2.2.8)$$

Consequently the condition for any particle pair to come into contact can be expressed as:

$$r_{ij} + V_{ij}t = \sigma \quad (2.2.9)$$

Squaring Equation (2.2.9) and rearranging leads to a quadratic equation in t, whose solution leads to an estimate of the time required to elapse for the collision of any particle pair:

$$\underline{r_{ij}}^{2} + 2\,\underline{r_{ij}}\,\underline{V_{ij}}\,t + (\underline{v_{ij}}\,t)^{2} - \sigma^{2} = 0 \qquad (2.2.10)$$

Equation (2.2.10) may be solved through the use of the quadratic equation solution formula, i.e.

$$t = -b \pm \frac{\sqrt{b^{2} - ac}}{a} \qquad (2.2.11)$$

In this instance the coefficients are defined as:

$$a = \underline{V_{ij}}^{2} \qquad (2.2.12)$$

$$b = \underline{r_{ij}}\,\underline{V_{ij}} \qquad (2.2.13)$$

$$c = \underline{r_{ij}}^{2} - \sigma^{2} \qquad (2.2.14)$$

A list of particle 'next-collision' times and collision partners is constructed at the outset of the simulation. The shortest of these collision times determines the duration of the initial simulation time increment. Particle position co-ordinates are simultaneously up-dated according to Equation (2.2.7), following which the two particles at contact are deemed to collide. For particles of equal mass undergoing a perfectly elastic collision, the relative velocity of the particles along the direction joining the particle centres is reversed. The relative velocity change in each cartesian dimension is given by:

$$\Delta\,\underline{V\alpha}\;ij\;(t) = -\,\underline{V\alpha}\;ij\;(o)\;\underline{r\alpha}\;ij^{2}\;(t)/\sigma^{2} \qquad (2.2.15)$$

Following the solution of this binary collision it is necessary to recalculate the next collision times of the two colliding particles, together with any particles previously destined to collide with either colliding particle. The recalculation of next collision times for all remaining particles is unnecessary owing to the remaining validity of the originally calculated value. The hard-sphere system is then allowed to evolve via the execution of a pre-selected number, typically several thousand, short cycles.

The discontinuous nature of the hard-sphere potential allows the exact solution of Newton's equation-of-motion without the requirement of many force-distance evaluations needed for closely approaching particles interacting through continuous potentials. Consequently, the hard-sphere system is particularly effective at traversing phase space.

Various properties of the hard-sphere system are calculated throughout the simulation. A time-average over, typically several thousand collisions is generally required to obtain a reliable system property estimate for systems of a few hundred particles.

The energy of a hard-sphere system is entirely kinetic and is calculated from the following expression:

$$E = \frac{1}{2} \sum_{i=1}^{N} mi \, \underline{V_i}^{2} \qquad (2.2.16)$$

For a single-component system at thermal equilibrium, temperature may then be defined as:

$$T = \frac{2}{3[N-1]k} E \qquad (2.2.17)$$

Calculation of osmotic pressure, is based on the Virial theorem(33):

$$\frac{P\,V}{N\,E} = 1 + \frac{1}{3NtkT} < \sum_{i=1}^{N} \underline{r_i} \, \underline{f_i} > \qquad (2.2.18)$$

where f_i is the force on particle i,

< > denotes ensemble averaging.

Since forces between hard-spheres are impulsive, acting only during infinitely short collisions, the averaging over all particles in Equation (2.2.16) is replaced by a summation over collisions:

$$\frac{P\ V}{N\ E} = 1 + \Sigma_t\ b^{\dagger}_{ij}/3Nt \qquad (2.2.19)$$

where $b^{\dagger}_{ij} = r_{\underline{ij}}\ V_{\underline{ij}}/\sigma^2$, the product of relative positions and velocities, respectively.

The simulations were initiated at a density well below the hard-sphere freezing transition, usually $\rho^{\dagger} = 0.3$. Particles were initially assigned position co-ordinates corresponding to lattice points of a face centred cubic crystalline arrangement. After allowing the system to equilibrate for several thousand collisions, the densification procedure originally described by Woodcock(37) was used to obtain amorphous systems of the desired density. This method enables the density of a hard-sphere system to be gradually increased by the simultaneous incrementation of particle diameters. In order to prevent the physically unrealistic situation of overlapping spheres the velocities of the two colliding spheres are increased by $(d\sigma/dt)^{\dagger}$ along the impact vector.

The vast bulk of hard-sphere simulations to be reported here have not been performed under equilibrium conditions, but under the effects of an applied shear field. This aspect of hard-sphere particulate dynamics simulations is described in the following section.

2.3 Superimposition of the Velocity Profile

A velocity profile was superimposed upon the hard-sphere system in a similar manner to that used by Naitoh and Ono(66,67), and Erpenbeck(68,69).

In all simulations the direction of flow has been in the x-direction with a velocity profile in the y-direction, as illustrated in Figure 2.3.1.

On initial application of shear the desired velocity profile is artificially created by the incrementation of particle velocities according to:

$$V_{xi}\ (\text{sheared}) = V_{xi}\ (\text{unsheared}) + \dot{\gamma}\ (r_{yi} - L/2) \qquad (2.3.1)$$

where $\dot{\gamma}$ is the shear rate and L is the unit cell dimension.

The 'Lees-Edwards' shearing boundaries(62) are initiated simultaneously to this artificial velocity profile induction. In this technique, periodic image cells in the upper and lower y-direction are deemed to translate in the positive and negative x-direction respectively. These translating periodic image cells ensure the shear gradient continuity throughout the length of the simulation in addition to maintaining periodicity in the direction of the velocity profile. Conventional periodic boundary conditions prevail in the remaining two cartesian dimensions.

Any particle leaving the central simulation cell through a 'shearing' face is replaced by a particle simultaneously re-entering the simulation cell through the opposite shearing face. The x-position co-ordinate of the particle entering the central simulation cell will differ to that of the leaving particle by an amount dependent on the distance translated by the periodic image cells. Additionally, the x-component of the particle velocity will differ by an amount $\dot{\gamma}^{\dagger}L$ to account for the difference in velocity profiles at the extremes of the central simulation cell in the velocity gradient direction.

Previous non-equilibrium studies(66-69) of the hard-sphere system were plagued by the energy rise of the system due to viscous heating, preventing the attainment of steady-state conditions. A novel aspect

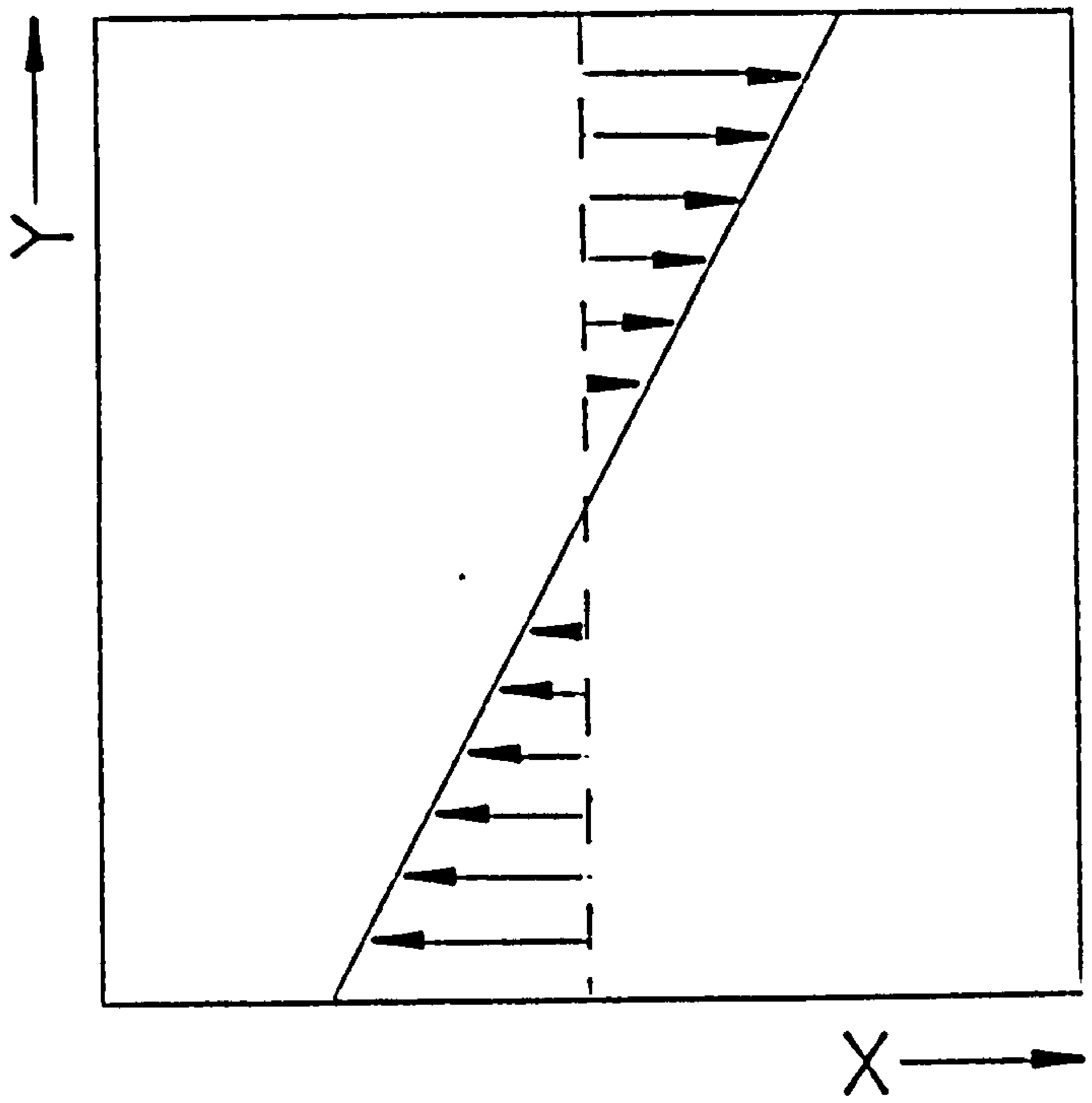

FIGURE 2.3.1: Schematic Representation of the Velocity Profile Employed in the Non-Equilibrium Simulations

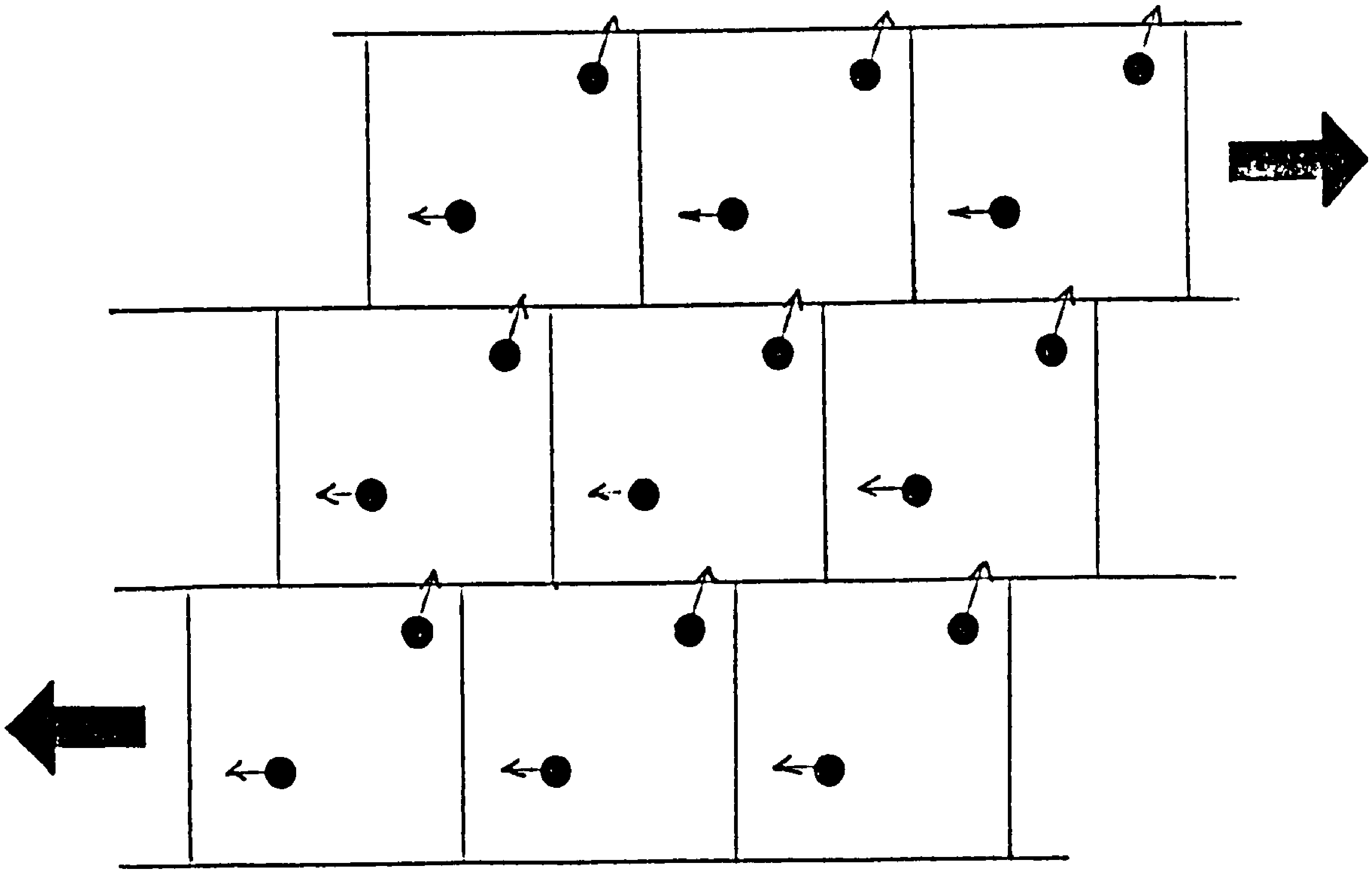

FIGURE 2.3.2: Lees-Edwards Shearing Boundary Conditions

of the simulations to be reported here is the incorporation of a kinetic energy rescaling procedure into the simulations.

The kinetic energy of the sheared system is expressed relative to the velocity profile, i.e.:

$$E = \frac{1}{2} \sum_{i=1}^{N} m_i \left(\underline{V_i} - \dot{\gamma}\,(Y)\right)^2 \qquad (2.3.2)$$

$$= \frac{1}{2} \sum_{i=1}^{N} m_i \left[\left(V_{xi} - \dot{\gamma}\,(r_{yi} - L/2)\right)^2 + V_{yi}^{2} + V_{zi}^{2} \right] \qquad (2.3.3)$$

In order to maintain isokinetic conditions, particle peculiar velocities are rescaled following a cross shearing-boundary collision. The x-component of relative velocity for a pair of particles colliding across a shearing boundary is incremented by $\dot{\gamma}$ L to eliminate differences in the local flow field for each particle. The rescaling factor, f, required to return the system kinetic energy E, to the desired value, E_o is defined by the following:

$$f = \left(\frac{E_o}{E} \right)^{\frac{1}{2}} \qquad (2.3.4)$$

A time average of the effective friction coefficient, C , required to maintain isokinetic conditions is calculated from:

$$C = \frac{\langle 1 - f \rangle}{\Delta t} \qquad (2.3.5)$$

where Δt is the mean rescaling frequency.

Diffusion coefficients of the sheared system are calculated from averaged mean squared displacements relative to the flow field:

$$D = \frac{\langle (\Delta(r_x - \dot{\gamma}\;(r_y - L/2)))^2 + \Delta r_y^{\,2} + \Delta r_z^{\,2} \rangle}{6t} \qquad (2.3.6)$$

The shear-stress response of the system may be resolved into two contributions, which have been referred to as the kinetic ($P_{xy}(K)$) and potential (P_{xy} ($\emptyset$)) contributions$^{(68)}$:

$$P_{xy} = P_{xy}(K) + P_{xy}(\emptyset) \qquad (2.3.7)$$

where:

$$P_{xy}(K) = \frac{1}{V} \sum_{i=1}^{N} m_i \left[V_{xi} - \dot{\gamma} \; (r_{yi} - L/2) \right] V_{yi} \qquad (2.3.8)$$

$$P_{xy}(\emptyset) = \frac{1}{V} \sum_{C} X_{ij} \, \Delta V_{yi} \, \delta \, (t - t_c) \qquad (2.3.9)$$

Equation (2.3.9) involves a summation over collisions; X_{ij} denotes the relative x-position of the colliding particles and ΔV_{yi} refers to the change in y-velocity during collision.

From a knowledge of the shear stress at a given shear rate, we can readily compute the viscosity, η from:

$$\eta = \frac{P_{xy}}{\dot{\gamma}} \qquad (2.3.10)$$

2.4 Colloidal Potential Particulate Dynamics

There is currently a considerable scientific interest in the behaviour of well-characterised suspensions comprising nearly monodisperse polymer latices suspended in Newtonian fluids. An important consideration in the choice of system studied is the system stability with respect to particle aggregation. Methods are available to improve stability; the method chosen often depending upon suspension medium properties$^{(106)}$. Colloidal particles often inherently possess an electrical charge. When such particles are dispersed in polar suspension media, stabilization occurs due to mutual electrostatic repulsions (Figure 2.4.2). Particles suspended in liquids of low polarity are often stabilized by the grafting of solvent-compatible polymer chains onto the particle surface. Inter-particle repulsion in these sterically stabilized systems involves deformation of the stabilizer layer (Figure 2.4.1). The simulations described in this section involve an effective pair-potential which aims to embody the effects of a stabilizer layer surrounding a hard particle-core. The continuous potential in question may be regarded as a perturbation of the hard-sphere potential, and is defined by the following:

$$\emptyset(r) = \varepsilon \left(\frac{\sigma}{r - \sigma} \right)^n \qquad (2.4.1)$$

$$\varepsilon = 10^{-m} E_o \qquad (2.4.2)$$

where $\emptyset(r)$ is the pair-potential at a separation of particle centres r, σ is the hard-core diameter, and E_o is the system unit of kinetic energy, i.e.:

$$\frac{1}{2N} \sum_{i=1}^{N} m_i \underline{V_i}^2 = 3/2 \, E_o \qquad (2.4.3)$$

The force between any particle-pair may be calculated from:

$$\underline{f_{ij}} = - d\emptyset_{ij}/d\underline{r_{ij}}$$

which for the colloidal potential is expressed by:

$$\underline{f_{ij}} = n \, \varepsilon \, (r^{\dagger} - 1)^{n-1} \qquad (2.4.4)$$

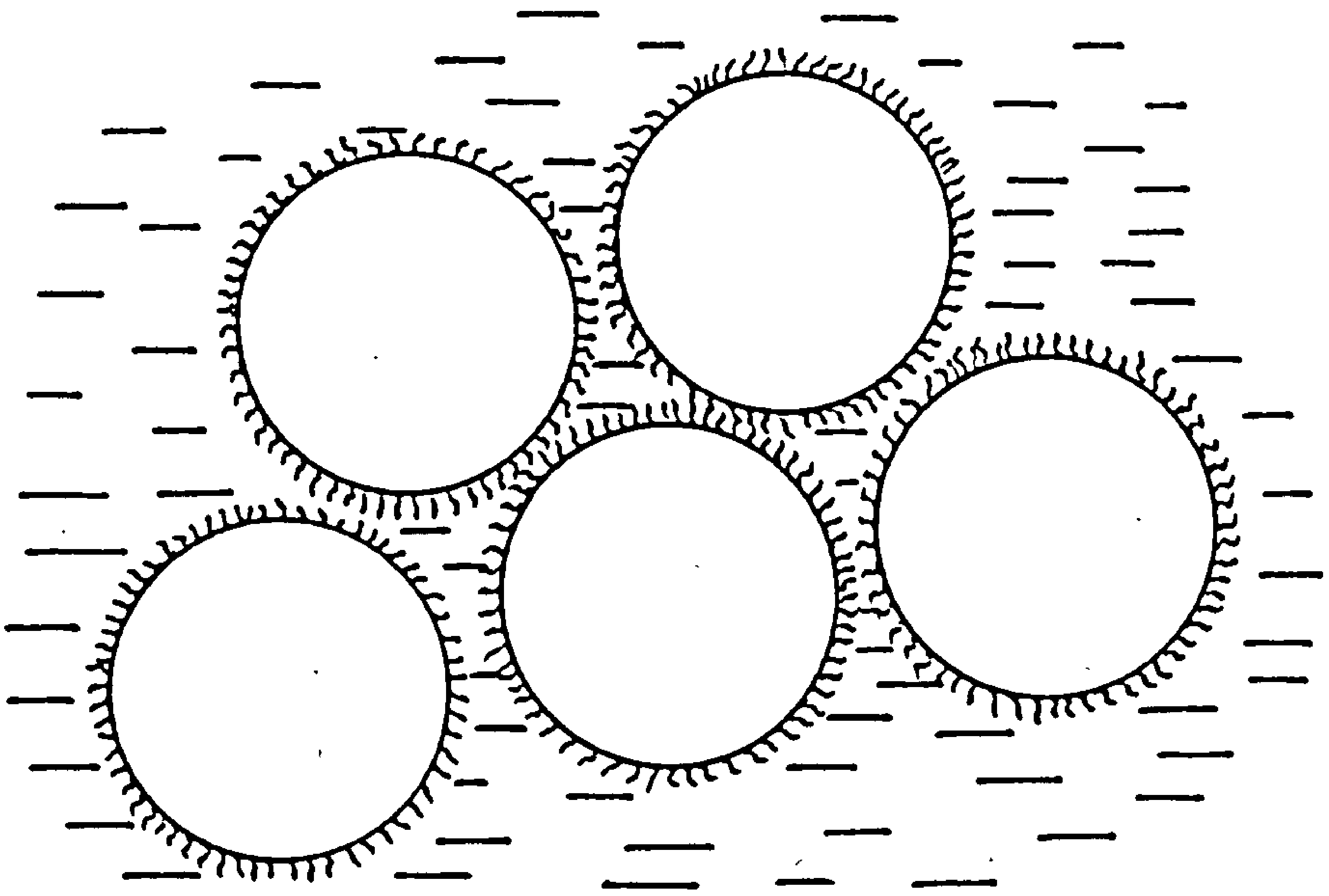

FIGURE 2.4.1: Sterically Stabilised Colloidal Particles

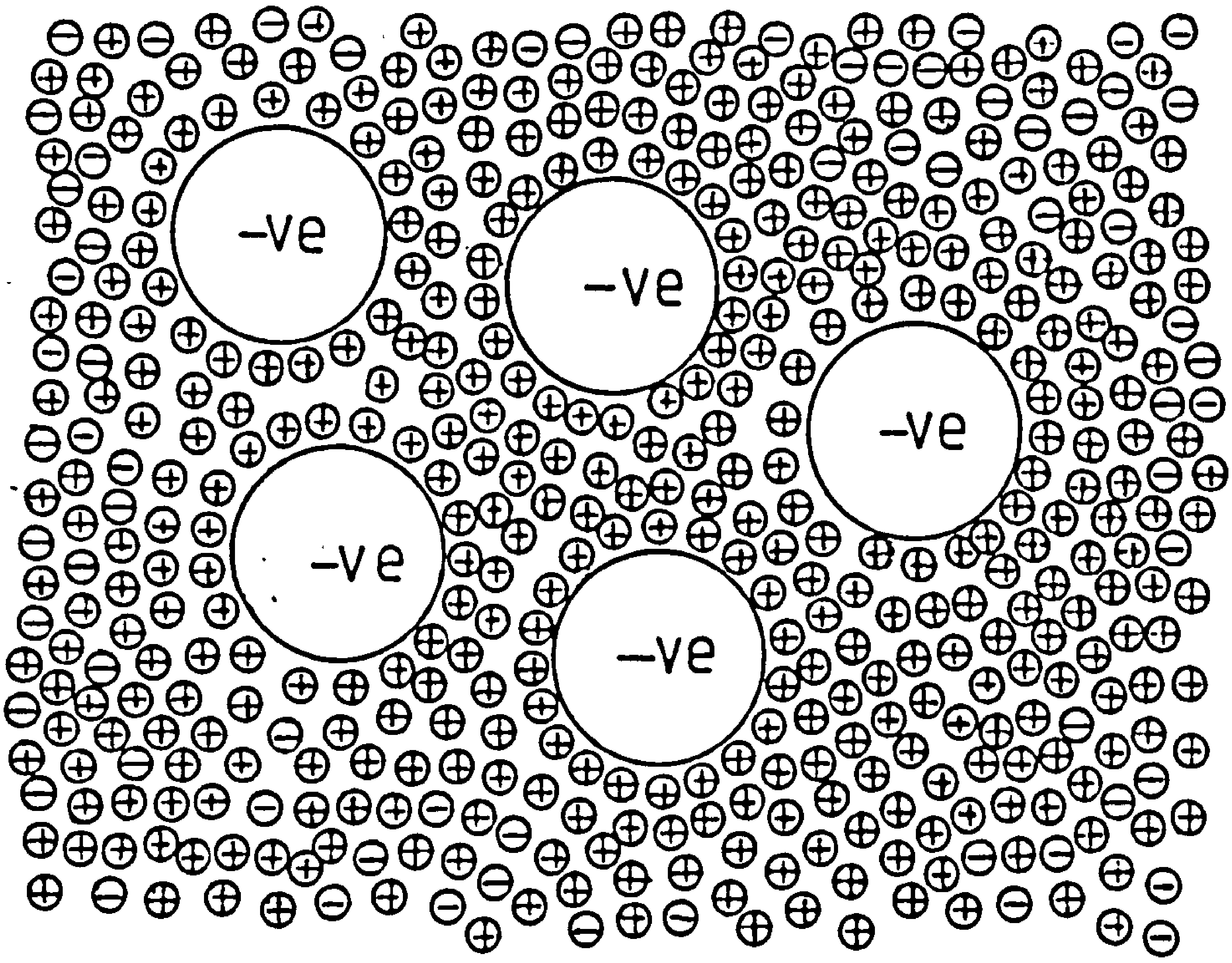

FIGURE 2.4.2: Electrostatically Stabilised Colloidal Particles

The vast majority of simulations presented here have involved a value of n = 12, however, a limited study has been undertaken to ascertain the effects of a change in the value of n. The value of m in the above definition determines the correspondence between system potential and kinetic energy. All simulations have involved a value of m = 12. The values of m and n used in the present simulations are such that the effective pair potential broadly resembles that of a sterically stabilized system, i.e. a fairly short-ranged repulsive skin originating at the particle surface (Figure 2.4.3). Variation in the values of m and n is possible, however, to effect a longer-range repulsion more appropriate to an electrostatically stabilized system.

A different approach to that described for hard spheres must be adopted in order to solve the equations-of-motion for particles interacting through continuous effective pair potentials. For isotropic continuous effective pair potentials, the equations-of-motion represent a set of 3N coupled differential equations of the form defined in Equation (2.1.2). The step-wise solution of these coupled differential equations is generally tackled through the use of finite difference methods, inevitably introducing approximations into the predicted particle trajectories. The technique used here is based on the method originally due to Verlet$^{(42)}$. The original derivation of Verlet's algorithm involves the Taylor expansion forwards and backwards in time about $\underline{r_i}(t)$ - the particle position at time t;

$$\underline{r_i}(t + dt) = \underline{r_i}(t) + dt\ \underline{V_i}(t) + \frac{1}{2}\, dt^2\ \underline{a_i}(t) + \ldots. \qquad (2.4.5)$$

$$\underline{r_i}(t - dt) = \underline{r_i}(t) - dt\ \underline{V_i}(t) + \frac{1}{2}\, dt^2\ \underline{a_i}(t) + \ldots. \qquad (2.4.6)$$

where $\underline{a_i}(t)$ represents particle acceleration at time t.

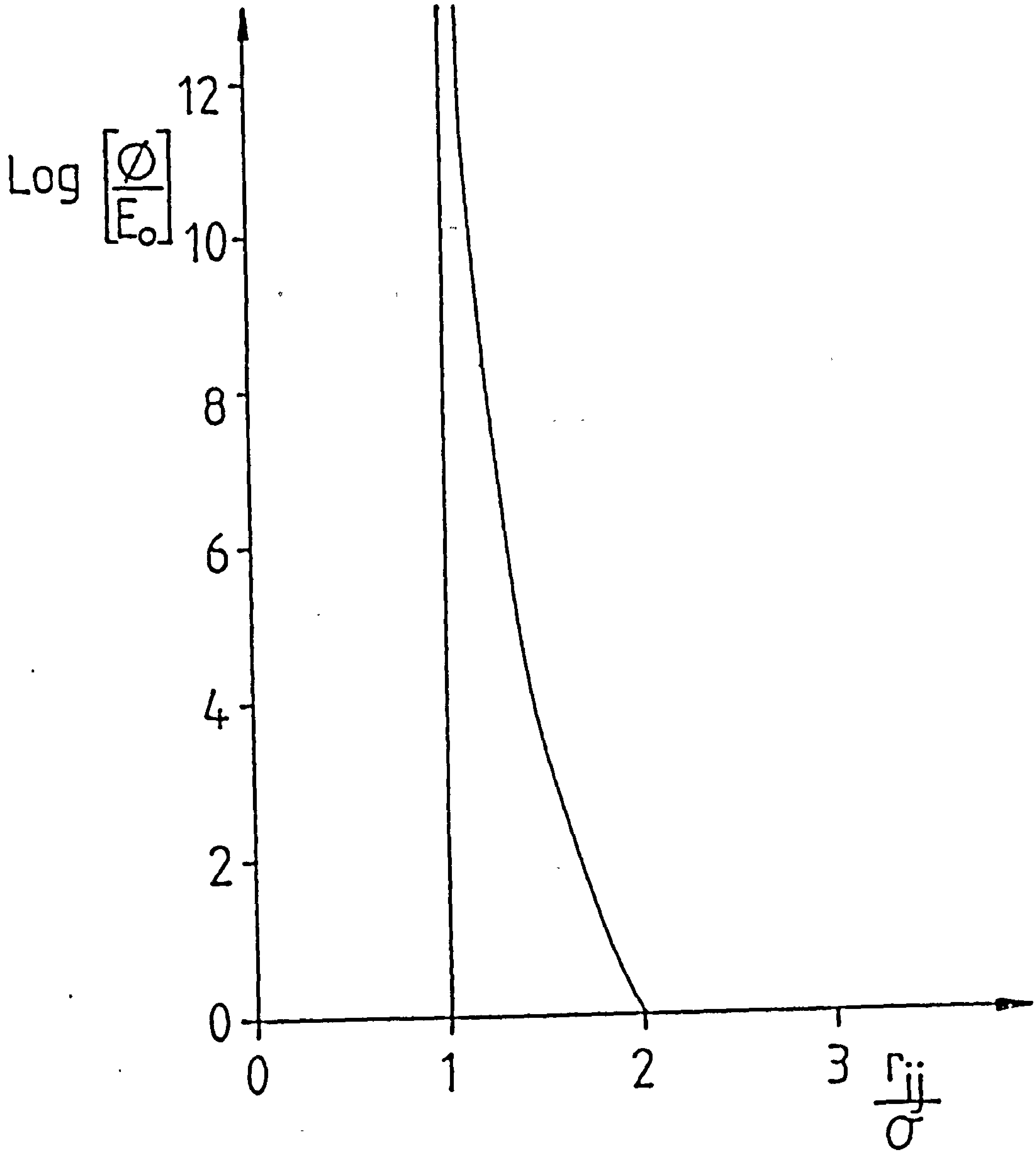

FIGURE 2.4.3: The Colloidal-Sphere Potential

Addition of Equations (2.3.4) and (2.3.5) yields the following equation for the advancement of particle positions:

$$\underline{r_i}(t + dt) = 2\underline{r_i}(t) - \underline{r_i}(t - dt) + dt^2\ \underline{a_i}(t) \qquad (2.4.7)$$

From Equation (2.4.7) it may be observed that the storage of individual particle velocities is unnecessary, making the method particularly efficient with respect to computer storage space. A knowledge of particle velocities however, is desirable for the evaluation of system kinetic energy, and consequently an equivalent expression for the advancement of particle positions involving the particle velocity at time t, $\underline{v_i}(t)$ was used:

$$\underline{r_i}(t + dt) = \underline{r_i}(t) + dt\ \underline{V_i}(t) + dt^2\ \underline{a_i}(t) \qquad (2.4.8)$$

where:

$$\underline{V_i}(t) = (\underline{r_i}(t) - \underline{r_i}(t - dt))/dt \qquad (2.4.9)$$

Isokinetic conditions were maintained throughout all simulation runs through the use of a similar velocity rescaling procedure to that used in the hard-sphere simulations described in Section 2.1.1. The choice of timestep in a dynamical simulation is based upon two opposing considerations, an increasing value obviously leading to a faster real-time evolution of particle trajectories, but with an associated higher degree of approximation. A good indication of satisfactory particle trajectory prediction is the conservation of total system energy of an equilibrium system. Explicit values of the time increments used will be given along with the simulation results in subsequent chapters.

Rapidly approaching particles at small particle separations inevitably lead to the introduction of significant approximations into predicted particle trajectories. In order to eliminate the separation of any particle pair from decreasing too rapidly in any single time increment, a safeguard was incorporated into the simulations allowing a temporary, smaller time-increment to be implemented if necessary. This variable time-increment procedure involved the calculation of potential collision times for every particle hard-core from the solution of Equation (2.2.10). A variable time increment dt_{var} was only implemented when the shortest potential collision time, t_{min} was less than $\frac{1}{10}$ of the standard time increment dt_{std}. In this instance the variable time increment was set at $\frac{1}{10}$ of the minimum potential collision time.

In summary:

$$dt = dt_{std} \qquad \text{when } t_{min} > \frac{dt_{std}}{10} \qquad (2.4.10)$$

$$dt = dt_{var} = \frac{t_{min}}{10} \quad \text{when } t_{min} < \frac{dt_{std}}{10} \qquad (2.4.11)$$

This variable time-increment procedure is only intended as a precautionary measure, and its frequent usage is taken as a signal to reduce the value of dt_{std}.

Incorporation of a distribution of particle sizes into simulations of particles interacting through a potential of the type defined in Equation (2.3.1) has proved to be relatively straightforward. Particle hard-core diameters were pseudo-randomly sampled from a normal distribution with a specified mean $\bar{\sigma}$, and standard deviation sd. The degree of polydispersity is expressed as the ratio of the two adjustable parameters:

$$\text{\% degree of polydispersity} = \frac{sd}{\sigma} \times 100 \qquad (2.4.12)$$

The characteristic unit of length used in these simulations and reduced units for polydisperse systems is the particle size distribution mean $\bar{\sigma}$. In all the simulations described here, particle masses have been deemed to be equivalent, irrespective of particle diameter.

Any comparison between monodisperse and polydisperse system properties are made at equivalent packing fraction y, calculated as:

$$y = \frac{\pi}{2DV} \sum_{i=1}^{N} \sigma_i^{D} \qquad (2.4.13)$$

where D represents the system dimensionality and V is the volume of the central simulation cell.

For a system of monodisperse particles the packing fraction can be calculated from:

$$y = \frac{\pi\rho^{\dagger}}{2D} \qquad (2.4.14)$$

Various thermodynamic properties of the system are evaluated at each time-step during the integration of the equations-of-motion. The formulae for the calculation of these properties are given below:

Potential energy (ϕ)

$$\phi = \frac{1}{N} \sum_{i=1}^{N} \sum_{j>i}^{N} \phi_{ij} \qquad (2.4.15)$$

Total Internal Energy (U)

$$U = \phi + E \qquad (2.4.16)$$

Pressure

$$P = \frac{N}{3V}\left[\Sigma\, m_i\, \underline{V_i}^2 + \sum_{i=1}^{N}\sum_{j>i}^{N} \underline{r_{ij}}\; \underline{f_{ij}}\right] \qquad (2.4.17)$$

Kinetic Component   Potential Component

since $$f_{ij} = -\frac{d\emptyset}{dr}(r_{ij})\; \underline{r_{ij}} \qquad (2.4.18)$$

$$P = \frac{N}{3V}\left[\sum_{i=1}^{N} m_i\, \underline{V_i}^2 - \sum_{i=1}^{N}\sum_{j>i}^{N} \frac{d\emptyset}{dr}(\underline{r_{ij}})\; \underline{r_{ij}}\right] \qquad (2.4.19)$$

alternatively;

$$P = \frac{N}{3V}\left[\sum_{i=1}^{N} m_i\, \underline{V_i}^2 - \psi\right] \qquad (2.4.20)$$

where the virial ψ is given by:

$$\psi = \sum_{i=1}^{N}\sum_{j>i}^{N} \frac{d\emptyset}{dr}(\underline{r_{ij}})\; \underline{r_{ij}} \qquad (2.4.21)$$

2.5 Superimposition of the Velocity Profile

The superimposition of a velocity profile upon the colloidal-sphere system is brought about in a slightly different manner than that used to shear the hard-sphere system. The method, which was initially suggested by Evans(87) involves the direct intervention into the development of particle trajectories. This intervention takes the form of an additional term in the position co-ordinate updating algorithm. For flow in the x-direction with a velocity gradient in the y-direction this becomes:

$$\underline{r_{xi}}(t + dt) = \underline{r_{xi}}(t) + \underline{V_{xi}}(t) + a_{xi}(t)\, dt^2 + \dot{\gamma}(\underline{r_{yi}}(t) - L/2)dt \quad (2.5.1)$$

$$\underline{r_{yi}}(t + dt) = \underline{r_{yi}}(t) + \underline{V_{yi}}(t) + \underline{a_{yi}}(t)\, dt^2 \qquad (2.5.2)$$

$$\underline{r_{zi}}(t + dt) = \underline{r_{zi}}(t) + \underline{V_{zi}}(t) + \underline{a_{zi}}(t)\, dt^2 \qquad (2.5.3)$$

Lees-Edwards shearing boundary conditions$^{(62)}$ are used in conjunction with the modified position updating algorithm in order to maintain periodicity in the direction of the velocity gradient. Conventional periodic image conditions prevail in the remaining two cartesian dimensions.

Viscous heating of the system is eliminated through the use of a similar velocity rescaling procedure to that previously described for the hard-sphere system. The shear-stress response to the imposed flow field is calculated as the appropriate off-diagonal component of the pressure tensor, i.e.

$$P_{xy} = \frac{1}{V} \left[\Sigma\, m_i\, V_{xi}\, V_{yi} - \Sigma\, \Sigma\, \frac{r_{xij}\, r_{yij}}{r_{ij}} \frac{d\phi_{ij}}{dr_{ij}} \right] \qquad (2.5.4)$$

From a knowledge of the shear-stress at any given shear-rate we can readily compute the viscosity from Equation (2.3.10).

TABLE 2.2.1

Reduced Unit Definitions

Property	Symbol	Reduced Unit
Density	$\rho^{\dagger}$	$N\sigma^3/V$
Time	$t^{\dagger}$	$(m\sigma^2/E_o)^{\frac{1}{2}}$
Pressure	$P^{\dagger}$	E_o/σ^3
Diffusion Coefficient	$D^{\dagger}$	$(\sigma^2\ E_o/m)^{\frac{1}{2}}$
Shear Rate	$\dot{\gamma}^{\dagger}$	$(E_o/m\sigma^2)^{\frac{1}{2}}$
Shear Stress	$P_{xy}^{\dagger}$	E_o/σ^3
Viscosity	$\eta^{\dagger}$	$(m\ E_o)^{\frac{1}{2}}/\sigma^2$
Rescaling Coefficient	$C^{\dagger}$	$(E_o/m\sigma^2)^{\frac{1}{2}}$

CHAPTER 3

RESULTS OF A NON-EQUILIBRIUM HARD-SPHERE PARTICULATE DYNAMICS STUDY

CHAPTER 3

RESULTS OF A NON-EQUILIBRIUM HARD-SPHERE PARTICULATE DYNAMICS STUDY

3.1 Introduction

Theoretical considerations of the transport properties of the hard-sphere fluid extend as far back as the beginning of the present century(118). These considerations originated in the development of the kinetic theory of gases, and consequently initial developments were applicable only to systems of low density(116). Some years later Enskog(117) proposed a method which allowed the extension of the Boltzmann equation to higher densities of the hard-sphere fluid. Implicit in Enskog's theory is the assumption of 'molecular chaos', i.e. that successive hard-sphere collisions are statistically uncorrelated.

The first computer simulation study of hard-sphere transport coefficients was described by Alder, Gass and Wainwright in 1970(55). Their equilibrium molecular dynamics approach allowed the zero shear-viscosity evaluation over the whole fluid density range. As a result of the impulsive nature of forces between hard-spheres, the usual method of transport coefficient estimation involving the time-integration of the appropriate auto-correlation function is not easily implemented. Instead, an estimate of the shear viscosity is evaluated via the use of an equivalent Einstein relation given in Equation 1.4.5. A comparison of the shear viscosity simulation results with those predicted by Enskog's theory reveals a good agreement at low densities. A sharp deviation is observed, however, for reduced density values greater than $\rho^* \sim 0.5$, where the molecular chaos approximation presumably ceases to be valid.

Subsequent computer simulation studies have concentrated upon methods where the shear-viscosity is evaluated in a more direct manner, i.e. as the system response to an artificially induced shear field. Naitoh and Ono(66,67) have published details of their non-equilibrium hard-sphere molecular dynamics simulations for a range of system sizes and densities. In these studies the velocity profile is superposed through the use of the Lees-Edwards shearing boundary conditions(62). Initial simulation results(66) for systems comprising N = 108 particles failed to extrapolate to the zero shear-rate viscosity obtained by Alder, Gass and Wainwright(55). Further simulations upon larger systems(67) however, allowed this discrepancy to be attributed to system-size effects. In all their reported studies Naitoh and Ono allowed system temperature to rise from the thermal energy generated as a result of viscous dissipation. Despite the small magnitude of temperature increase at the vanishing shear-rates employed, the attainment of steady-state conditions is strictly prevented.

In order that the hard-sphere fluid might be subjected to slightly higher shear-rates, Erpenbeck(68) has examined two modifications to the method originally employed by Naitoh and Ono. In the 'trajectory averaged' approach, several equilibrium hard-sphere configurations are generated through a Monte-Carlo sampling procedure. Each system configuration is then subjected to similar shearing conditions, and the system response averaged over the several resultant phase-space trajectories. Averaging of the system response allows the study of shorter phase-space trajectories, thereby limiting the system temperature rise. Estimates of the shear viscosity from this method must be corrected for the finite temperature rise associated with each trajectory from the following:

$$\left(\frac{T}{T_o}\right)^{\frac{1}{2}} \times \eta \, (\rho, \dot{\gamma}^1) \; = \; - \frac{P_{xy}}{\dot{\gamma}} \qquad (3.1.1)$$

$$\dot{\gamma}^1 = \dot{\gamma}\left(\frac{T_o}{T}\right)^{\frac{1}{2}} \tag{3.1.2}$$

Where T is the system temperature at the end of a trajectory, $\dot{\gamma}$ is the shear rate at the desired temperature T_o, $\dot{\gamma}^1$ is the effective shear-rate, P_{xy} is the shear stress, and η is the shear viscosity. The use of this 'trajectory-averaged' scheme to study systems at high shear-rates where structural rearrangement occurs, requiring lengthy simulation runs for the attainment of steady-state conditions would clearly not be practicable. The second method examined by Erpenbeck(68) incorporates a temperature rescaling procedure into the simulations. Here system temperature is returned to the desired value by the periodic rescaling of particle peculiar velocities. Erpenbeck's initial simulation studies(68) were performed on hard-sphere systems with a reduced density $\rho^† = 0.884$ at moderately low shear-rates. These studies showed that both methods produced results that agreed within the estimated statistical uncertainty. Further studies upon systems with reduced densities $\rho^† = 0.70$ and $=0.884$(69) employed the peculiar velocity rescaling procedure to study the behaviour of the hard-sphere system at higher shear-rates. Shear-induced structural ordering was observed at both system densities, the higher density system ordering at lower shear-rate values.

The following section of this chapter (3.2) describes the results of a series of isokinetic simulations at relatively low shear-rates. The simulations, which have previously been described in Section 2 span a reduced density range $\rho^† = 0.80 - 1.10$. Section 3.3 presents the results of a series of simulations at a reduced density $\rho^† = 0.90$ over an extended shear-rate range. The kinetic energy-shear-rate scaling property of the hard-sphere model, together with the implications to the study of experimental systems are discussed in Section 3.4. Applications of the present results in the context of dense suspension rheology are finally discussed in Section 3.5.

3.2 Low Shear-Rate Behaviour of the Isokinetic Hard-Sphere Model

The low shear-rate behaviour of an isokinetic hard-sphere system containing N = 500 particles has been examined in a series of dynamical simulations, as described in Chapter 2. Four reduced density points have been studied, i.e. $\rho^{\dagger}$ = 0.80, 0.90, 1.00 and 1.10. The kinetic-energy of all simulations was maintained at a value $E^{\dagger}$ = 1.50. In order to obtain hard-sphere systems at the desired density, an amorphous hard-sphere system was compressed from an initial density $\rho^{\dagger}$ = 0.30 to a final density $\rho^{\dagger}$ = 1.10. A description of the densification procedure used appears in Chapter 2. After allowing this high-density configuration to reach apparent steady state conditions (as judged by the absence of any drift in system pressure when viewed over 150,000 collisions), systems at each of the lower densities were created by the instantaneous contraction of particle diameters. These newly created lower-density systems were then allowed to evolve under static conditions (i.e. in the absence of shear) for a further 150,000 collisions in order to ensure the attainment of steady-state conditions (as judged by the above criterion).

At the thermal energy state considered here, the hard-sphere model is known to exhibit a freezing transition at a reduced density $\rho^{\dagger} \sim 0.943$, and a melting transition at $\rho^{\dagger} \sim 1.053$. The intermediate density region corresponds to co-existing solid and fluid phases. Woodcock(37) has published equation-of-state data of the high-density, metastable, hard-sphere fluid obtained from lengthy molecular dynamics simulations. In addition, the Carnahan-Starling equation(112), Equation (4.2.3.7), is generally accepted to predict the equation-of-state of the hard-sphere fluid over the entire density range. A comparison of the pressure exhibited by the hard-sphere systems under static conditions in the present work with the previously published data of Woodcock(37), and the prediction due to Carnahan and Starling(112) is made in Figure 3.2.1. Good agreement between the three sets of data may be observed at reduced densities of $\rho^{\dagger} = 0.80$, 0.90 and 1.00. The pressure value at $\rho^{\dagger} = 1.10$ in the present work is seen to be marginally higher than for either of the comparisons. This discrepancy suggests that the system at $\rho^{\dagger} = 1.10$ in the present work is not at steady state. The absence of any drift in system pressure when viewed over 150,000 collisions is probably attributable to the long structural relaxation time at this high density, resulting in the imperceptibly slow movement of the system towards steady-state conditions. The general conclusion that may be drawn from Figure 3.2.1 is that each of the four systems considered in the present section has an amorphous fluid configuration under static conditions.

Shearing conditions (described in Section 2.3) were initiated after the properties at each reduced density had been obtained. The behaviour of each system over a limited shear-rate range was then studied by successive, step-wise shear-rate increases. Re-attainment of apparent steady-state conditions following a shear-rate increase was usually complete after $\sim$ 40,000 collisions. However, in the case that this steady-state re-attainment involved an abrupt structural change, much longer times were required ($\sim$ 200,000 collisions). Following steady-state re-establishment, system properties were averaged over, typically 100,000 collisions. At very low shear-rate conditions the system response of an isokinetic system is very small, and hence the inherent statistical uncertainty is large. System properties in this shear-rate region were consequently averaged over a greater number of collisions, typically 240,000, in an attempt to increase the reliability of the results. Various bulk properties were continually monitored in the direction of

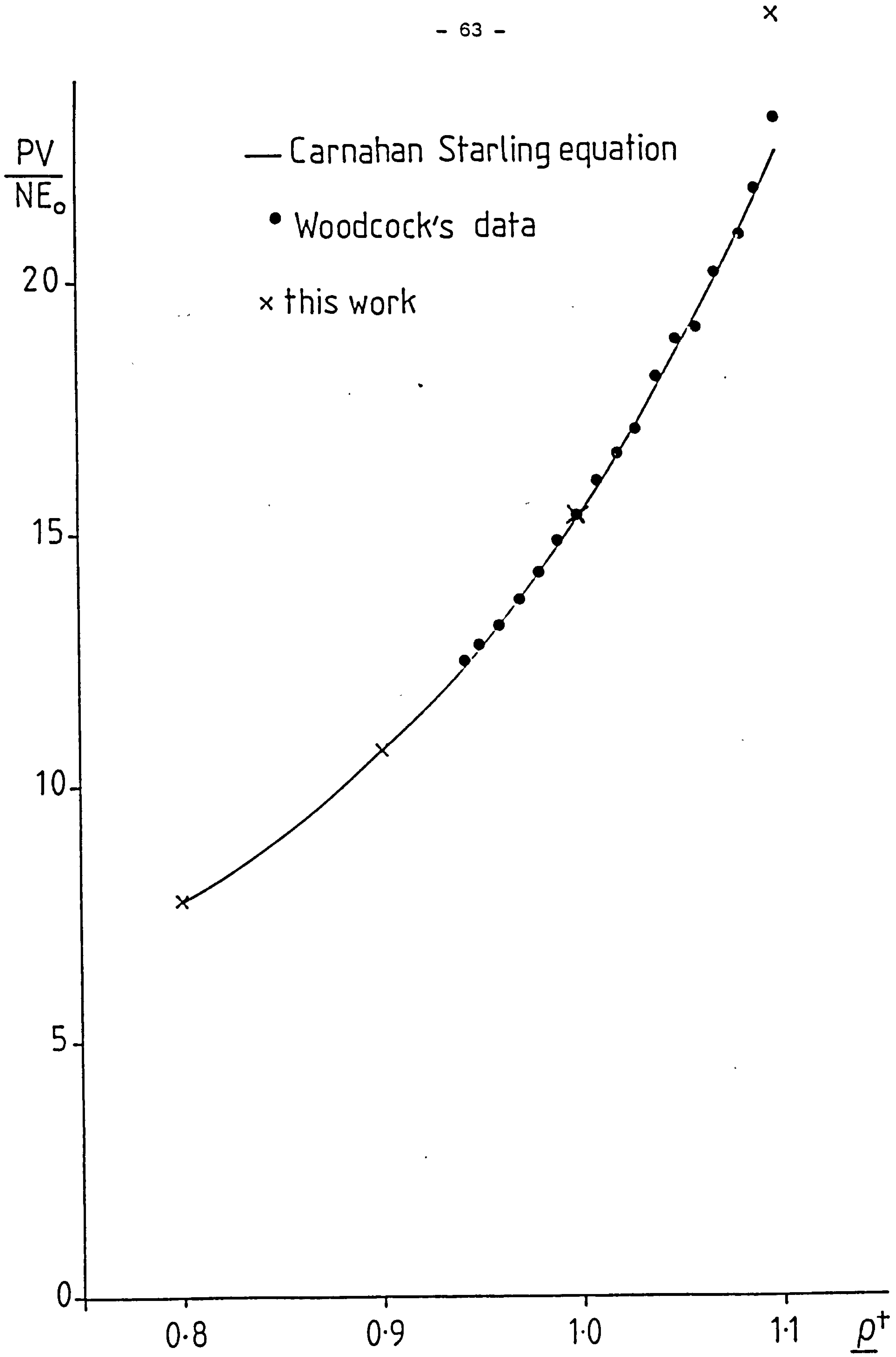

FIGURE 3.2.1: Comparison of the Pressure Obtained from the Present Equilibrium Hard-Sphere Simulations with the Predicted Value from the Carnahan-Starling equation(112) and the Previously Published Data of Woodcock(37)

the velocity gradient by splitting the central simulation cell into 20 segments. Kinetic energy, density and x-velocity profiles were then averaged over 40,000 collisions in each segment. Graphical representations of these bulk-property profiles at a reduced density $\rho^{\dagger} = 0.90$ and a shear-rate $\dot{\gamma}^{\dagger} = 0.50$ appear in Figures 3.2.3 - 3.2.4, where the monitored system properties are shown to be fairly constant in the y-cartesian dimension.

System properties of the isokinetic hard-sphere systems at the reduced density points studied are presented in Tables 3.2.1 - 3.2.4. In these and subsequent tables of system properties, estimates of the associated uncertainty calculated as the standard deviation of several independent sub-averages are quoted in parentheses.

One aspect of the results of non-equilibrium molecular dynamics simulations that has received a considerable amount of attention in the past is the description of shear viscosity at vanishing shear-rate. This attention has been motivated in part by the need to be able to extrapolate the shear viscosity to the zero shear limit. A comparison with the zero-shear viscosity obtained through the integration of the velocity auto-correlation function in an equilibrium molecular dynamics simulation can then be made. Ashurst and Hoover(61) have made use of a $\sinh^{-1}(\dot{\gamma})/\dot{\gamma}$ viscosity dependence as originally put forward by Ree, Ree and Eyring(120). More recent work by Naitoh and Ono(67), Evans(121) and Heyes(122) has used a $\dot{\gamma}^{\frac{1}{2}}$ viscosity dependence to fit their data.

Figures 3.2.5 - 3.2.8 show the present low shear-rate viscosity results plotted against $\dot{\gamma}^{\frac{1}{2}}$ for each of the reduced density points considered. Within the estimated limits of uncertainty, the square-root relationship is seen to hold for systems at $\rho^{\dagger} = 0.80$ and 0.90. The viscosity at higher reduced densities however, appears to diverge as the shear rate approaches zero, preventing the estimation of a zero-shear-rate viscosity. This divergence in viscosity at vanishing shear

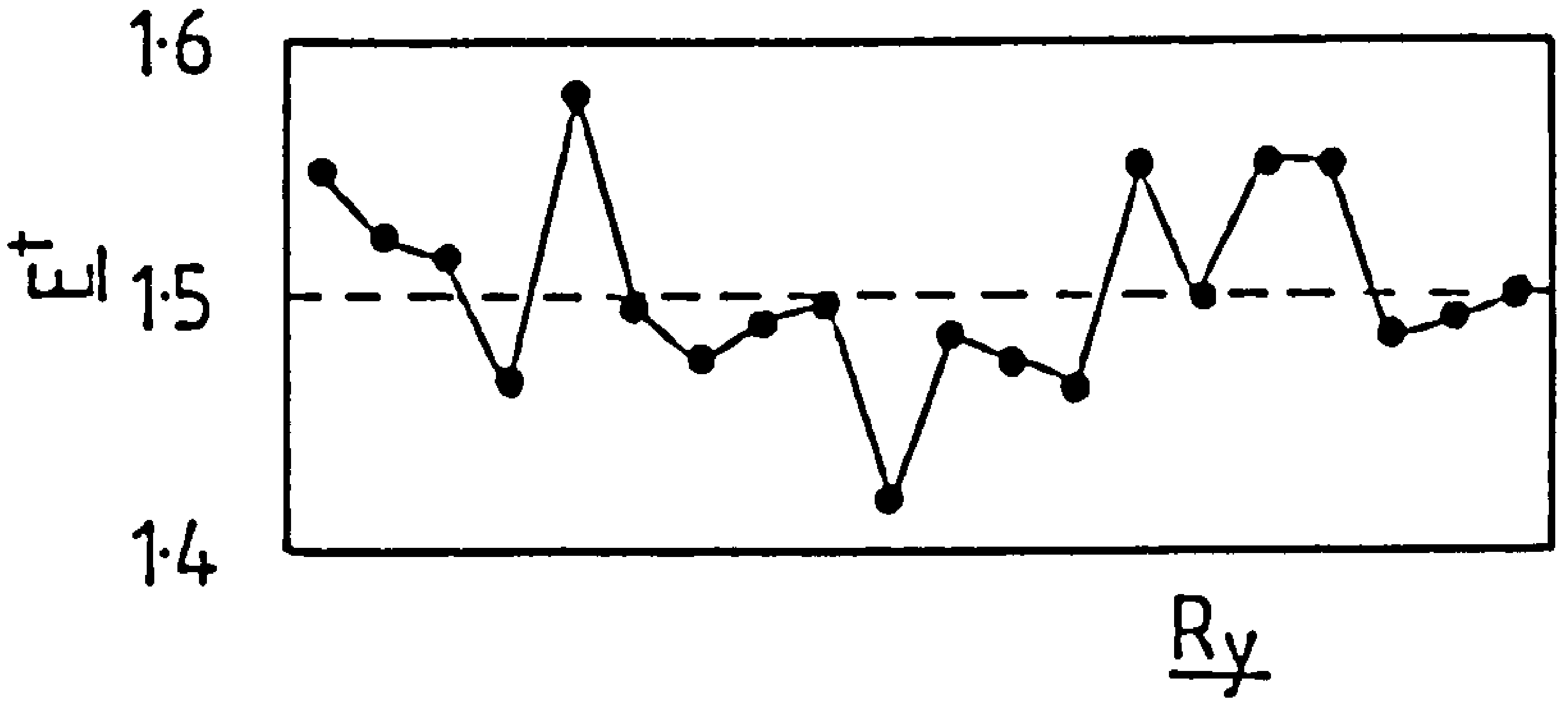

FIGURE 3.2.2: Y-directional Kinetic Energy Profile of the Hard-Sphere System at a Reduced Density $\rho^{\dagger}$ = 0.90 and a shear rate $\dot{\gamma}^{\dagger}$ = 0.50

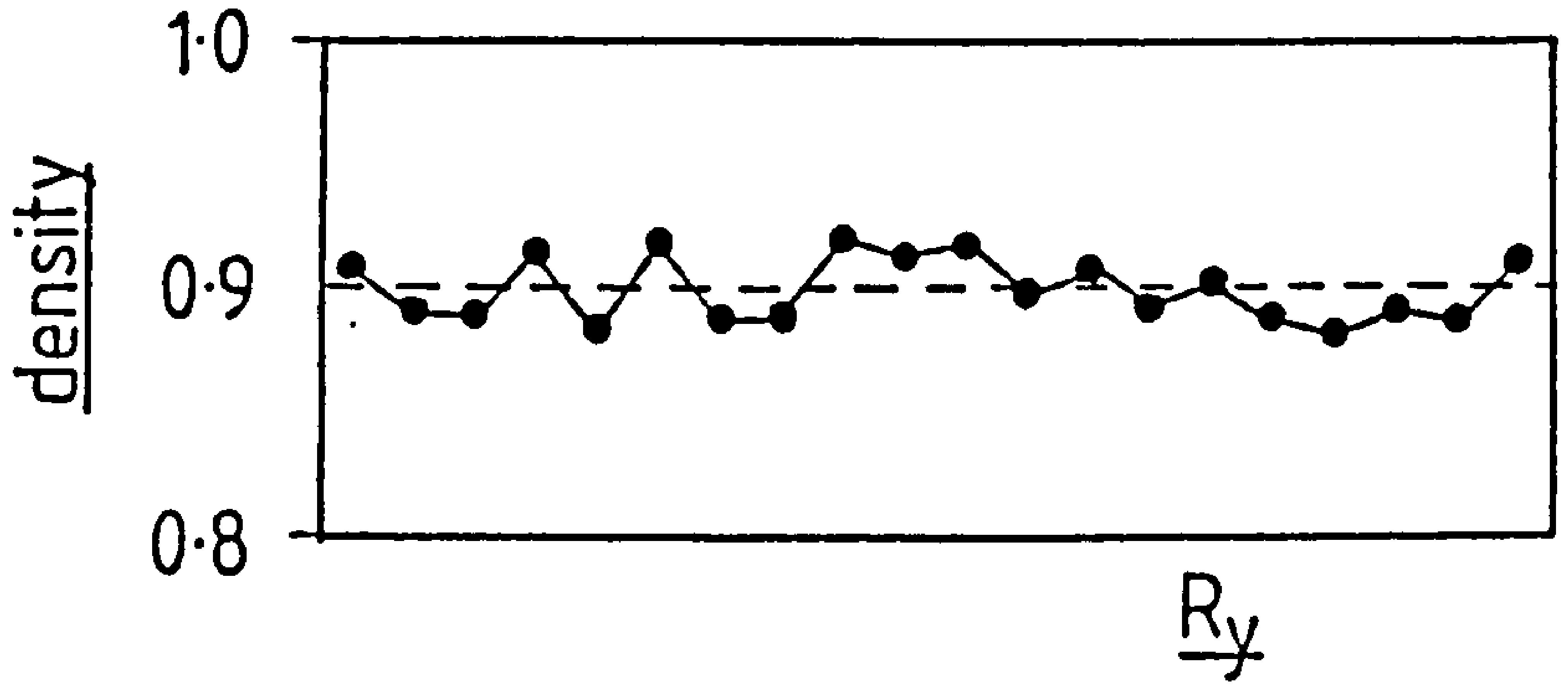

FIGURE 3.2.3: Y-directional Density Profile of the Hard-Sphere System at a Reduced Density $\rho^{\dagger}$ = 0.90 and a Shear Rate $\dot{\gamma}^{\dagger}$ = 0.50

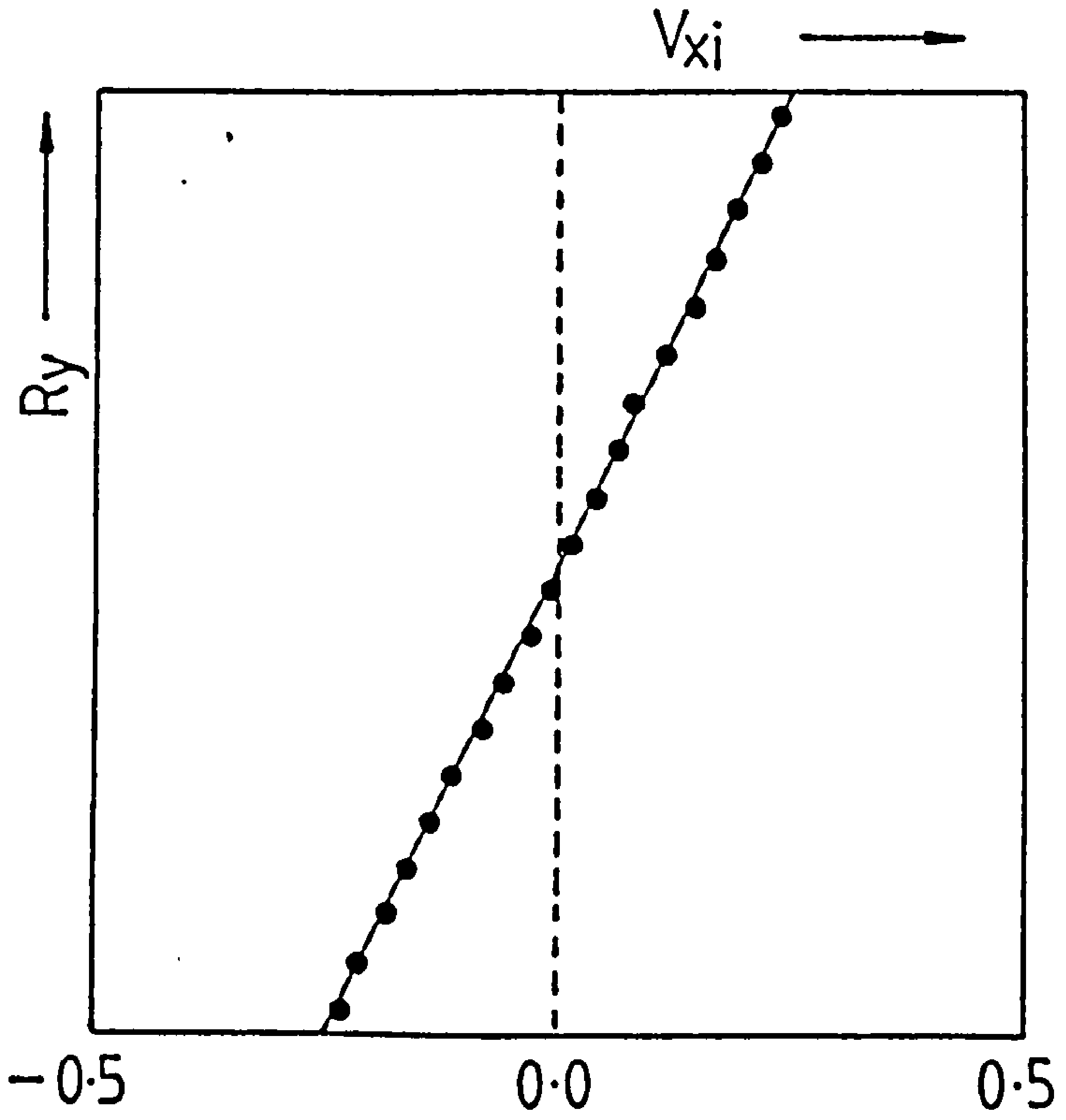

FIGURE 3.2.4: Y-directional Velocity Profile of the Hard-Sphere System at a Reduced Density $\rho^{\dagger}$ = 0.90 and a Shear Rate $\dot{\gamma}^{\dagger}$ = 0.50. The Solid Line Represents the Theoretically Expected Value.

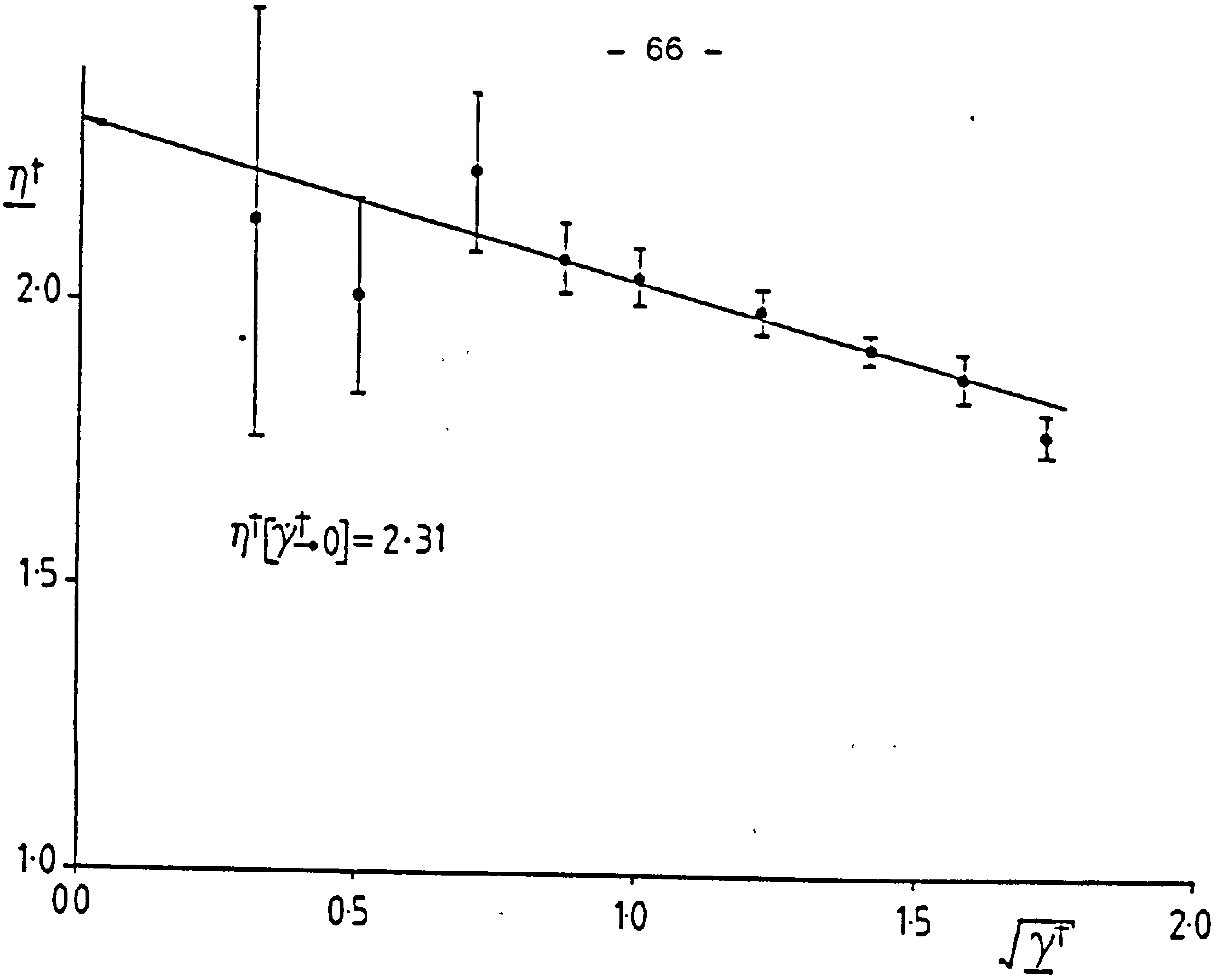

FIGURE 3.2.5: Low Isokinetic Shear Rate Behaviour of the Hard-Sphere Model; $\rho^\dagger = 0.80$

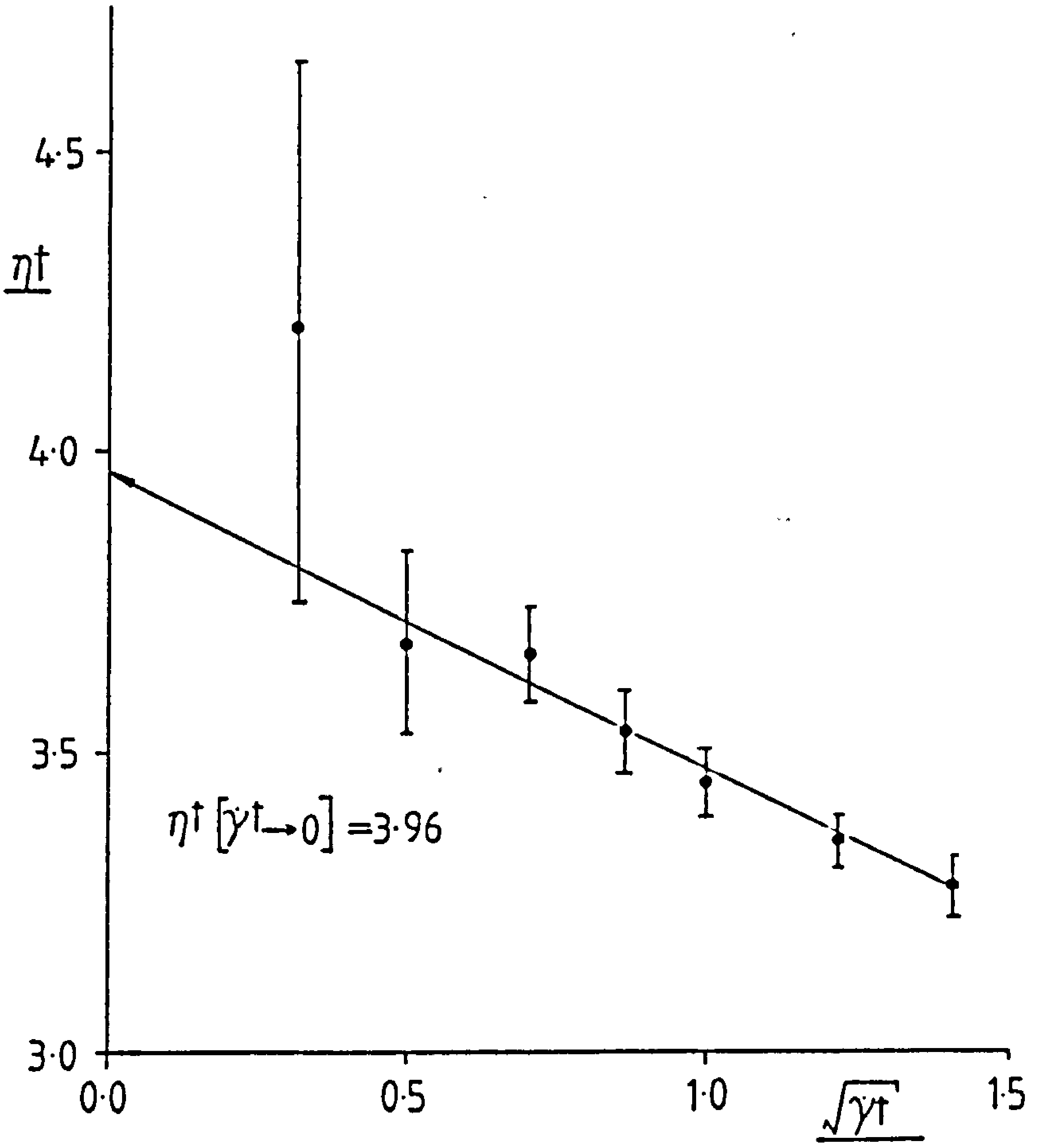

FIGURE 3.2.6: Low Isokinetic Shear Rate Behaviour of the Hard-Sphere Model; $\rho^\dagger = 0.90$

rate is reminiscent of a solid-like response to an imposed flow field. Figure 3.2.9 shows the estimates of zero-shear-rate viscosity for reduced densities $\rho^{\dagger} = 0.80$ and 0.90 plotted in the context of previously estimated values(55). Despite differences in the reduced density points studied, a good agreement between the zero shear-rate viscosity estimated in the present and previous study(55) may be inferred.

The pressure of the hard-sphere model is plotted as a function of shear-rate in Figure 3.2.10. At reduced densities $\rho^{\dagger} = 0.80$ and 0.90, pressure is seen to undergo a sharp discontinuity at these moderate shear-rates. The shear-rate at the onset of this discontinuity in the present data is higher for the system at $\rho^{\dagger} = 0.80$ than for that at $\rho^{\dagger} = 0.90$. Woodcock(4) has previously attributed the qualitatively similar behaviour of the sheared soft-sphere model to a shear-induced perturbation of the equilibrium phase-behaviour. The low shear-rate branches of the $\rho^{\dagger} = 0.80$ and $\rho^{\dagger} = 0.90$ isotherms correspond to a fluid state, whilst the high shear rate branches represent a sheared crystalline phase. In the thermodynamic limit, an extrapolation of the finite shear-rate solid-fluid co-existence pressure back to zero shear-rate should lead to the equilibrium freezing pressure. The current simulations may be far from the thermodynamic limit of large N and long times in the transition region, and consequently the solid-fluid co-existence line on Figure 3.2.10 is severely blurred. The major difficulty preventing the location of this co-existence line is system metastability in the transition region.

Consideration of the zero shear-rate pressure of the hard-sphere system at a reduced densitv $\rho^{\dagger} = 1.0$ earlier in this section has shown the system to be in a metastable fluid state. On application of a shear-field the system pressure is observed to increase smoothly, suggesting that the system remains as a metastable sheared fluid over the limited shear-rate range studied.

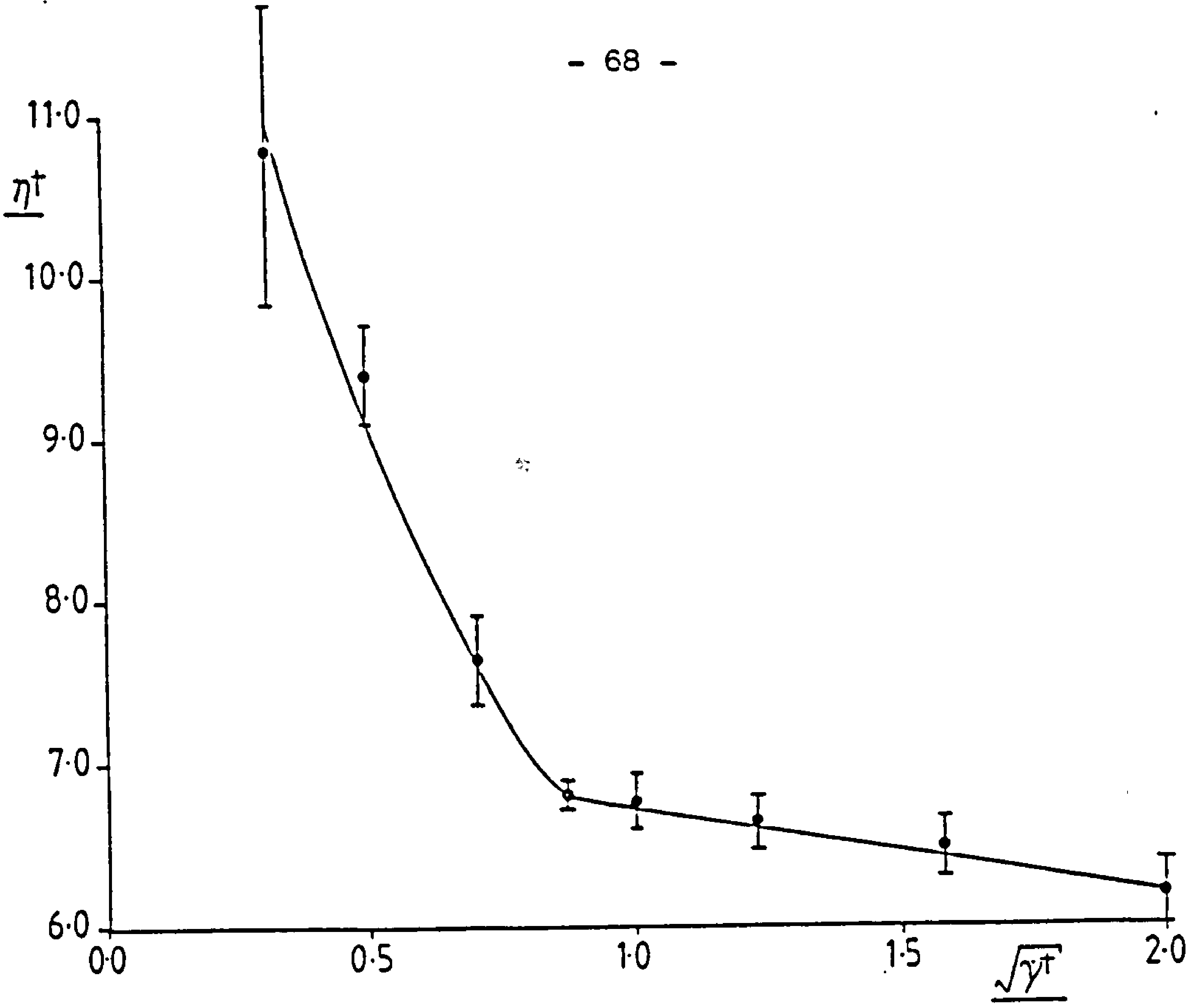

FIGURE 3.2.7: Low Isokinetic Shear Rate Behaviour of the Hard-Sphere Model; $\rho^\dagger = 1.00$

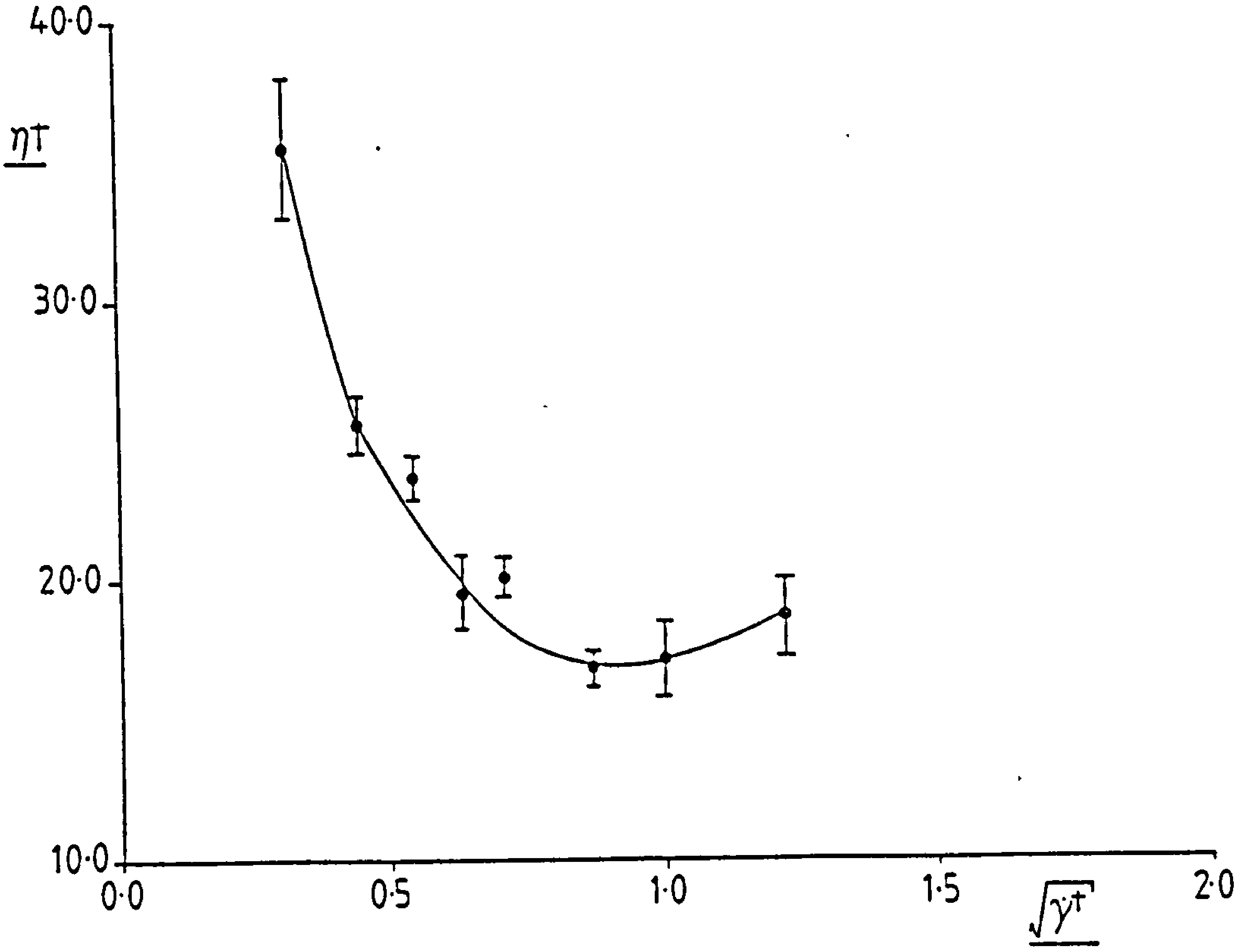

FIGURE 3.2.8: Low Isokinetic Shear Rate Behaviour of the Hard-Sphere Model; $\rho^\dagger = 1.10$

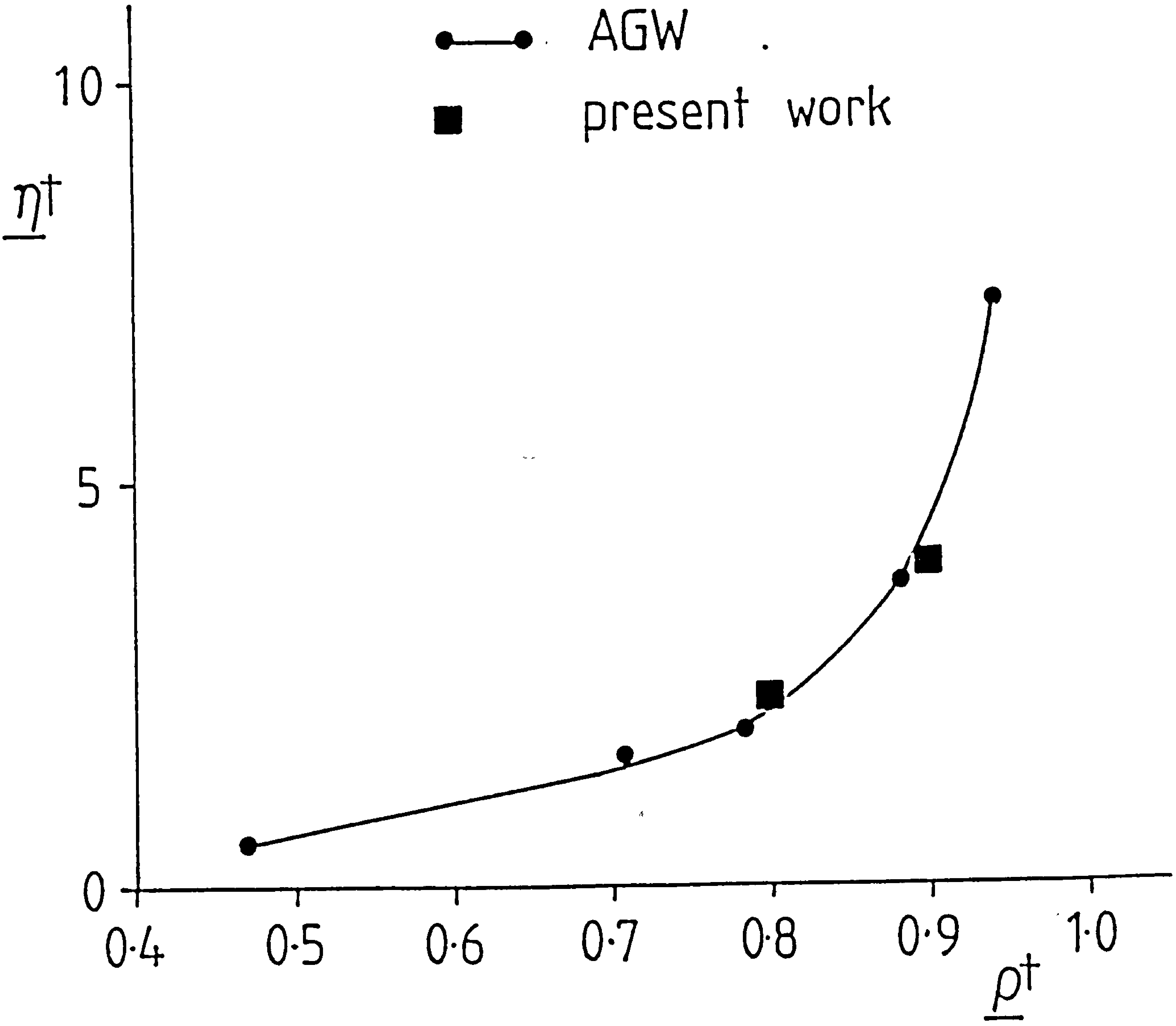

FIGURE 3.2.9: Comparison of the Zero Isokinetic Shear Rate Viscosity EStimated from the Present Work with the Previously Published Data of Alder, Gass and Wainwright

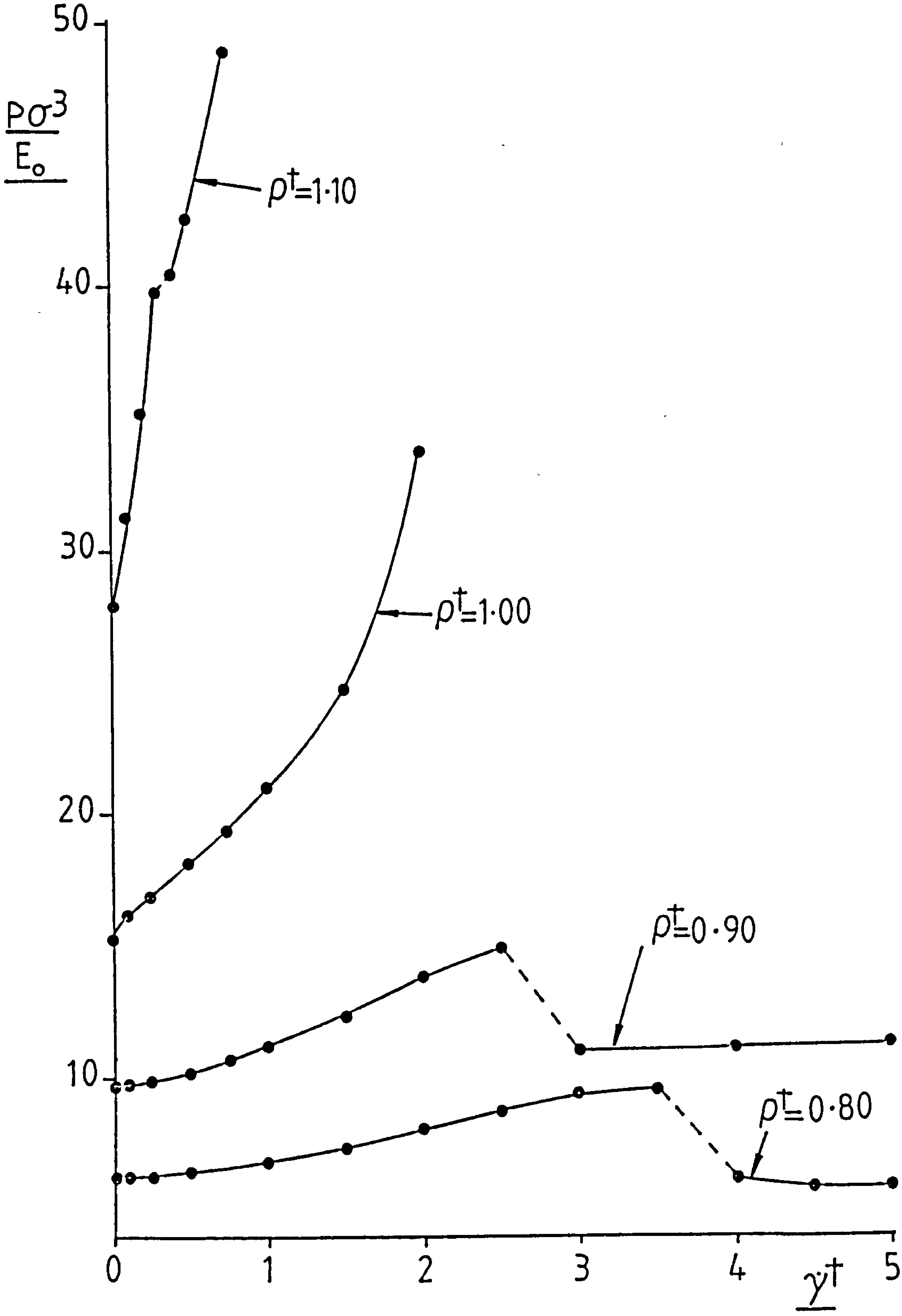

FIGURE 3.2.10: Pressure of the Hard-Sphere Model at Low Isokinetic Shear Rates

The hard-sphere system at $\rho^{\dagger} = 1.10$ has similarly been shown to represent a slightly unstable fluid state. Indeed, Woodcock(37) has reported evidence to suggest that equilibrium hard-sphere systems with reduced densities in excess of $\rho^{\dagger} = 1.08$ undergo spontaneous crystallisation. The crystallisation of the system at $\rho^{\dagger} = 1.10$ at a relatively low shear rate, leading to a pressure discontinuity, is consequently hardly surprising.

Diffusion coefficients for the system with a reduced density $\rho^{\dagger} = 0.90$ at low shear rate have been evaluated from the mean squared displacements relative to the flow field, as defined in Equation (2.3.6) Relatively long runs, of typically 400,000 collisions were performed in order to increase the reliability of the diffusion coefficient estimates.

Speedy(39) has recently proposed the following equation to describe the diffusivity of the hard-sphere fluid under static conditions as a function of density:

$$D_{sp} = \left(\frac{D_o}{\rho^{\dagger}} \right) \left(1 - \frac{\rho^{\dagger}}{1.09} \right) (1 + \rho^{\dagger 2} (0.4 - 0.83\, \rho^{\dagger 2})) \qquad (3.2.1)$$

where $$D_o = \frac{3}{8} \left(\frac{E_o}{\pi m} \right)^{\frac{1}{2}}$$

The hard-sphere diffusion coefficient estimated in the present work can be found in Table 3.2.5. This data is plotted against shear rate in Figure 3.2.11. The zero shear rate value according to Speedy(39) is in good agreement with the present calculation of $D^{\dagger}$. At very low shear rates an increase in the isokinetic hard-sphere model diffusivity may be observed. However, a sharp decrease occurs at shear rates greater than that corresponding to the observed pressure discontinuity (Figure 3.2.10).

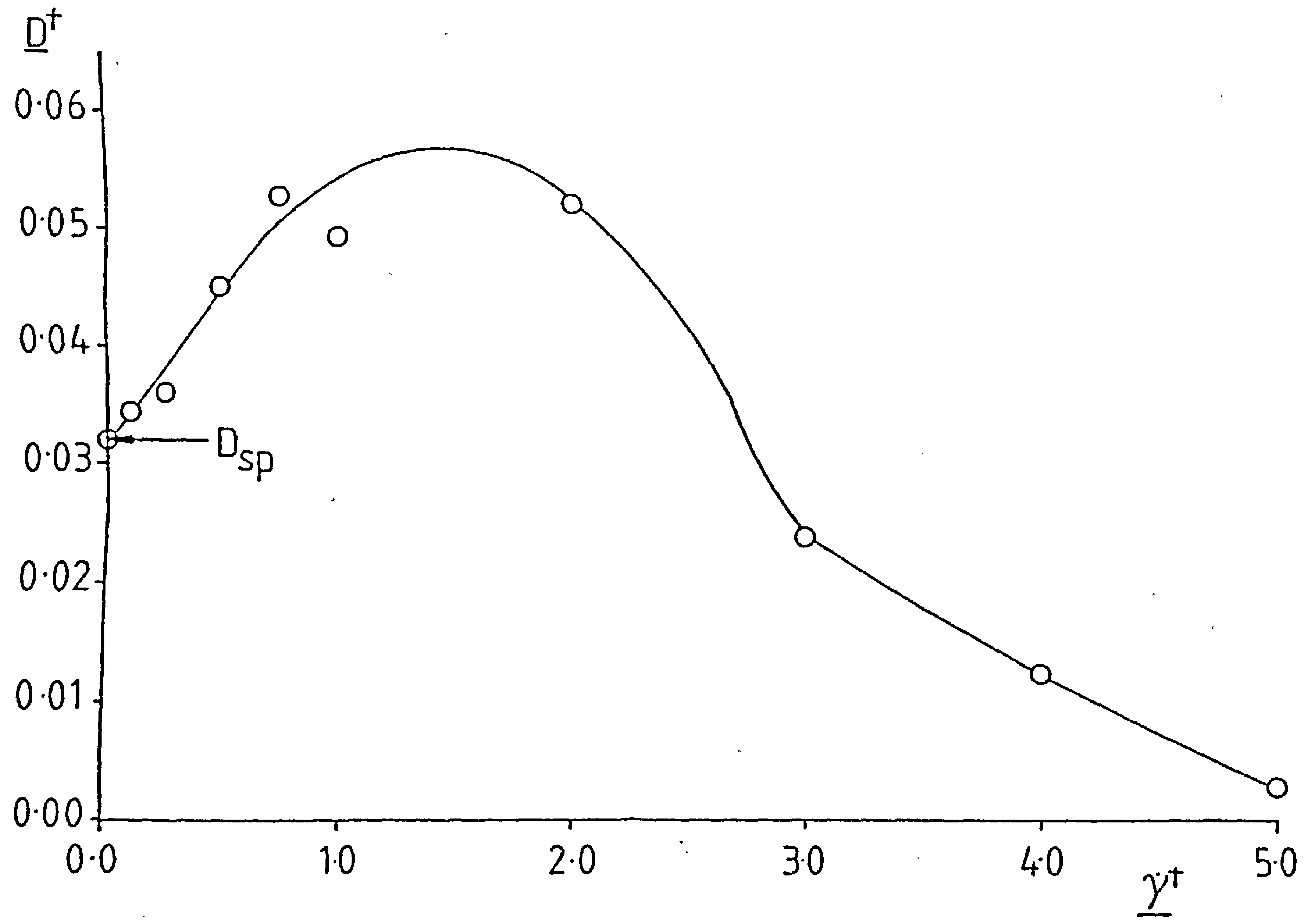

FIGURE 3.2.11: Diffusivity of the Hard-Sphere Model with a Reduced Density $\rho^{\dagger} = 0.90$ at Low Isokinetic Shear Rates. The Equilibrium Value Calculated According to Speedy(39) is Denoted by D_{sp}

Implications of the isokinetic simulation results presented in this section to the study of dense suspension rheology will be discussed in subsequent sections of this chapter.

3.3 Higher Shear Rate Behaviour of the Isokinetic Hard-Sphere Model

The shear-rate range studied in the previous section of this chapter has been extended for the system with a reduced density $\rho^{+} = 0.90$. This reduced density was selected for more extensive study due to its position close to the freezing transition in the fluid region of the equilibrium phase diagram. Experimental systems have been observed to exhibit strongly non-Newtonian rheological behaviour in this packing-fraction regime(119). The simulations at these higher shear rates were performed as a continuation of the low shear rate simulations described in the previous section. Reattainment of apparent steady state conditions following a shear rate increase was usually complete after 40,000 collisions. System properties were then averaged over, typically 120,000 collisions.

In the interests of computational efficiency, thermostatting of the sheared hard-sphere system is effected by the intermittent rescaling of particle peculiar velocities as described in Section 2. Inevitably, a slight amount of system heating occurs inbetween this intermittent rescaling procedure. The magnitude of this kinetic energy increase is negligible at low shear rates, and only becomes noticeable at the very highest shear rates studied here. This deviation of kinetic energy is illustrated in Figure 3.3.1, where the mean kinetic energy is plotted over the entire shear rate range. In the limit that system thermostatting is implemented after each collision, the kinetic energy deviation from the desired value would disappear. More frequent thermostatting however, leads to a decrease in computational efficiency. In this instance the observed kinetic energy rise was considered to be tolerable.

FIGURE 3.3.1: Kinetic Energy of the Sheared Hard-Sphere Model Over the Entire Shear Rate Range Studied. A Slight Deviation from the Desired Value of $E^{+} = 1.50$ can be Observed at the Highest Isokinetic Shear Rates Studied.

In a similar manner to the simulations described at low shear rate, local system density, kinetic energy and velocity profiles were continually monitored in the direction of the velocity gradient. Figures 3.3.2 - 3.3.7 show the behaviour of these local characteristics at shear rates of $\dot{\gamma}^{+} = 10.0$ and 60.0. The widely fluctuating variation in local system density at a shear rate $\dot{\gamma}^{+} = 10.0$ is attributable to a shear-induced structural ordering that will be demonstrated later. That this wide density fluctuation is not evident at $\dot{\gamma}^{+} = 60.0$ is worthy of note at this point. The slight overall increase in system kinetic energy at high shear rates is reflected in Figures 3.3.2 and 3.3.5. Despite this overall increase there would appear to be no evidence of any inhomogeneity of local kinetic energy in the direction of the velocity gradient. Velocity profiles are plotted in Figure 3.3.4 and 3.3.7. The ideal velocity profile in each case is denoted by a solid line. Excellent agreement is observed between ideal and actual velocity profiles, even at the highest shear rate point studied.

The isokinetic hard-sphere flow curve at a reduced density $\rho^{+} = 0.90$ is plotted over the entire shear rate range studied in Figure 3.3.8. The low shear rate data originally presented in the previous section is also plotted. Figure 3.3.9 plots the corresponding pressure behaviour against the same logarithmic shear rate scale as Figure 3.3.8. Consideration of these two figures reveals that the sharp decrease in viscosity occurs at the same pressure discontinuity discussed in the previous section. A second pressure discontinuity can be observed at $\log(\dot{\gamma}^{+}) = 1.30$ but there is no corresponding viscosity discontinuity.

The relationship between the observed macroscopic behaviour and the underlying structure of the hard-sphere system will be discussed in Section 3.5, along with the applications of this behaviour with respect to dense suspension rheology.

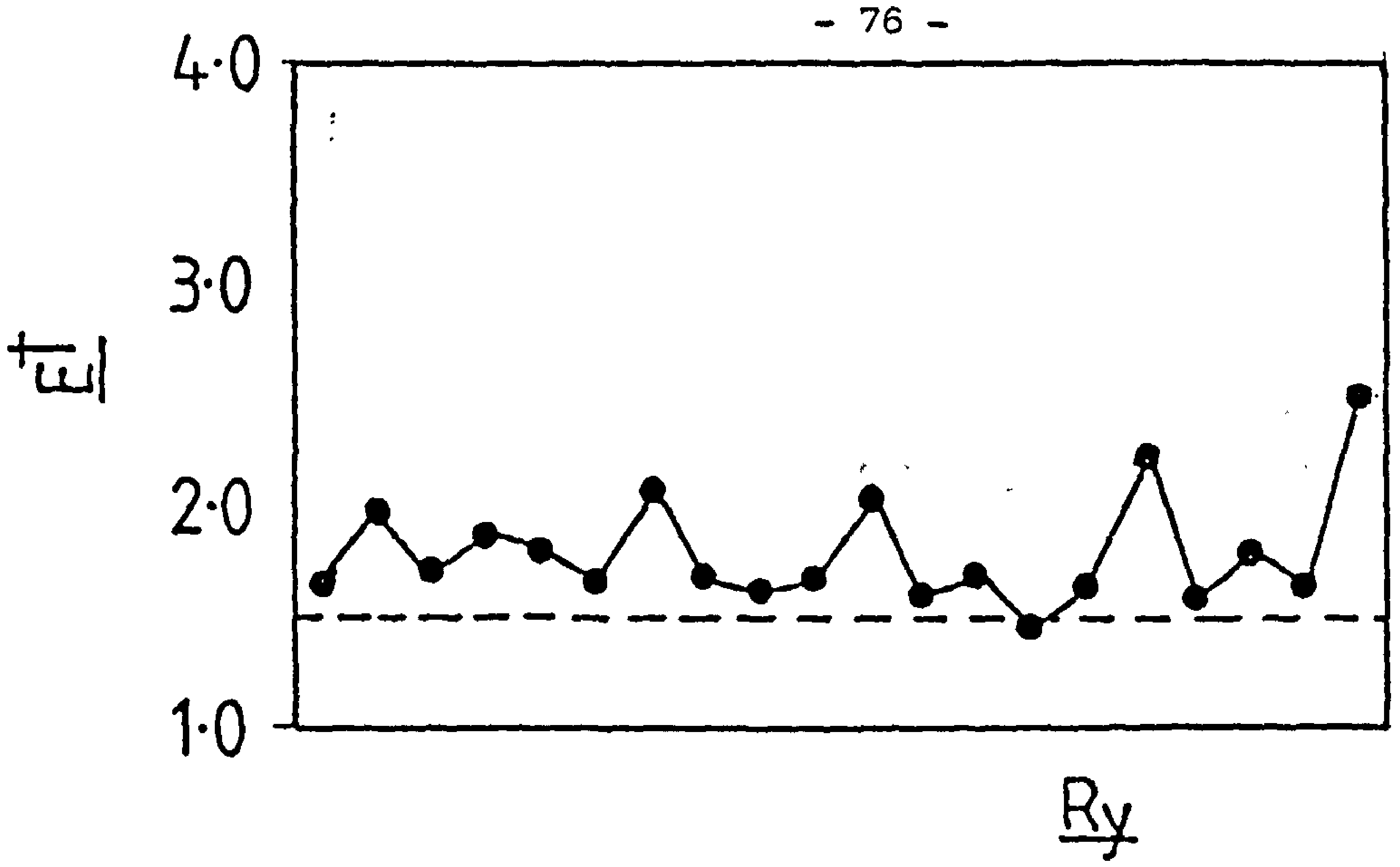

FIGURE 3.3.2: Y-directional Kinetic Energy Profile of the Hard-Sphere System at a Reduced Density $\rho^{\dagger} = 0.90$ and a Shear Rate $\dot{\gamma}^{\dagger} = 10.0$

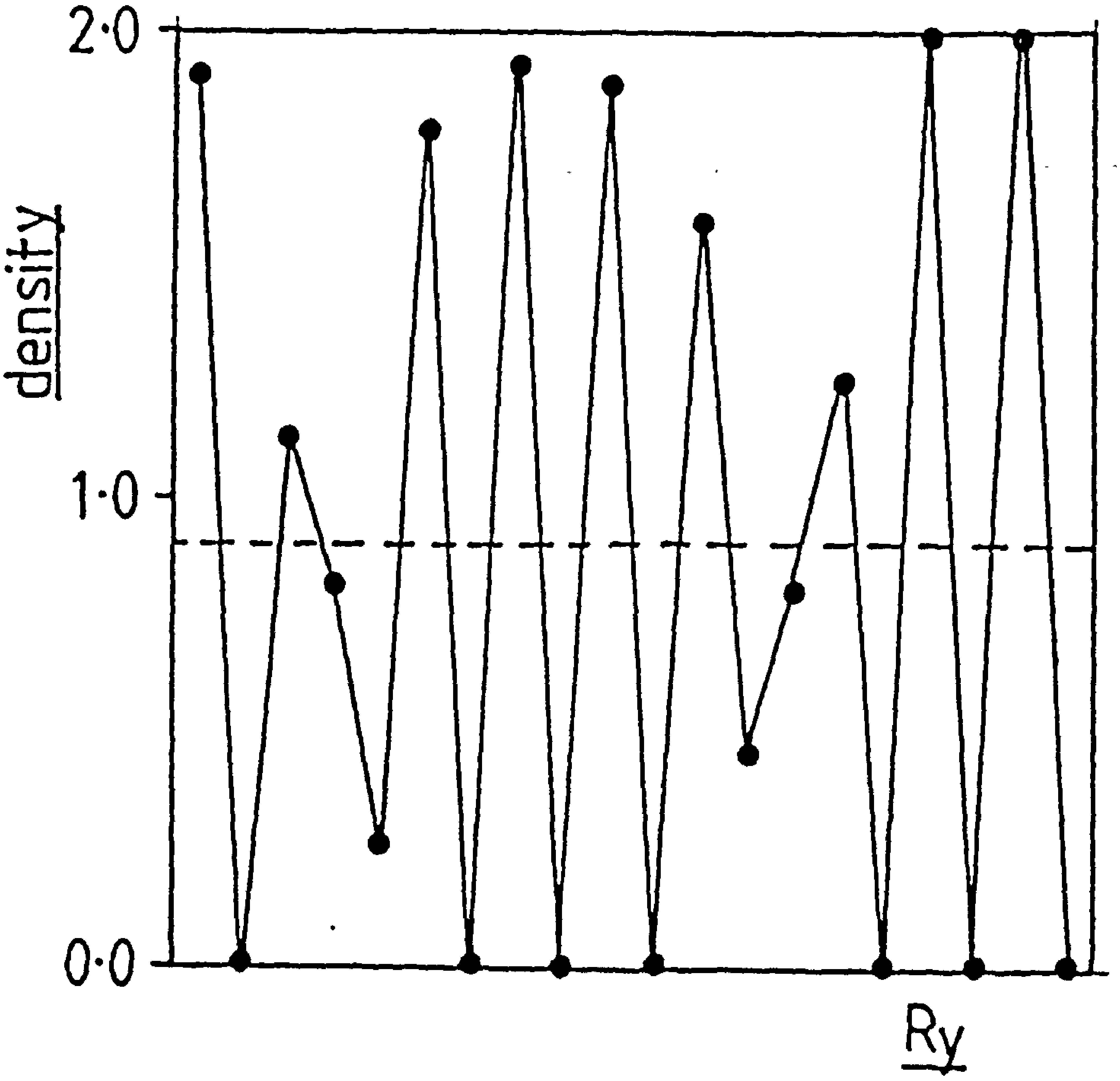

FIGURE 3.3.3: Y-directional Density Profile of the Hard-Sphere System at a Reduced Density $\rho^{\dagger} = 0.90$ and a Shear Rate $\dot{\gamma}^{\dagger} = 10.0$

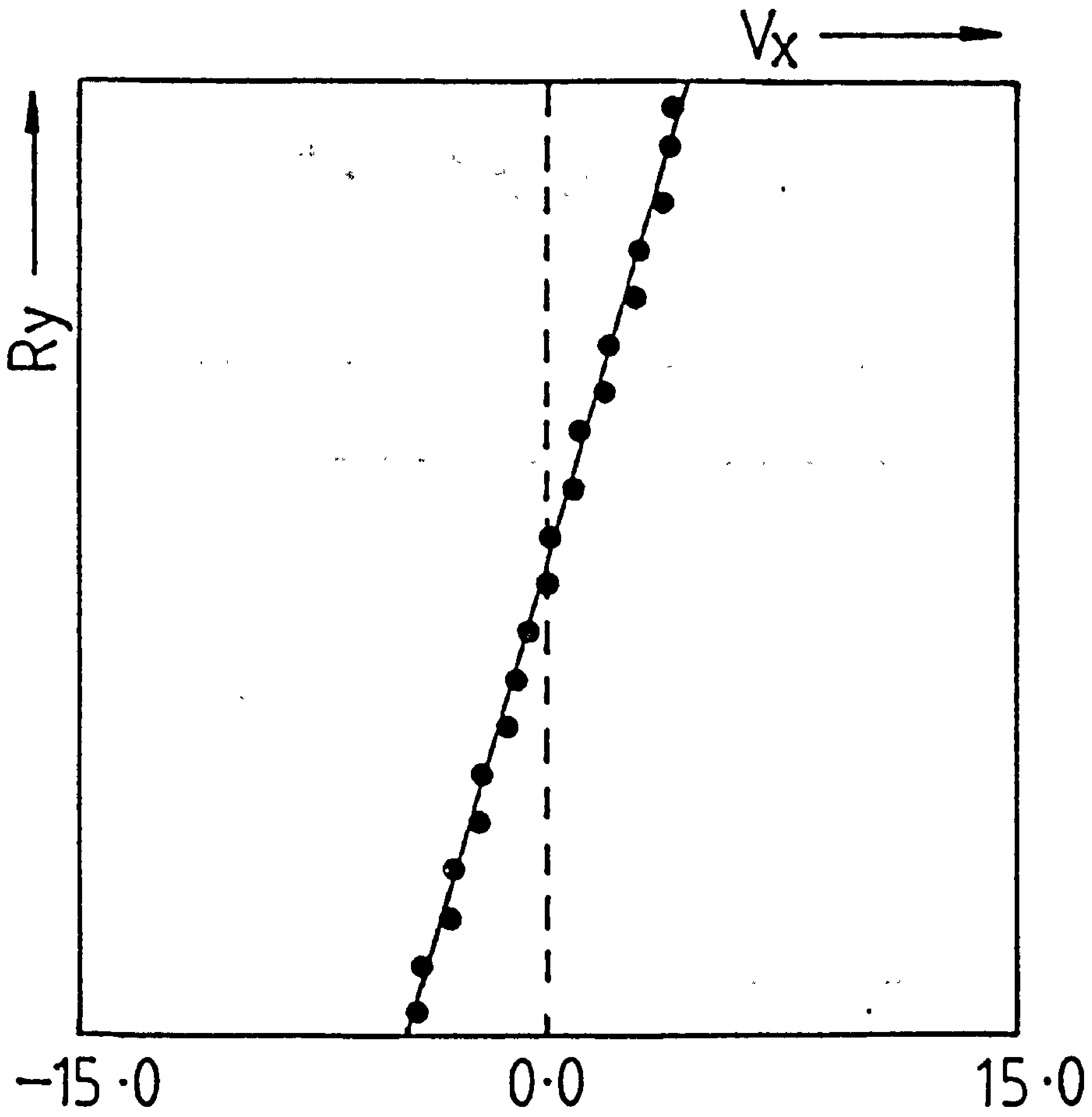

FIGURE 3.3.4: Y-directional Velocity Profile of the Hard-Sphere System at a Reduced Density $\rho^{\dagger} = 0.90$ and a Shear Rate $\dot{\gamma}^{\dagger} = 10.0$. The Solid Line Represents the Theoretically Expected Value.

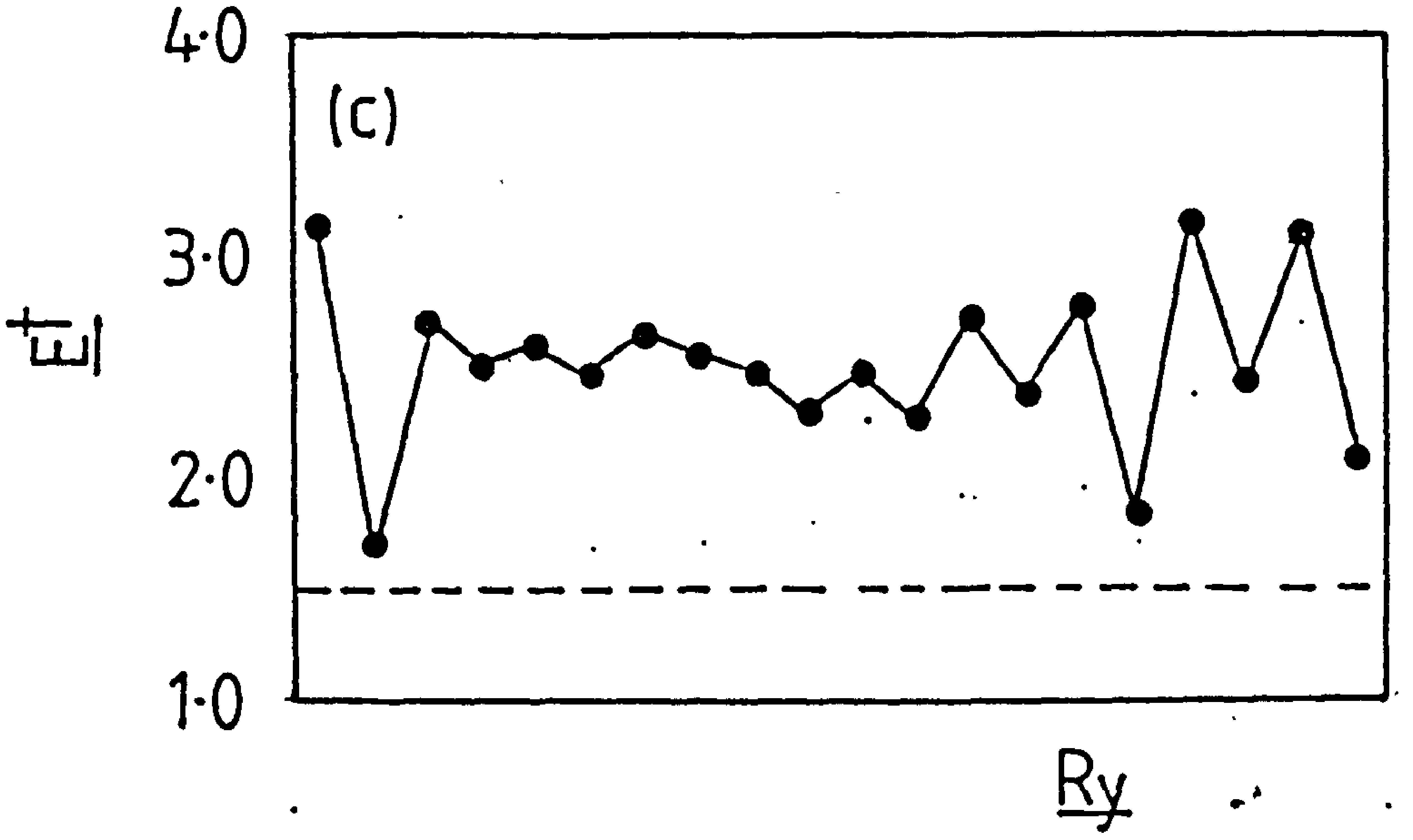

FIGURE 3.3.5: Y-directional Kinetic Energy Profile of the Hard-Sphere System at a Reduced Density $\rho^\dagger = 0.90$ and a Shear Rate $\dot{\gamma}^\dagger = 60.0$.

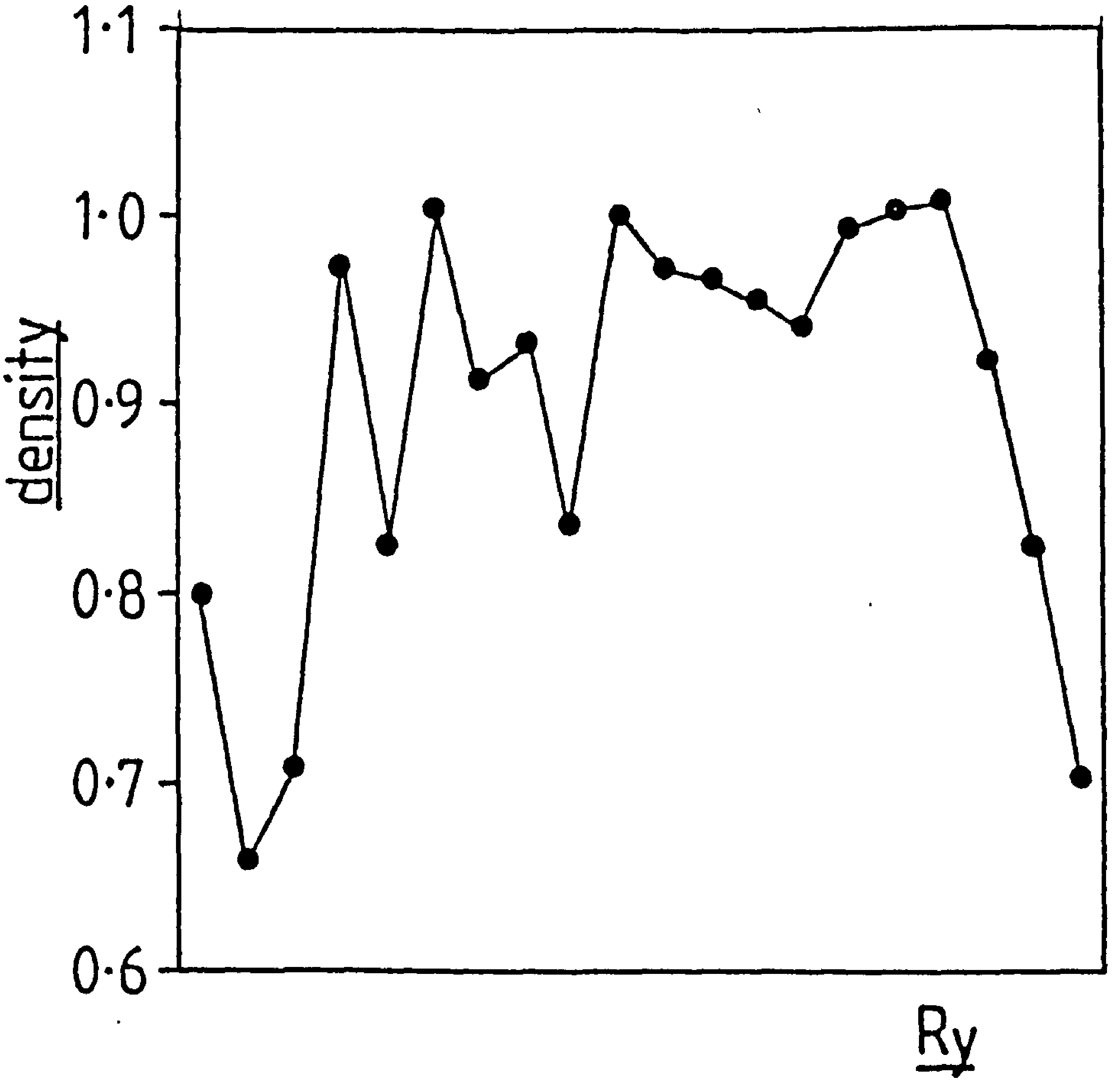

FIGURE 3.3.6: Y-directional Profile of the Hard-Sphere System at a Reduced Density $\rho^\dagger = 0.90$ and a Shear Rate $\dot{\gamma}^\dagger = 60.0$.

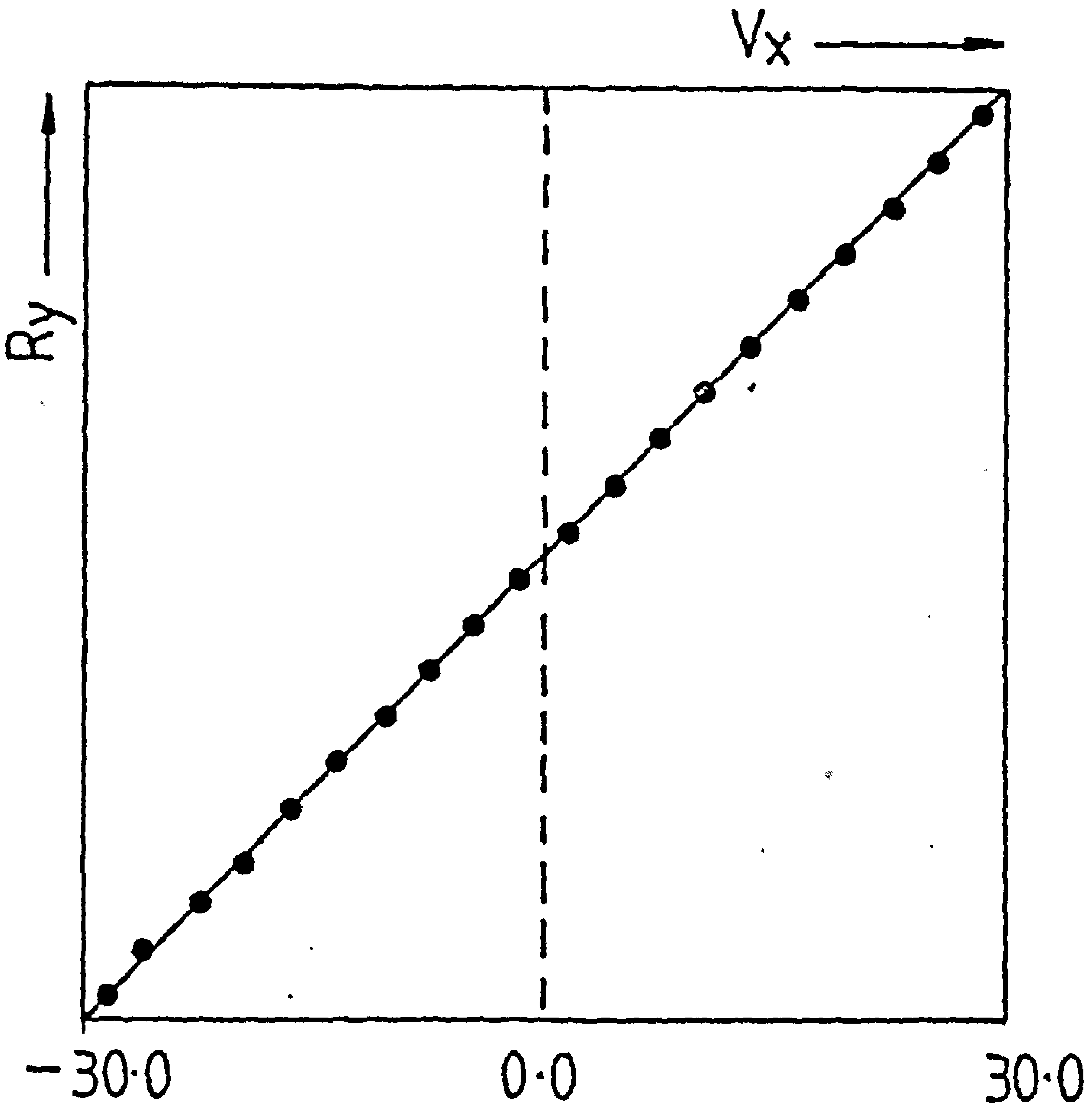

FIGURE 3.3.7: Y-directional Velocity Profile of the Hard-Sphere System at a Reduced Density $\rho^{\dagger} = 0.90$ and a Shear Rate $\dot{\gamma}^{\dagger} = 60.0$. The solid line represents the theoretically expected value.

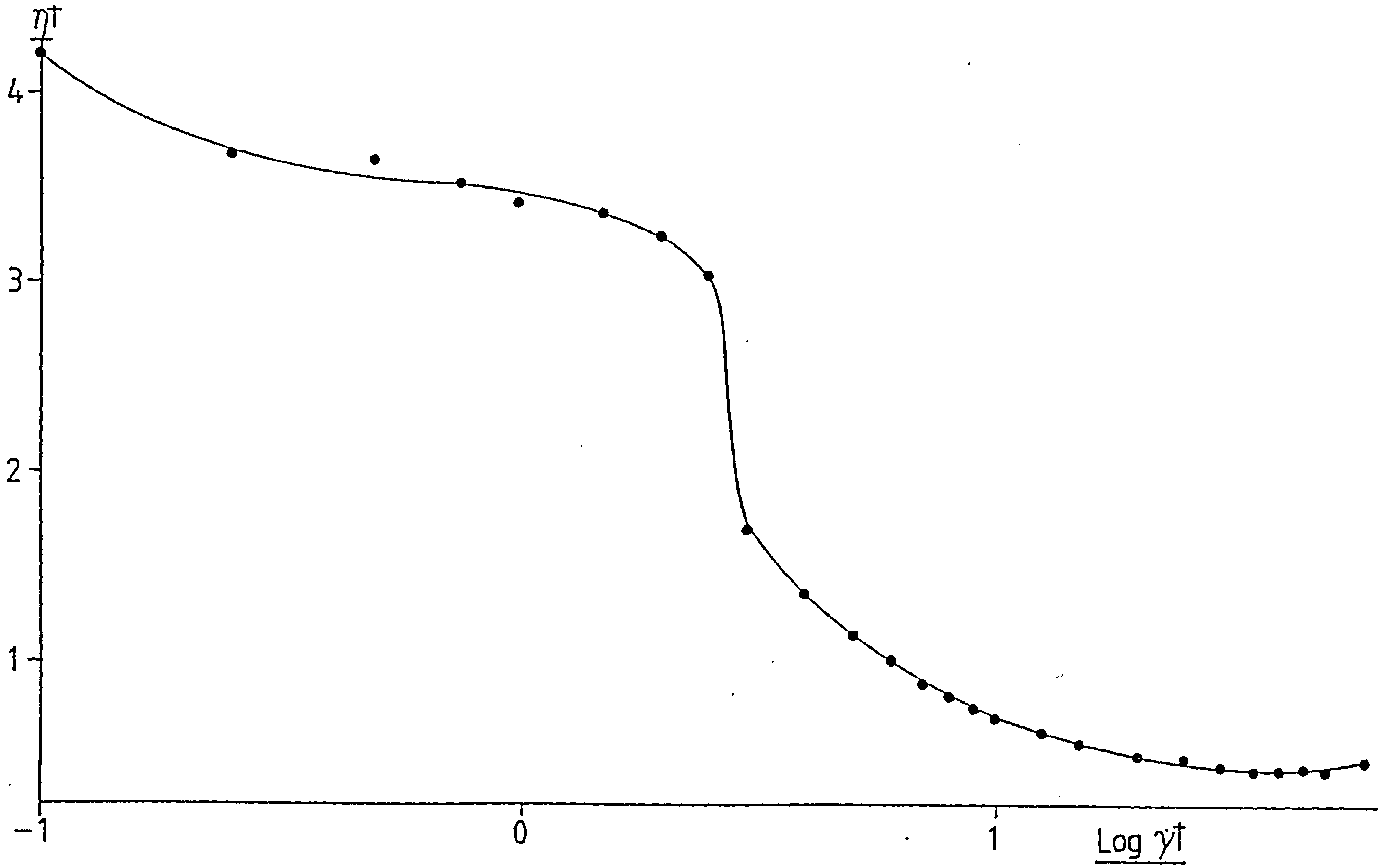

FIGURE 3.3.8: Viscosity of the Isokinetic Hard-Sphere Model Over the Entire Shear Rate Range Studied. $\rho^{\dagger} = 0.90$

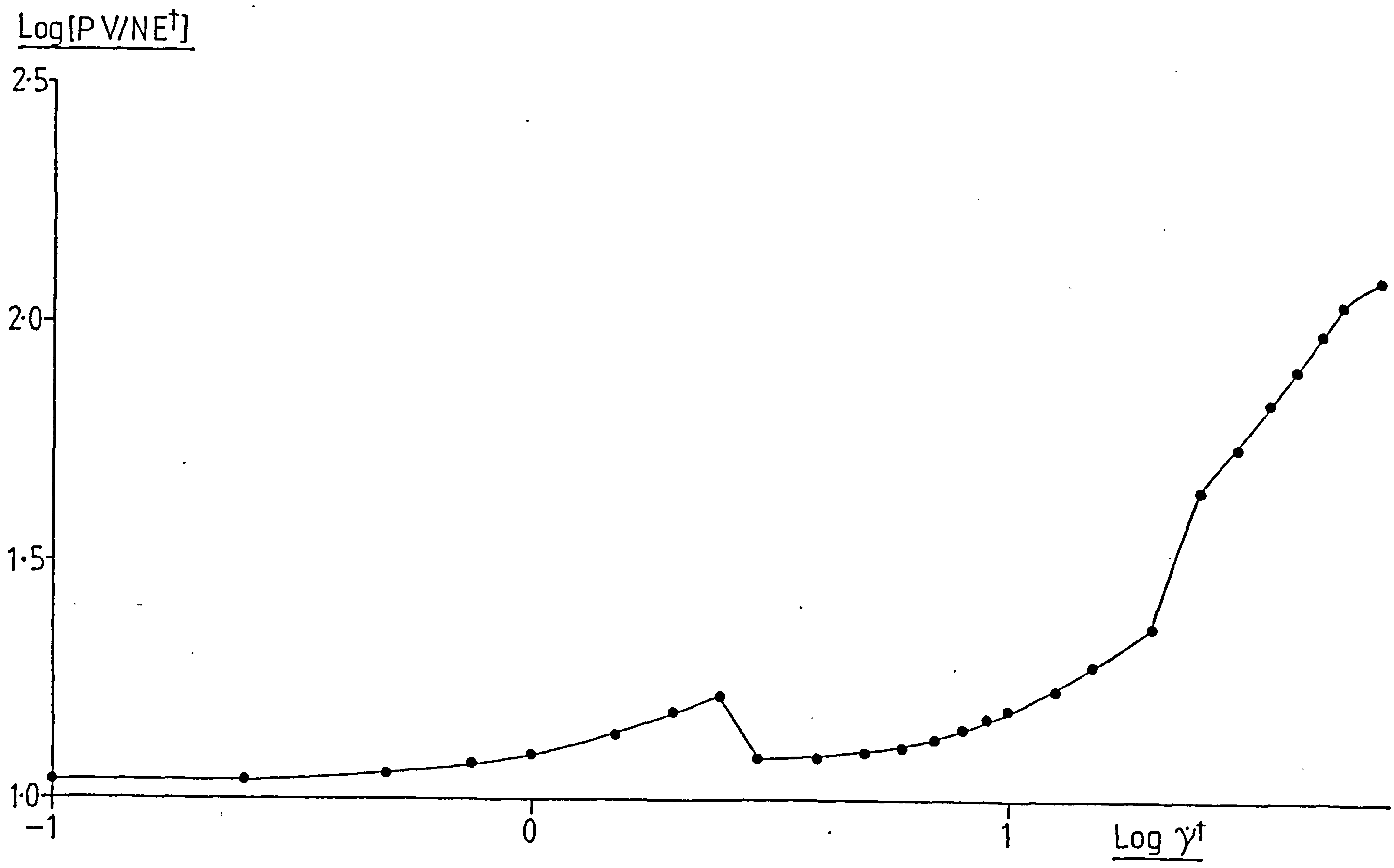

FIGURE 3.3.9: Pressure of the Isokinetic Hard-Sphere Model Over the Entire Shear Rate Range Studied $\rho^{\dagger} = 0.90$

3.4 Kinetic Energy-Shear Rate Scaling Properties of the Hard-Sphere Model

Naitoh and Ono(67) originally pointed out the kinetic energy-shear-rate scaling behaviour of the classical hard-sphere system. This behaviour leads to the observation that, in order to shear two hard-sphere systems differing only in kinetic energy at 'corresponding states' shear rates the following relation must hold:

$$\frac{\dot{\gamma}^{\dagger}}{\sqrt{E^{\dagger}}} = \text{constant} \qquad (3.4.1)$$

where $\dot{\gamma}$ is the shear rate and E is the system kinetic energy.

From the above equation, it can be seen that a change in energy (since the energy of a hard-sphere system is entirely kinetic) is formally equivalent to a change in the 'corresponding states' shear rate.

In order to create 'steady state' conditions in the simulations described herein, particle peculiar velocities (i.e. relative to the flow field) are regularly rescaled so as to maintain isokinetic conditions. These isokinetic conditions are clearly in contrast to an experimentally sheared suspension, where the energy input at low shear rates is given by:

$$Q = \eta \dot{\gamma}^2 \qquad (3.4.2)$$

where Q is the energy input per unit volume, η is the viscosity, and $\dot{\gamma}$ is the shear rate.

Simultaneous consideration of Equations (3.4.1) and (3.4.2) allows an important observation to be made concerning the application of the results of isokinetic non-equilibrium hard-sphere simulations to the rheology of solid/liquid suspensions.

Consider a typical experimental determination of the apparent viscosity of a solid/liquid suspension, where the laboratory shear rate is increasing. Since E, the energy of the particles, increases as $\dot{\gamma}^2$ the corresponding states shear rate as defined in Equation (3.4.1) is clearly decreasing. Contrast this situation to an isokinetic simulation of a sheared hard-sphere fluid, where the 'corresponding states' shear rate is increasing linearly. Consequently, the form of a flow curve obtained from an isokinetic non-equilibrium simulation is inverted with respect to the shear rate scale when compared to an experimental flow curve.

Woodcock(65) recently described the implications of the artificial thermostatting procedure often incorporated into non-equilibrium particulate dynamics simulations, and describes an alternative approach which more closely resembles an experimental situation. This new approach involves the replacement of particle velocity damping by a variable amount such that isokinetic conditions are maintained, by a constant rate of particle velocity damping. Consequently, this 'mean field' Stokesian dynamics approach leads to equilibration of the system kinetic energy at a unique value for each shear rate point studied.

Since energy is no longer a fixed system parameter, it no longer enters into the definition of reduced system properties as is the case for isokinetic simulations. Reduced properties are now defined in terms of particle mass (m), diameter (σ), and effective rescaling coefficient (c). Definitions of reduced units (denoted by a superscript asterisk *) are summarised in Table 3.4.1.

In the limit that particle velocities are rescaled continuously, the dynamical sequence of the sheared 'isokinetic' system is identical to that of the sheared 'Stokesian' system, the difference being in the time scale for collisions. Moreover, the properties of one system are entirely predictable from those of the other, assuming a knowledge of:

TABLE 3.4.1

'Stokesian' Reduced Quantities

Time	$t^{*} = tc$
Shear Rate	$\gamma^{*} = \dot{\gamma}/c$
Friction Coefficient	$c = \frac{3\pi\sigma}{m}\,\eta_m$
Kinetic Energy	$E^{*} = \frac{E}{m\sigma^2c^2} = \frac{E^{\dagger}}{c^{\dagger 2}}$
Pressure	$p^{*} = \frac{p\sigma}{mc^2} = \frac{p^{\dagger}}{c^{\dagger 2}}$
Viscosity	$\eta^{*} = \frac{\eta}{3\pi\eta_m} = \frac{\eta^{\dagger}}{c^{\dagger}}$
Diffusivity	$D^{*} = \frac{D}{c\sigma^2} = \frac{D^{\dagger}}{c^{\dagger}}$

(Reproduced from Reference 65)

$c^{\dagger}\ (y,\ \dot{\gamma}^{\dagger})$

or $E^{*}\ (y,\ \dot{\gamma}^{*})$

3.5 Applications to the Study of Suspension Rheology

The simple scaling argument originally due to Woodcock(65), presented in the previous section of this chapter demonstrates the necessity to present the results of isokinetic non-equilibrium particulate dynamics simulations in terms of 'Stokesian' reduced units, before any parallels with dense suspension rheology can be drawn. The implications of this observation with respect to the intepretation of isokinetic non-equilibrium simulations are enormous. One such implication being that the shear-induced perturbation of equilibrium phase behaviour observed at low shear rates in isokinetic simulations does not correspond to the shear thinning behaviour of dense suspensions as previously thought. Instead this behaviour corresponds to the well known shear-thickening transition exhibited by dense suspensions at higher shear rates. All the results to be presented in this section correspond to the hard-sphere system with a reduced density $\rho^{\dagger} = 0.90$ which has been studied over the widest shear rate range.

Figure 3.5.1 shows a qualitative estimate of the rapidly increasing level of system kinetic energy with increasing shear rate of a dense suspension. In this figure we can clearly see two distinct branches corresponding to an ordered and disordered microstructure, to be shown shortly. The overlap of these branches may be attributed to metastability, leading to an 'overshoot' in the amorphous state lifetime.

Qualitatively the behaviour of the sheared hard-sphere suspension osmotic pressure (Figure 3.5.2) and diffusivity (Figure 3.5.3) exhibit

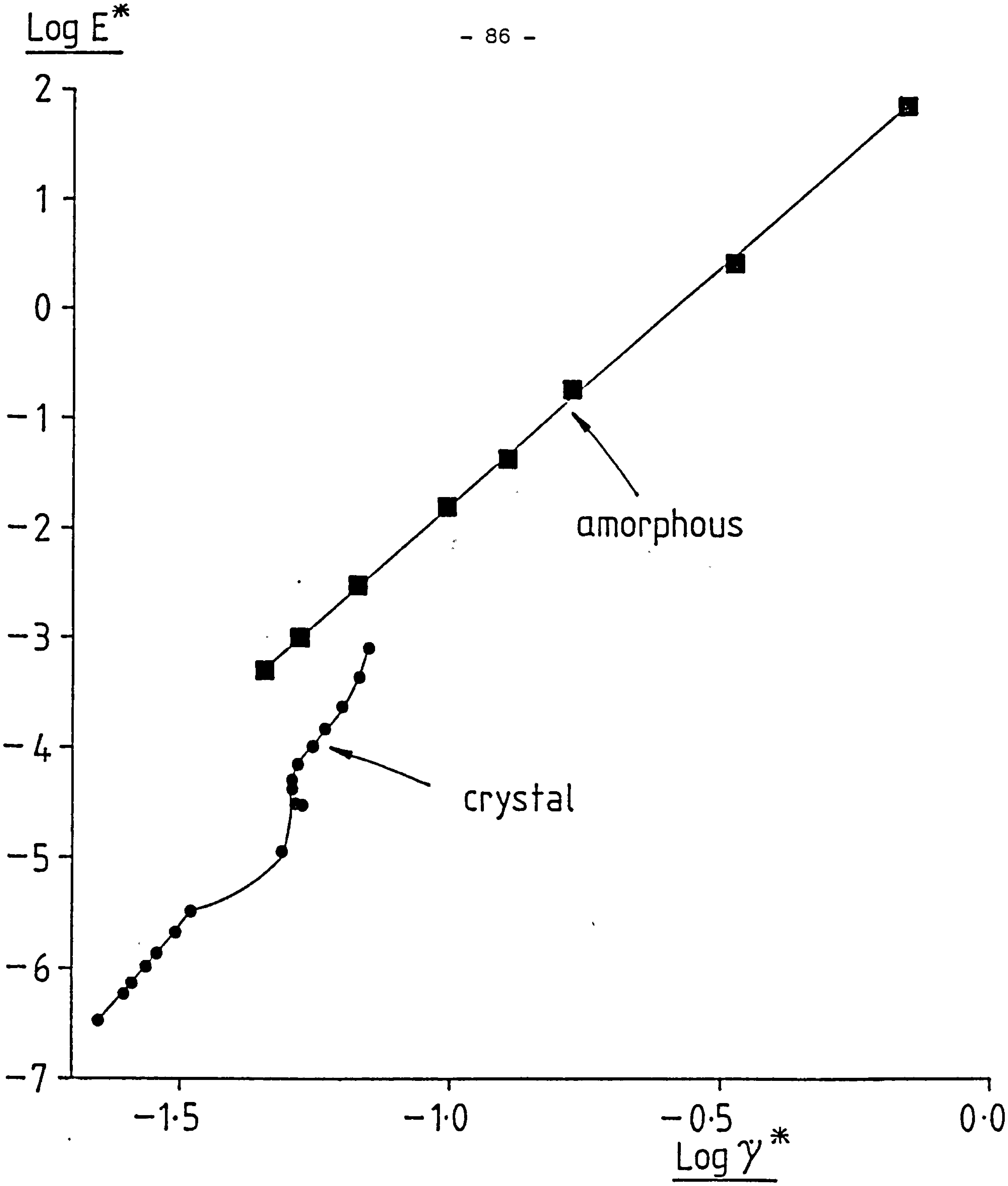

FIGURE 3.5.1: Kinetic Energy of the Sheared Hard-Sphere Suspension $\rho^{\dagger} = 0.90$

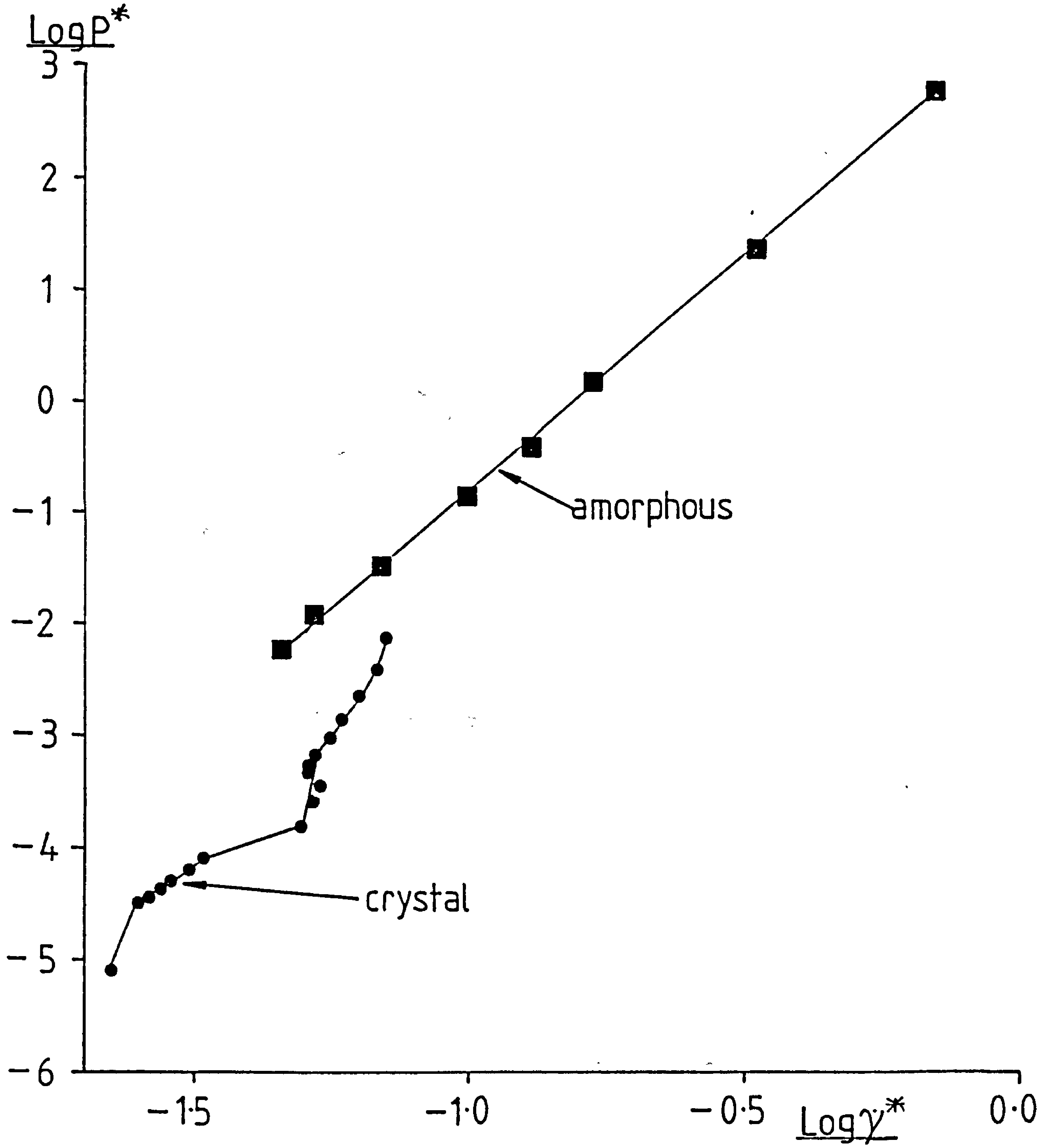

FIGURE 3.5.2: Osmotic Pressure of the Sheared Hard-Sphere Suspension $\rho^{\dagger} = 0.90$

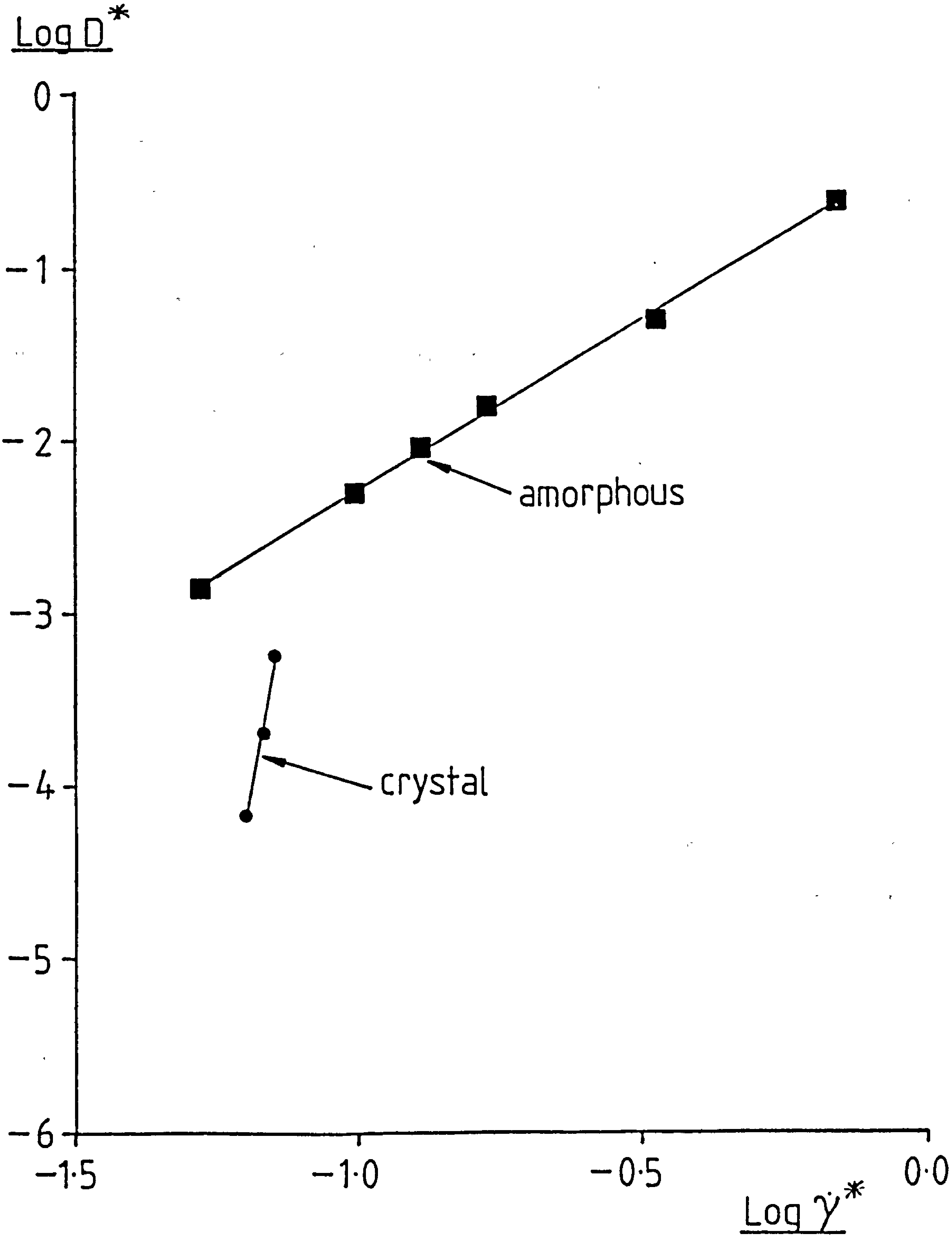

FIGURE 3.5.3: Diffusivity of the Sheared Hard-Sphere Suspension $\rho^{+} = 0.90$

a similar type of behaviour to that of kinetic energy, i.e. an overall rapid increase with increasing shear rate, but with two distinct branches.

The calculated viscosity of the hard-sphere system throughout a dynamical simulation (Equation 2.3.10) corresponds to the osmotic or collisional contribution to the overall observed viscosity of a hard-sphere suspension. Neglecting many-body hydrodynamic contributions the remaining shear rate independent, 'intrinsic' contribution was originally calculated by Einstein(16). The relative viscosity η_r^*, as plotted in Figure 3.5.4 is therefore calculated from(65):

$$\eta_r^* = 1 + \frac{5}{2} y + 3\pi \eta^* \; . \; \ldots\ldots \qquad (3.5.1)$$

At the lower end of the Stokesian shear rate range studied (region a on Figure 3.5.4), the osmotic contribution to the overall relative viscosity is negligible. The relative viscosity in this region is therefore constant, taking a value of $(1 + 5/2\, y)$. At higher shear rates, however, (regions b and c) the osmotic contribution rapidly becomes dominant. Osmotic pressure, kinetic energy and diffusivity are all also rapidly increasing in this shear rate regime. Experimental attempts to characterise the rheological properties of a suspension in this region are increasingly fraught with difficulties. Rapidly increasing osmotic pressure would be manifested experimentally as dilatancy, whilst increasing diffusivity corresponds to a shortening of the time required for particle migration. Both these effects have been observed experimentallv(119,24).

One great advantage of computational particulate dynamics simulations is that system configurations may be readily analysed at any time during a simulation. A convenient method of representing three-dimensional particulate systems graphically is to produce a set of three plots, each of which projects particle co-ordinates onto a different cartesian dimensional plane. Each plot is then akin to viewing the central simulation

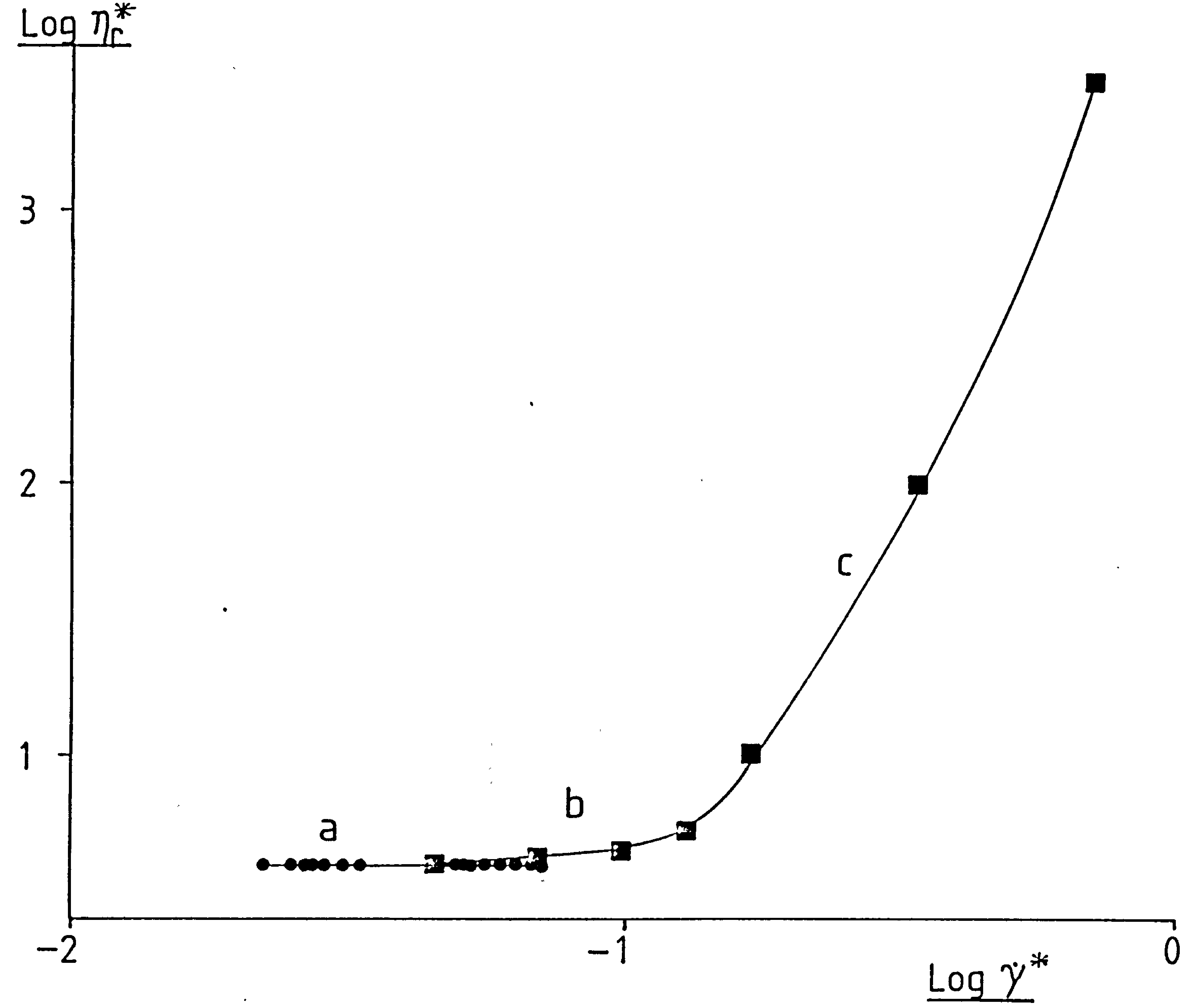

FIGURE 3.5.4: Relative Viscosity of the Sheared Hard-Sphere Suspension

cell from one of three orthogonal viewpoints. These three viewpoints are illustrated with respect to the direction of flow and velocity gradient in Figure 3.5.5. In the configurational plots that follow, the size of the circle used to denote particle positions is purely arbitrary, and is unrelated to the hard-sphere diameter.

A set of orthogonally viewed particle configurations at each of the shear rates corresponding to regions a, b and c of Figures 3.5.1 - 3.5.4 constitute Figures 3.5.6 - 3.5.8 respectively. From these figures we can see that the microstructure at the shear rate corresponding to region (a) on each of Figures 3.5.1 - 3.5.4 is highly ordered. In this shear rate regime particles are effectively traversing along cylinders bounded by neighbouring cylinders. Moving to higher shear rates, corresponding to region (b), we can see that a slight structure change has occurred within the system; particles are less tightly aligned and there is evidence of disorder in some regions of the cell. It is tempting to compare the state of the system in this shear rate regime to the two-phase behaviour exhibited by the equilibrium hard-sphere system. At even higher shear rates, corresponding to region (c) we can see that the system has become completely disordered as viewed from all three orthogonal viewpoints. Kinetic energy, osmotic pressure and diffusivity of the system at this shear rate region lie on the second, high shear rate branch, as shown in Figures 3.5.1 - 3.5.3. Viscosity is increasing rapidly (Figure 3.5.4) since the co-operative particle motion occurring at lower shear rates has ceased.

Resolution of pressure, kinetic energy and diffusivity into contributions arising from the three mutually perpendicular cartesian dimensions is possible, such that:

$$P^* = \frac{1}{3}\ (P^*_{xx} + P^*_{yy} + P^*_{zz}) \qquad (3.5.2)$$

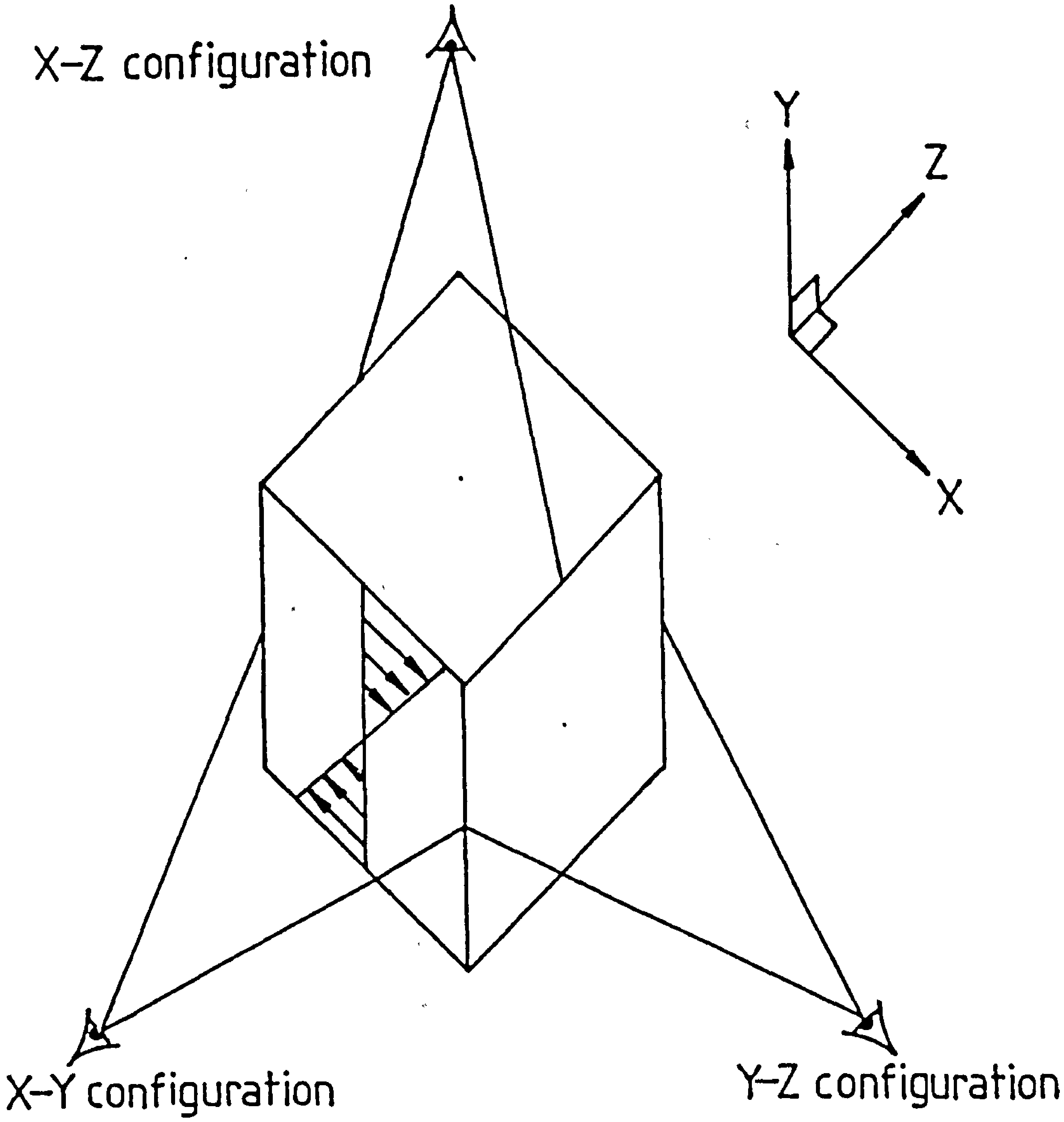

FIGURE 3.5.5: Orthogonal Viewpoints of the Central Simulation Cell

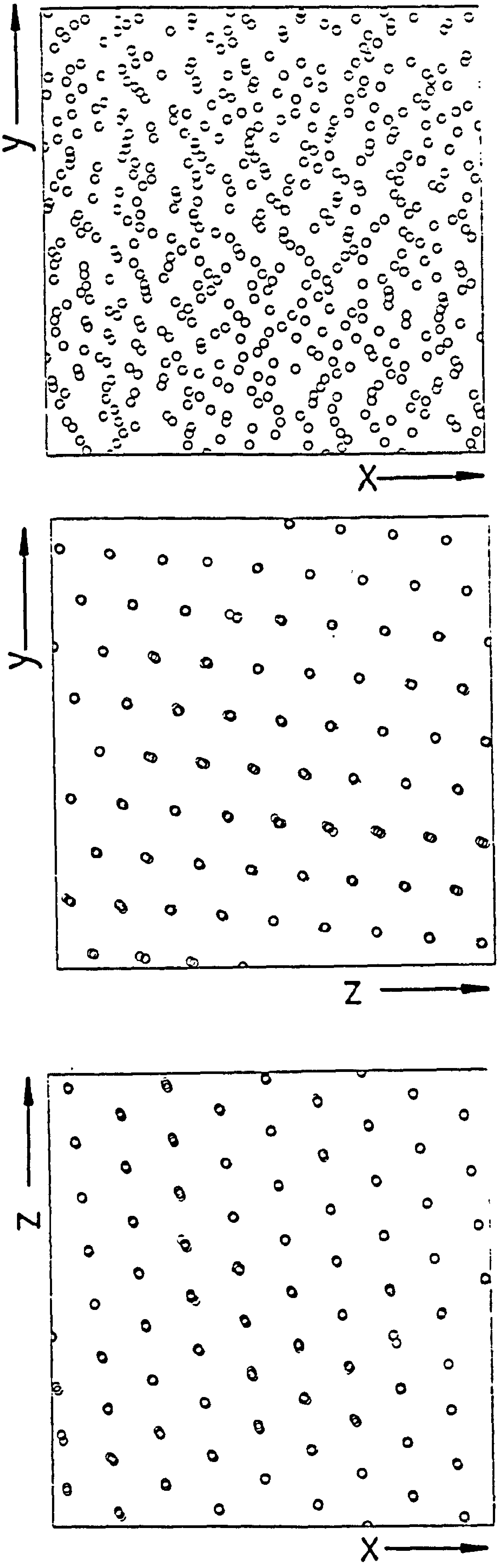

FIGURE 3.5.6: Configurational Plots of the Hard-Sphere Suspension at a Reduced Density $\rho^{\dagger} = 0.90$ and a Stokesian Reduced Shear Rate $\dot{\gamma}^{*} = 0.025$ ($\gamma^{\dagger} = 50.0$)

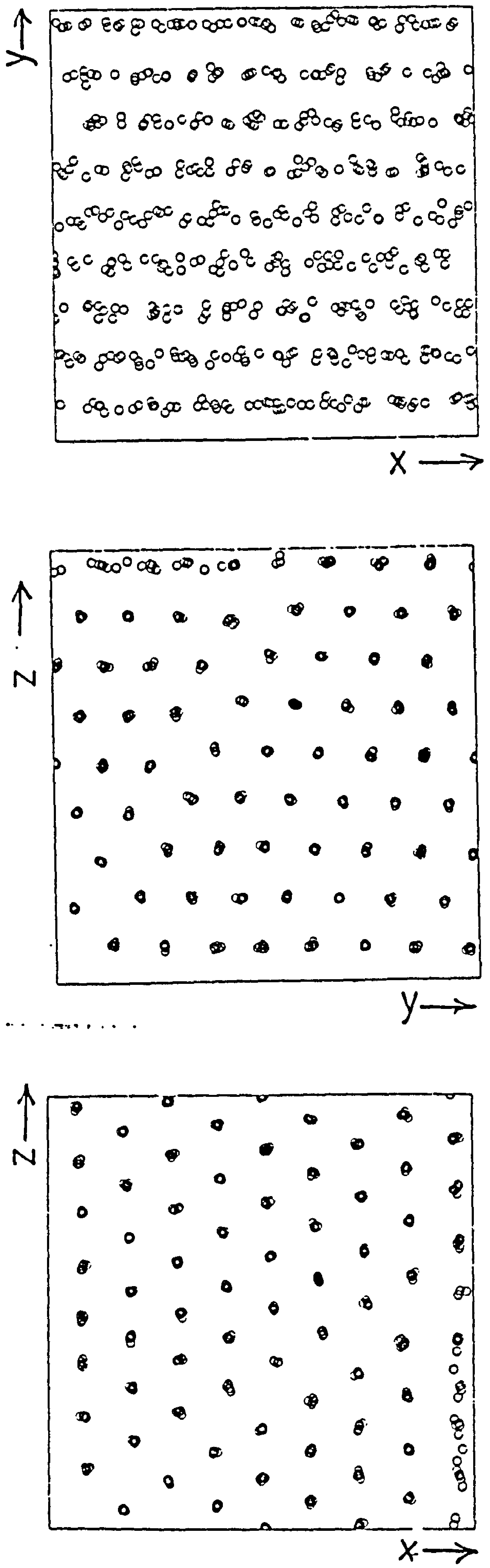

FIGURE 3.5.7: Configurational Plots of the Hard-Sphere Suspension at a Reduced Density $\rho^\dagger = 0.90$ and a Stokesian Reduced Shear Rate $\dot{\gamma}^* = 0.052$ ($\dot{\gamma}^\dagger = 10.0$)

FIGURE 3.5.8: Configurational Plots of the Hard-Sphere Suspension at a Reduced Density $\rho^{\dagger} = 0.90$ and a Stokesian Reduced Shear Rate $\dot{\gamma}^{*} = 0.099$ ($\dot{\gamma}^{\dagger} = 1.0$)

$$E^* = \frac{1}{3} (E^*_{xx} + E^*_{yy} + E^*_{zz}) \qquad (3.5.3)$$

$$D^* = \frac{1}{3} (D^*_{xx} + D^*_{yy} + D^*_{zz}) \qquad (3.5.4)$$

These resolved contributions are plotted as a function of shear rate in Figures 3.5.9 - 3.5.11. In agreement with the behaviour seen so far, these three system properties exhibit normal differences at the lower end of the shear rate range studied, where structural anisotropy prevails. These normal differences disappear at the higher shear rate studied, where the system exhibits an amorphous structure.

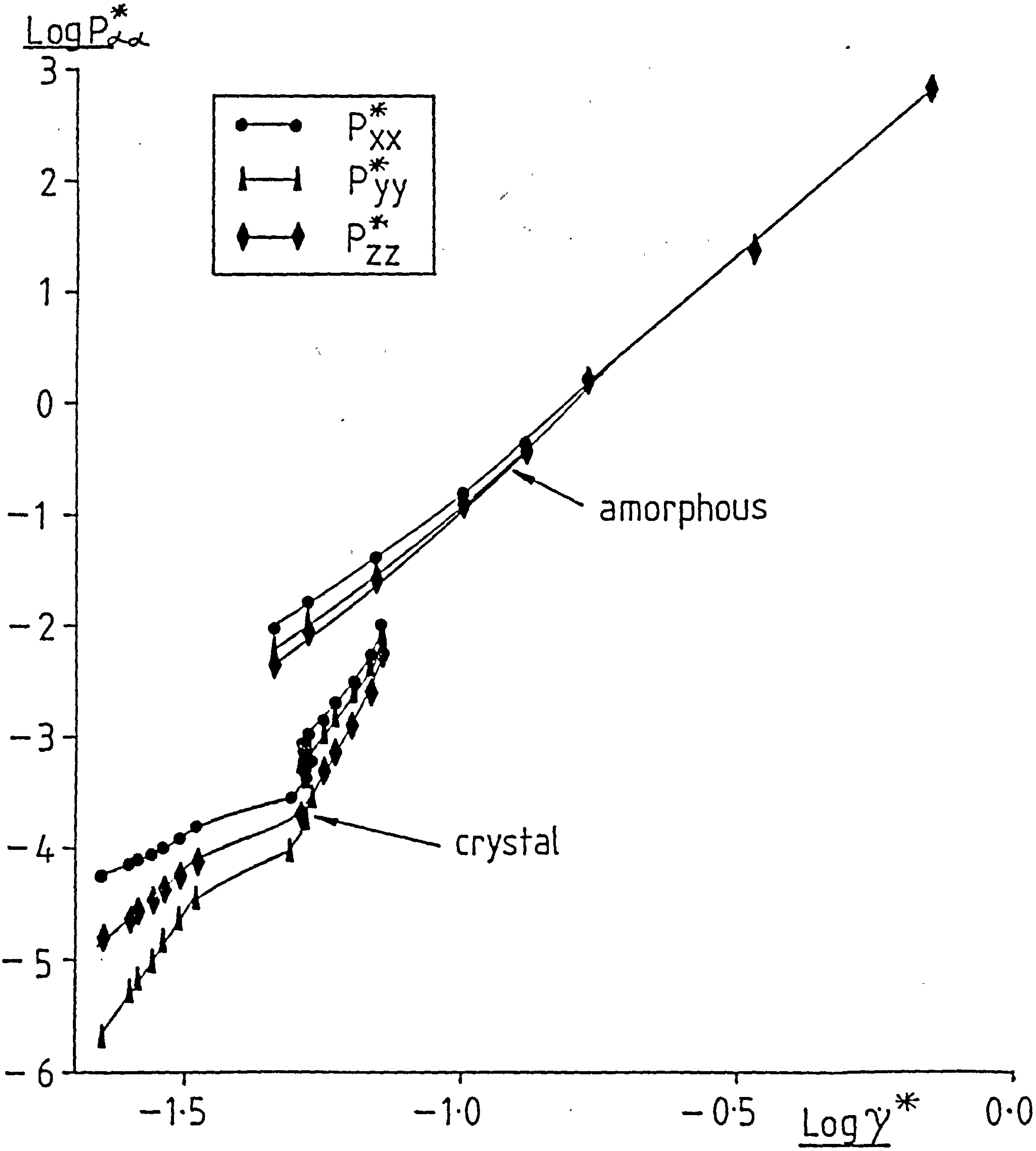

FIGURE 3.5.9: Orthogonal Contributions to the Osmotic Pressure of the Hard-Sphere Suspension; $\rho^{\dagger} = 0.90$

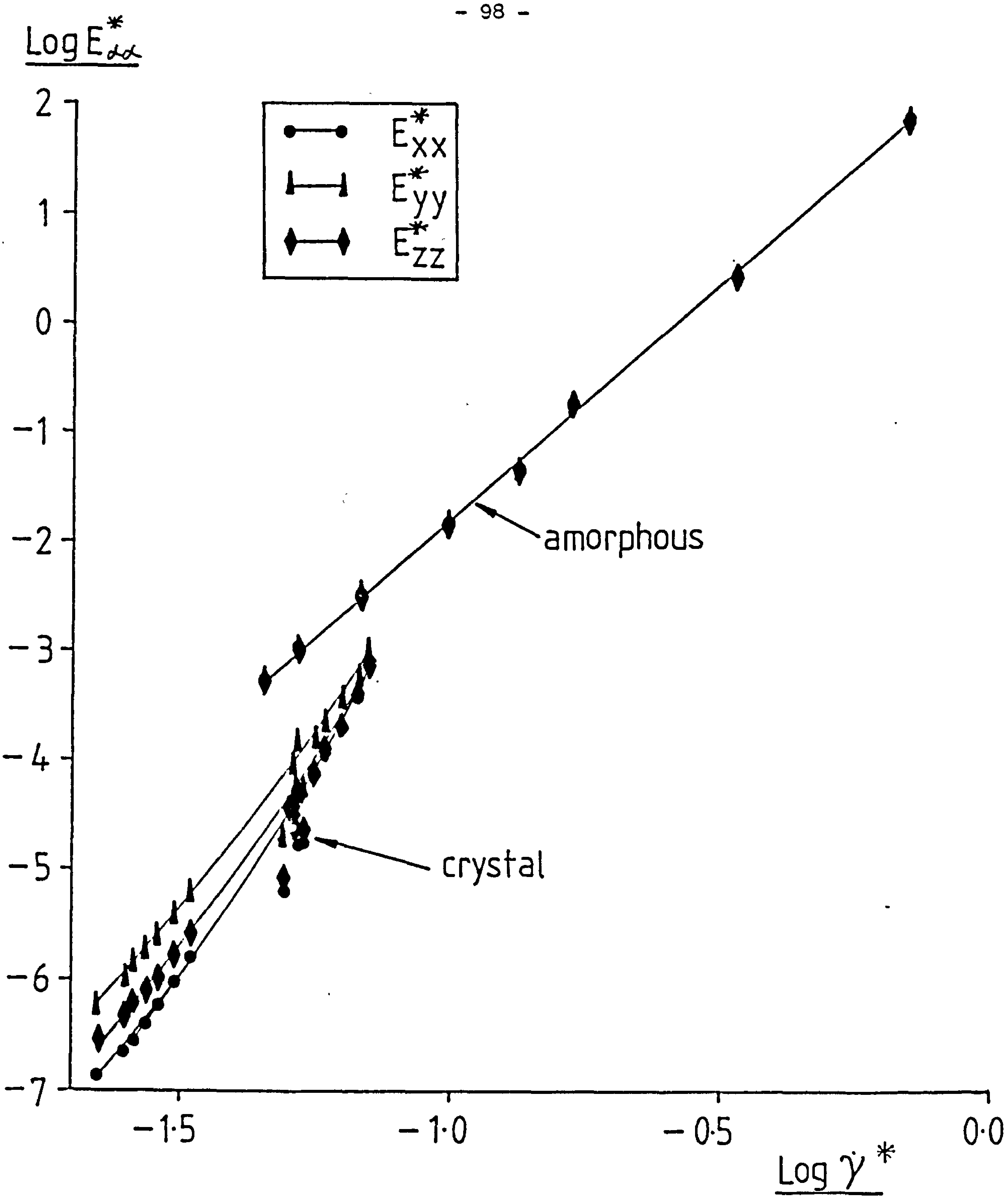

FIGURE 3.5.10: Orthogonal Contributions to the Kinetic Energy of the Hard-Sphere Suspension; $\rho^{\dagger} = 0.90$

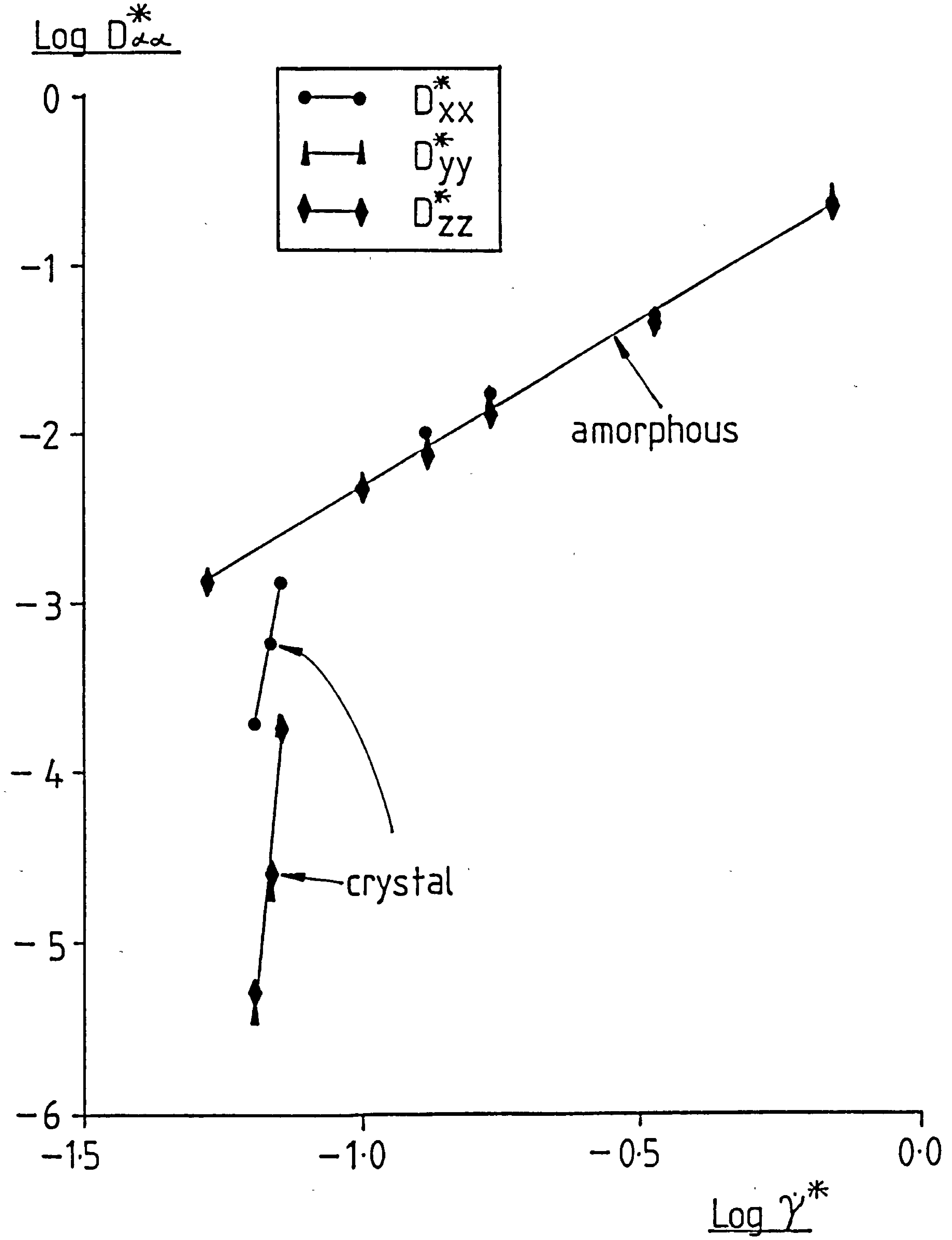

FIGURE 3.5.11: Orthogonal Contributions to the Diffusivity of the Hard-Sphere Suspension; $\rho^{\dagger} = 0.90$

TABLE 3.2.1

Low Shear Rate Behaviour of the Hard-Sphere Model at Constant Kinetic Energy

$\rho^{+} = 0.80$

$\dot{\gamma}$ $\left[\frac{E_o}{m\sigma^2}\right]^{\frac{1}{2}}$	$P_{xy}(K\ )$ $\left[\frac{E_o}{\sigma^3}\right]$	$P_{xy}(\phi)$ $\left[\frac{E_o}{\sigma^3}\right]$	η $\left[\frac{(mE_o)^{\frac{1}{2}}}{\sigma^2}\right]$	c $\left[\frac{E_o}{m\sigma^2}\right]^{\frac{1}{2}}$	$\frac{PV}{NE_o}$
0.00	-	-	-	0.00 (0.00)	7.78 (0.10)
0.10	- 0.02 (0.01)	- 0.20 (0.07)	2.14 (0.74)	0.08 (0.02)	7.81 (0.09)
0.25	- 0.03 (0.01)	- 0.47 (0.08)	2.01 (0.34)	0.45 (0.03)	7.81 (0.07)
0.50	- 0.07 (0.01)	- 1.05 (0.08)	2.23 (0.18)	1.80 (0.12)	8.01 (0.49)
0.75	- 0.10 (0.01)	- 1.46 (0.08)	2.08 (0.12)	3.97 (0.19)	8.18 (0.05)
1.00	- 0.14 (0.01)	- 1.91 (0.09)	2.05 (0.09)	6.88 (0.27)	8.38 (0.09)
1.50	- 0.19 (0.01)	- 2.80 (0.10)	1.99 (0.06)	15.12 (0.32)	9.07 (0.05)
2.00	- 0.24 (0.00)	- 3.63 (0.03)	1.93 (0.02)	26.43 (0.72)	9.96 (0.02)
2.50	- 0.28 (0.01)	- 4.42 (0.16)	1.88 (0.07)	40.20 (1.26)	10.91 (0.16)
3.00	- 0.19 (0.01)	- 5.03 (0.18)	1.78 (0.06)	54.03 (1.78)	11.71 (0.18)
3.50	- 0.34 (0.01)	- 5.17 (0.27)	1.57 (0.08)	63.39 (3.97)	11.89 (0.37)
4.00	- 0.35 (0.01)	- 4.31 (0.12)	1.17 (0.03)	57.32 (1.71)	10.08 (0.17)
4.50	- 0.38 (0.01)	- 4.25 (0.09)	1.03 (0.02)	62.19 (1.04)	9.79 (0.13)
5.00	- 0.40 (0.00)	- 4.22 (0.10)	0.92 (0.02)	68.69 (1.38)	9.77 (0.17)

TABLE 3.2.2

Low Shear Rate Behaviour of the Hard-Sphere Model at Constant Kinetic Energy

$\rho^{\dagger} = 0.90$

$\dfrac{\dot{\gamma}}{\left[\dfrac{E_o}{m\sigma^2}\right]^{\frac{1}{2}}}$	$\dfrac{P_{xy}(K)}{\left[\dfrac{E_o}{\sigma^3}\right]}$	$\dfrac{P_{xy}(\Phi)}{\left[\dfrac{E_o}{\sigma^3}\right]}$	$\dfrac{\eta}{\left[\dfrac{(mE_o)^{\frac{1}{2}}}{\sigma^2}\right]}$	$\dfrac{c}{\left[\dfrac{E_o}{m\sigma^2}\right]^{\frac{1}{2}}}$	$\dfrac{PV}{NE_o}$
0.00	-	-	-	0.00 (0.00)	10.74 (0.04)
0.10	- 0.01 (0.01)	- 0.41 (0.09)	4.21 (0.92)	0.14 (0.03)	10.86 (0.09)
0.25	- 0.03 (0.01)	- 0.89 (0.06)	3.68 (0.03)	0.73 (0.05)	10.95 (0.08)
0.50	- 0.06 (0.01)	- 1.77 (0.08)	3.66 (0.16)	2.86 (0.12)	11.31 (0.09)
0.75	- 0.09 (0.01)	- 2.56 (0.10)	3.53 (0.14)	5.87 (0.18)	11.87 (0.12)
1.00	- 0.12 (0.01)	- 3.36 (0.12)	3.46 (0.13)	10.06 (0.37)	12.41 (0.15)
1.50	- 0.17 (0.01)	- 4.91 (0.15)	3.39 (0.10)	21.80 (0.66)	13.66 (0.29)
2.00	- 0.22 (0.01)	- 6.31 (0.20)	3.27 (0.10)	38.03 (1.29)	15.36 (0.32)
2.50	- 0.25 (0.00)	- 7.39 (0.27)	3.06 (0.11)	54.74 (2.00)	16.57 (0.37)
3.00	- 0.29 (0.01)	- 4.82 (0.17)	1.70 (0.06)	42.12 (1.23)	12.21 (0.32)
4.00	- 0.37 (0.01)	- 5.10 (0.12)	1.37 (0.03)	58.66 (1.90)	12.26 (0.19)
5.00	- 0.45 (0.01)	- 5.28 (0.07)	1.15 (0.01)	78.47 (0.66)	12.51 (0.17)

TABLE 3.2.3

Low Shear Rate Behaviour of the Hard-Sphere Model at Constant Kinetic Energy

$\rho^{\dagger} = 1.00$

$\dot{\gamma} \Big/ \left[\frac{E_o}{m\sigma^2}\right]^{\frac{1}{2}}$	$P_{xy}(K) \Big/ \left[\frac{E_o}{\sigma^3}\right]$	$P_{xy}(0) \Big/ \left[\frac{E_o}{\sigma^3}\right]$	$\eta \Big/ \left[\frac{(mE_o)^{\frac{1}{2}}}{\sigma^2}\right]$	$c \Big/ \left[\frac{E_o}{m\sigma^2}\right]^{\frac{1}{2}}$	$\frac{PV}{NE_o}$
0.00	-	-	-	0.00 (0.00)	15.32 (0.18)
0.100	- 0.01 (0.01)	- 1.07 (0.24)	10.78 (1.91)	0.45 (0.07)	16.21 (0.14)
0.25	- 0.03 (0.01)	- 2.32 (0.15)	9.39 (0.60)	1.49 (0.11)	16.93 (0.31)
0.50	- 0.05 (0.01)	- 3.77 (0.27)	7.63 (0.55)	4.87 (0.32)	18.21 (0.18)
0.75	- 0.08 (0.00)	- 5.02 (0.07)	6.80 (0.09)	9.87 (0.62)	19.31 (0.11)
1.00	- 0.11 (0.01)	- 6.65 (0.33)	6.76 (0.34)	17.39 (0.59)	21.03 (0.37)
1.50	- 0.15 (0.01)	- 9.80 (0.52)	6.64 (0.35)	38.03 (2.49)	24.72 (0.88)
2.50	- 0.21 (0.03)	- 15.98 (0.80)	6.48 (0.31)	101.61 (4.85)	33.68 (1.18)
4.00	- 0.32 (0.02)	- 24.39 (2.44)	6.18 (0.61)	271.88 (35.01)	52.77 (6.41)

TABLE 3.2.4

Low Shear Rate Behaviour of the Hard-Sphere Model at Constant Kinetic Energy

$\rho^{\dagger} = 1.10$

$\dfrac{\dot{\gamma}}{\left[\dfrac{E_o}{m\sigma^2}\right]^{\frac{1}{2}}}$	$\dfrac{P_{xy}(K\ \ )}{\left[\dfrac{E_o}{\sigma^3}\right]}$	$\dfrac{P_{xy}(\Phi)}{\left[\dfrac{E_o}{\sigma^3}\right]}$	$\dfrac{\eta}{\left[\dfrac{(mE_o)^{\frac{1}{2}}}{\sigma^2}\right]}$	$\dfrac{c}{\left[\dfrac{E_o}{m\sigma^2}\right]^{\frac{1}{2}}}$	$\dfrac{PV}{NE_o}$
0.00	-	-	-	0.00 (0.00)	25.27 (0.41)
0.10	- 0.01 (0.01)	- 3.54 (0.55)	35.47 (5.11)	0.83 (0.12)	28.35 (0.67)
0.20	- 0.01 (0.00)	- 5.11 (0.38)	25.61 (1.88)	2.34 (0.20)	31.98 (0.66)
0.30	- 0.01 (0.00)	- 7.10 (0.47)	23.71 (1.56)	4.70 (0.13)	36.10 (0.65)
0.40	- 0.02 (0.01)	- 7.79 (1.06)	19.53 (2.65)	7.37 (0.67)	36.74 (0.64)
0.50	- 0.03 (0.02)	- 10.04 (0.73)	20.12 (1.46)	11.06 (0.81)	38.67 (1.62)
0.75	- 0.05 (0.02)	- 12.57 (0.92)	16.83 (1.23)	21.81 (1.49)	44.41 (1.35)
1.00	- 0.06 (0.02)	- 17.02 (0.93)	17.08 (0.93)	39.30 (2.82)	52.44 (2.45)
1.50	- 0.10 (0.01)	- 27.90 (1.10)	18.67 (0.74)	95.75 (3.14)	75.59 (1.63)

TABLE 3.2.5

Diffusivity of the Sheared Isokinetic Hard-Sphere Model, $\rho^{\dagger} = 0.90$

$\dot{\gamma}^{\dagger}$	$D^{\dagger}$
0.0	0.0321
0.1	0.0343
0.25	0.0360
0.50	0.0453
0.75	0.0530
1.00	0.0495
2.00	0.0526
3.00	0.0242
4.00	0.0124
5.00	0.0054

TABLE 3.3.1

Shear Behaviour of the Hard-Sphere System at Constant Kinetic Energy

$\rho^{\dagger} = 0.90$

$\dfrac{\dot{\gamma}}{\left[\dfrac{E_o}{m\sigma^2}\right]^{\frac{1}{2}}}$	$\dfrac{P_{xy}(K\ \ )}{\left[\dfrac{E_o}{\sigma^3}\right]}$	$\dfrac{P_{xy}(\phi)}{\left[\dfrac{E_o}{\sigma^3}\right]}$	$\dfrac{\eta}{\left[\dfrac{(mE_o)^{\frac{1}{2}}}{\sigma^2}\right]}$	$\dfrac{c}{\left[\dfrac{E_o}{m\sigma^2}\right]^{\frac{1}{2}}}$	$\dfrac{PV}{NE_o}$
6.00	- 0.51 (0.0)	- 5.54 (0.04)	1.01 (0.01)	101.18 (1.04)	12.91 (0.08)
7.00	- 0.57 (0.0)	- 5.76 (0.17)	0.90 (0.02)	124.87 (0.98)	13.45 (0.13)
8.00	- 0.61 (0.01)	- 5.93 (0.08)	(0.82) (0.01)	151.22 (0.99)	14.07 (0.14)
9.00	- 0.63 (0.01)	- 6.15 (0.08)	0.75 (0.01)	175.83 (1.84)	14.83 (0.09)
10.00	- 0.63 (0.02)	- 6.36 (0.08)	0.70 (0.01)	193.49 (5.91)	15.46 (0.11)
12.50	- 0.61 (0.01)	- 7.19 (0.12)	0.62 (0.01)	231.57 (3.39)	17.01 (0.22)
15.00	- 0.64 (0.01)	- 7.78 (0.18)	0.56 (0.01)	287.81 (4.32)	19.20 (0.33)
20.00	- 0.67 (0.02)	- 9.56 (0.26)	0.51 (0.01)	402.71 (10.23)	23.22 (0.75)
25.00	- 0.72 (0.01)	- 11.56 (0.31)	0.49 (0.01)	751.53 (4.51)	45.05 (0.62)
30.00	- 0.73 (0.02)	- 13.03 (0.89)	0.46 (0.03)	964.79 (11.22)	55.61 (0.89)
35.00	- 0.73 (0.02)	- 14.38 (0.83)	0.43 (0.02)	1221.00 (24.08)	69.13 (2.44)
40.00	- 0.75 (0.03)	- 17.66 (1.32)	0.46 (0.03)	1462.01 (14.04)	83.07 (2.35)
45.00	- 0.74 (0.02)	- 19,28 (0.98)	0.44 (0.02)	1730.02 (33.08)	97.11 (2.84)
50.00	- 0.73 (0.03)	- 20.79 (1.56)	0.43 (0.03)	1985.06 (25.01)	113.01 (3.02)
60.00	- 0.72 (0.04)	- 28.43 (2.40)	0.49 (0.04)	2679.08 (79.03)	157.42 (7.78)

TABLE 3.3.2

Resolved Orthogonal Contributions to Hard-Sphere System Pressure and Kinetic Energy

$\rho^{\dagger} = 0.90$

$\dfrac{\dot{\gamma}}{\left[\dfrac{E_o}{m\sigma^2}\right]^{\frac{1}{2}}}$	$\dfrac{P_{xx}\,V}{N\,E_o}$	$\dfrac{P_{yy}\,V}{N\,E_o}$	$\dfrac{P_{zz}\,V}{N\,E_o}$	$\dfrac{E_{xx}}{E_o}$	$\dfrac{E_{yy}}{E_o}$	$\dfrac{E_{zz}}{E_o}$
0.00	10.73 (0.10)	10.74 (0.09)	10.75 (0.09)	0.504 (0.005)	0.500 (0.002)	0.496 (0.006)
0.10	10.94 (0.13)	10.80 (0.12)	10.85 (0.14)	0.501 (0.004)	0.498 (0.002)	0.501 (0.003)
0.25	11.04 (0.19)	11.02 (0.07)	10.79 (0.11)	0.503 (0.006)	0.499 (0.003)	0.498 (0.005)
0.50	11.71 (0.14)	11.27 (0.18)	10.95 (0.12)	0.517 (0.005)	0.497 (0.004)	0.490 (0.007)
0.75	12.78 (0.08)	11.65 (0.24)	11.58 (0.30)	0.510 (0.003)	0.503 (0.006)	0.490 (0.002)
1.00	13.76 (0.21)	12.07 (0.26)	11.73 (0.40)	0.515 (0.005)	0.505 (0.003)	0.486 (0.003)
1.50	16.77 (0.41)	12.78 (0.32)	11.44 (0.22)	0.528 (0.006)	0.511 (0.008)	0.472 (0.005)
2.00	20.74 (0.49)	13.55 (0.28)	11.99 (0.22)	0.532 (0.004)	0.520 (0.005)	0.466 (0.006)
2.50	23.95 (0.70)	13.95 (0.21)	12.17 (0.30)	0.545 (0.008)	0.531 (0.008)	0.450 (0.007)
3.00	15.47 (0.74)	12.51 (0.11)	8.66 (0.26)	0.487 (0.006)	0.586 (0.005)	0.454 (0.004)
4.00	16.15 (0.49)	13.00 (0.13)	7.62 (0.21)	0.448 (0.008)	0.652 (0.004)	0.441 (0.005)
5.00	16.70 (0.13)	13.76 (0.14)	7.03 (0.10)	0.404 (0.004)	0.719 (0.004)	0.431 (0.003)
6.00	18.04 (0.10)	14.10 (0.15)	6.60 (0.17)	0.378 (0.007)	0.775 (0.005)	0.414 (0.007)
7.00	19.54 (0.25)	14.35 (0.22)	6.46 (0.17)	0.355 (0.003)	0.830 (0.002)	0.401 (0.004)

continued

TABLE 3.3.2 continued ......

$\frac{\dot{\gamma}}{\left[\frac{E_o}{m\sigma^2}\right]^{\frac{1}{2}}}$	$\frac{P_{xx}\ V}{N\ E_o}$	$\frac{P_{yy}\ V}{N\ E_o}$	$\frac{P_{zz}\ V}{N\ E_o}$	$\frac{E_{xx}}{E_o}$	$\frac{E_{yy}}{E_o}$	$\frac{E_{zz}}{E_o}$
8.00	21.44 (0.28)	14.61 (0.19)	6.24 (0.16)	0.337 (0.004)	0.876 (0.003)	0.404 (0.004)
9.00	23.18 (0.12)	14.71 (0.18)	6.55 (0.26)	0.323 (0.003)	0.914 (0.006)	0.381 (0.005)
10.00	24.67 (0.33)	14.20 (0.36)	7.40 (0.62)	0.316 (0.003)	0.931 (0.015)	0.393 (0.012)
12.50	28.36 (0.31)	13.13 (0.27)	9.56 (0.47)	0.314 (0.007)	0.950 (0.012)	0.419 (0.007)
15.00	32.82 (0.49)	13.35 (0.21)	11.42 (0.43)	0.312 (0.007)	1.004 (0.005)	0.423 (0.005)
20.00	42.51 (1.16)	13.61 (0.25)	13.53 (1.32)	0.336 (0.024)	1.078 (0.032)	0.438 (0.009)
25.00	79.71 (0.83)	16.92 (2.18)	37.52 (1.05)	0.307 (0.008)	1.139 (0.014)	0.497 (0.007)
30.00	103.20 (1.51)	18.27 (0.36)	43.35 (1.85)	0.299 (0.008)	1.205 (0.017)	0.523 (0.006)
35.00	133.59 (3.15)	18.43 (0.34)	55.36 (5.07)	0.286 (0.012)	1.260 (0.021)	0.550 (0.012)
40.00	167.79 (3.00)	17.65 (1.65)	63.27 (3.24)	0.290 (0.006)	1.336 (0.014)	0.587 (0.010)
45.00	202.01 (5.66)	17.88 (0.95)	70.56 (3.42)	0.288 (0.006)	1.365 (0.031)	0.613 (0.009)
50.00	241.59 (4.88)	17.42 (1.61)	79.97 (4.94)	0.297 (0.012)	1.374 (0.035)	0.636 (0.018)
60.00	357.38 (1.24)	13.29 (1.89)	101.53 (12.57)	0.331 (0.015)	1.391 (0.056)	0.698 (0.023)

CHAPTER 4

EQUILIBRIUM BEHAVIOUR OF THE COLLOIDAL POTENTIAL SYSTEM

CHAPTER 4

EQUILIBRIUM BEHAVIOUR OF THE COLLOIDAL POTENTIAL SYSTEM

Progress over the last few decades towards the understanding of the liquid state has led to the realisation that the structure and order-disorder behaviour of dense liquids is overwhelmingly dominated by geometric packing effects(107). The parallels that may be drawn between such behaviour and that exhibited by well-characterised colloidal solid/ liquid suspensions suggest that many of the properties of dense suspensions may be attributable to similar effects. The non-Newtonian behaviour accompanied by structural anisotropy observed in previous dynamical simulations of simple model fluids has been explained as a shear perturbation of this equilibrium phase behaviour. An appreciation of the equilibrium behaviour would therefore appear to be essential before a study of the non-equilibrium behaviour is embarked upon.

The present chapter contains the results of a series of simulations aimed at the study of the equilibrium behaviour of the colloidal-sphere model. Initial simulations were restricted to two dimensions due to the less prohibitive computer time requirements as compared to three-dimensional simulations. In addition, two-dimensional configurations can readily be represented graphically. Of greater relevance to the non-equilibrium simulations presented in Chapter 5 are the three-dimensional equilibrium simulations, whose results are presented in the latter section of this chapter.

4.1 The Two-Dimensional Case

4.1.1 Monodisperse system behaviour

Simulations of the two-dimensional colloidal potential model spanning a reduced density range $\rho^{\dagger} = 0.10 - 1.00$ for systems comprising $N = 1600$ particles have been performed. In each instance, particles were initially assigned position co-ordinates corresponding to the lattice points of a hexagonal array (Figure 4.1.1.1). A cut-off distance equivalent to 2.5σ was utilised, along with a time increment $\Delta t^{\dagger} = 0.001$.

The simulations were typically allowed to progress for ten thousand time increments. For each state point studied, calculated system properties attained steady-state values after less than three thousand time increments. System properties and their associated uncertainty are calculated as the mean and standard deviation of several independent sub-averages respectively.

Systems at the upper end of the density range studied exhibited very constant properties throughout the whole simulation period. Properties of lower density systems however, displayed a noticeable change during the initial 'equilibration' period, corresponding to a 'melting' of the two-dimensional structure.

Results of the simulations are summarised in Table 4.1.1.1, where estimates of uncertainty are enclosed in brackets. The equation-of-state curve for the two-dimensional system is plotted in Figure 4.1.1.2, clearly showing two branches corresponding to the amorphous and crystalline sides of the order-disorder phase transition.

The dependence of system properties upon N, the number of particles comprising the simulation system has been checked by the simulation of $N = 900$ and $N = 2500$ particle systems at two state points. The results of these simulations (Tables 4.1.1.2, 4.1.1.3) suggest any N-dependence to be negligible, at least for the system size and density points studied.

4.1.2 Polydisperse system behaviour

The simulation methods described throughout this thesis were initially

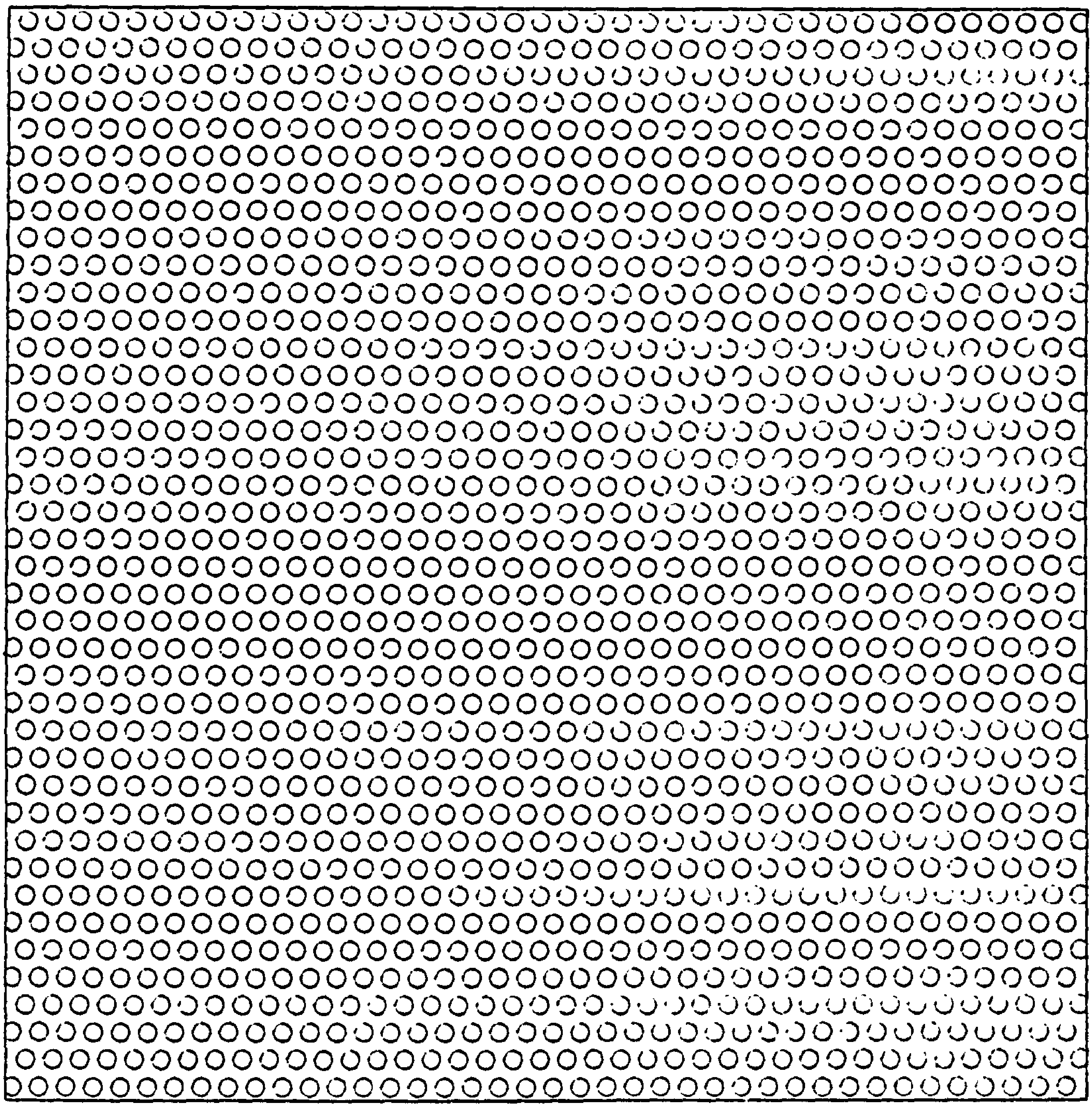

FIGURE 4.1.1.1: Illustration of Two-Dimensional Hexagonal Lattice

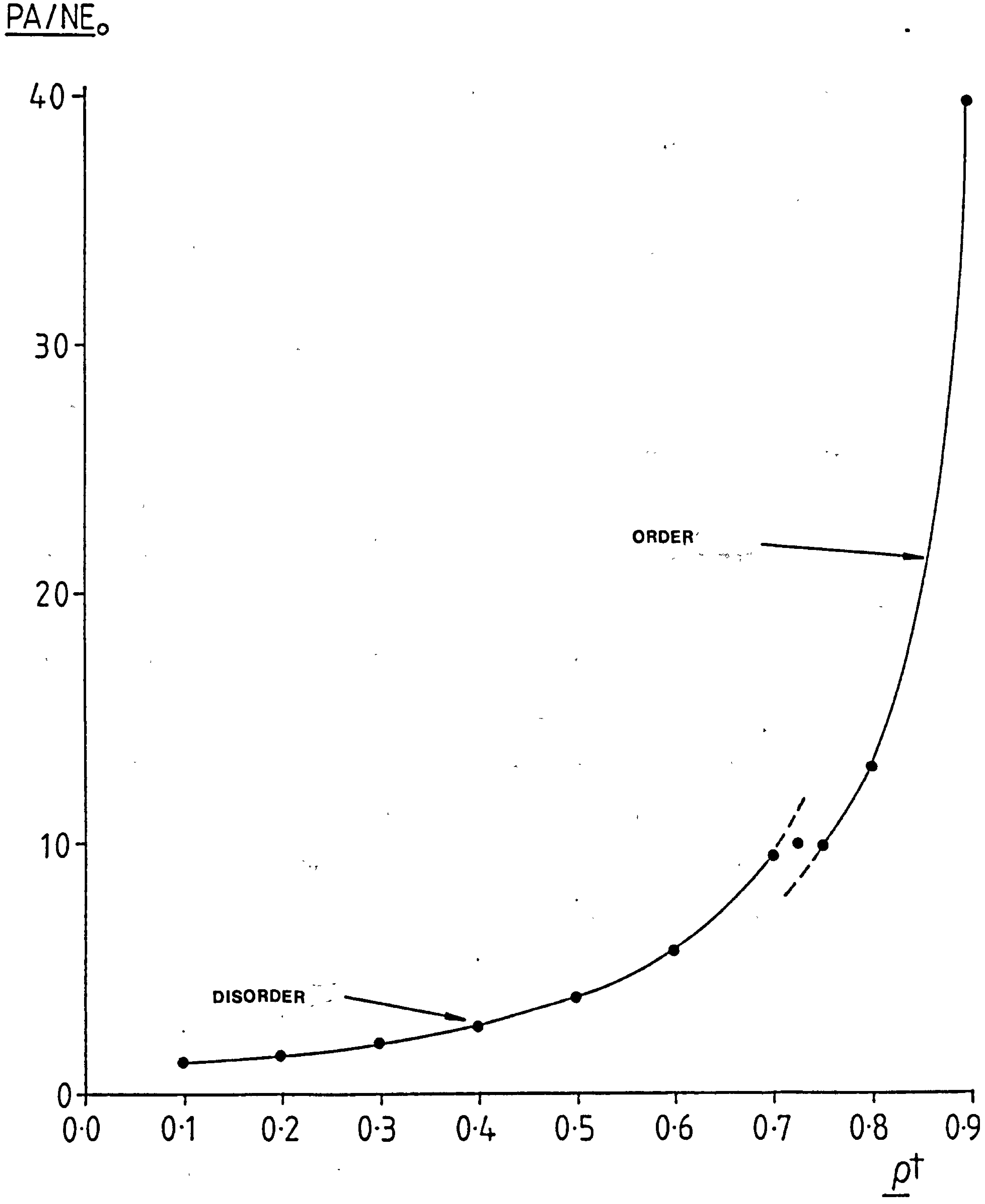

FIGURE 4.1.1.2: Equation of State of the Two-Dimensional Monodisperse Colloidal Potential System

developed in order to study one-component simple liquids. One very important difference, however, between these systems and the colloidal solid/liquid suspensions of interest here, is the inevitable complication of a particle shape and size distribution associated with the latter. Systems of anisotropic particles are amenable to study via particle-dynamics simulations, but the added difficulty due to particle orientation complicates the situation considerably. Incorporation of a particle-size distribution into simulations involving the colloidal potential however, is relatively straightforward.

A series of two-dimensional simulations have been performed in which the monodisperse particle system in the previously described study has been replaced by a distribution of particle sizes. Particle diameters were initially sampled from a normal distribution having a mean equal to a fraction of the diameter of a monodisperse particle at a reduced density $\rho^{\dagger} = 0.30$. The degree of polydispersity is calculated from the distribution-mean and standard deviation, as defined in Equation (2.3.11). Since particle diameters are normally distributed, as opposed to particle volumes/areas, the reduced density-packing fraction relationship as defined in Equation (2.3.13) for monodisperse systems, does not hold for polydisperse systems. Comparisons between monodisperse and polydisperse systems are therefore conducted at equivalent values of hard-core packing fraction, as calculated from Equation (2.3.12). Systems at both 30% and 50% polydispersity have been studied.

Once again particles were assigned position co-ordinates describing a hexagonal array. Precautions were taken to prevent the physically unrealistic starting situation of neighbouring particle overlap. The initial low packing-fraction configurations were allowed to equilibrate for five thousand time increments, after which the system appeared to have attained a steady-state. The arrival of the system at steady-state conditions was judged by the absence of any drift in the values of system pressure and potential energy when observed over several thousand time increments. Lower packing-fraction configurations were created by an instantaneous contraction of particle diameters. Following an equilibration period of approximately three thousand time increments, system properties were typically averaged for a further six thousand time increments. The standard time increment used at higher packing-fractions was $\Delta t^{\dagger} = 0.0005$ whilst a value $\Delta t^{\dagger} = 0.001$ was used for the lower density systems. A cut-off distance of $3\bar{\sigma}$ was used throughout.

The equilibrium properties of the polydisperse colloidal potential systems are presented in Tables 4.1.2.1 and 4.1.2.2. Figure 4.1.2.1 shows the equation of state behaviour of the polydisperse systems alongside the monodisperse case for comparison. Configurational plots at a packing fraction $y = 0.589$ for each system appear in Figures 4.1.2.2 and 4.1.2.3. The osmotic pressure exhibited at low packing fractions is shown to be relatively independent of polydispersity. At higher packing fractions however, we can see that an increasing degree of polydispersity leads to an osmotic pressure decrease for amorphous systems. A similar trend has been predicted by Dickinson(108) for systems with rectangular, triangular and normal distributions from a consideration of the van der Waals one-fluid approximation.

The present results allow little to be concluded concerning the existence of a two-dimensional polydisperse ordered phase or position of any phase transition. There are a vast number of theoretically possible ordered arrangements of a polydisperse system involving segregation of particle size fractions and/or the accommodation of smaller particles in the interstices created by larger particles. Whilst a study of the various possible arrangements would be feasible through computer simulation, a thorough study involving the evaluation of free-energies would in itself constitute a major research undertaking, and

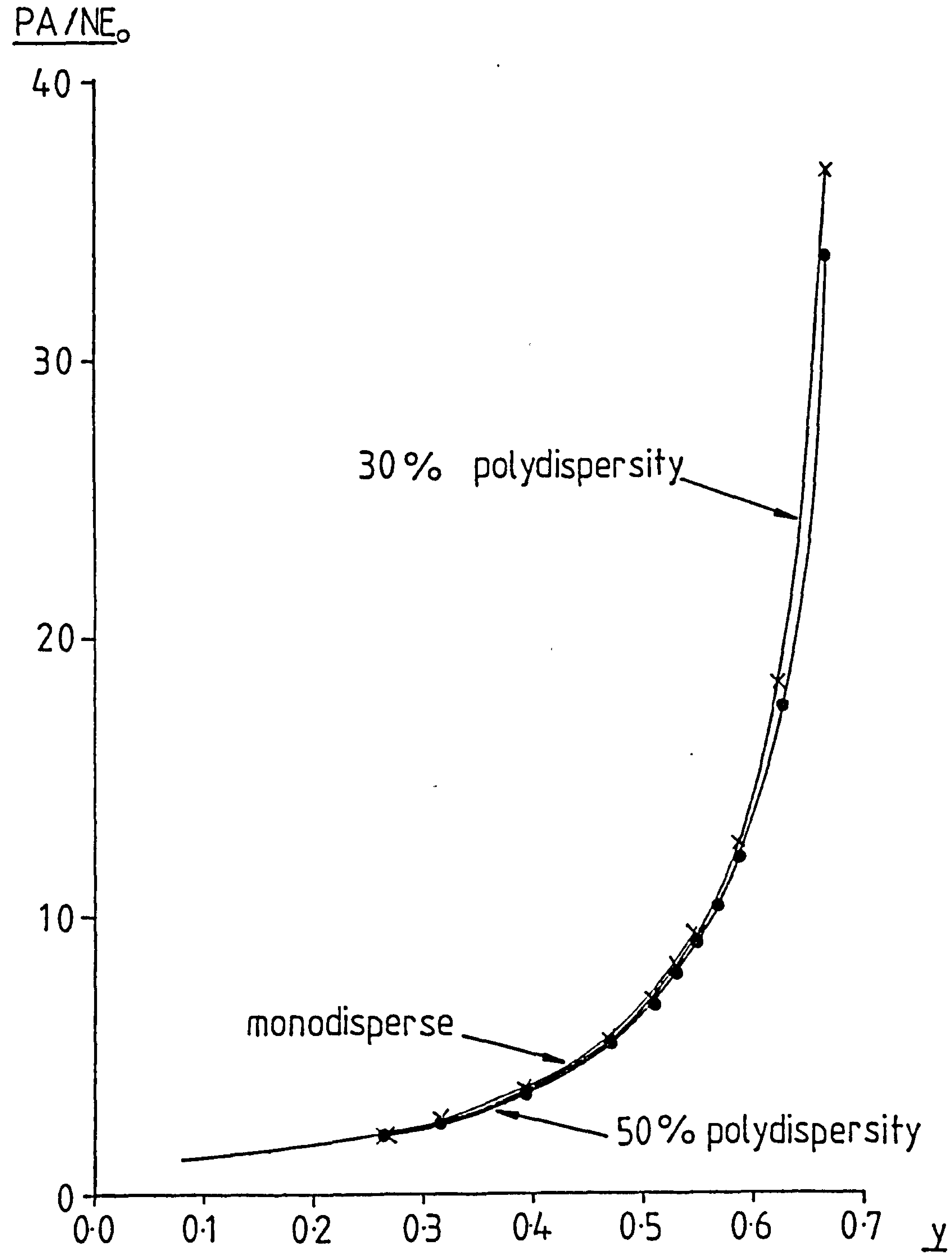

FIGURE 4.1.2.1: Equation of State of the Two-Dimensional Polydisperse Colloidal Potential System. The Monodisperse System Behaviour is also Plotted for Comparison.

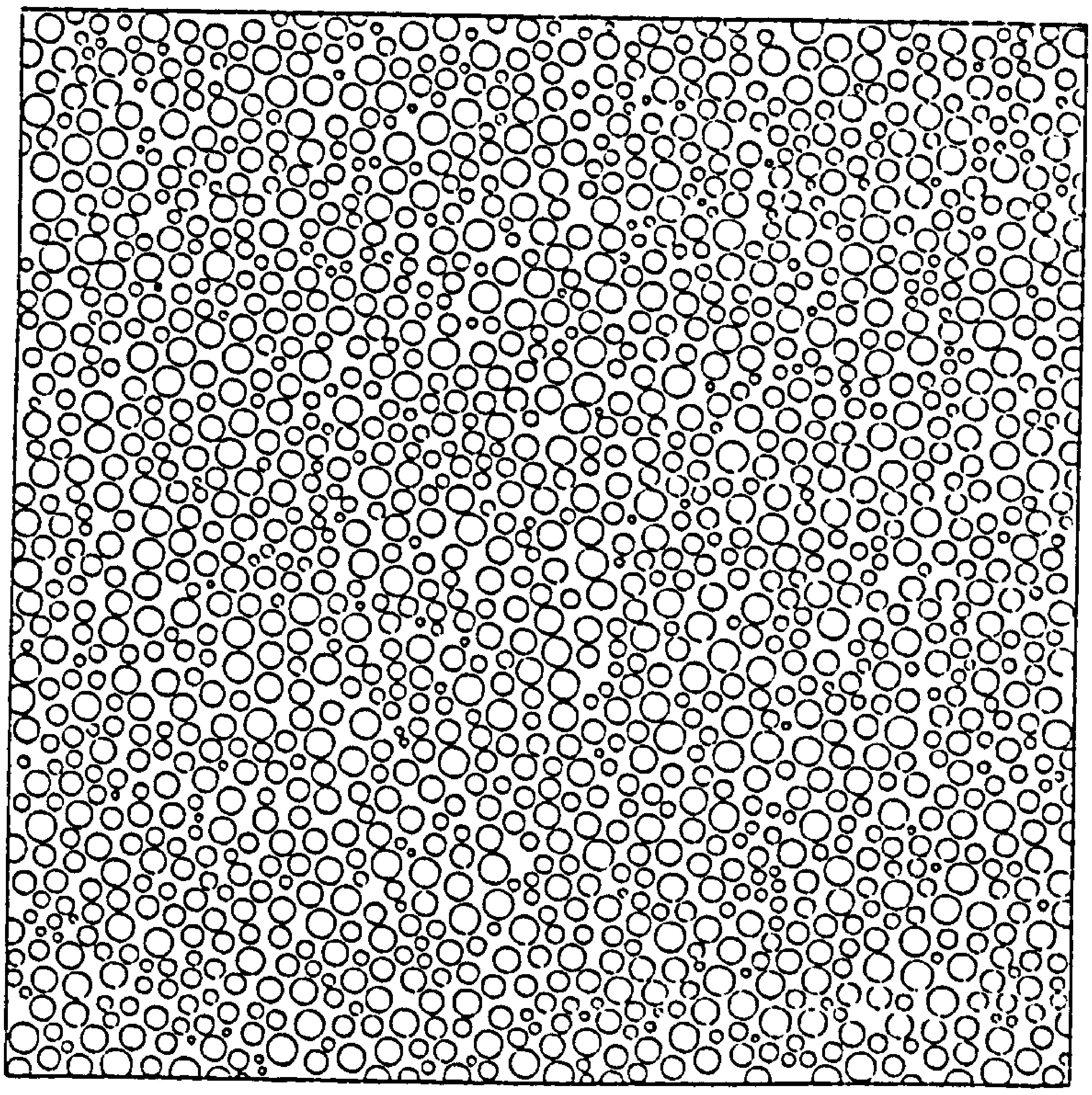

FIGURE 4.1.2.2: Two-Dimensional Colloidal Potential System with a Hard-Core Packing Fraction of 0.589 and 50% Polydispersity

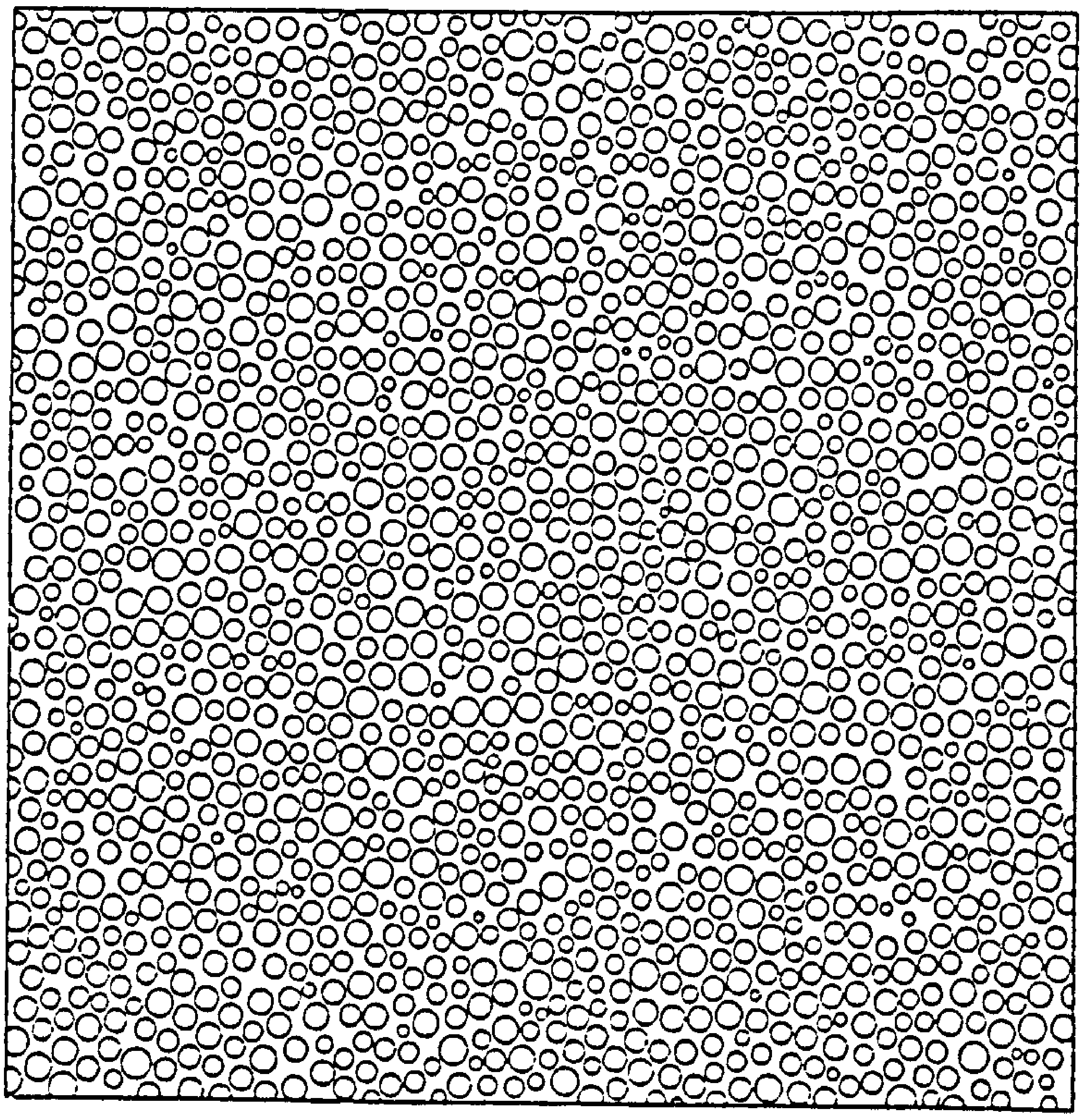

FIGURE 4.1.2.3: Two-Dimensional Colloidal Potential System with a Hard-Core Packing Fraction of 0.589 and 30% Polydispersity

is clearly beyond the scope of this work.

Number dependency checks, summarised in Tables 2.1.2.3 and 2.1.2.4 show system behaviour to be independent of system size for the density and size points studied.

4.2 The Three-Dimensional Case

4.2.1 Monodisperse system behaviour

Three-dimensional systems comprising $N = 500$ monodisperse particles, with both ordered and disordered particulate configurations have been studied over a wide density range. Experimental studies upon well-characterised colloidal suspensions(109) suggest these adopt Face Centre Cubic (FCC) crystalline arrangements at high packing fractions. The present simulation studies of states lying on the ordered branch of the phase diagram have FCC crystalline configurations.

Amorphous configurations were created by allowing a low-density FCC configuration to 'melt' for 6000 time increments. Higher density amorphous configurations were then obtained by a gradual, step-wise incrementation of particle diameters at a densification rate $(d\sigma/dt)^{\dagger} = 0.001$ until the desired system density was achieved. Heating of the system was eliminated by the damping of particle velocities as described previously.

A time increment $\Delta t^{\dagger} = 0.001$ was used for the lower density simulations, whilst a value of $\Delta t^{\dagger} = 0.0005$ was used at the higher end of the density range studied. The decision to shorten the time increment was based upon the operational frequency of the variable time increment procedure described in Section 2.3. A 4 x 4 x 4 matrix of link cells was employed.

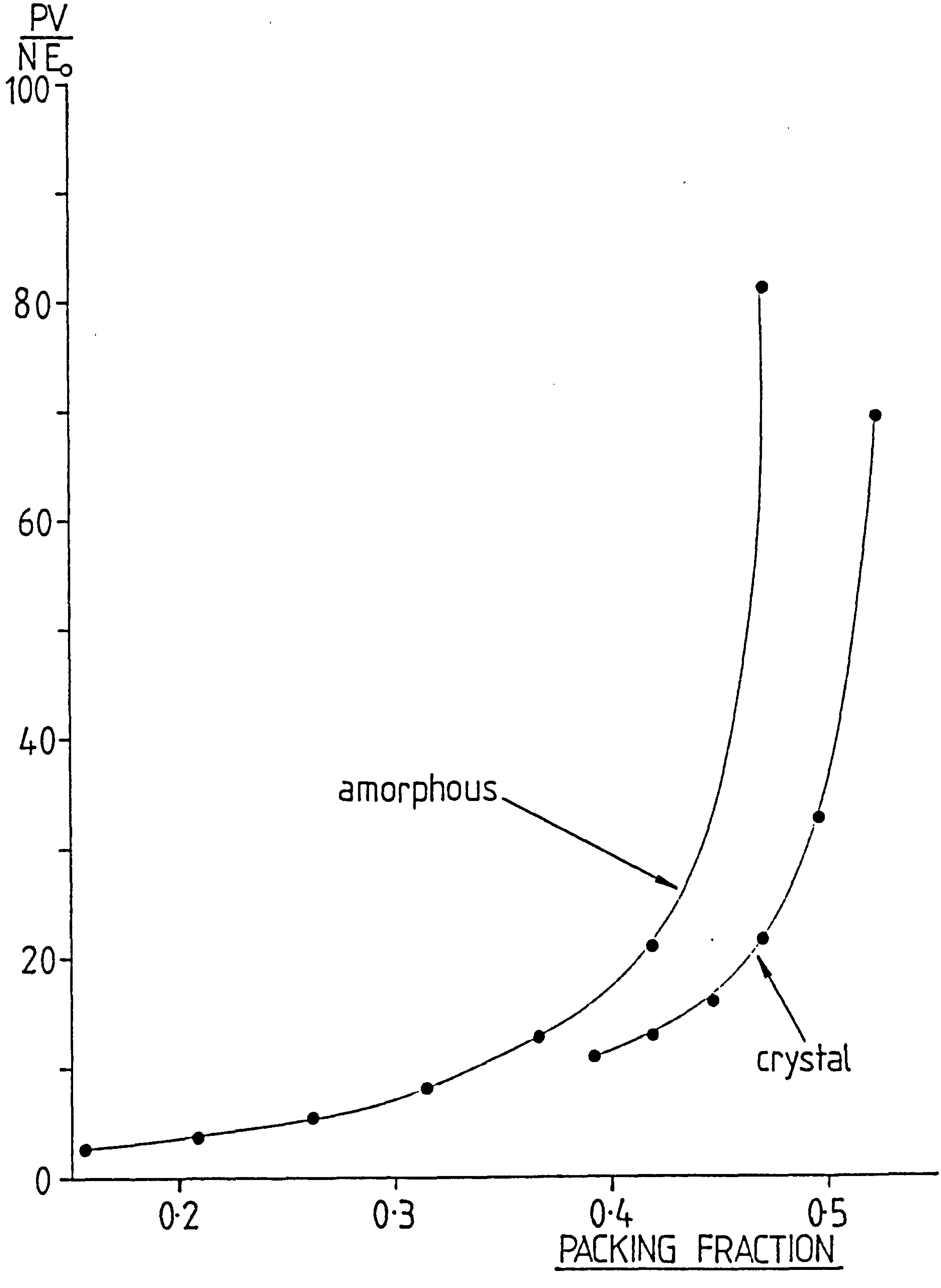

FIGURE 4.2.1.1: Equation of State of the Three-Dimensional Monodisperse Colloidal-Sphere System

The equilibrium behaviour of the monodisperse colloidal-sphere system is summarised in Table 4.2.1.1. Figure 4.2.1.1 shows the equation of state behaviour, clearly illustrating two branches corresponding to amorphous and crystalline states. This plot is qualitatively reminiscent of the general behaviour of hard or soft-sphere systems which have been shown to exhibit a first order freezing transition(107).

Technical difficulties have led to a lack of published osmotic pressure data upon colloidal solid liquid suspensions around the order-disorder transition to date. These technical difficulties are attributable to the non-reproducibility of nearly-monodisperse suspensions; the very low osmotic pressure values requiring measurement; and the long timescales required by the systems for the attainment of steady-state conditions. Pusey and van Megen(5) however, have qualitatively demonstrated the order-disorder phenomena in colloidal suspensions through the use of light-scattering techniques.

Simulations upon systems comprising N = 256 and N = 864 particles at reduced density values $\rho^{\dagger} = 0.70$ and $\rho^{\dagger} = 0.80$, corresponding to amorphous and crystalline configurations respectively show number dependency to be negligible at the system size/density points studied (Table 4.2.1.2).

4.2.2 Modification of Repulsion Steepness

Most of the colloidal potential simulations described in this thesis correspond to an exponent value n = 12 in the definition of the effective pair-potential (Equation 2.3.1). In order to make progress towards the ultimate objective of these types of dynamical simulations, i.e. a quantitative description of material properties, it may well be necessary to parameterise the form of an effective pair-potential to fit available experimental data. An ideal starting point would appear to be the modification of a pair-potential to fit osmotic equation of state behaviour. An appreciation, therefore of the effects of modifying the form of any inter-particle potential is of great importance.

This section contains the results of a series of equilibrium simulations in which the exponent value has been given a value of n = 9 and 6. In each case systems with amorphous particle configurations have been studied. Equilibrated systems at a range of densities were obtained in a similar manner to that described for the simulations involving an exponent value n = 12. A time increment of $\Delta t^{+} = 0.001$ was used at lower densities and $\Delta t^{+} = 0.0005$ for the higher densities studied. A 4 x 4 x 4 matrix of link cells was used in all the simulations.

The effects of the change in n upon the shape of the colloidal potential can be observed from Figure 4.2.2.1, where a family of colloidal potentials are plotted for n = 12, 9 and 6. Clearly an increase in the value of n leads to an increased repulsion when compared at equivalent small particle separations.

The simulation results for two 500 particle systems interacting through colloidal potentials having exponent values n = 9 and 6 are presented in Tables 4.2.2.1 and 4.2.2.2 respectively. Figure 4.2.2.2 shows the amorphous equation of state behaviour for the exponent values studied. In this figure, system density has been defined as the packing fraction of particle hard-cores, and osmotic pressure is seen to decrease with decreasing n. An experimental analogue to these simulations in which the repulsive inter-particle potential is modified, involves the modification of potentials between real suspended particles through the adjustment of electrolyte concentration in the polar suspension medium. An increase in the electrolyte concentration leads to a contraction in the electrical double layer surrounding suspended charged particles due to charge screening. The resultant effect is a shortening of the electrostatic repulsion range.

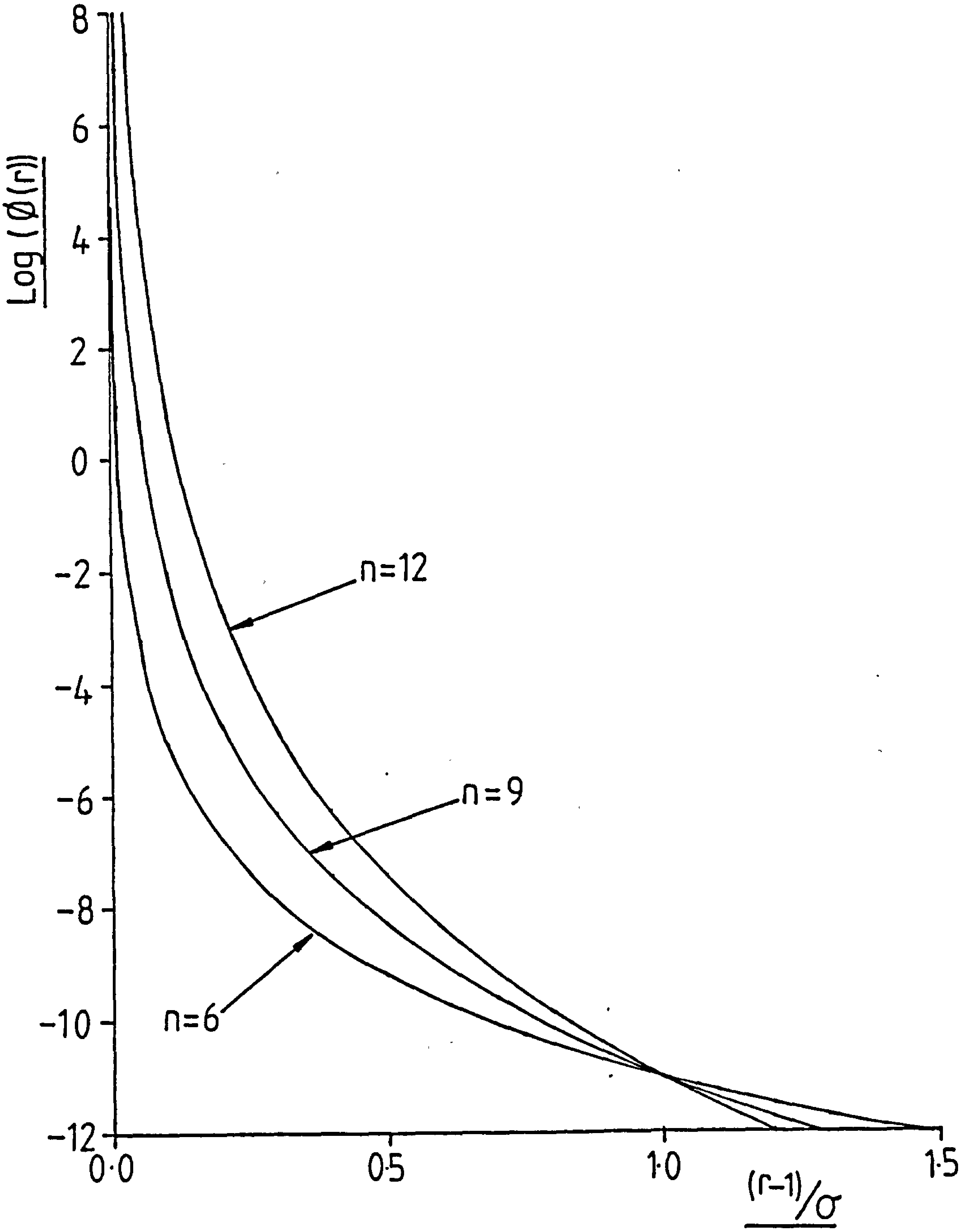

FIGURE 4.2.2.1: Family of Colloidal Potentials Varying Only in the Value of Exponent n

Such an experimental study has been reported by Ottewill and Richardson(110) involving the use of light-scattering to study the interaction of well characterised, nearly monodisperse polystyrene latices. An indirect evaluation of the osmotic pressure is possible from the results of these light-scattering experiments. Figure 4.2.2.4 shows the change in osmotic pressure behaviour as a function of electrolyte concentration reproduced from reference (110). A qualitative similarity can be observed between the results of these experimental studies and the analogous simulations, summarised in Figure 4.2.2.2.

From a comparison of their results with the hard-sphere theory of Percus-Yevick(111), Ottewill and Richardson(110) are able to estimate an 'effective' hard-sphere diameter, described as the distance of closest approach of 2 particles in a dilute suspension. It is possible to estimate a similar effective hard-sphere diameter for the present simulations. An intuitively appealing and simple definition for this parameter is the distance of separation of particle centres at which the inter-particle potential equals E_o, the unit of kinetic energy. By equating this simulation unit of kinetic energy to the usual experimental definition, i.e. KT (K is Boltzmann's constant and T is the absolute temperature) a direct comparison of Ottewill and Richardson's data with the present simulation results is possible. Figure 4.2.2.3 shows a plot of osmotic pressure against effective hard-sphere packing fraction for the simulations involving differing values of the exponent n in the effective pair potential definition (Equation 2.3.1). An excellent agreement between these plotted points and the hard-sphere equation of state as calculated from the Carnahan-Starling equation(112) can readily be observed. Ottewill and Richardson's quasi-experimental data points are also plotted on Figure 4.2.2.3 for comparison. Despite a limited overlap in the effective hard-sphere packing fraction range covered by the quasi-experi-

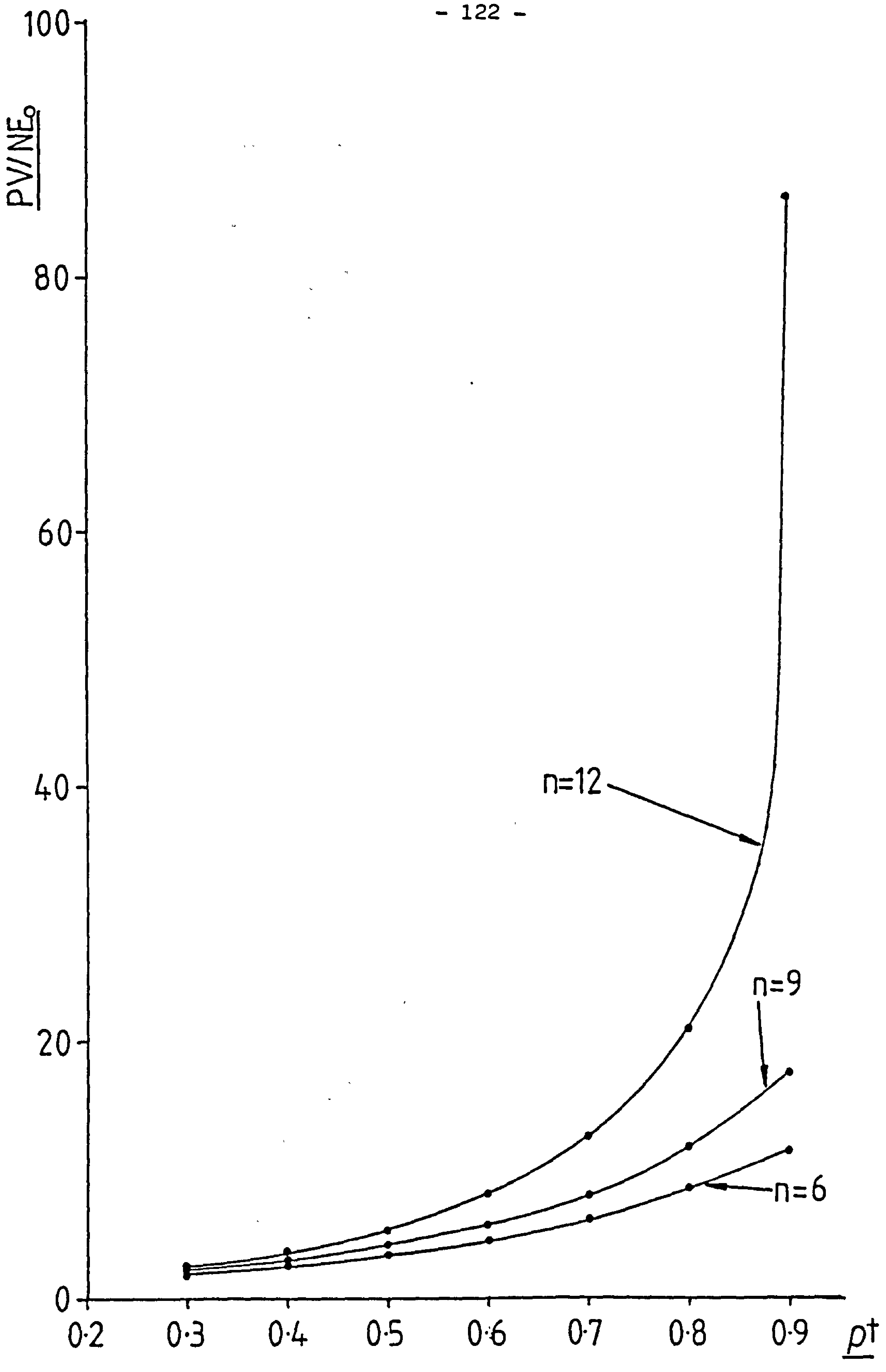

FIGURE 4.2.2.2: Equation of State Behaviour of Systems Interacting Through the Colloidal Potential with Varying Values of Exponent n

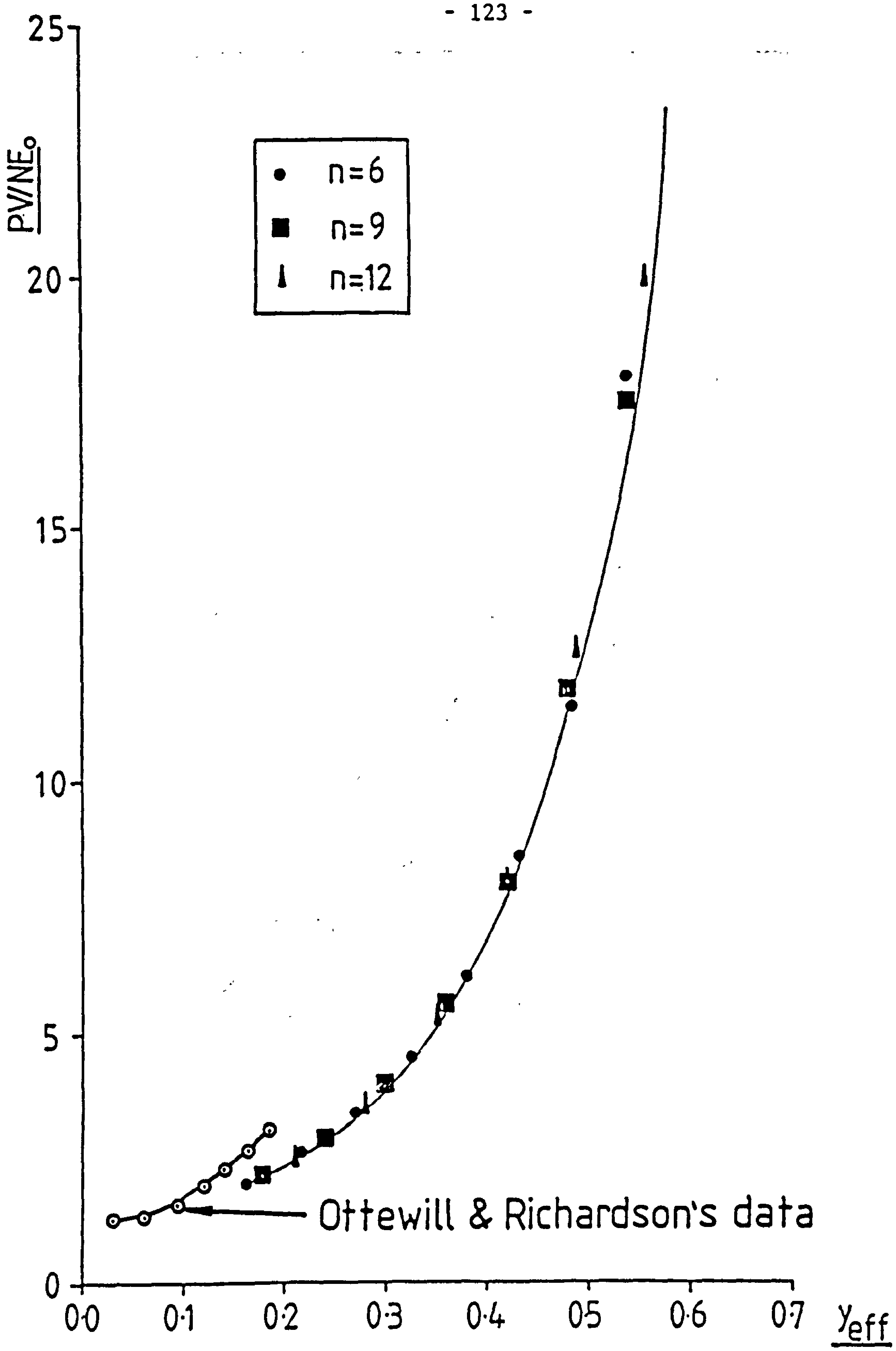

FIGURE 4.2.2.3: Comparison of the Pressure Exhibited by Particulate Systems Interacting Through the Colloidal Potential with Varying Values of Exponent n, with that Predicted by the Carnahan-Starling Equation (112) for the Hard-Sphere Model. Comparisons are Made at Equivalent Effective Hard-Sphere Packing Fractions, y_{eff}.

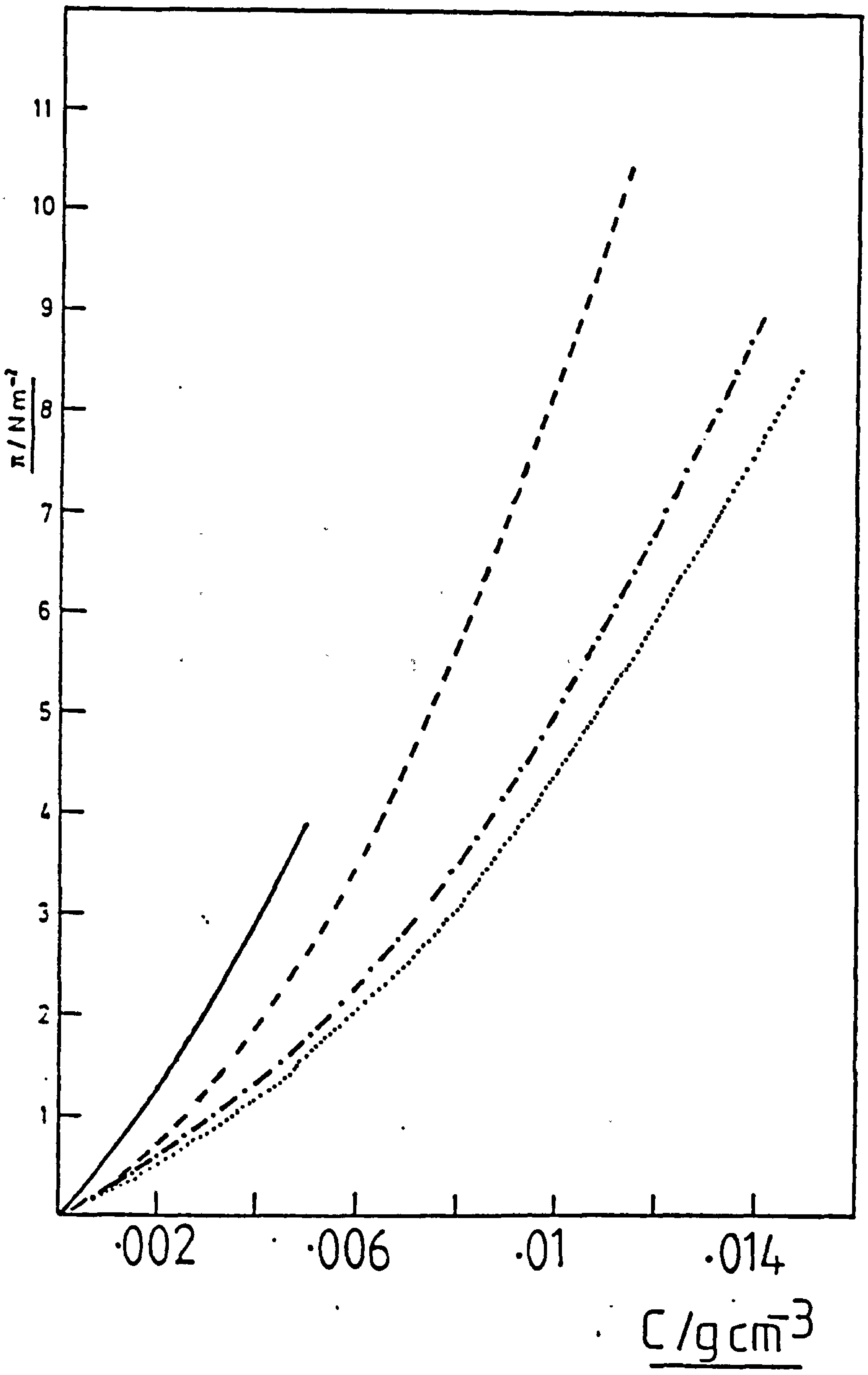

FIGURE 4.2.2.4: Osmotic Pressure, Against Latex Concentration in g cm^{-3}. Results in Various Electrolyte Concentrations -, Ion Exchanged System; -- 10^{-4} mol dm^{-3}; -.-, 10^{-3} mol dm^{-3}; .... 5 x 10^{-3} mol dm^{-3}.
(Reproduced from Reference (110))

mental and simulation results, a correspondence between the two sets of results is observable.

The validity of the hard-sphere model to the description of sterically-stabilised colloidal suspensions has long been recognised(103,104), but the demonstrated applicability to electrostatically stabilised colloidal suspensions at low concentrations is less intuitively obvious.

An important conclusion that may be drawn from the present results is that the osmotic pressure exhibited by dilute, stable colloidal suspensions is relatively insensitive to the complex nature of the real inter-particle potential, but can be adequately described by an effective hard-sphere diameter. The validity of this observation for highly concentrated, electrostatically stabilised colloidal suspensions, where the effective hard-sphere packing fraction becomes physically unrealistic however, is questionable.

4.2.3 Scaling properties of the colloidal sphere model

The superimposition of osmotic pressure data when expressed as a function of effective hard-sphere packing fraction (Figure 4.2.2.3) demonstrates that the colloidal potential retains interesting scaling properties related to those exhibited by the soft sphere model for atomic systems(114). Since system density and temperature of the soft sphere model are inter-dependent and cannot be independently varied, a single reduced hybrid state variable $\tilde{T}$ completely specifies the state of a system, i.e. (in three-dimensions):

$$\tilde{T} = \frac{KT}{\varepsilon}\left(\frac{V}{N\sigma^3}\right)^{n/3} \qquad (4.2.3.1)$$

where the soft-sphere potential, ϕ_{ss}, is defined by:

$$\phi_{ss}(r) = \varepsilon\left(\frac{\sigma}{r}\right)^n \qquad (4.2.3.2)$$

One obvious corollary of this scaling behaviour is that, given a knowledge of the equation of state along a single isotherm, the equation of state along any other isotherm may be predicted. A similar scaling feature of the colloidal potential allows the equation of state of systems with varying values of exponent n to be predicted, along any isotherm from a knowledge of the equation of state along a single isotherm, at a single value of n.

A generalisation of the colloidal potential may be written:

$$\phi(r) = 10^{m} E_{o} \left(\frac{\sigma}{r - \sigma} \right)^{n} \qquad (4.2.3.3)$$

An effective hard-sphere diameter σ_{eff}, defined as the separation of particle centres at which:

$$\phi(r) = E_{o} \qquad (4.2.3.4)$$

can be readily calculated for any member of the colloidal potential from:

$$\sigma^{\dagger}_{eff} = 1 + 10^{m/n} \qquad (4.2.3.5)$$

The effective hard-sphere packing fraction y_{eff} of a monodisperse system can then be calculated from:

$$y_{eff} = \frac{\pi N \sigma^{3}_{eff}}{6V} \qquad (4.2.3.6)$$

Figure 4.2.3.1 shows the superposition of the osmotic pressure exhibited by systems of colloidal spheres when compared at equivalent effective hard-sphere packing fractions. Furthermore, it has been shown in the previous section that the osmotic pressure behaviour expressed in this manner is accurately described by the hard-sphere fluid equation of state, e.g. as calculated from the Carnahan-Starling (112) equation, i.e.:

$$\frac{PV}{NE} = \frac{1 + y_{eff} + y_{eff}^2 - y_{eff}^3}{(1 - y_{eff})^3} \qquad (4.2.3.7)$$

This observation is based on the results of simulations involving a limited range of exponent values n = 6, 9 and 12. At the constant value of m = 12 used in all the simulations, the colloidal-potential represents the short-ranged potential between sterically stabilised colloidal particles. Analogous experimental studies(110) have shown that the concept of an effective hard-sphere diameter is also a useful concept in the description of the equation of state behaviour of stable electrocratic colloidal suspensions. Van Megen and Snook(103,104) have previously pointed out that the hard-sphere potential contains the essential physics of equilibrium colloidal systems.

From the available evidence described above, it would appear reasonable to assume that the hard-sphere fluid equation of state when calculated from the effective hard-sphere packing fraction, provides an accurate description of the fluid equation of state branch for the entire family of colloidal potentials. Providing this assumption holds, the prediction of the equation of state behaviour for amorphous systems of colloidal spheres with varying repulsive potential steepness is relatively straightforward. Figure 4.2.3.1 shows the predicted amorphous equation of state curves for colloidal spheres with a range of exponent n values. These comparisons are made at a constant value of m = 12. A similar illustration of the effects of a variable value of m is given

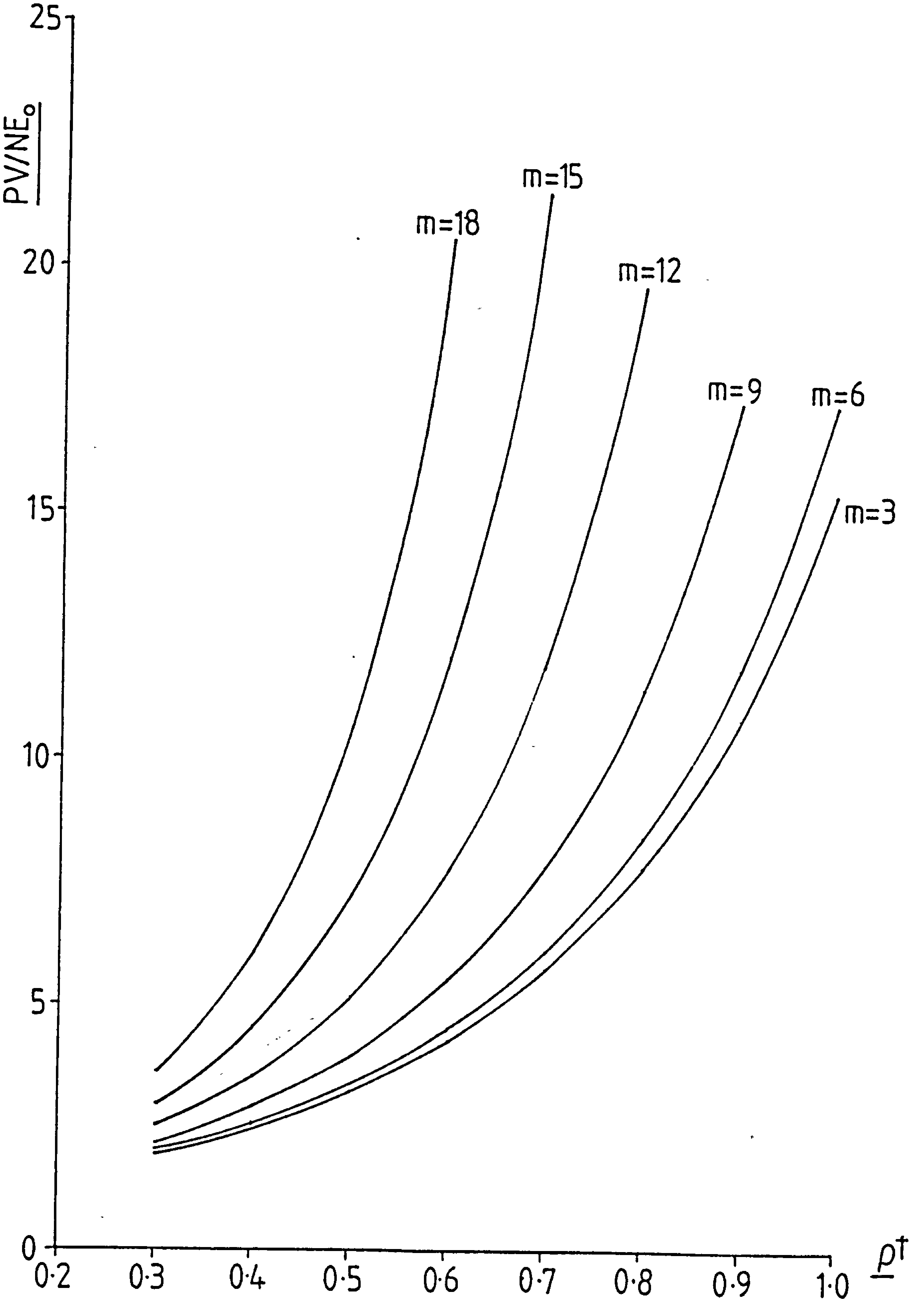

FIGURE 4.2.3.1: Predicted Equation of State Behaviour of Colloidal-Sphere Systems with Varying Values of n

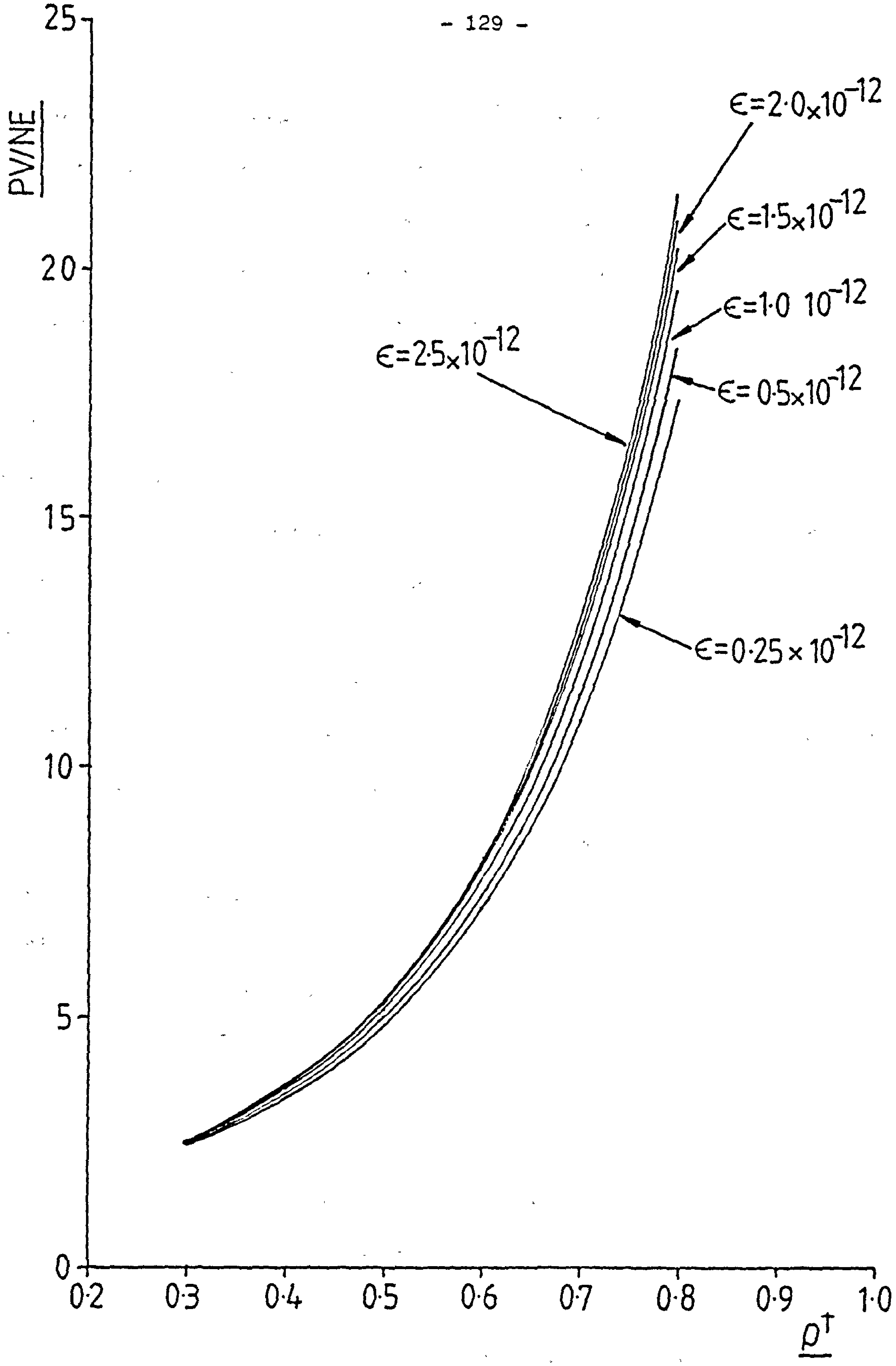

FIGURE 4.2.3.2: Predicted Equation of State Behaviour of the Colloidal-Sphere System with n = 12, Along Several Isotherms

in Figure 4.2.3.2, where the quantity 10^m is referred to as ε. The apparent insensitivity of the osmotic pressure with respect to ε as suggested by Figure 4.2.3.2 is somewhat disguised by the manner in which the predicted data is presented, i.e. in terms of PV/NE. The trends exhibited by the osmotic pressure with variations in the colloidal potential are directly attributable to the resultant changes in effective hard-sphere packing fraction, which in turn may be readily appreciated from Equations (4.2.3.5) and (4.2.3.6).

In agreement with the previous conclusions concerning the behaviour of simple liquids(107), it would appear that the equation of state behaviour exhibited by stable amorphous colloidal suspensions is relatively insensitive to the complex nature of real inter-particle potentials. An effective hard-sphere packing fraction provides a satisfactory description.

The rheological behaviour of colloidal suspensions is now widely believed to originate from this equilibrium phase behaviour(65). Consequently, it would appear reasonable to assume that the shear behaviour of simple model systems such as the hard and colloidal-spheres studied here, might eventually serve as a basis upon which to build a quantitative description of colloidal suspension rheology.

4.2.4 Polydisperse system behaviour

This section is concerned with the equilibrium behaviour of the three-dimensional polydisperse colloidal-sphere model. Organisation of the simulations was essentially as described in Section 4.1.2 for the two-dimensional case. Particle diameters were pseudo-randomly sampled from a normal distribution whose standard deviation was set equal to $0.5 \times \bar{\sigma}$, the distribution mean and characteristic length of the system.

Table 4.2.4.1 summarises the packing-fraction-dependent behaviour of a system comprising N = 500 particles. Time increments used in the simulations ranged from $\Delta t^{+} = 0.001$ to $\Delta t^{+} = 0.0005$ at the highest packing fractions considered.

A lowering of the osmotic pressure exhibited by systems at equivalent packing fractions is shown in Figure 4.2.4.1, where the amorphous equation of state is plotted for both monodisperse and polydisperse systems. The lowering is more pronounced than for the corresponding two-dimensional simulations described in Section 4.1.2. Such a trend has been theoretically predicted for a polydisperse hard-sphere system from a consideration of the van der Waals one fluid approximation(108). From an extension of the Evans-Napper cell model(115), Dickinson has considered the osmotic pressure behaviour of an ordered polydisperse model colloidal system(116). The predicted osmotic pressure increase with polydispersity is postulated to be increasingly sensitive for systems with decreasing double-layer thickness. A particulate dynamics simulation study of 108 particles interacting through a DLVO potential(49) has shown that the order-disorder phase transition shifts to higher densities with increasing polydispersity, at constant kinetic energy. Furthermore, the volume change associated with melting is shown to decrease as the degree of polydispersity increases. A 'critical' degree of polydispersity corresponding to zero volume change is estimated, at which the order-disorder transition is predicted to disappear(50). The equation of state behaviour obtained by Parker(117) from a dynamical simulation study, showing the effects of polydispersity upon the amorphous and crystalline branches is reproduced from reference (117) in Figure 4.2.4.2.

The strong dependence of the equilibrium phase behaviour at relatively low degrees of polydispersity suggests a similar strong dependence of the non-Newtonian rheology of these systems. The following chapter includes the results of a simulation study of the effects of small

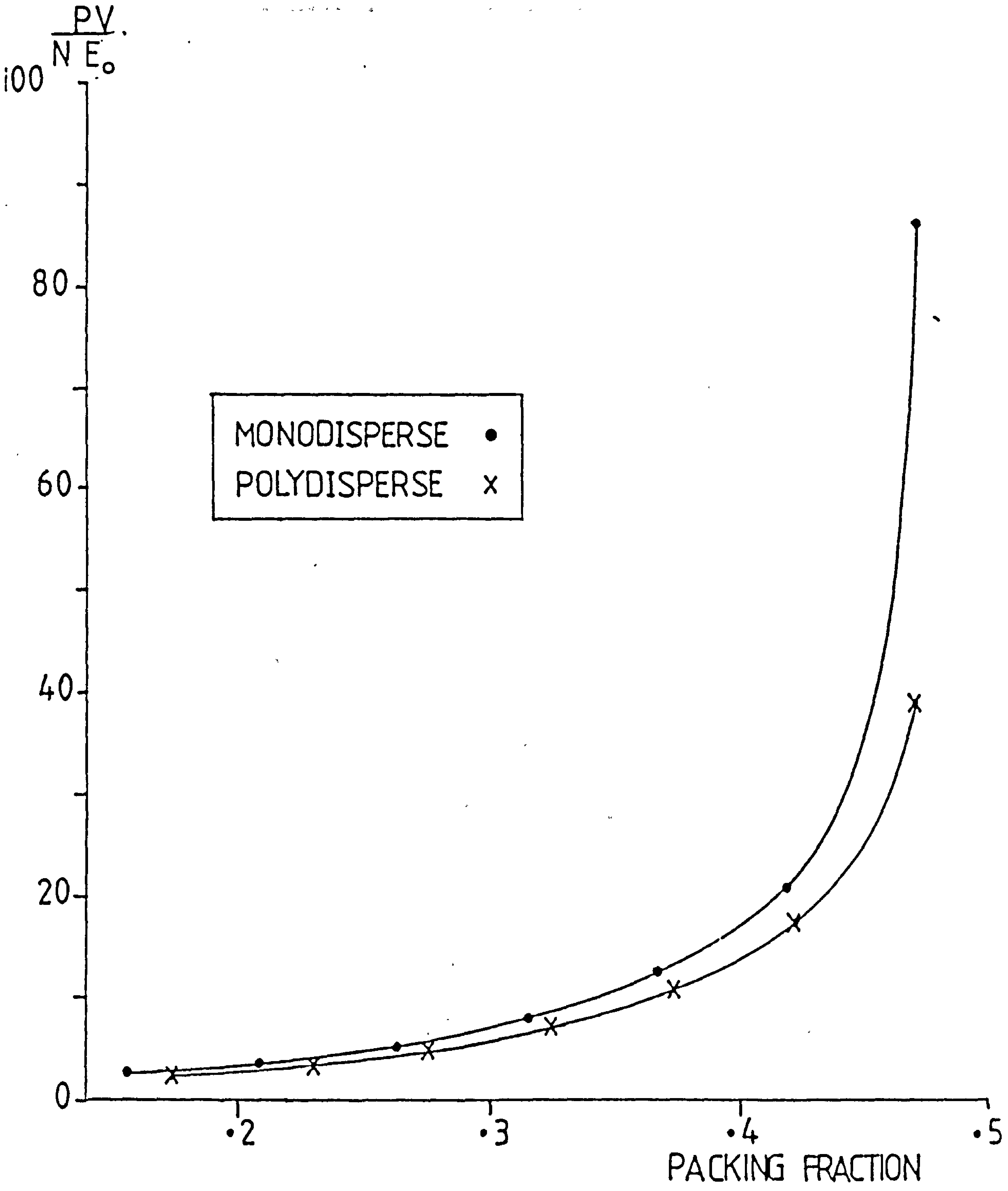

FIGURE 4.2.4.1: Equation of State Behaviour of the Three-Dimensional Polydisperse Colloidal-Sphere System

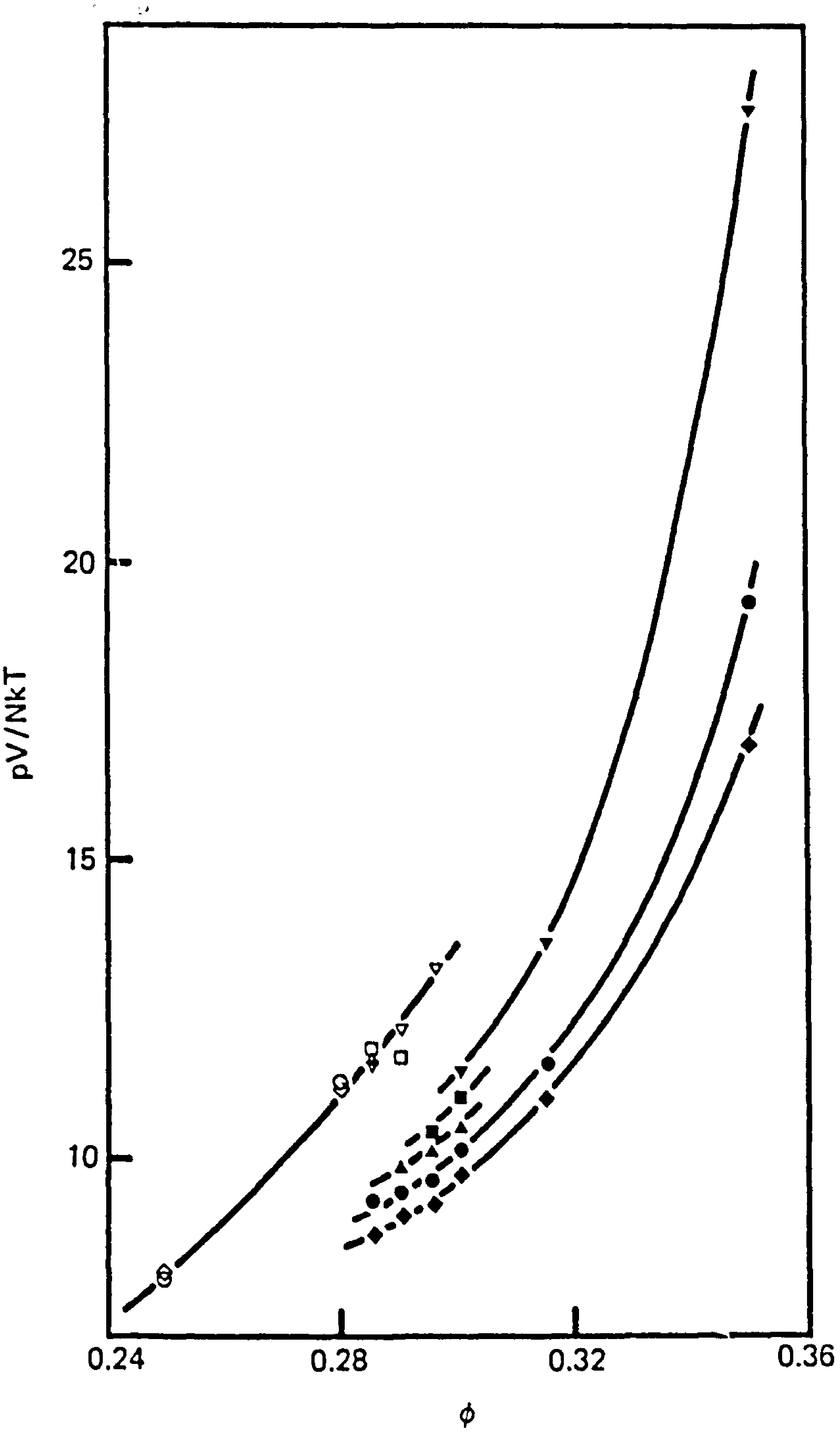

FIGURE 4.2.4.2: Phase Diagram of Polydisperse Colloidal System. The Compressibility Factor PV/NKT is Plotted Against the Particle Volume Fraction 0 for Five Degrees of Polydispersity: ◇, ◆ = 0.000; 0, ● = 0.100; △ , ▲ = 0.141, □, ■ = 0.173, ▽ , ▼ = 0.200. The Open Symbols Refer to the Disordered State Points.

degrees of polydispersity upon dense colloidal suspension rheology.

TABLE 4.1.1.1

Equilibrium Properties of the Two-Dimensional Monodisperse Colloidal Potential System (N = 1600)

$\rho^{\dagger}$	ϕ/E_o	U/E_o	$PV/N.E_o$
0.100	0.004 (0.000)	1.504 (0.000)	1.235 (0.007)
0.200	0.009 (0.000)	1.509 (0.000)	1.548 (0.020)
0.300	0.017 (0.001)	0.517 (0.001)	2.047 (0.040)
0.400	0.027 (0.000)	1.527 (0.000)	2.688 (0.026)
0.500	0.045 (0.001)	1.545 (0.001)	3.841 (0.065)
0.600	0.074 (0.001)	1.574 (0.001)	5.680 (0.067)
0.700	0.133 (0.001)	1.633 (0.001)	9.427 (0.048)
0.725	0.142 (0.001)	1.642 (0.001)	9.985 (0.068)
0.75	0.140 (0.001)	1.640 (0.001)	9.870 (0.074)
0.800	0.190 (0.001)	1.690 (0.001)	13.02 (0.08)
0.900	0.609 (0.001)	2.109 (0.001)	39.84 (0.072)
1.000	102.5 (0.0)	104.0 (0.0)	8874 (0)

Number Dependency Checks Upon the Two-Dimensional Monodisperse Colloidal Potential System

TABLE 4.1.1.2

N = 900

$\rho^{\dagger}$	ϕ/E_o	U/E_o	$PV/N\ E_o$
0.300	0.017 (0.001)	1.517 (0.001)	2.051 (0.0032)
0.600	0.076 (0.002)	1.576 (0.002)	5.688 (0.074)
0.800	0.194 (0.002)	1.694 (0.002)	13.10 (0.10)

TABLE 4.1.1.3

N = 2500

$\rho^{\dagger}$	ϕ/E_o	U/E_o	$PV/N\ E_o$
0.300	0.017 (0.001)	1.517 (0.001)	2.046 (0.038)
0.600	0.075 (0.001)	1.575 (0.001)	5.678 (0.064)
0.800	0.190 (0.001)	1.690 (0.001)	12.98 (0.07)

TABLE 4.1.2.1

Equilibrium Properties of the 30% Polydisperse Two-Dimensional Colloidal Potential System (N = 1600)

y	ϕ/E_o	U/E_o	$PV/N\ E_o$
0.263	0.016 (0.000)	1.516 (0.000)	2.039 (0.021)
0.314	0.025 (0.000)	1.525 (0.000)	2.602 (0.026)
0.393	0.041 (0.000)	1.541 (0.000)	3.668 (0.033)
0.471	0.070 (0.001)	1.570 (0.001)	5.526 (0.046)
0.511	0.093 (0.001)	1.593 (0.001)	6.9 (0.070)
0.530	0.109 (0.001)	1.609 (0.001)	7.980 (0.057)
0.550	0.127 (0.002)	1.627 (0.002)	9.186 (0.092)
0.569	0.149 (0.001)	1.649 (0.001)	10.62 (0.08)
0.589	0.178 (0.002)	1.678 (0.02)	12.48 (0.11)
0.628	0.266 (0.002)	1.766 (0.002)	18.29 (0.05)
0.668	0.547 (0.003)	2.047 (0.003)	36.76 (0.29)
0.707	2.356 (0.019)	3.856 (0.019)	163.6 (2.4)

TABLE 4.1.2.2

Equilibrium Properties of the 50% Polydisperse Two-Dimensional Colloidal Potential System (N = 1600)

y	ϕ/E_o	U/E_o	$PV/N\ E_o$
0.263	0.016 (0.000)	1.516 (0.000)	2.053 (0.025)
0.314	0.023 (0.001)	1.523 (0.001)	2.512 (0.040)
0.393	0.038 (0.000)	1.538 (0.001)	3.512 (0.038)
0.471	0.066 (0.001)	1.566 (0.001)	5.310 (0.069)
0.511	0.088 (0.001)	1.588 (0.001)	6.727 (0.061)
0.530	0.103 (0.001)	1.603 (0.001)	7.738 (0.045)
0.550	0.121 (0.001)	1.621 (0.001)	8.845 (0.082)
0.569	0.142 (0.001)	1.642 (0.001)	10.28 (0.08)
0.589	0.170 (0.001)	1.670 (0.001)	12.01 (0.03)
0.628	0.250 (0.002)	1.750 (0.002)	17.52 (0.09)
0.668	0.505 (0.011)	2.05 (0.011)	33.65 (0.52)
0.707	2.356 (0.019)	3.856 (0.019)	163.6 (2.4)

System Size Checks Upon the 30% Polydisperse Two-Dimensional Colloidal Potential System

TABLE 4.1.2.3

N = 900

y	ϕ/E_o	U/E_o	$PV/N\ E_o$
0.254	0.016 (0.000)	1.516 (0.000)	2.064 (0.022)
0.550	0.125 (0.001)	1.625 (0.001)	9.127 (0.097)
0.628	0.268 (0.004)	1.768 (0.004)	18.48 (0.17)

TABLE 4.1.2.4

N = 2500

y	ϕ/E_o	U/E_o	$PV/N\ E_o$
0.252	0.016 (0.000)	1.516 (0.000)	2.020 (0.024)
0.550	0.127 (0.001)	1.627 (0.001)	9.167 (0.036)
0.628	0.275 (0.002)	1.775 (0.002)	18.88 (0.13)

System Size Checks Upon the 50% Polydisperse Two-Dimensional Colloidal Potential System

TABLE 4.1.2.5

$N = 900$

y	$\emptyset/E_o$	U/E_o	$PV/N\ E_o$
0.263	0.016 (0.001)	1.516 (0.001)	2.034 (0.033)
0.550	0.120 (0.002)	1.620 (0.002)	8.857 (0.137)
0.628	0.254 (0.001)	1.754 (0.001)	17.70 (0.24)

TABLE 4.1.2.6

$N = 2500$

y	$\emptyset/E_o$	U/E_o	$PV/N\ E_o$
0.258	0.015 (0.000)	1.515 (0.000)	2.009 (0.024)
0.550	0.121 (0.002)	1.621 (0.002)	8.896 (0.096)
0.628	0.257 (0.002)	1.757 (0.002)	17.74 (0.07)

TABLE 4.2.1.1

Equilibrium Properties of the Monidisperse Three-Dimensional Colloidal Sphere System (N = 500)

Amorphous Particle Configuration

$\rho^{\dagger}$	ϕ/E_o	U/E_o	PV/NE_o
0.300	0.037 (0.001)	1.537 (0.001)	2.560 (0.06)
0.400	0.063 (0.001)	1.563 (0.001)	3.650 (0.061)
0.500	0.103 (0.002)	1.603 (0.002)	5.352 (0.073)
0.600	0.166 (0.002)	1.666 (0.002)	8.003 (0.074)
0.700	0.275 (0.001)	1.775 (0.001)	12.609 (0.058)
0.800	0.470 (0.005)	1.970 (0.005)	20.952 (0.204)
0.900	1.925 (0.006)	3.425 (0.006)	86.124 (0.271)
1.000	179.7 (0.0)	181.2 (0.0)	10880 (0)

Face Centre Cubic Crystalline particle Configuration

$\rho^{\dagger}$	ϕ/E_o	U/E_o	PV/NE_o
0.700	0.209 (0.007)	1.709 (0.007)	9.783 (0.289)
0.750	0.228 (0.001)	1.728 (0.001)	10.569 (0.03)
0.800	0.276 (0.001)	1.776 (0.001)	12.570 (0.043)
0.850	0.352 (0.000)	1.852 (0.000)	15.744 (0.022)
0.900	0.485 (0.001)	1.985 (0.001)	21.271 (0.035)
0.950	0.753 (0.001)	2.253 (0.001)	32.496 (0.028)
1.000	1.495 (0.002)	2.995 (0.002)	64.103 (0.071)

TABLE 4.2.1.2

Number-Dependency of the Equilibrium Properties of the Three-Dimensional Colloidal-Sphere System

$\rho^{\dagger}$	N	State	ϕ/E_o	U/E_o	$PV/N\,E_o$
0.700	256	amorphous	0.274 (0.000)	1.774 (0.000)	12.573 (0.701)
0.700	864	amorphous	0.273 (0.003)	1.773 (0.003)	12.511 (0.133)
0.800	256	crystalline	0.280 (0.001)	1.780 (0.001)	12.576 (0.043)
0.800	864	crystalline	0.277 (0.001)	1.777 (0.001)	12.572 (0.036)

TABLE 4.2.2.1

Equilibrium Properties of the n = 9 Colloidal Potential

$\rho^{\dagger}$	ϕ/E_o	U/E_o	$PV/N\,E_o$
0.300	0.019 (0.001)	1.519 (0.001)	2.209 (0.039)
0.400	0.031 (0.001)	1.531 (0.001)	2.981 (0.035)
0.500	0.049 (0.001)	1.549 (0.001)	4.082 (0.053)
0.600	0.073 (0.002)	1.573 (0.002)	5.611 (0.093)
0.700	0.111 (0.001)	1.611 (0.001)	8.009 (0.028)
0.800	0.170 (0.003)	1.670 (0.003)	11.80 (0.20)
0.900	0.259 (0.001)	1.759 (0.001)	17.48 (0.08)
1.000	0.620 (0.016)	2.120 (0.016)	41.21 (1.11)

TABLE 4.2.2.2

Equilibrium Properties of the n = 6 Colloidal Potential Model

$\rho^{\dagger}$	ϕ/E_o	U/E_o	$PV/N\ E_o$
0.300	0.006 (0.000)	1.506 (0.000)	2.011 (0.067)
0.400	0.009 (0.000)	1.509 (0.000)	2.649 (0.072)
0.500	0.014 (0.001)	1.514 (0.001)	3.462 (0.110)
0.600	0.020 (0.000)	1.520 (0.000)	4.533 (0.090)
0.700	0.029 (0.001)	1.529 (0.001)	6.152 (0.153)
0.800	0.042 (0.001)	1.542 (0.001)	8.510 (0.149)
0.900	0.058 (0.001)	1.508 (0.001)	11.47 (0.14)
1.000	0.094 (0.002)	1.594 (0.002)	17.99 (0.35)

TABLE 4.2.4.1

Equilibrium Properties of the 50% Polydisperse, Three-Dimensional Colloidal Potential System (N = 500)

y	ϕ/E_o	U/E_o	$PV/N E_o$
0.175	0.033 (0.001)	1.533 (0.001)	2.459 (0.067)
0.225	0.055 (0.001)	1.551 (0.001)	3.392 (0.051)
0.275	0.089 (0.002)	1.589 (0.002)	4.883 (0.097)
0.324	0.143 (0.001)	1.643 (0.001)	7.229 (0.055)
0.374	0.227 (0.002)	1.727 (0.002)	10.840 (0.094)
0.422	0.373 (0.004)	1.873 (0.004)	17.25 (0.15)
0.471	0.853 (0.002)	2.353 (0.002)	38.89 (0.07)
0.524	16.94 (0.02)	18.44 (0.002)	917.2 (1.2)

TABLE 4.2.4.2

System Size Checks Upon the 50% Polydisperse, Three-Dimensional Colloidal-Sphere Model

y	N	ϕ/E_o	U/E_o	$PV/N\ E_o$
0.225	256	0.056 (0.001)	1.556 (0.001)	3.442 (0.061)
0.225	864	0.055 (0.000)	1.556 (0.000)	3.403 (0.052)
0.374	256	0.239 (0.002)	1.739 (0.002)	10.916 (0.088)
0.374	864	0.230 (0.001)	1.730 (0.001)	10.842 (0.077)

CHAPTER 5

RESULTS OF NON-EQUILIBRIUM COLLOIDAL-SPHERE PARTICULATE DYNAMICS SIMULATIONS

CHAPTER 5

RESULTS OF NON-EQUILIBRIUM COLLOIDAL-SPHERE PARTICULATE DYNAMICS SIMULATIONS

The behaviour of the sheared colloidal-potential system as observed from a series of non-equilibrium particulate dynamics simulations is described in this chapter. Results from the initial simulations, focussing upon monodisperse systems are described in Section 5.1. Subsequent simulations have incorporated a narrow distribution of particle diameters. Results from these polydisperse non-equilibrium simulations are presented in Section 5.2. The scaling relationships used to express the sheared hard-sphere system properties as Stokesian reduced quantities are used once again here. Properties of the sheared colloidal-sphere system are presented as Stokesian-reduced quantities in Section 5.3. Expression of system properties in such a manner allows a qualitative comparison with experimentally observed behaviour to be made.

5.1 Monodisperse Non-Equilibrium Simulation Results

Monodisperse colloidal-sphere systems at a range of reduced densities $\rho^{\dagger} = 0.60 - 0.80$ have been studied in a series of non-equilibrium simulations as described in Section 2.5. The kinetic energy of each sheared system has been maintained at a value $E^{\dagger} = 1.50$ throughout by the use of a similar velocity rescaling procedure used to maintain isokinetic conditions in the previously described non-equilibrium hard-sphere simulations. The equilibrium behaviour of the colloidal-sphere model described in Chapter 3 suggests the system to exhibit an order-disorder transition within the reduced-density range studied here.

Each series of simulations originated with a static, steady state configuration of the desired reduced-density. These starting configurations were produced by the densification of an equilibrated, amorphous system at a reduced-density $\rho^{\dagger} = 0.30$ to the desired value. A densification rate of $(d\sigma/dt)^{\dagger} = 0.001$ was used in each case. The densification procedure has been described in Section 2.4. On arrival at the desired reduced-density value, steady state conditions were judged to have been achieved after, typically 5000 time increments of $\Delta t^{\dagger} = 0.001$. The vast majority of simulations have involved a system size of N = 500 particles. A less extensive study upon systems containing N = 256 and N = 864 particles has also been performed in order to determine any system-size dependency.

Following the initiation of shearing conditions, several thousand time increments were allowed for the system to reattain steady state conditions. Reattainment of steady state conditions was deemed to be complete in each case when monitored system properties were judged to be absent of any drift in value when observed over $t^{\dagger} \sim 1.00$. The results of these monodisperse non-equilibrium simulations expressed as 'isokinetic' reduced quantities defined in Table 2.1.1 can be found in Tables 5.1.1 - 5.1.3. Estimates of the uncertainty associated with each data point calculated as the standard deviation of several independent sub-averages are once again quoted in parentheses.

Much of the interesting behaviour exhibited by the sheared isokinetic colloidal-sphere system over the density range studied occurs at relatively low shear rates as compared to the wider shear rate range studied. For this reason the behaviour of the system up to a shear rate $\dot{\gamma}^{\dagger} = 12.50$ is represented in the first three figures of this chapter. Figure 5.3.1 demonstrates the qualitative similarity of the sheared colloidal-sphere system pressure to that of the sheared hard-sphere model under isokinetic

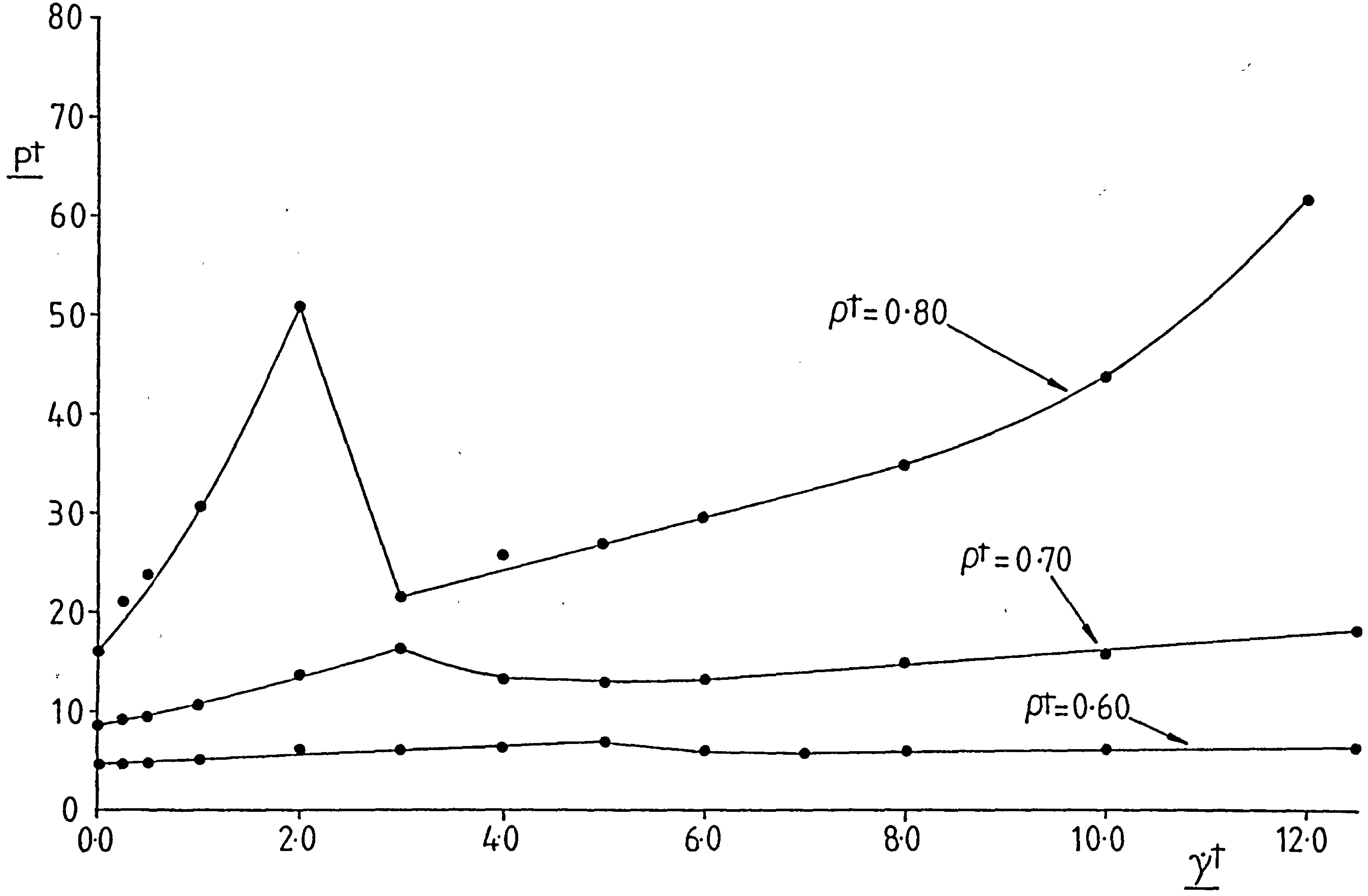

FIGURE 5.1.1: Pressure of the Sheared Isokinetic Monodisperse Colloidal-Sphere Model at Low Shear Rates

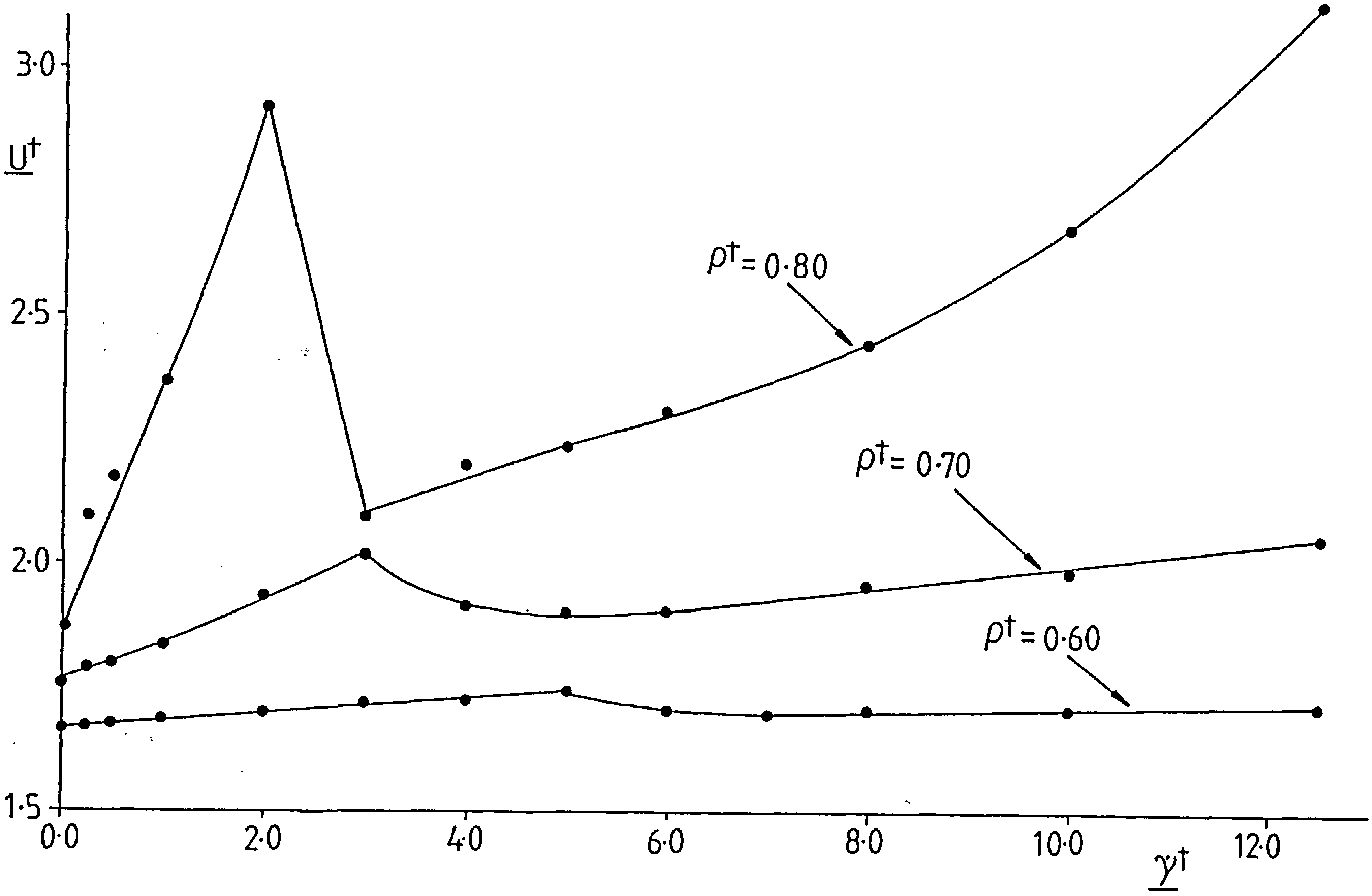

FIGURE 5.1.2: Total Internal Energy of the Sheared Isokinetic Monodisperse Colloidal-Sphere Model at Low Shear Rates

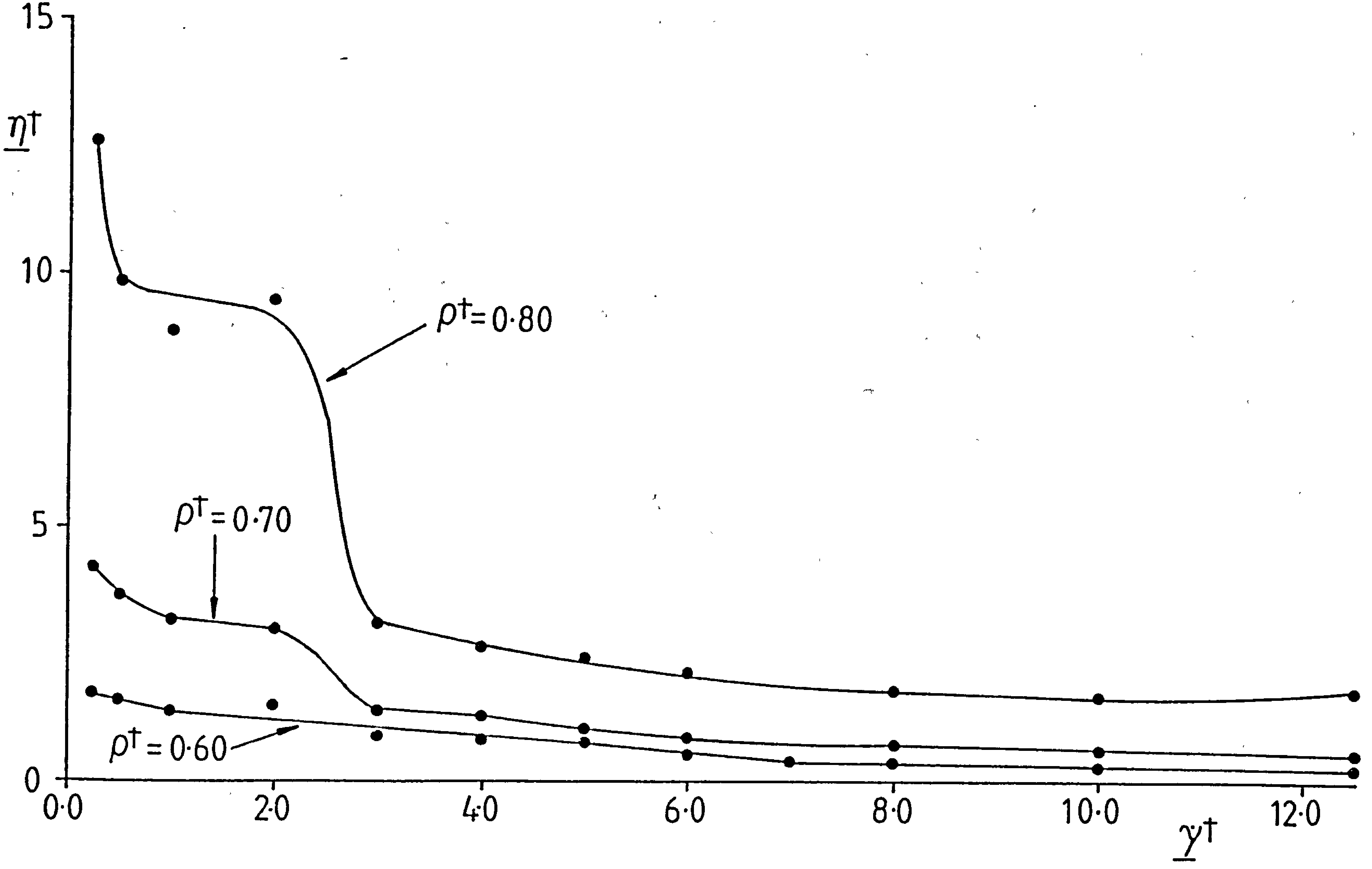

FIGURE 5.1.3: Viscosity of the Sheared Isokinetic Monodisperse Colloidal-Sphere Model at Low Shear Rates

conditions. Two distinct pressure branches may be observed at each density studied. These branches correspond to amorphous and ordered system configurations, once again providing supporting evidence for the explanation of the observed behaviour in terms of a perturbation of the equilibrium phase behaviour. The position of this pressure discontinuity tends towards lower shear rates with increasing system density. In the thermodynamic limit this transition should disappear at a density corresponding to the equilibrium freezing transition. A further observation that can be made from Figure 5.1.1 is the increasing pressure difference across the transition with increasing system density. This trend possibly reflects increased metastability in the transition region at higher densities.

Total energy of the sheared colloidal-potential system, as plotted in Figure 5.3.2 exhibits a similar pattern of behaviour as that shown for system pressure in Figure 5.3.1, i.e. a discontinuity of decreasing magnitude, occurring at higher shear rates with decreasing system density. Since isokinetic conditions are maintained throughout, any change in total energy is directly attributable to a change in potential energy $\phi^{\dagger}$.

The viscosity of the sheared isokinetic colloidal-sphere system at relatively low shear rates is plotted in Figure 5.1.3 for each density point. At the highest reduced density point studied $\rho^{\dagger} = 0.80$, viscosity decreases rapidly at very low shear rates before levelling off to a transient plateau value. A further sharp viscosity increase occurs, originating at a shear rate corresponding to the pressure and internal energy discontinuity shown in Figures 5.1.1 and 5.1.2 respectively. A similar trend is observed in the isokinetic flow curve, at a density $\rho^{\dagger} = 0.70$, but with less abrupt viscosity decreases with increasing shear rate. At the lowest reduced density $\rho^{\dagger} = 0.60$, the sharp viscosity increase at vanishing shear rate exhibited by the higher density systems is not evident from the present data.

The abrupt changes in system properties at finite shear rates may be explained in terms of shear-induced changes in the system microstructure. Configurational plots demonstrating these structural changes will be presented in Section 5.3, where the results of these isokinetic simulations will be scaled to allow comparsion with experimental observations of dense suspension rheology.

The behaviour of system pressure, internal energy and viscosity of the sheared isokinetic colloidal-sphere system is plotted over the whole shear rate range studied, on a logarithmic scale in Figures 5.1.4 - 5.1.6 respectively. Beyond the discontinuity discussed earlier, system pressure and internal energy exhibit a general upward trend with increasing shear rate. The rate of increase is much greater for the highest reduced density studied, i.e. $\rho^{\dagger} = 0.80$. Viscosity however, exhibits an overall decrease with increasing shear rate. One notable exception to this overall viscosity decrease is the system at a reduced density $\rho^{\dagger} = 0.80$ which exhibits an extremely sharp viscosity increase at the highest shear rate point studied, $\dot{\gamma}^{\dagger} = 75.00$. A similar abrupt viscosity increase at high shear rates has been reported for the soft-sphere(4) and Lennard-Jones systems(121). Despite studying the lower density colloidal-potential systems to much higher shear rates, no evidence of any abrupt viscosity increase could be observed.

A further interesting aspect of the sheared colloidal system behaviour is evident from the properties of the system at a reduced density $\rho^{\dagger} = 0.60$. At a shear rate $\dot{\gamma}^{\dagger} = 30.00$ ($\log \dot{\gamma}^{\dagger} = 1.477$) a small, sharp increase may be observed in pressure, internal energy and viscosity. Consideration of snapshot configurational plots of the system microstructure at a shear rate just before ($\dot{\gamma}^{\dagger} = 25.00$; $\log \dot{\gamma}^{\dagger} = 1.398$) and a shear rate corresponding to ($\dot{\gamma}^{\dagger} = 30.00$; $\log \dot{\gamma}^{\dagger} = 1.477$) this distontinuity allows us to gain an insight into the origins of this observed behaviour.

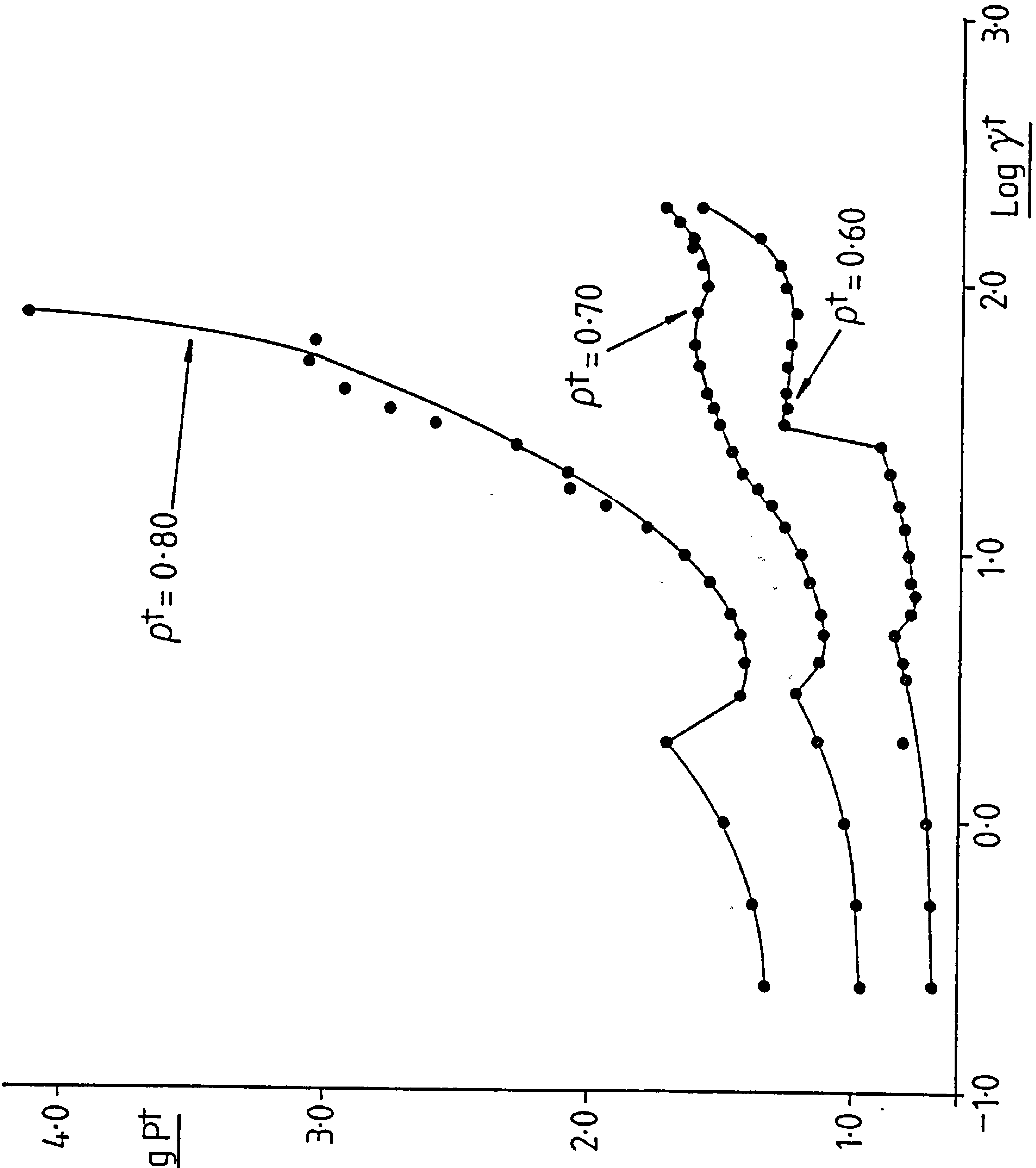

FIGURE 5.1.4: Pressure of the Sheared Isokinetic Monodisperse Colloidal-Sphere Model Over the Whole Shear Rate Range Studied

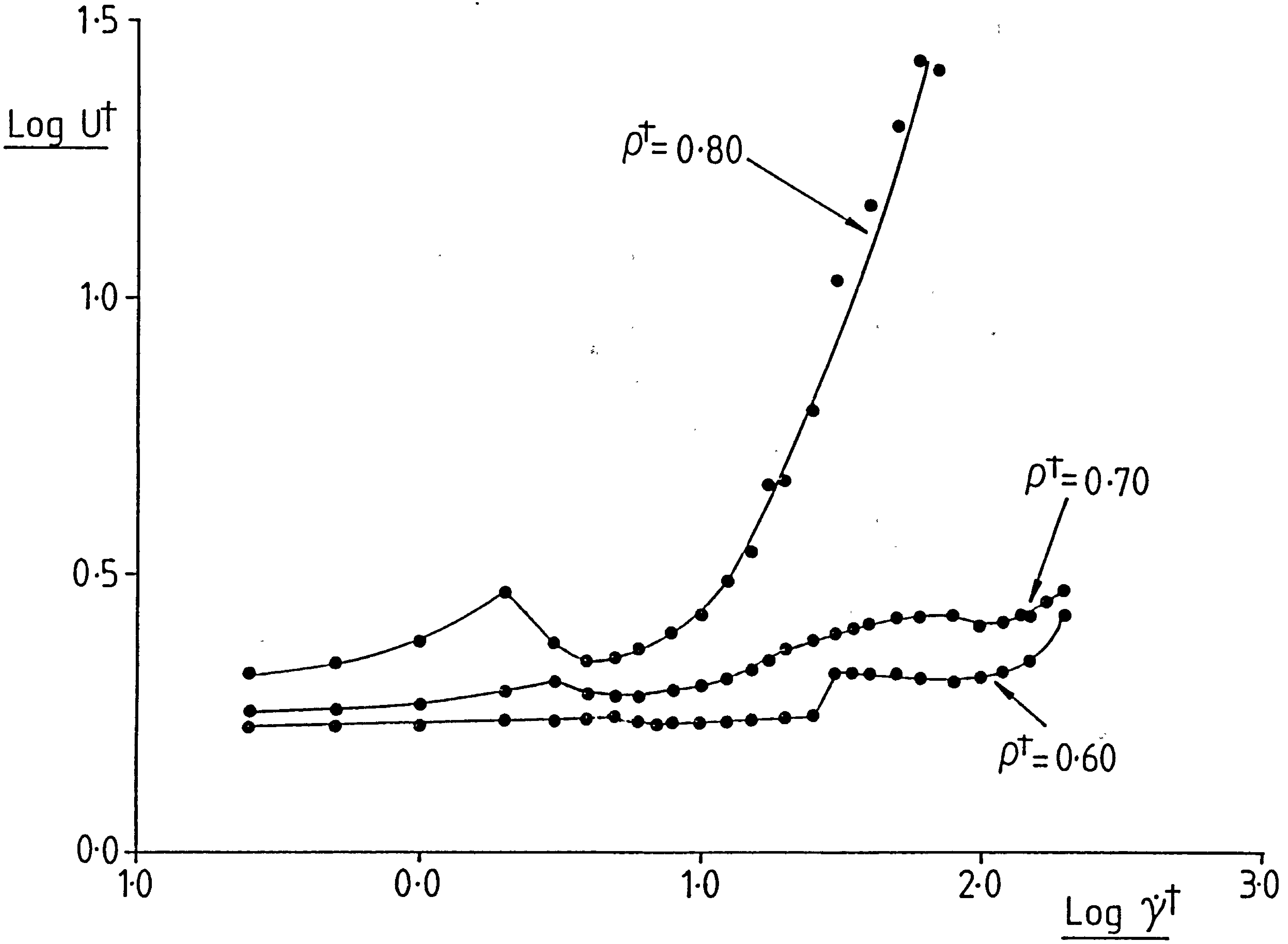

FIGURE 5.1.5: Total Internal Energy of the Sheared Isokinetic Monodisperse Colloidal-Sphere Model Over the Whole Shear Rate Range Studied

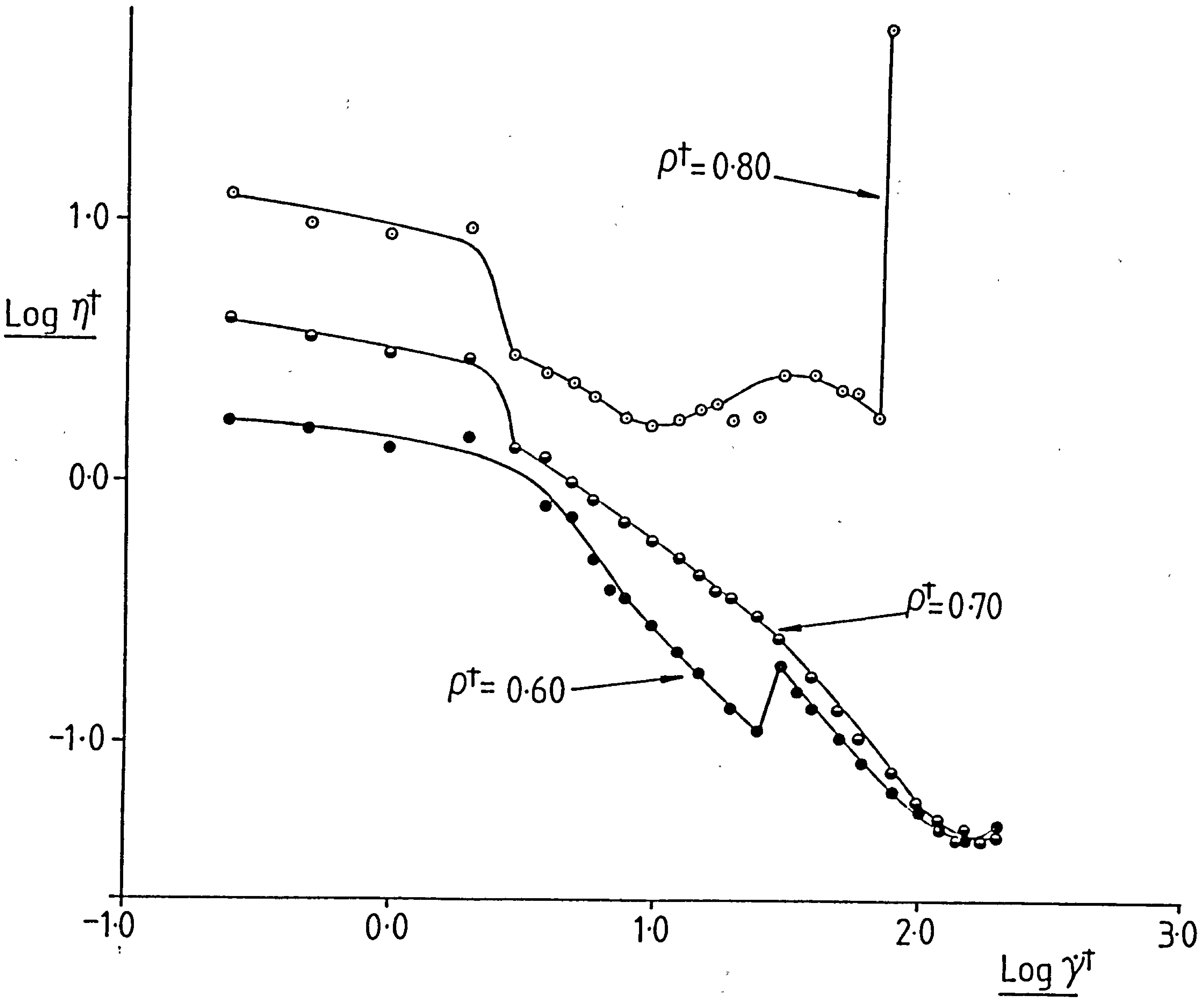

FIGURE 5.1.6: Viscosity of the Sheared Isokinetic Monodisperse Colloidal-Sphere Model Over the Whole Shear Rate Range Studied

These configurational plots are similar to those used to illustrate the microscopic state of the sheared hard-sphere system in Chapter 3. Although the explanatory notes accompanying the configurational plots given previously will not be repeated, they are equally applicable to the plots to be presented here and in later sections of this chapter. Figure 5.1.7 shows a set of three orthogonal configurational plots of the colloidal-sphere system at a density $\rho^{\dagger} = 0.60$ and a shear rate $\dot{\gamma}^{\dagger} = 25.00$. An illustration of the orthogonal viewpoints with respect to the direction of flow and velocity gradient can be found in Figure 3.5.5. Consideration of the particle configuration from the xy viewpoint in Figure 5.1.7 shows the system microstructure to have adopted a layered arrangement in the x-direction. When viewed from the xz-viewpoint however, the system appears to exhibit a much lower degree of structural order. The remaining configurational plot of Figure 5.1.7, showing the system as viewed along the yz-plane shows the clearest representation of the system microstructure at a shear rate $\dot{\gamma}^{\dagger} = 25.0$. The system is demonstrated to have formed a highly ordered arrangement over the bulk of the central simulation cell. In this ordered region flow is facilitated by the translation of particles along streamlined cylinders bounded by neighbouring cylinders. The lower region of the simulation cell as viewed from the yz-direction, however, may be clearly seen to exhibit a disordered structure. It would appear that the crystalline arrangement originally adopted is incompatible with the geometric constraints of the central simulation cell.

Figure 5.1.8 shows a similar set of configurational plots at a shear rate $\dot{\gamma}^{\dagger} = 30.0$, corresponding to the discontinuity in system properties represented in Figures 5.1.4 - 5.1.6. Consideration of the system microstructure from both xy and xz-viewpoints shows the system to exist as tightly packed layers in the direction of flow.

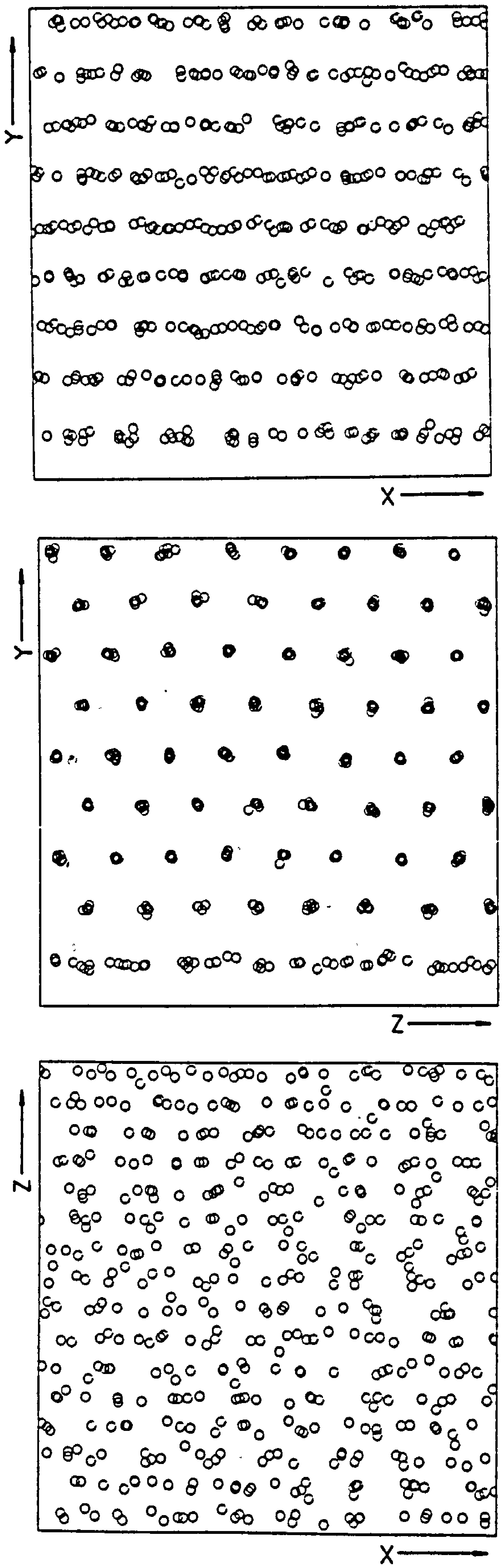

FIGURE 5.1.7: Configurational Plots of the Sheared Isokinetic Monodisperse Colloidal-Sphere Model with a Reduced Density $\rho^{\dagger}$ = 0.60 at a Shear Rate $\dot{\gamma}^{\dagger}$ = 25.0. This Shear Rate Corresponds to the Point Immediately Prior to the Discontinuity in System Properties at Intermediate Shear Rates Demonstrated in Figures 5.1.4 - 5.1.6.

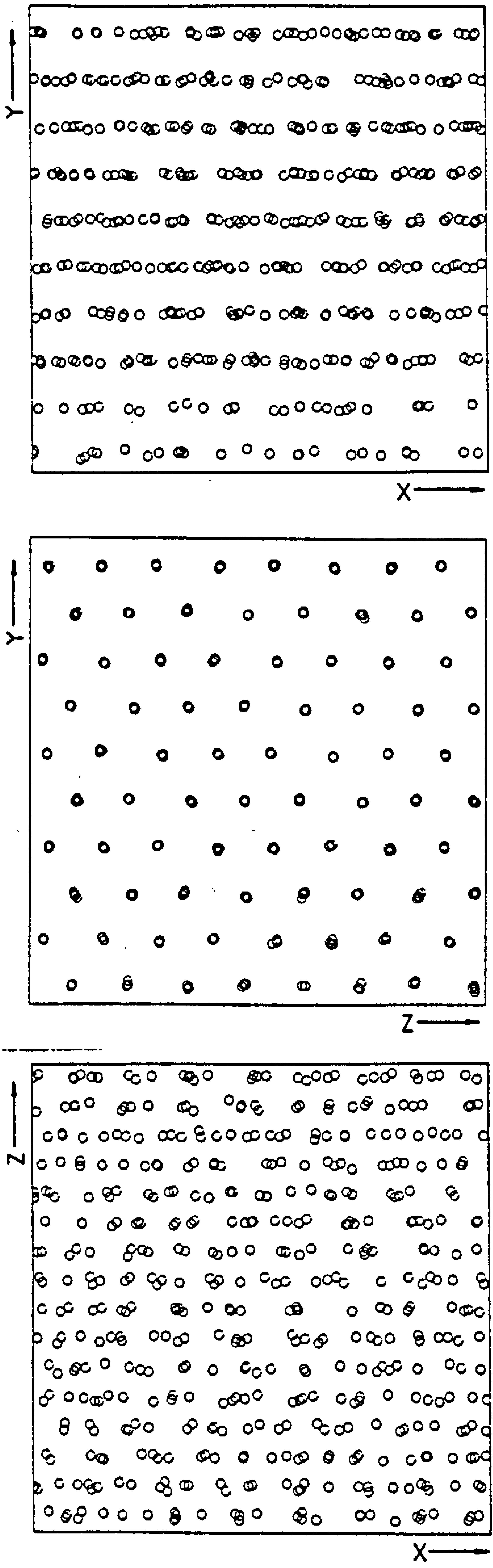

FIGURE 5.1.8: Configurational Plots of the Sheared Isokinetic Monodisperse Colloidal-Sphere Model with a Reduced Density $\rho^{T} = 0.60$ at a Shear Rate $\dot{\gamma}^{+} = 30.0$. This Shear Rate Corresponds to the Point Immediately After the Discontinuity in System Properties at Intermediate Shear Rates Demonstrated in Figures 5.1.4 - 5.1.6.

Examination of the system from the remaining yz-viewpoint shows the system to have adopted a very highly-ordered structure. A co-operative particle rearrangement has occurred, in order to accommodate the whole system as an ordered arrangement within the confines of the central simulation cell. From the information presently available, it is not possible to elucidate the origin of the observed shear induced structural rearrangement any further. The geometry of the central simulation cell with respect to the ordered arrangement adopted however, appears to affect the preferred system microstructure. Experimental suspensions of well-characterised colloidal lattices at equilibrium have been observed to order into face-centre-cubic (fcc) arrangements(29). Body-centre-cubic (bcc) arrangements are known to be unstable with respect to slippage along one plane. It seems reasonable to assume that the ordered arrangement showing instability with respect to slip at equilibrium, will become the preferred arrangement under shearing conditions. Consequently, it is tempting to speculate that the behaviour of the colloidal-sphere system at a density $\rho^{\dagger} = 0.60$ is attributable to a shear induced fcc-bcc polymorphic transition.

Number-dependency checks have been performed for the colloidal-sphere system at a reduced density $\rho^{\dagger} = 0.70$ at selected shear rate points. The results for systems containing $N = 256$ and $N = 864$ particles are presented in Tables 5.1.4 and 5.1.5 respectively. Comparisons of the pressure, internal energy and viscosity exhibited by the three system sizes studied are made in Figures 5.1.9 - 5.1.11 respectively. The most striking difference which can be observed from these comparisons is the sudden large increase in all three properties of the largest system at a shear rate $\dot{\gamma}^{\dagger} = 75.0$. This sudden abrupt increase resembles the behaviour of the colloidal-sphere system at a reduced density $\rho^{\dagger} = 0.80$ (see Figures 5.1.4 - 5.1.6). Attempts to study the ($N = 864$;

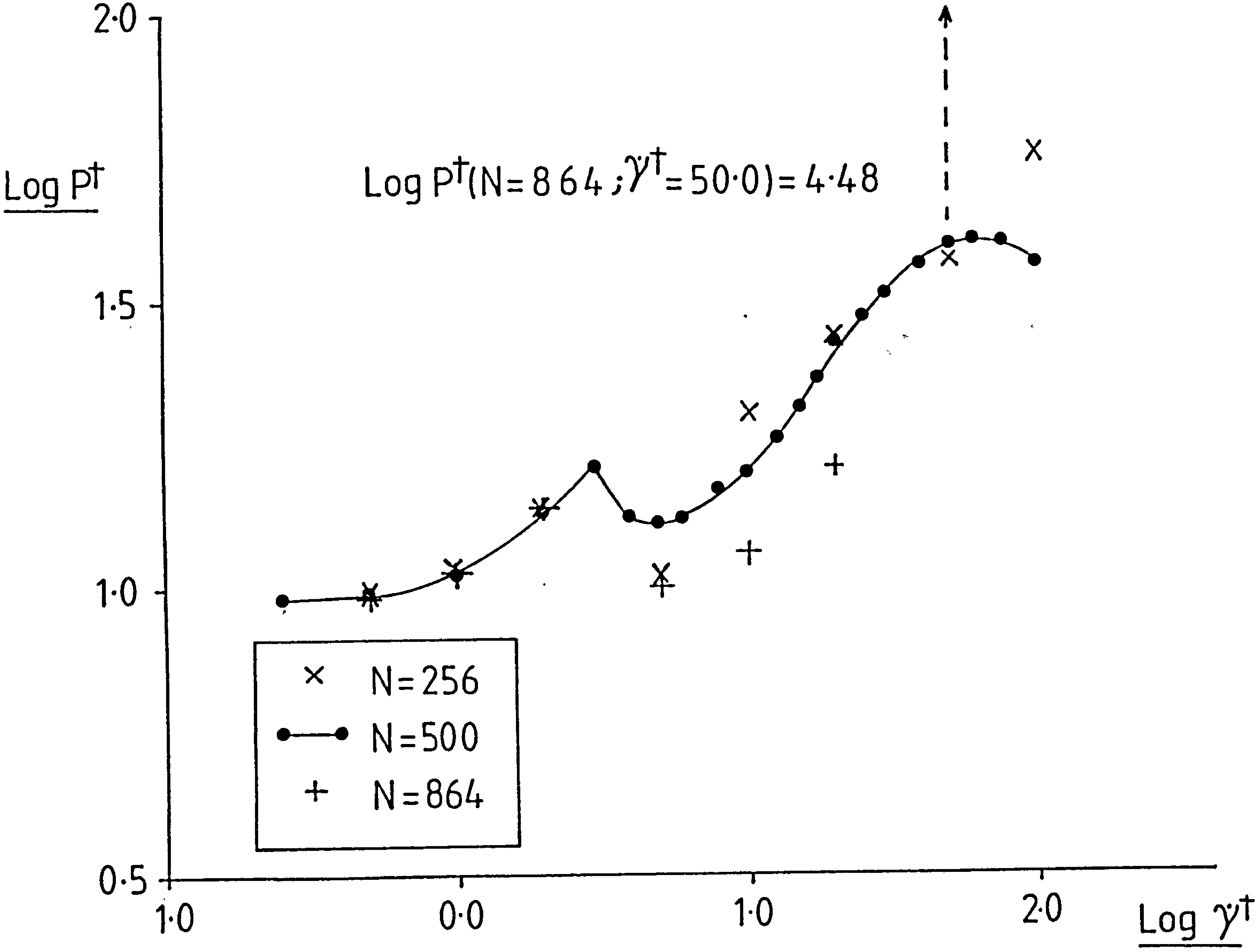

FIGURE 5.1.9: A Comparison of the Pressure Exhibited by Sheared Isokinetic Monodisperse Colloidal-Sphere Systems of Differing Size

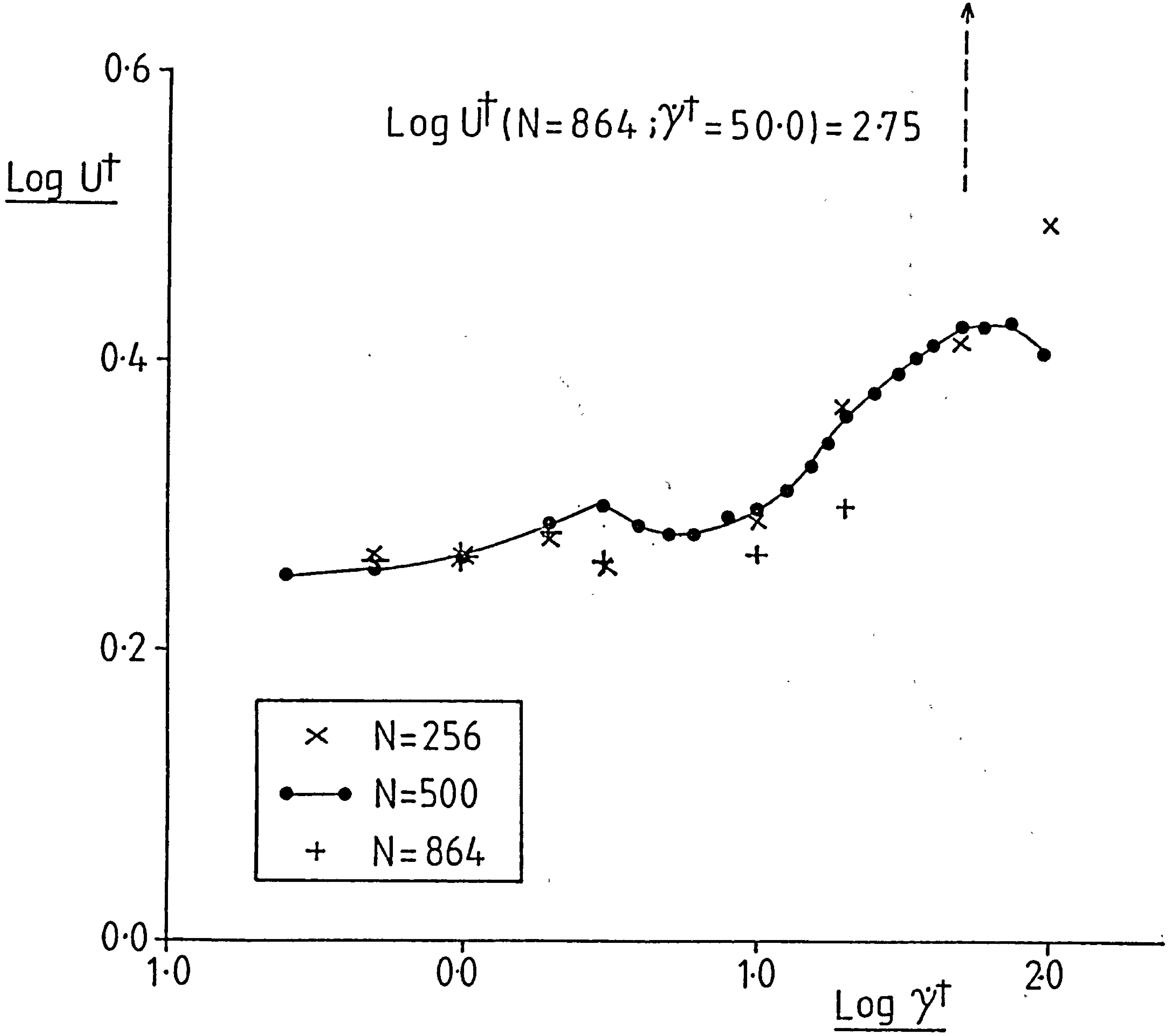

FIGURE 5.1.10: A Comparison of the Total Internal Energy Exhibited by Sheared Isokinetic Monodisperse Colloidal-SphereSystems of Differing Size

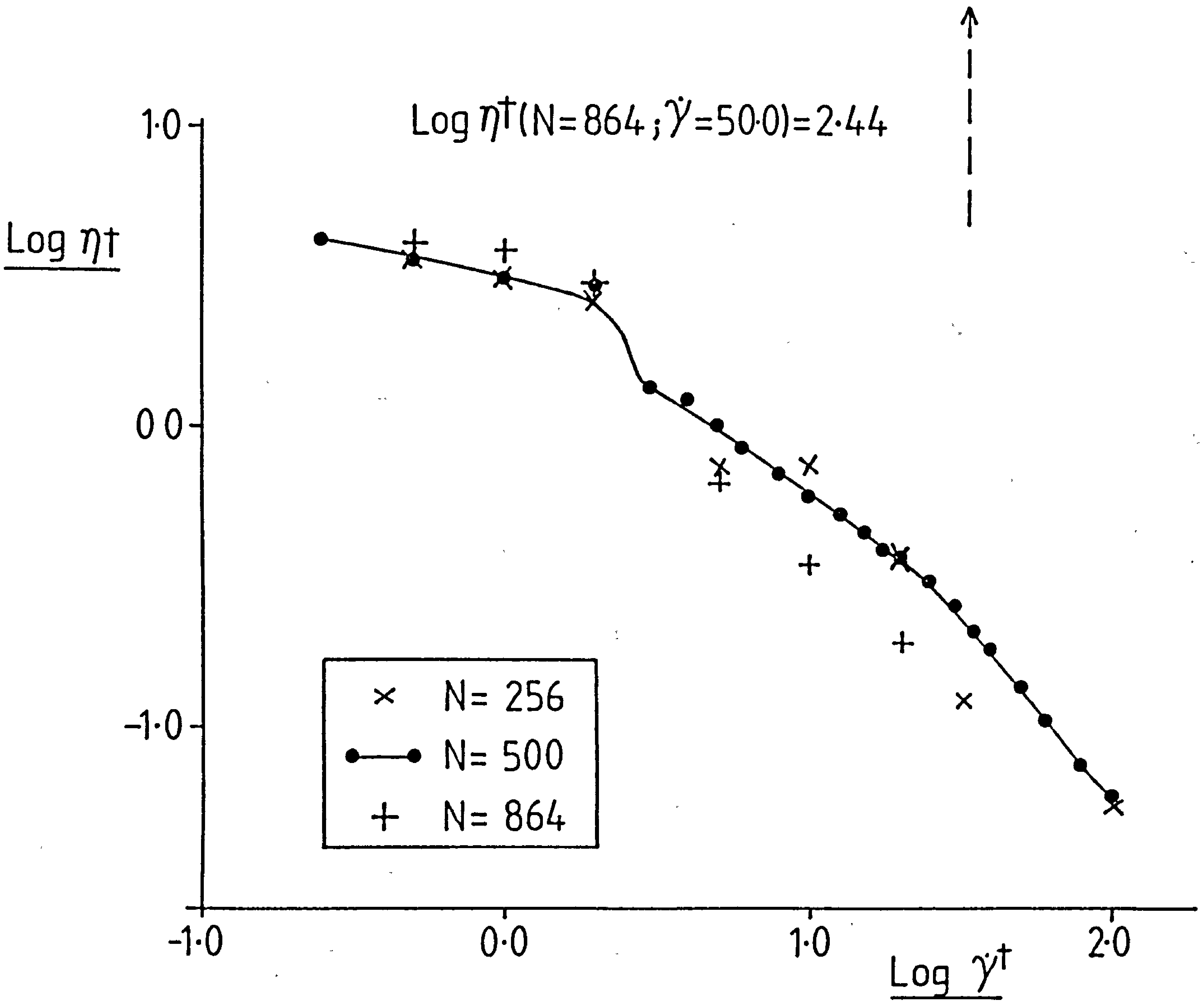

FIGURE 5.1.11: A Comparison of the Viscosity Exhibited by Sheared Isokinetic Monodisperse Colloidal-Sphere Systems of Differing Size

$\rho^{\dagger} = 0.70$) system at even higher shear rates were similarly fraught with difficulties due to non-equilibration of the system to steady state conditions. Less dramatic discrepancies between the properties of different sized systems can be observed at lower shear rates. From the available data however, there is no positive evidence of any correlation between system size and observed behaviour.

5.2 Polydisperse Non-Equilibrium Simulation Results

Two colloidal-sphere systems, each containing N = 500 particles and differing only in the degree of polydispersity (defined in Equation (2.4.12) have been studied through a series of simulations as described in Chapter 2. In each system the hard-core packing fraction, y, was set equal to that of a monodisperse system at a reduced density $\rho^{\dagger} = 0.70$, i.e. y = 0.367. Amorphous initial configurations at this packing fraction were created by use of the densification procedure used to create amorphous configurations in the monodisperse simulation studies, and described in Chapter 2. A densification rate of $\left[\frac{d\sigma}{dt}\right]^{\dagger} = 0.001$ was used.

In common with the monodisperse non-equilibrium studies presented in the previous section of this chapter, simulations were performed in ascending shear rate order. Higher shear rate studies were successively started from the product configuration of the previous, lower shear rate study. Once again, system kinetic energy was constrained to a value $E^{\dagger} = 1.50$ through continuous peculiar velocity rescaling. Values of the time increment used varied from $\Delta t^{\dagger} = 0.001$ at low shear rates to $\Delta t = 0.00005$ at the highest shear rates studied. A 3 x 3 x 3 matrix of link cells was used throughout.

Tables 5.2.1 and 5.2.2 summarise the results of these polydisperse simulations. Comparisons of polydisperse system properties with that of the monodisperse system at equivalent hard-core packing fraction are made in Figures 5.2.1 - 5.2.3. The pressure behaviour of each system is shown to exhibit two well-defined branches separated by a sharp discontinuity (Figure 5.2.1). Each branch shows an increasing value with increasing shear rate. The low shear-rate branch of the three systems are virtually superimposable. From the presently available data it is not possible to distinguish between the occurrence of the pressure discontinuity of the 5% polydisperse and monodisperse systems, the 10% polydisperse system however, is clearly shown to undergo a pressure discontinuity at a higher shear rate value. These higher shear rate pressure branches diverge with increasing shear rate, higher pressures being exhibited by more polydisperse systems. Qualitatively similar behaviour may be observed by the internal-energy-shear rate relationship, which is plotted in Figure 5.2.2.

The viscosity exhibited by each of the isokinetic colloidal-sphere systems as a function of shear rate is plotted in Figure 5.2.3. At low shear rates the viscosity is shown to be relatively independent of polydispersity for the narrow particle size distributions considered here. A sharp viscosity decrease is exhibited by each system at a shear rate which increases with the degree of polydispersity. At intermediate shear rates the viscosity of each system exhibits a general downward trend with increasing shear rate. A noticeable difference however, exists between the viscosity of each system in this shear rate regime; viscosity increasing with polydispersity. Figures 5.2.4 and 5.2.5 show a set of configurational plots for the monodisperse and 10% polydisperse systems at a shear rate $\dot{\gamma}^{\dagger} = 10.0$. Figure 5.2.5 demonstrates the inability of the polydisperse system to pack efficiently into streamlined cylinders, as compared to the corresponding monodisperse case (Figure 5.2.4). The higher viscosities of systems with increasing polydispersity in these studies can thus be explained in terms of this inefficient packing. An abrupt viscosity increase is shown by each of

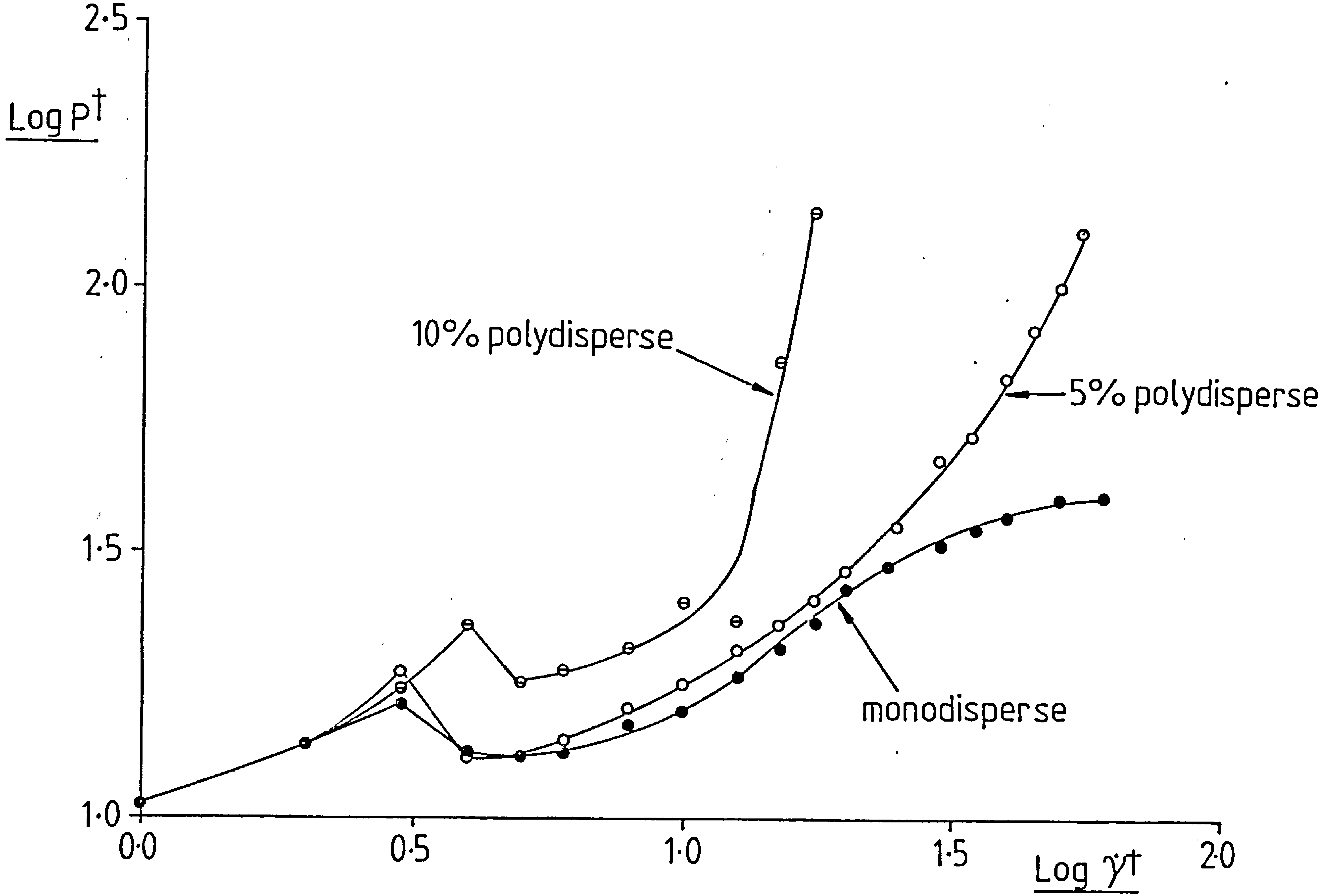

FIGURE 5.2.1: A Comparison of the Pressure Exhibited by Sheared Isokinetic Colloidal-Sphere Systems with Narrow Distributions of Particle Sizes. Each System has a Hard-Core Packing Fraction of y = 0.367.

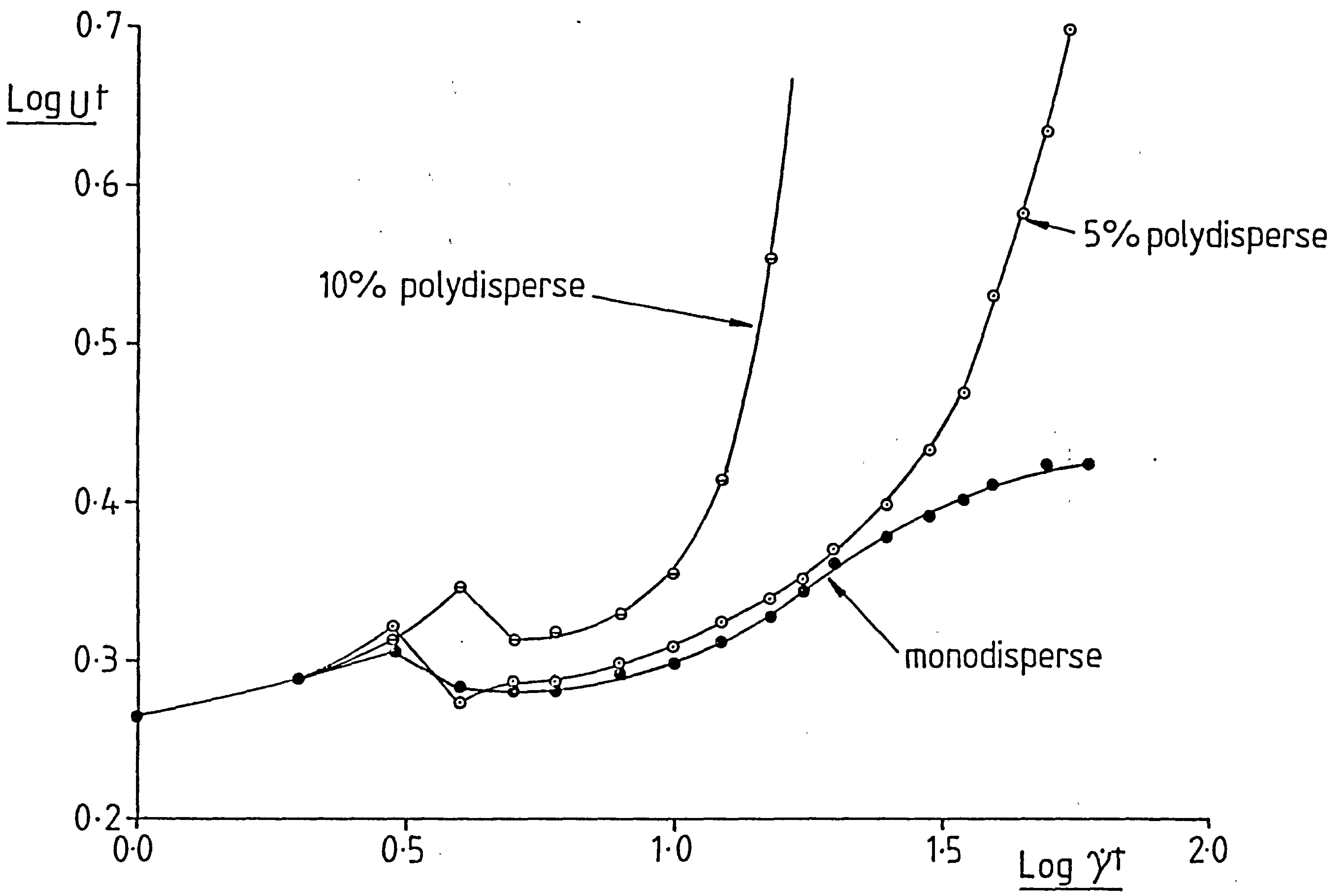

FIGURE 5.2.2: A Comparison of the Total Internal Energy Exhibited by Sheared Isokinetic Colloidal-Sphere Systems with Narrow Distribution of Particle Sizes. Each System has a Hard-Core Packing Fraction of $y = 0.367$.

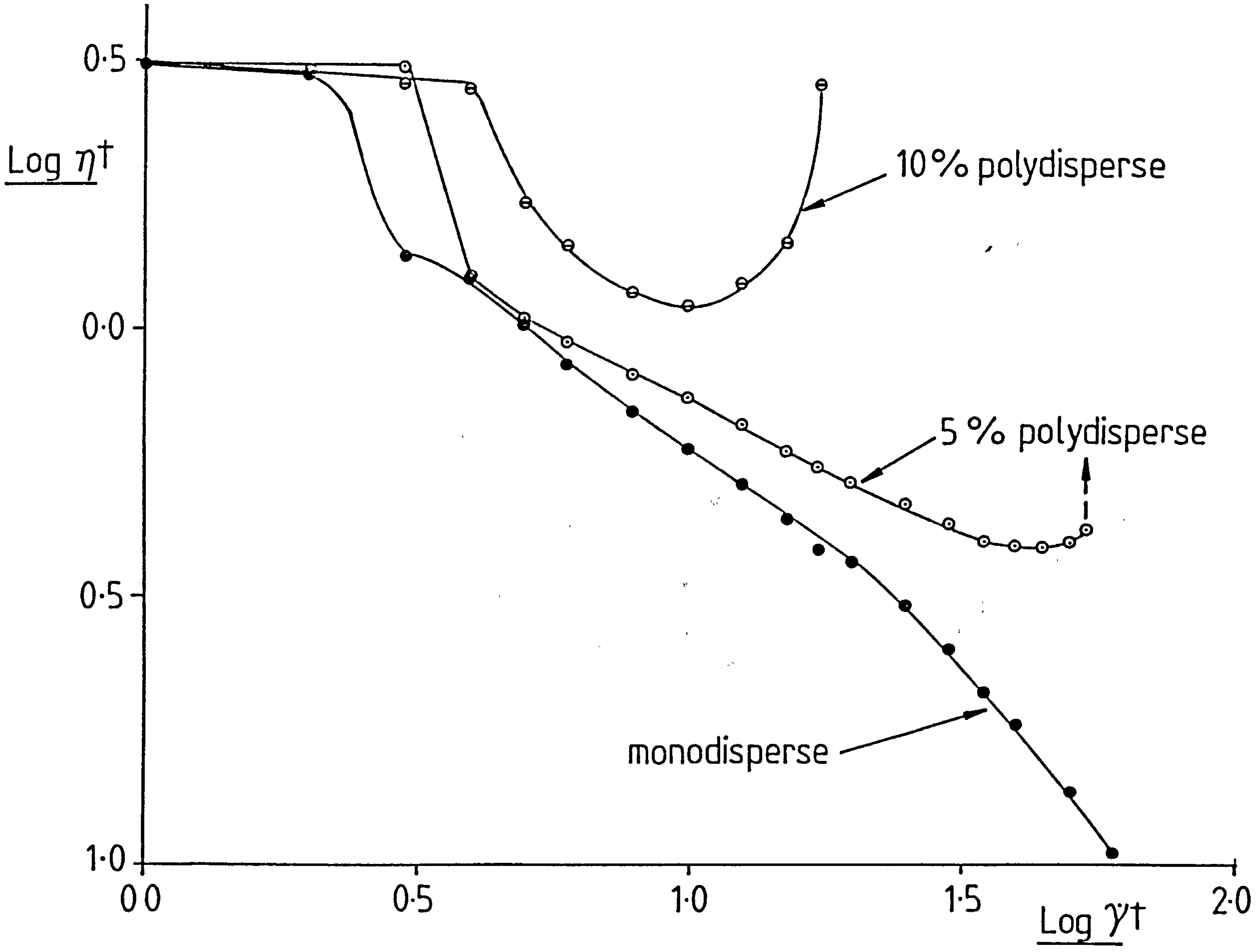

FIGURE 5.2.3: A Comparison of the Viscosity Exhibited by Sheared Isokinetic Colloidal-Sphere Systems with a Narrow Distribution of Particle Sizes. Each System has a Hard-Core Packing Fraction of y = 0.367.

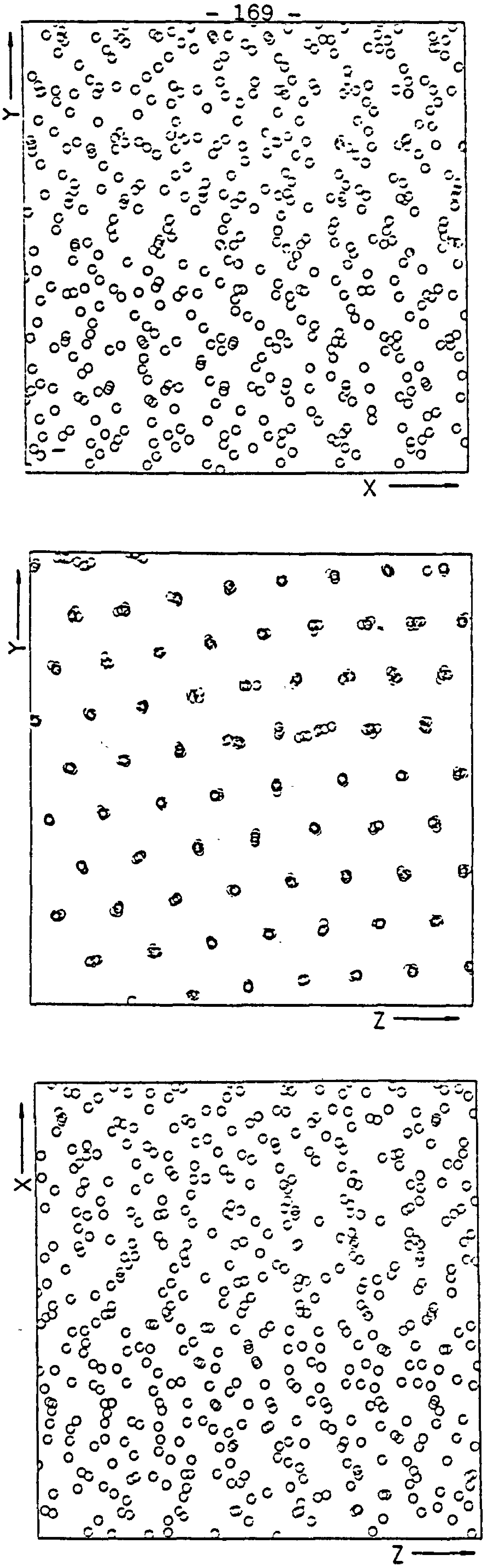

FIGURE 5.2.4: Configurational Plots of the Sheared Isokinetic Monodisperse Colloidal-Sphere System with a Reduced Density of $\rho^{\dagger} = 0.70$ ($y = 0.367$) at a Shear Rate $\dot{\gamma}^{\dagger} = 12.50$

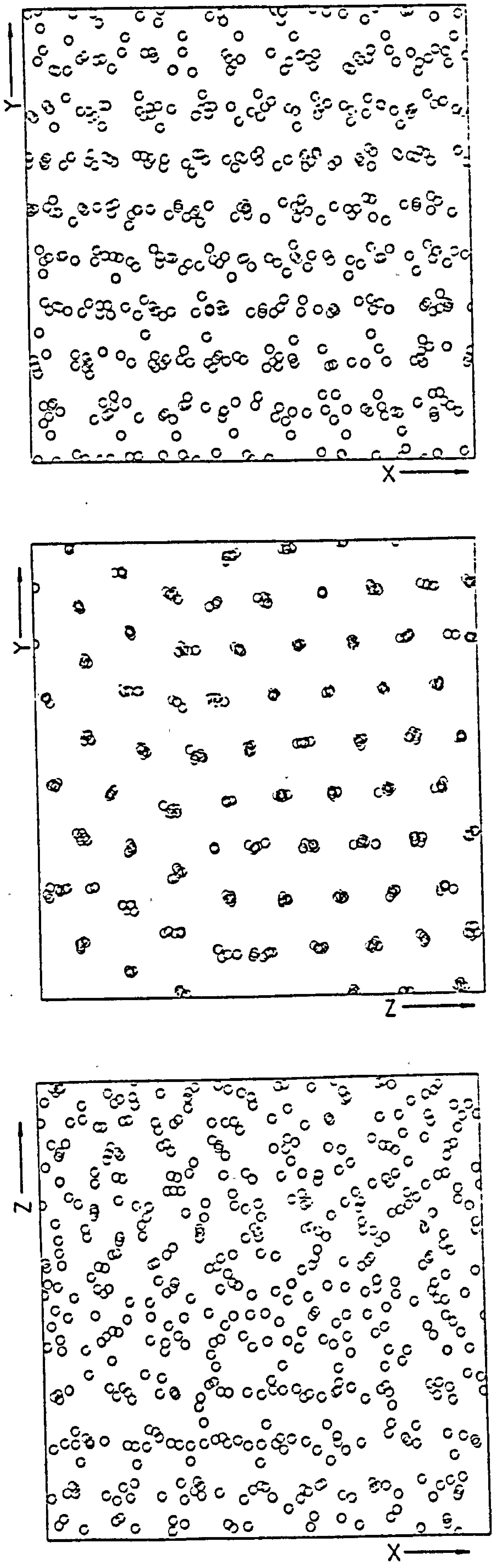

FIGURE 5.2.5: Configurational Plots of the Sheared Isokinetic Colloidal-Sphere System with 10% Polydispersity. The System is at a Hard-Core Packing Fraction of 0.367, and a Shear Rate $\dot{\gamma}^{\dagger}$ = 12.50. Comparison of these Plots with those of the Corresponding Monodisperse Case (Figure 5.2.4) Reveals an Inefficient Packing of Particles into 'Strings' Parallel to the Direction of Flow.

the polydisperse systems at higher shear rates. The shear rate corresponding to the onset of this viscosity increase decreases markedly with increasing polydispersity.

The results presented in this section confirm that the trends previously reported(46,49,50) for equilibrium systems, i.e. that the introduction of a narrow degree of polydispersity into a system destabilizes the ordered phase with respect to the disordered phase, are equally applicable to sheared systems. Implications of this observation with respect to dense suspension rheology will be discussed in the following section.

5.3 Applications to Dense Suspension Rheology

From the scaling argument presented in Section 3.4, it is evident that the shear rate dependent behaviour of an isokinetic system of model particles bears little resemblance to that of experimentally sheared suspensions. In order to make a qualitative comparison of the behaviour observed in isokinetic non-equilibrium simulations with the observed rheology of dense suspensions it is necessary to express the results in the appropriately reduced form. Woodcock(65) has proposed such a set of reduced quantities which comprise parameters that are constant in a sheared model hard-sphere suspension, i.e. particle mass (m), diameter (σ) and frictional constant (c). These 'Stokesian' reduced quantities, together with their relationship to conventional 'isokinetic' reduced units (Table 2.1.1) have already been presented in Table 3.4.1. Conversion of system properties expressed as 'isokinetic' reduced quantities to the 'Stokesian' reduced form requires a knowledge of the effective friction constant, $c^{\dagger}$, as a function of shear rate.

It is possible to derive an expression for the effective friction constant from a consideration of the energy balance for a sheared isokinetic hard-sphere system(65), i.e.

$$3 N E_o < f(t) - 1 > = < \eta \dot{\gamma}^2 V dt > \qquad (5.3.1)$$

The left hand side of Equation (5.3.1) refers to the energy removed by velocity rescaling, whilst the right hand side represents the viscous heating of the system.

Rearranging the above equation, and substituting for:

$$C dt = f(t) - 1 \qquad (5.3.2)$$

leads to the following expression for C when expressed in 'isokinetic' units:

$$C^{\dagger} = \frac{\eta^{\dagger} \gamma^{\dagger 2}}{3\rho^{\dagger}} \qquad (5.3.3)$$

Equation (5.3.2) is strictly only applicable for estimating the effective friction constant of the sheared hard-sphere system, where the energy is entirely kinetic. A short series of simulations have been performed in order to estimate $C^{\dagger}$ at selected shear rate points. These simulations have utilised product configurations of the non-equilibrium colloidal-sphere simulations discussed in Section 5.3.1. A comparison of the effective rescaling coefficient obtained from these simulations with that predicted from Equation (5.3.2) is made in Figure 5.3.1. Since good agreement may be observed between the estimated and simulation results, the use of the former to convert the present simulation results into 'Stokesian' reduced quantities would, to a first approximation appear to be valid.

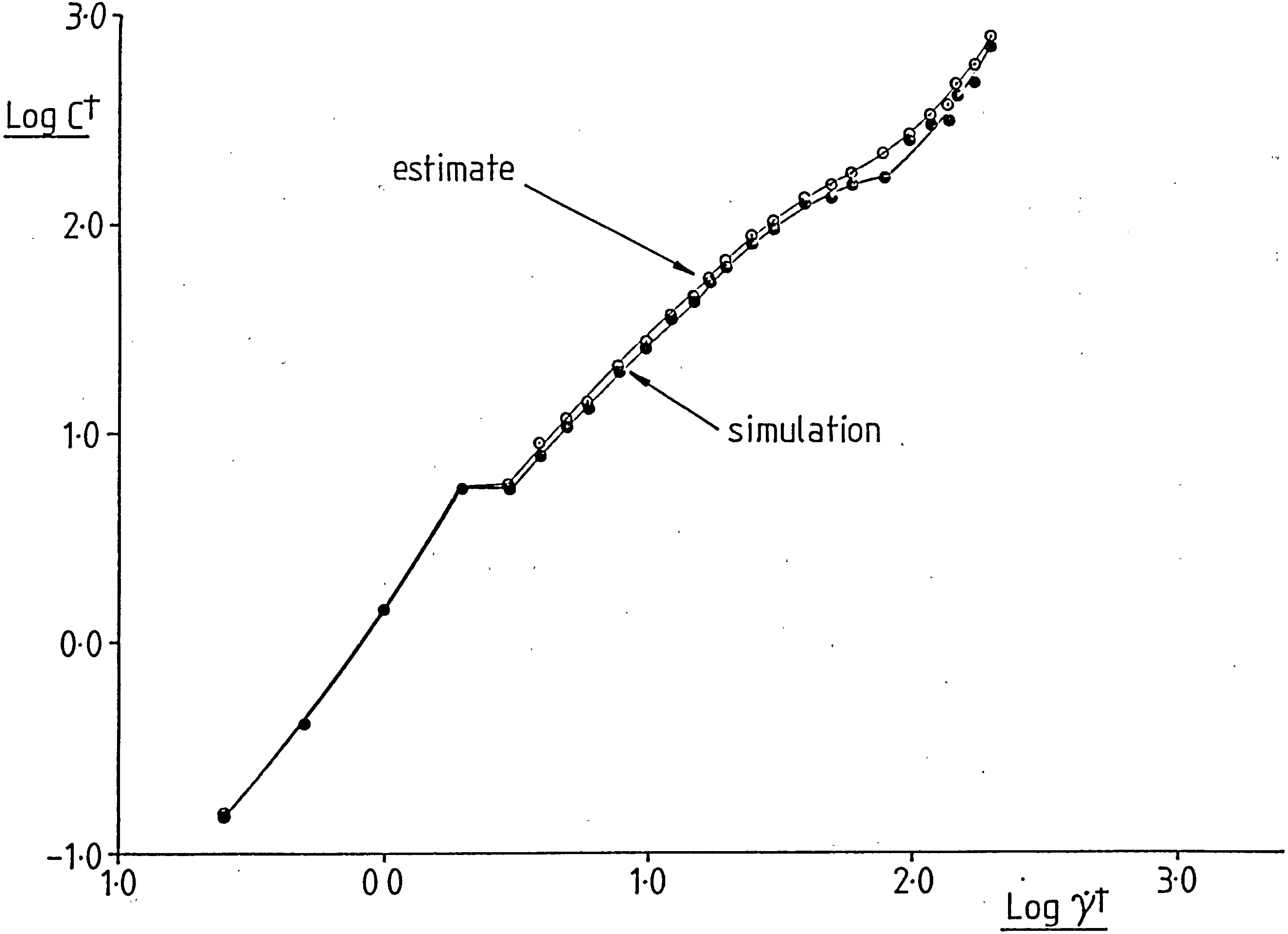

FIGURE 5.3.1: A Comparison of the Effective Friction Coefficient C^+ as Predicted from Equation (5.3.3) with the Value Obtained from Isokinetic Non-Equilibrium Simulations. The comparison is Made for the System with a Reduced Density $\rho^\dagger$ = 0.70

Figure 5.3.2 shows the predicted osmotic internal energy behaviour of the sheared colloidal-sphere suspension at the three density points studied. Qualitatively the behaviour resembles that of the sheared hard-sphere suspension plotted in Figure 3.5.2. In general the osmotic internal-energy may be observed to increase rapidly with advancing shear rate. Each system exhibits a discontinuity towards the higher end of the Stokesian shear rate range studied. This discontinuity stems from the same shear-induced structural transition responsible for the non-linear behaviour observed in the isokinetic results presented in Section 5.1. The changing ordered arrangement of the system with a reduced density $\rho^{\dagger} = 0.60$ which was demonstrated in Figures 5.1.7-5.1.8 is responsible for the low Stokesian shear rate discontinuity in Figure 5.3.2. Osmotic pressure of the sheared colloidal-sphere suspension is similarly shown to exhibit an overall rapid increase with increasing shear rate. Structural rearrangements at varying shear rate points are again responsible for discontinuities in system properties.

Values of the shear rate dependent relative viscosity, η_r^*, have been estimated from Equation (3.5.1), which was also used to calculate the relative viscosity of the hard-sphere suspension. Flow curves at each system density appear in Figure 5.3.4, demonstrating that higher density systems are observed to undergo a shear thickening transition at lower shear rates. Barnes(119) has recently published a review of the experimental rheology literature concerning the shear thickening behaviour of dense suspensions. The general trends at varying values of suspended phase-volume are embodied in Figure 5.3.5, which has been reproduced from Reference (119). Decreasing vlaues of the 'critical' shear rate, corresponding to the onset of shear thickening as suspended phase-volume increases is in good qualitative agreement with the findings of the present work.

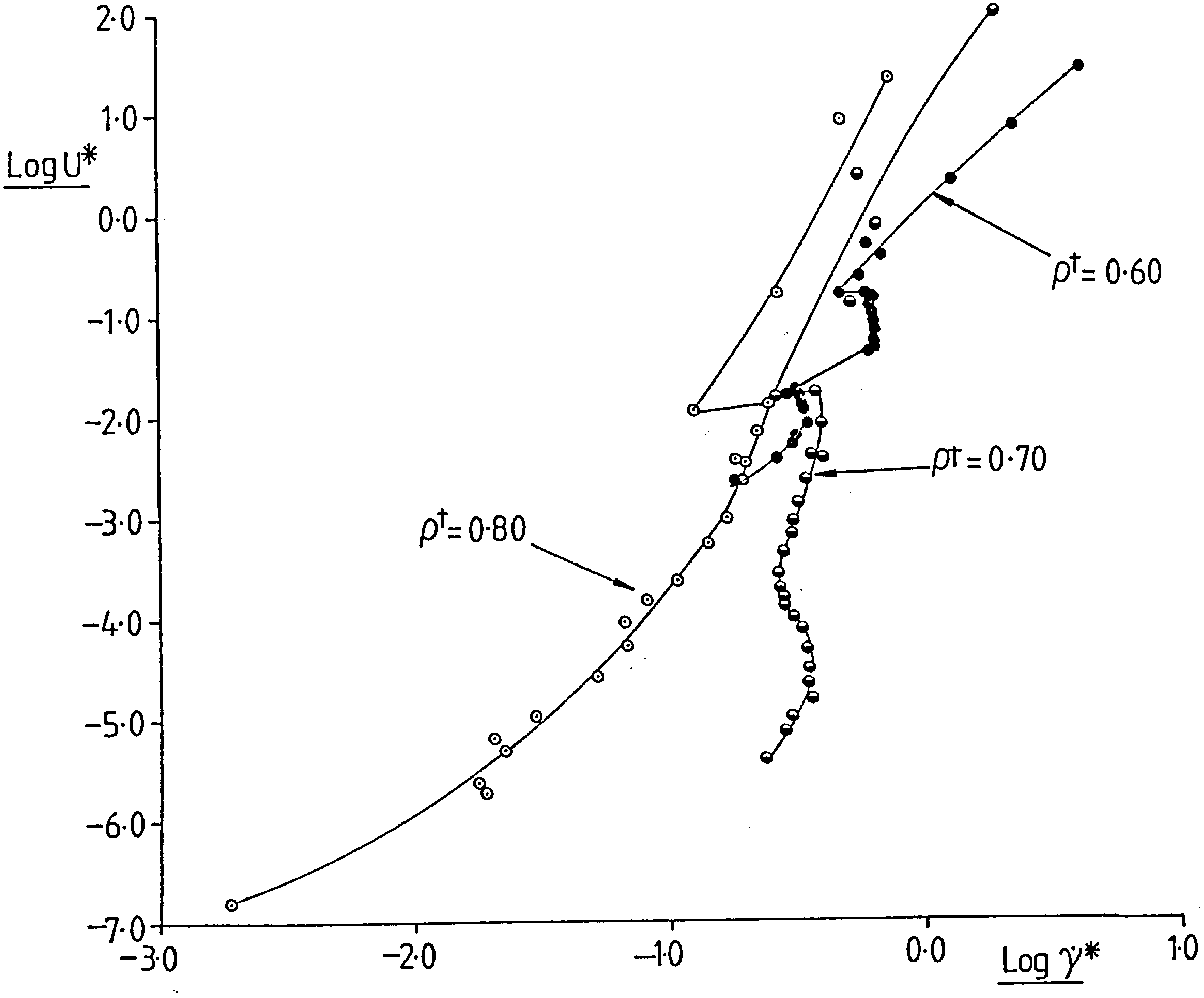

FIGURE 5.3.2: Total Osmotic Internal Energy of the Sheared Monodisperse Colloidal-Sphere Model Suspension

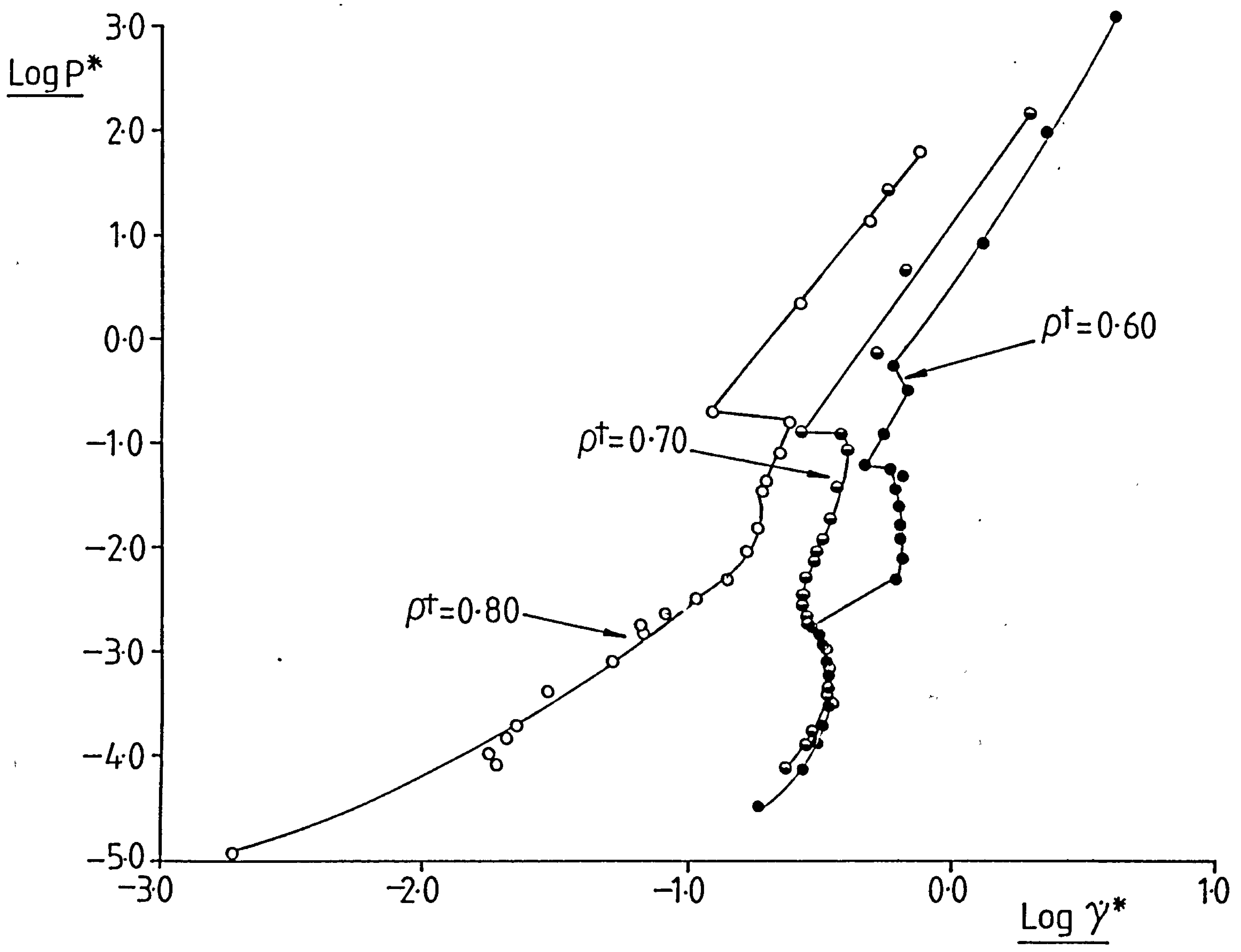

FIGURE 5.3.3: Osmotic Pressure of the Sheared Monodisperse Colloidal-Sphere Model Suspension

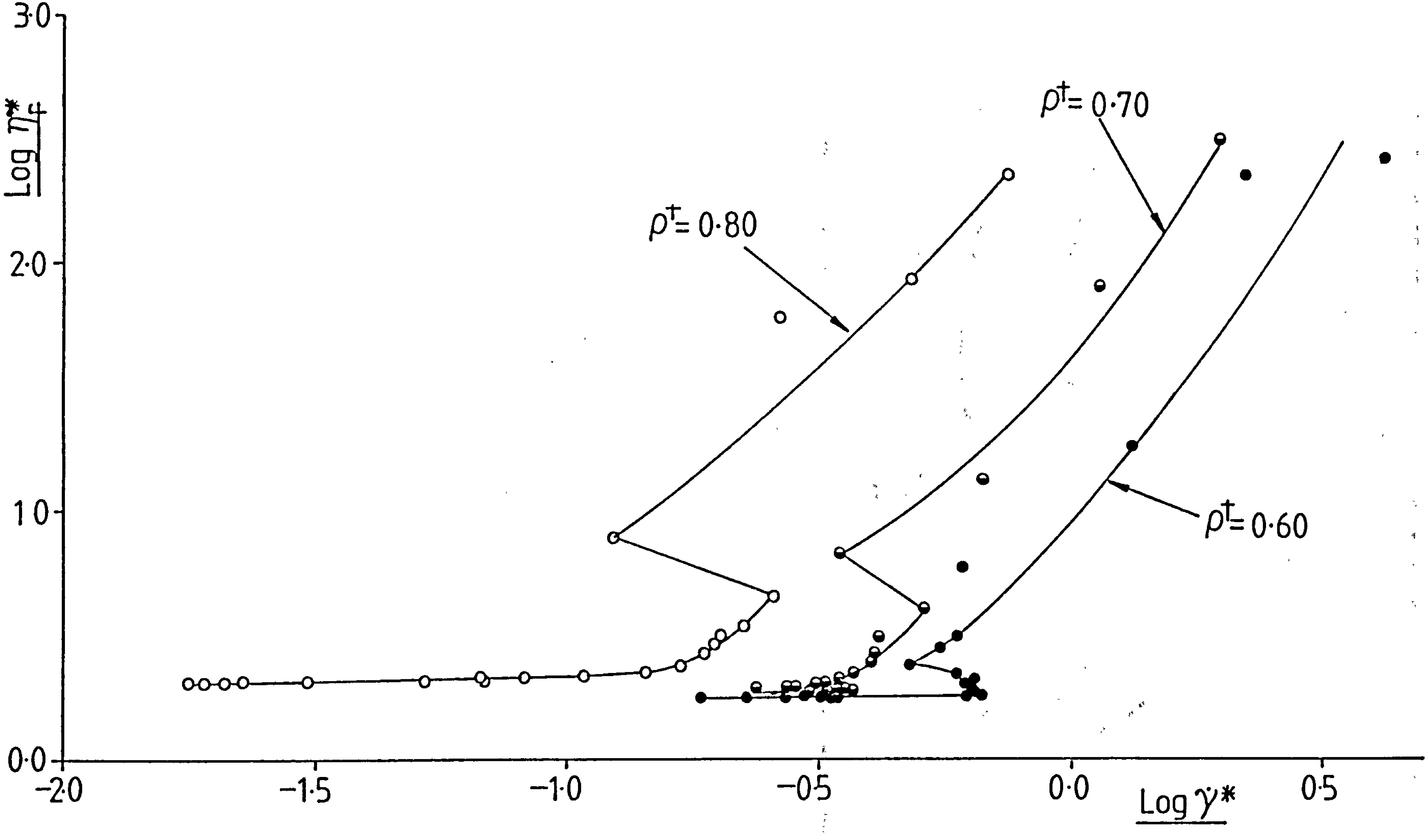

FIGURE 5.3.4: Relative Viscosity of the Sheared Monodisperse Colloidal-Sphere Model Suspension

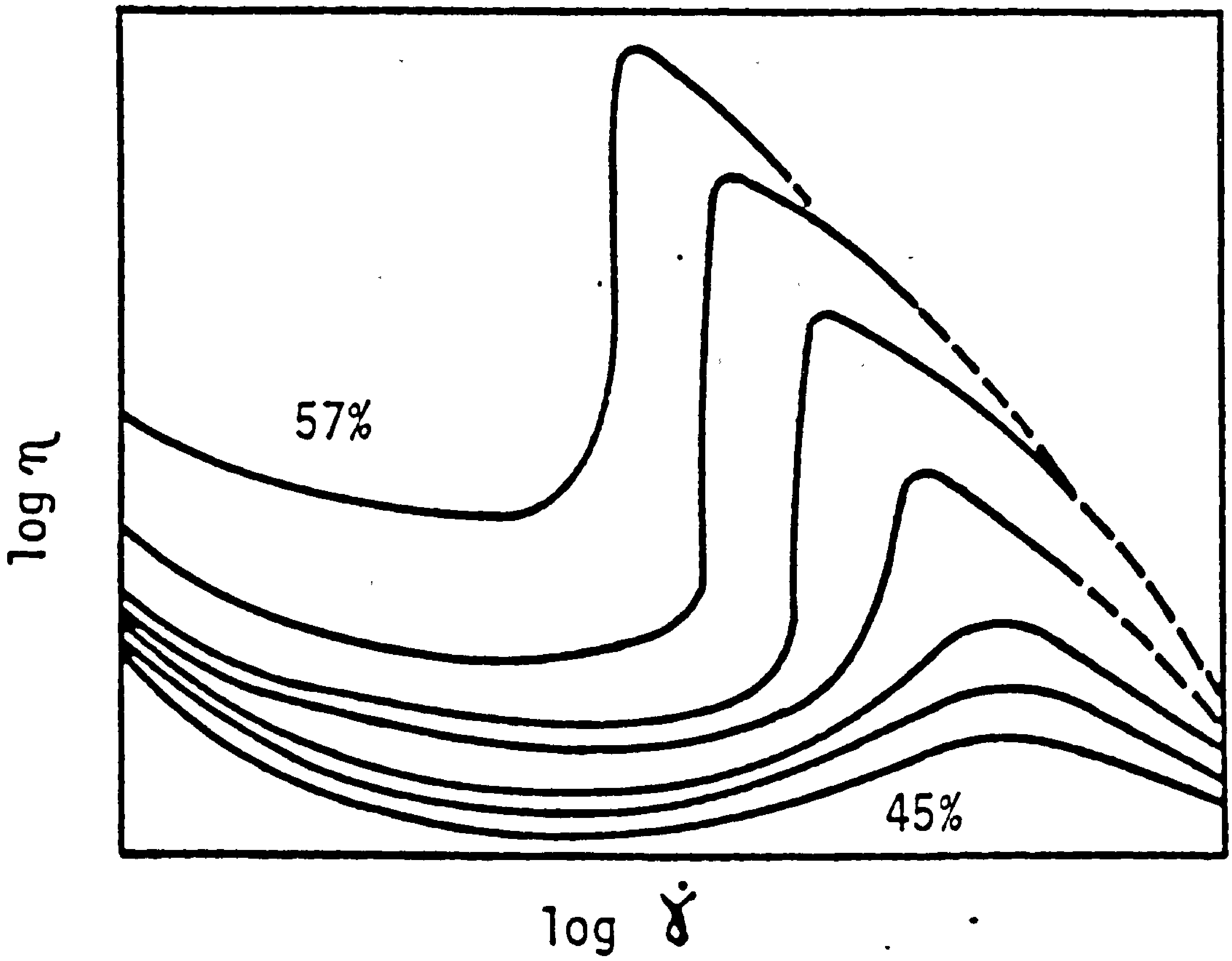

FIGURE 5.3.5: A Summary of the Experimentally Observed Shear Thickening Transition in Suspensions of Varying Packing Fraction (Reproduced from Reference (119)). A Qualitative Agreement with Figure 5.3.4 may be noted.

In order to illustrate the microstructure responsible for the properties of the sheared colloidal-sphere suspension presented in Figures 5.3.2 - 5.3.4, a set of orthogonal configurational plots of the systems at a reduced density $\rho^{+} = 0.70$ and differing shear rate points are presented in Figures 5.3.6 - 5.3.7. The highly ordered structure of the system at the lower end of the Stokesian shear rate range studied is demonstrated in Figure 5.3.6. The highly anisotropic nature of diffusivity and osmotic pressure shown by the hard-sphere suspension in this shear rate regime is equally applicable to the sheared colloidal-sphere suspension. Figure 5.3.7 shows this ordered structure to have been completely disrupted in the higher shear rate regime in Figures 5.3.2 - 5.3.4.

Hysteresis is commonly encountered in experimentally determined dense suspension flow curves due to the shear history dependence of dense suspension properties. A typical flow curve that might be obtained from an experimental study in which a cyclic shear rate is imposed upon the system is presented in Figure 5.3.8. The observed viscosity during the initial increasing shear rate period exhibits a lower value than during the subsequent period of decreasing shear rate. Figure 5.3.4 shows the existence of two viscosity branches corresponding to the ordered and disordered system microstructure illustrated in Figures 5.3.5 and 5.3.6 respectively. Metastability of the system around the discontinuity separating these viscosity branches provides a plausible explanation of flow curve hysteresis.

The effects of a narrow degree of polydispersity upon the shear behaviour of the colloidal-sphere suspension are represented in Figures 5.3.9 - 5.3.11. At higher Stokesian shear rates corresponding to an amorphous microstate, total osmotic internal energy and osmotic pressure is observed to be independent of the narrow degrees of polydispersity

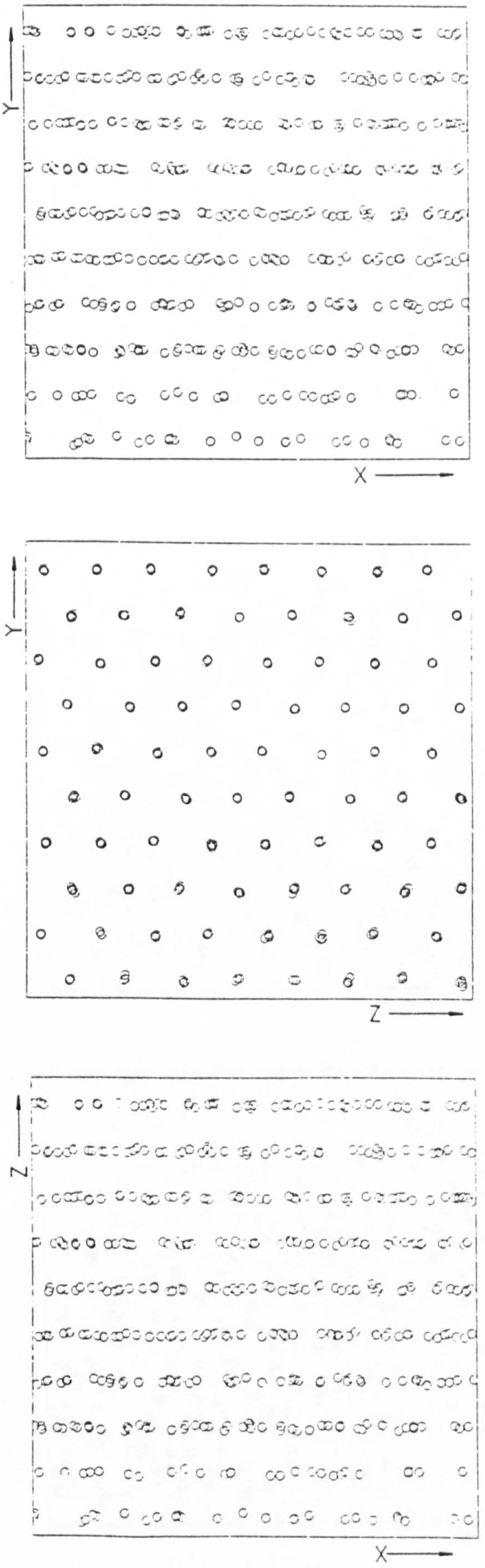

FIGURE 5.3.6: Configurational Plots of the Sheared Monodisperse Colloidal-Sphere Model Suspension with a Reduced Density $\rho^{+} = 0.60$ at a Shear Rate $\dot{\gamma}^{*} = 0.344$

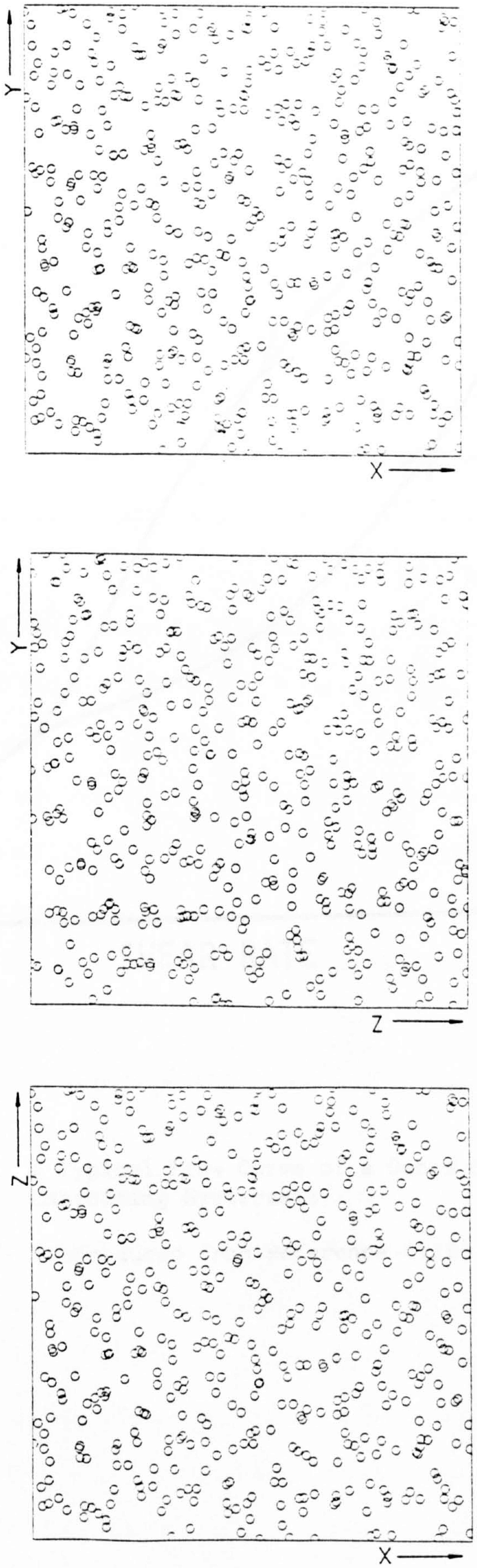

FIGURE 5.3.7: Configurational Plots of the Sheared Monodisperse Colloidal-Sphere Model Suspension with a Reduced Density $\rho^{\dagger} = 0.60$ at a Shear Rate $\dot{\gamma}^{*} = 0.612$

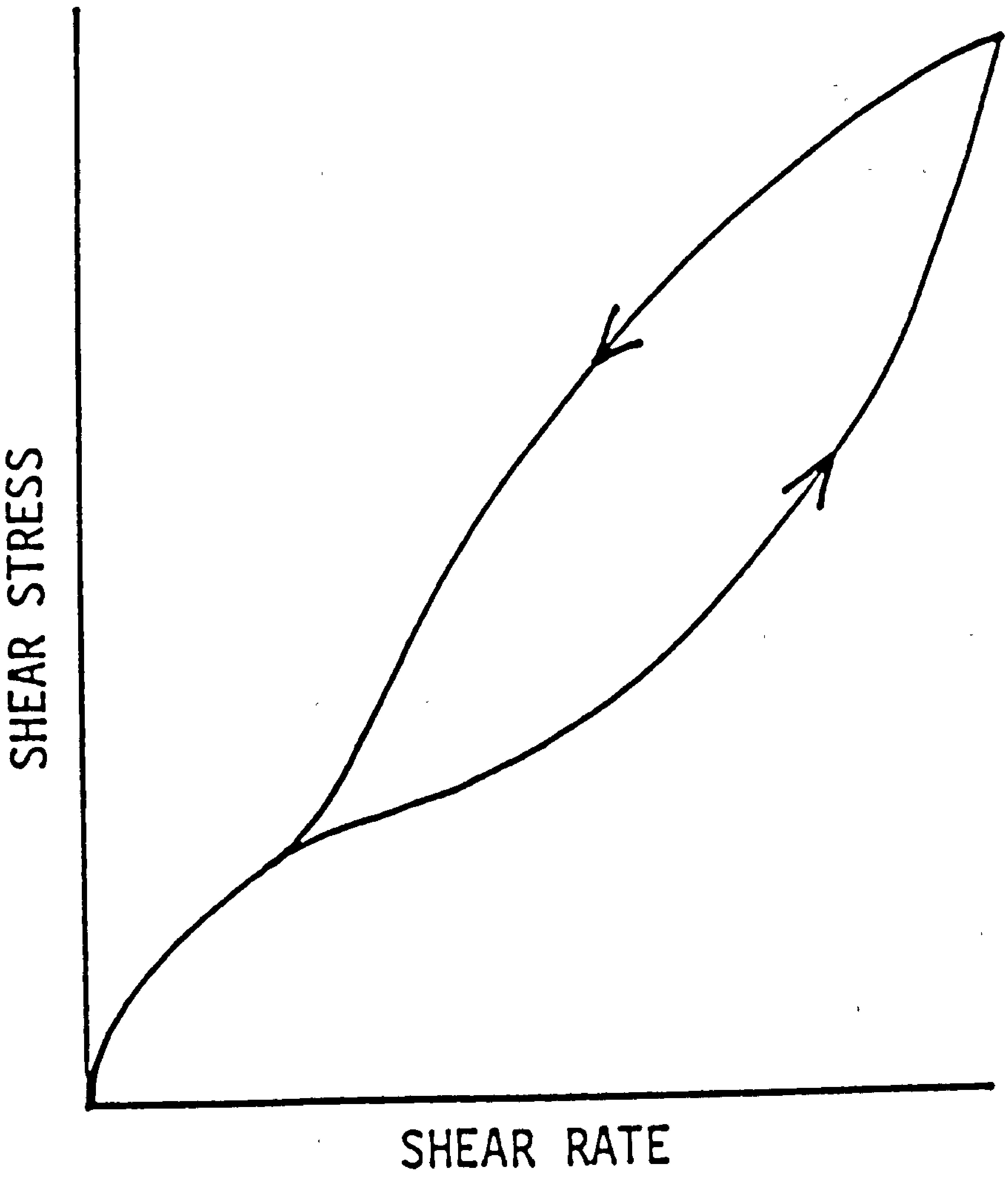

FIGURE 5.3.8: A Typical Flow Curve of a Dense Suspension Exhibiting Hysteresis

(Reproduced from Reference (119))

considered here. Only at the lower end of the Stokesian shear rate range do these system properties show significant differences; both properties increasing with polydispersity. This increase reflects the destabilization of the ordered microstructure as polydispersity increases.

The decreasing stability of the ordered state leads to a reduction in 'critical' shear rate with increasing polydispersity (Figure 5.3.11). Despite the considerable effort that has been expended towards the production of experimental monodisperse suspensions of colloidal particles, the synthesis of suspensions with levels of polydispersity much below the highest level considered here is not yet possible. Comparison of the behaviour shown in Figure 5.3.11 with experimental findings is consequently not possible as yet.

Computer simulation studies of any macroscopic phenomena must ultimately provide a quantitative agreement with any experimentally measurable properties of the material under scrutiny. The present work demonstrates the ability of particulate dynamics simulations to provide a qualitative description of many aspects of dense suspension rheology. Of critical importance in the scaling of the present results onto experimental data is a knowledge of the frictional forces opposing the translation of suspended particles. These frictional forces have been shown to determine the time scale for dynamical events and henceforth to dominate the behaviour of sheared solid-liquid suspensions.

Attempts to scale the results from non-equilibrium studies of the soft-sphere potential using Stokes equation to describe the damping of particle velocities have failed to map simulation data onto an experimental flow curve(65). The reasons behind the discrepancy are suspected to be largely attributable to the severe deviation of solvent viscosity when located in the interstices between suspended particles from the 'bulk' value substituted into Stokes' equation. Further complications will inevitably arise due to polydispersity, system size effects and deviation from particle sphericity.

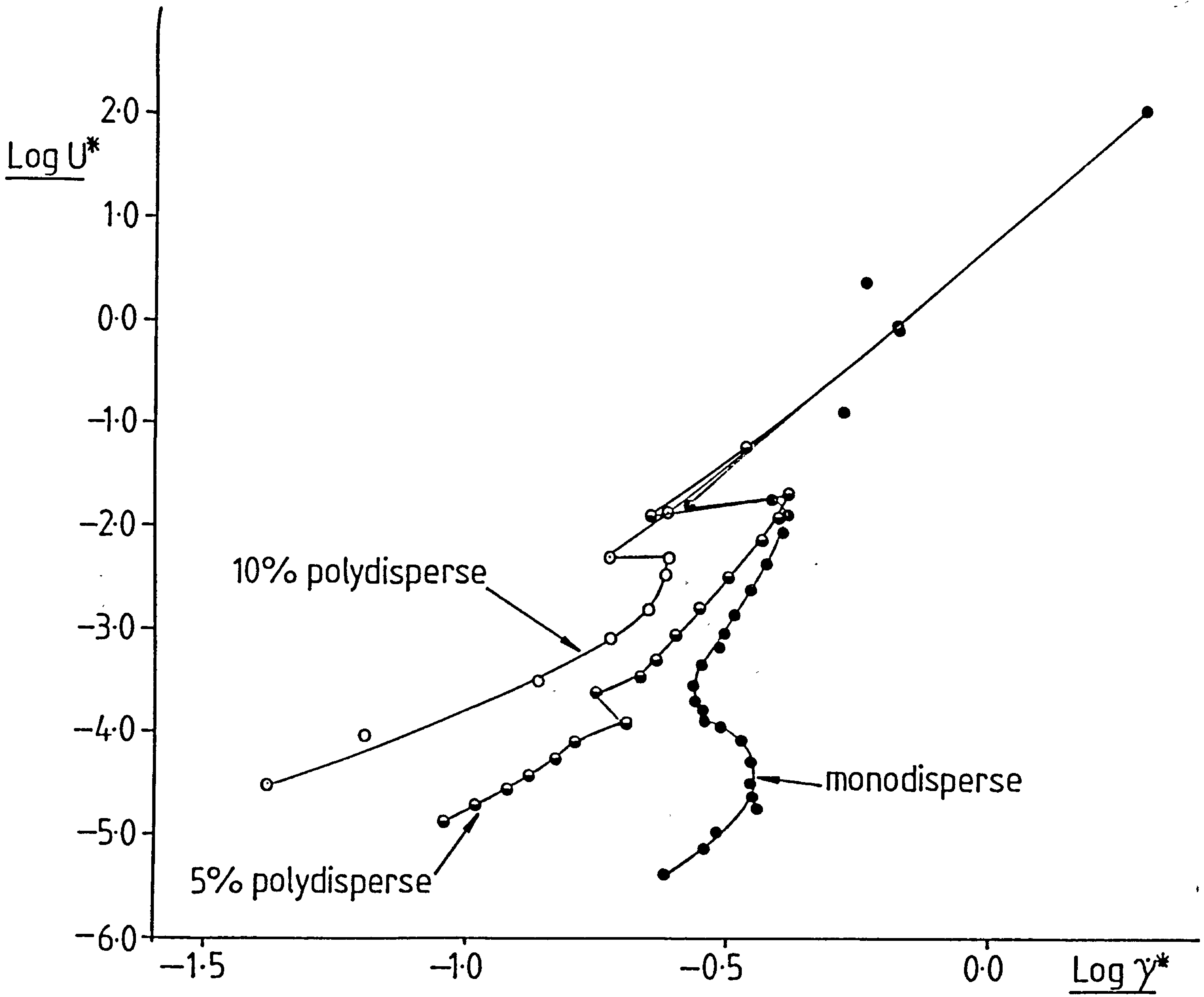

FIGURE 5.3.9: A Comparison of the Internal Energy Exhibited by Sheared Colloidal-Sphere Model Suspensions with Narrow Distributions of Particle Sizes. Each System has a Hard-Core Packing Fraction of y = 0.367.

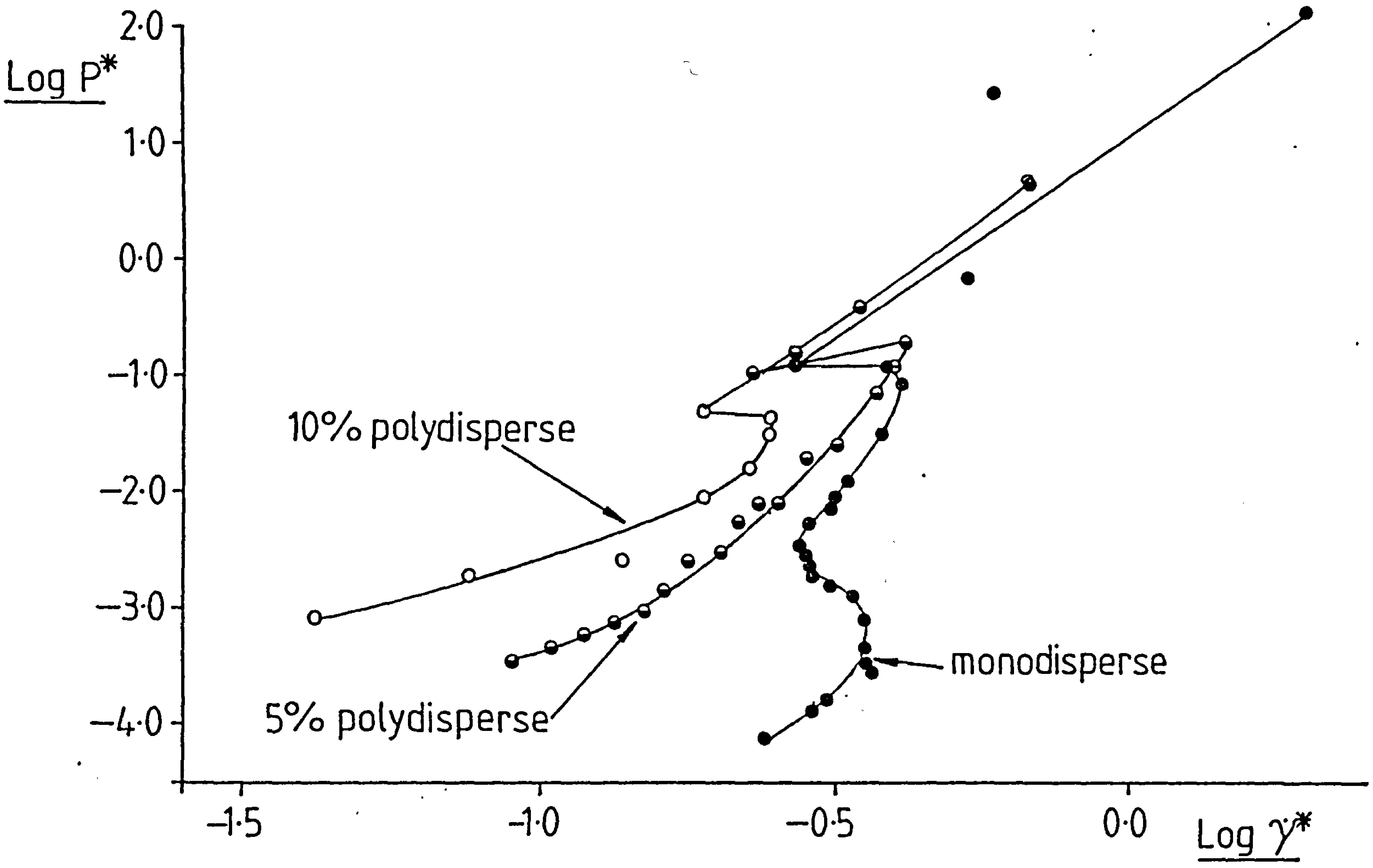

FIGURE 5.3.10: A Comparison of the Pressure Exhibited by Sheared Colloidal-Sphere Model Suspensions with Narrow Distributions of Particle Sizes. Each System has a Hard-Core Packing Fraction of 0.367.

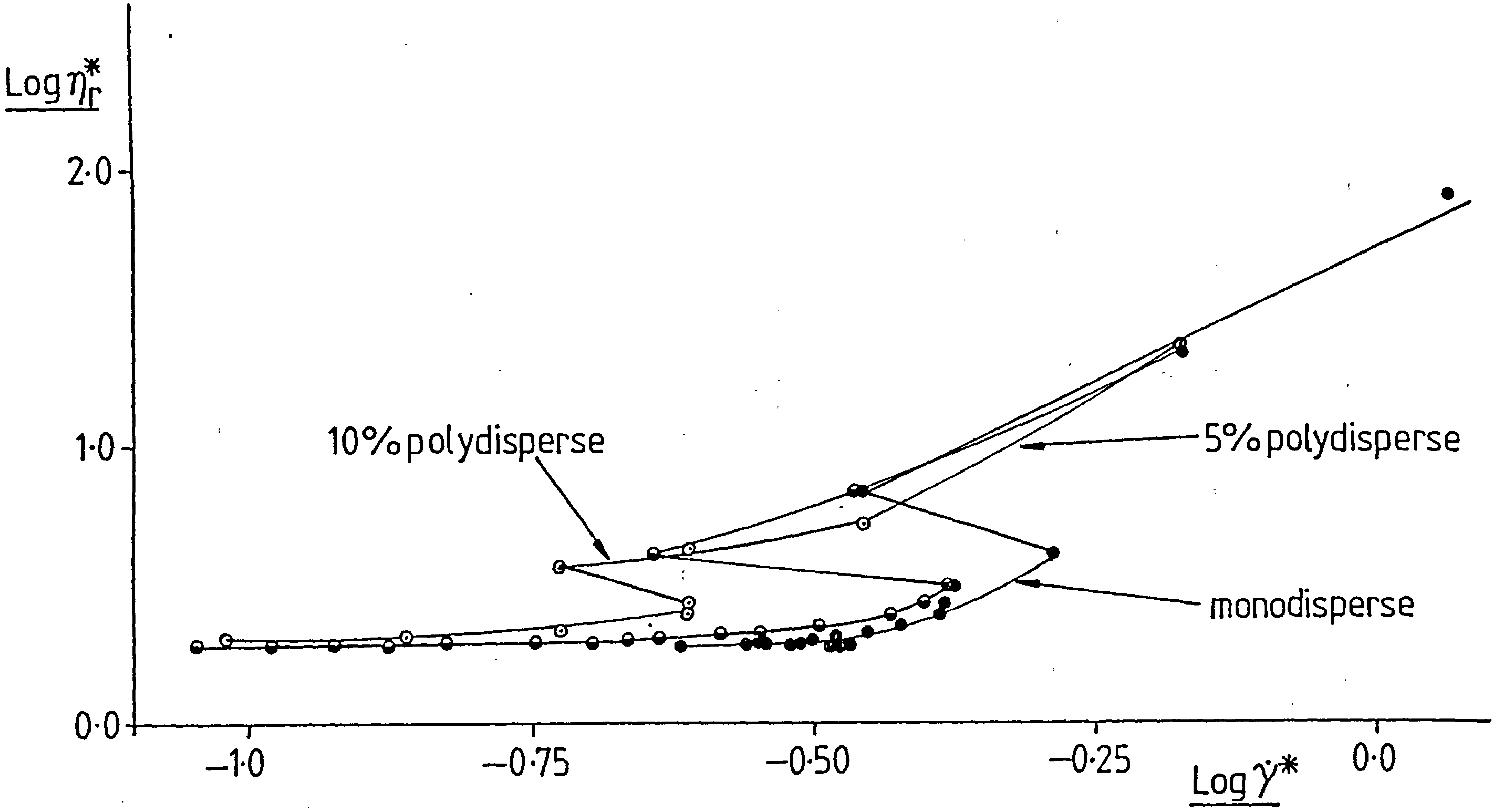

FIGURE 5.3.11: A Comparison of the Relative Viscosity Exhibited by Sheared Colloidal-Sphere Model Suspensions with Narrow Distributions of Particle Sizes. Each System has a Hard-Core Packing Fraction of 0.367.

TABLE 5.1.1

Monodisperse Non-Equilibrium Simulation Results

$N = 500;\ \rho^{\dagger} = 0.60$

$\dfrac{\dot{\gamma}}{\left[\dfrac{E_o}{m\sigma^2}\right]^{\frac{1}{2}}}$	$\dfrac{\phi}{E_o}$	$\dfrac{U}{E_o}$	$\dfrac{PV}{N\ E_o}$	$\dfrac{P_{xy}(K)}{\left[\dfrac{E_o}{\sigma^3}\right]}$	$\dfrac{P_{xy}(\phi)}{\left[\dfrac{E_o}{\sigma^3}\right]}$	$\dfrac{\eta}{\left[\dfrac{(mE_o)^{\frac{1}{2}}}{\sigma^2}\right]}$
0.0	0.166 (0.002)	1.666 (0.002)	8.00 (0.07)	-	-	-
0.25	0.170 (0.004)	1.670 (0.004)	8.14 (0.19)	- 0.042 (0.050)	- 0.312 (0.162)	1.816 (0.645)
0.50	0.174 (0.006)	1.674 (0.006)	8.31 (0.25)	- 0.035 (0.012)	- 0.756 (0.182)	1.582 (0.321)
1.0	0.186 (0.008)	1.686 (0.008)	8.64 (0.26)	- 0.073 (0.022)	- 1.509 (0.259)	1.582 (0.099)
2.0	0.201 (0.010)	1.701 (0.010)	9.24 (0.31)	- 0.099 (0.021)	- 2.773 (0.230)	1.436 (0.119)
3.0	0.219 (0.011)	1.719 (0.011)	10.43 (0.49)	- 0.155 (0.017)	- 2.421 (0.214)	0.859 (0.077)
4.0	0.225 (0.015)	1.725 (0.015)	10.80 (0.69)	- 0.202 (0.027)	- 3.025 (0.292)	0.807 (0.075)
5.0	0.243 (0.011)	1.743 (0.011)	11.65 (0.50)	- 0.236 (0.021)	- 3.493 (0.290)	0.746 (0.060)
6.0	0.207 (0.007)	1.707 (0.007)	10.10 (0.31)	- 0.218 (0.011)	- 2.730 (0.170)	0.491 (0.042)
7.0	0.198 (0.009)	1.698 (0.009)	9.73 (0.42)	- 0.221 (0.020)	- 2.550 (0.173)	0.396 (0.026)
8.0	0.204 (0.009)	1.704 (0.009)	10.11 (0.42)	- 0.221 (0.017)	- 2.650 (0.135)	0.359 (0.017)
10.0	0.208 (0.006)	1.708 (0.005)	10.32 (0.29)	- 0.215 (0.018)	- 2.573 (0.160)	0.279 (0.017)
12.5	0.216 (0.009)	1.716 (0.009)	10.80 (0.42)	- 0.198 (0.025)	- 2.562 (0.192)	0.221 (0.016)

continued ......

TABLE 5.1.1 continued ......

$\dfrac{\dot{\gamma}}{\left[\dfrac{E_0}{m\sigma^2}\right]^{\frac{1}{2}}}$	$\dfrac{\phi}{E_0}$	$\dfrac{U}{E_0}$	$\dfrac{PV}{N\,E_0}$	$\dfrac{P_{xy}(K)}{\left[\dfrac{E_0}{\sigma^3}\right]}$	$\dfrac{P_{xy}(\phi)}{\left[\dfrac{E_0}{\sigma^3}\right]}$	$\dfrac{\eta}{\left[\dfrac{(mE_0)^{\frac{1}{2}}}{\sigma^2}\right]}$
15.0	0.224 (0.009)	1.724 (0.009)	11.19 (0.41)	- 0.196 (0.015)	- 2.547 (0.167)	0.183 (0.011)
20.0	0.242 (0.016)	1.742 (0.016)	12.20 (0.75)	- 0.167 (0.030)	- 2.540 (0.247)	0.135 (0.013)
25.0	0.264 (0.020)	1.764 (0.020)	13.32 (0.97)	- 0.168 (0.043)	- 2.658 (0.328)	0.113 (0.014)
30.0	0.618 (0.023)	2.118 (0.023)	30.82 (1,17)	- 0.278 (0.008)	- 5.756 (0.343)	0.201 (0.012)
35.0	0.599 (0.019)	2.099 (0.019)	30.12 (0.96)	- 0.278 (0.014)	- 5.315 (0.287)	0.160 (0.008)
40.0	0.603 (0.016)	2.103 (0.016)	30.63 (0.86)	- 0.271 (0.011)	- 5.210 (0.278)	0.137 (0.007)
50.0	0.584 (0.014)	2.084 (0.014)	30.22 (0.75)	- 0.271 (0.013)	- 5.027 (0.210)	0.106 (0.004)
60.0	0.563 (0.020)	2.063 (0.020)	29.40 (1.09)	- 0.281 (0.022)	- 4.882 (0.277)	0.086 (0.006)
80.0	0.529 (0.034)	2.029 (0.034)	28.28 (1.70)	- 0.295 (0.039)	- 4.950 (0.300)	0.066 (0.004)
100.0	0.566 (0.040)	2.066 (0.040)	31.21 (2.89)	- 0.268 (0.050)	- 4.967 (0.831)	0.052 (0.011)
120.0	0.600 (0.041)	2.100 (0.041)	32.71 (2.37)	- 0.261 (0.025)	- 5.427 (0.690)	0.047 (0.006)
150.0	0.707 (0.038)	2.207 (0.038)	38.78 (2.34)	- 0.239 (0.030)	- 6.408 (1.009)	0.044 (0.006)
200.0	1.173 (0.149)	2.673 (0.149)	65.47 (10.91)	- 0.144 (0.051)	-10.070 (5.047)	0.051 (0.019)

TABLE 5.1.2

Monodisperse Non-Equilibrium Simulation Results

$N = 500;\ \rho^{\dagger} = 0.70$

$\dfrac{\dot{\gamma}}{\left[\dfrac{E_o}{m\sigma^2}\right]^{\frac{1}{2}}}$	$\dfrac{\Phi}{E_o}$	$\dfrac{U}{E_o}$	$\dfrac{PV}{N\ E_o}$	$\dfrac{P_{xy}(K)}{\left[\dfrac{E_o}{\sigma^3}\right]}$	$\dfrac{P_{xy}(\Phi)}{\left[\dfrac{E_o}{\sigma^3}\right]}$	$\dfrac{\eta}{\left[\dfrac{(mE_o)^{\frac{1}{2}}}{\sigma^2}\right]}$
0.0	0.259 (0.023)	1.759 (0.023)	12.60 (0.09)	-	-	-
0.25	0.287 (0.004)	1.787 (0.004)	13.11 (0.19)	- 0.021 (0.019)	- 1.027 (0.111)	4.192 (0.448)
0.50	0.300 (0.006)	1.800 (0.006)	13.69 (0.28)	- 0.037 (0.013)	- 1.767 (0.143)	3.608 (0.291)
1.0	0.335 (0.008)	1.835 (0.008)	15.19 (0.34)	- 0.068 (0.011)	- 3.048 (0.144)	3.116 (0.146)
2.0	0.434 (0.014)	1.934 (0.014)	15.40 (0.75)	- 0.147 (0.020)	- 3.812 (0.323)	1.980 (0.144)
3.0	0.520 (0.014)	2.020 (0.014)	23.46 (0.65)	- 0.179 (0.030)	- 7.623 (0.341)	2.601 (0.141)
4.0	0.418 (0.015)	1.918 (0.015)	19.12 (0.66)	- 0.208 (0.021)	- 5.195 (0.307)	1.351 (0.079)
5.0	0.404 (0.008)	1.904 (0.008)	18.59 (0.38)	- 0.252 (0.013)	- 4.818 (0.236)	1.014 (0.046)
6.0	0.408 (0.013)	1.908 (0.013)	18.89 (0.59)	- 0.255 (0.011)	- 4.867 (0.259)	0.854 (0.044)
8.0	0.461 (0.009)	1.961 (0.009)	21.39 (0.43)	- 0.295 (0.011)	- 5.295 (0.306)	0.699 (0.039)
10.0	0.486 (0.011)	1.986 (0.011)	22.69 (0.52)	- 0.313 (0.014)	- 5.626 (0.198)	0.594 (0.020)
12.5	0.558 (0.021)	2.058 (0.021)	26.17 (0.97)	- 0.314 (0.015)	- 6.068 (0.211)	0.511 (0.018)
15.0	0.630 (0.032)	2.130 (0.032)	29.66 (1.46)	- 0.297 (0.011)	- 6.326 (0.216)	0.442 (0.014)

continued ......

TABLE 5.1.2 continued ......

$\dfrac{\dot{\gamma}}{\left[\dfrac{E_o}{m\sigma^2}\right]^{\frac{1}{2}}}$	$\dfrac{\phi}{E_o}$	$\dfrac{U}{E_o}$	$\dfrac{PV}{N\,E_o}$	$\dfrac{P_{xy}(K)}{\left[\dfrac{E_o}{\sigma^3}\right]}$	$\dfrac{P_{xy}(\phi)}{\left[\dfrac{E_o}{\sigma^3}\right]}$	$\dfrac{\eta}{\left[\dfrac{(mE_o)}{\sigma^2}\right]^{\frac{1}{2}}}$
17.5	0.706 (0.030)	2.206 (0.030)	33.31 (1.41)	- 0.272 (0.007)	- 6.483 (0.308)	0.386 (0.018)
20.0	0.804 (0.032)	2.304 (0.032)	38.41 (1.88)	- 0.283 (0.029)	- 7.055 (0.276)	0.367 (0.015)
25.0	0.890 (0.019)	2.390 (0.019)	42.69 (0.88)	- 0.276 (0.007)	- 7.333 (0.103)	0.304 (0.004)
30.0	0.968 (0.017)	2.468 (0.017)	46.79 (0.83)	- 0.254 (0.007)	- 7.267 (0.210)	0.251 (0.007)
35.0	1.028 (0.022)	2.528 (0.022)	49.95 (1.09)	- 0.240 (0.010)	- 7.119 (0.328)	0.210 (0.009)
40.0	1.082 (0.028)	2.582 (0.028)	52.87 (1.54)	- 0.227 (0.010)	- 6.998 (0.174)	0.181 (0.007)
50.0	1.161 (0.164)	2.661 (0.164)	57.05 (0.78)	- 0.199 (0.007)	- 6.574 (0.159)	0.135 (0.003)
60.0	1.161 (0.147)	2.661 (0.147)	58.02 (1.18)	- 0.193 (0.010)	- 6.058 (0.281)	0.104 (0.004)
80.0	1.146 (0.057)	2.646 (0.057)	57.51 (3.81)	- 0.208 (0.025)	- 5.745 (0.435)	0.074 (0.005)
100.0	1.055 (0.032)	2.555 (0.032)	52.97 (1.75)	- 0.255 (0.026)	- 5.664 (0.494)	0.059 (0.005)
120.0	1.097 (0.067)	2.597 (0.067)	55.60 (3.82)	- 0.232 (0.051)	- 5.682 (0.670)	0.049 (0.006)
140.0	1.170 (0.037)	2.670 (0.037)	59.80 (2.13)	- 0.176 (0.034)	- 5.581 (0.831)	0.041 (0.006)
150.0	1.153 (0.085)	2.653 (0.085)	59.28 (4.83)	- 0.260 (0.065)	- 6.645 (0.967)	0.046 (0.007)
175.0	1.332 (0.103)	2.832 (0.103)	68.95 (6.42)	- 0.171 (0.073)	- 7.105 (2.023)	0.042 (0.017)
200.0	1.457 (0.096)	2.977 (0.096)	77.25 (6.94)	- 0.146 (0.050)	- 8.570 (3.020)	0.044 (0.015)

TABLE 5.1.3

Monodisperse Non-Equilibrium Simulation Results

$N = 500;\ \rho^{+} = 0.80$

$\dfrac{\dot{\gamma}}{\left[\dfrac{E_o}{m\sigma^2}\right]^{\frac{1}{2}}}$	$\dfrac{\phi}{E_o}$	$\dfrac{U}{E_o}$	$\dfrac{PV}{N\,E_o}$	$\dfrac{P_{xy}(K)}{\left[\dfrac{E_o}{\sigma^3}\right]}$	$\dfrac{P_{xy}(\phi)}{\left[\dfrac{E_o}{\sigma^3}\right]}$	$\dfrac{\eta}{\left[\dfrac{(mE_o)^{\frac{1}{2}}}{\sigma^2}\right]}$
0.0	0.373 (0.004)	1.873 (0.004)	17.25 (0.15)	-	-	-
0.25	0.597 (0.013)	2.097 (0.013)	26.44 (0.57)	- 0.007 (0.004)	- 3.036 (0.185)	12.172 (1.407)
0.50	0.675 (0.014)	2.175 (0.014)	29.85 (0.60)	- 0.023 (0.010)	- 4.893 (0.244)	9.832 (0.498)
1.0	0.870 (0.020)	2.370 (0.202)	38.44 (0.90)	- 0.041 (0.006)	- 8.837 (0.324)	8.878 (0.3 5)
2.0	1.424 (0.083)	2.924 (0.083)	63.66 (3.82)	- 0.089 (0.009)	-18.844 (1.470)	9.467 (0.735)
3.0	0.598 (0.031)	2.098 (0.031)	26.96 (1.32)	- 0.257 (0.119)	- 8.980 (0.194)	3.079 (0.065)
4.0	0.701 (0.029)	2.201 (0.029)	32.43 (1.84)	- 0.303 (0.030)	-10.155 (0.433)	2.615 (0.109)
5.0	0.741 (0.032)	2.241 (0.032)	33.69 (1.49)	- 0.417 (0.020)	-11.421 (0.716)	2.368 (0.132)
6.0	0.814 (0.031)	2.314 (0.031)	37.15 (1.38)	- 0.437 (0.017)	-12.303 (0.450)	2.123 (0.074)
8.0	0.952 (0.035)	2.452 (0.035)	43.91 (1.61)	- 0.470 (0.022)	-13.793 (0.494)	1.783 (0.086)
10.0	1.188 (0.035)	2.688 (0.035)	55.10 (1.61)	- 0.502 (0.024)	-16.035 (0.556)	1.654 (0.056)
12.5	1.646 (0.053)	3.146 (0.053)	77.65 (2.62)	- 0.499 (0.014)	-21.490 (0.978)	1.759 (0.078)
15.0	2.327 (0.159)	3.827 (0.159)	112.12 (7.73)	- 0.485 (0.016)	-28.518 (0.968)	1.934 (0.064)

TABLE 5.1.3 continued ......

$\frac{\dot{\gamma}}{\left[\frac{E_o}{m\sigma^2}\right]^{\frac{1}{2}}}$	$\frac{\Phi}{E_o}$	$\frac{U}{E_o}$	$\frac{PV}{N\,E_o}$	$\frac{P_{xy}(K)}{\left[\frac{E_o}{\sigma^3}\right]}$	$\frac{P_{xy}(\Phi)}{\left[\frac{E_o}{\sigma^3}\right]}$	$\frac{\eta}{\left[\frac{(mE_o)^{\frac{1}{2}}}{\sigma^2}\right]}$
17.5	3.133 (0.211)	4.633 (0.211)	152.68 (10.54)	- 0.445 (0.008)	- 34.913 (1.669)	2.020 (0.096)
20.0	3.156 (0.103)	4.656 (0.103)	155.01 (5.29)	- 0.421 (0.009)	- 34.365 (1.263)	1.739 (0.063)
25.0	4.771 (0.405)	6.271 (0.405)	241.75 (21.30)	- 0.373 (0.021)	- 45.310 (2.006)	1.827 (0.080)
30.0	9.318 (0.447)	10.818 (0.447)	496.72 (25.50)	- 0.306 (0.011)	- 78.726 (3.447)	2.619 (0.115)
40.0	13.396 (0.996)	14.896 (0.996)	736.64 (59.00)	- 0.252 (0.011)	-104.591 (7.557)	2.621 (0.196)
50.0	19.123 (0.210)	20.623 (0.210)	1087.4 (73.3)	- 0.208 (0.008)	-114.911 (4.576)	2.302 (0.092)
60.0	25.723 (1.759)	27.223 (1.759)	1503.1 (115.5)	- 0.162 (0.009)	-134.726 (6.856)	2.248 (0.114)
70.0	24.681 (1.943)	26.181 (1.943)	1432.2 (119.4)	- 0.152 (0.020)	-126.467 (9.718)	1.809 (0.142)
75.0	242.62 (50.16)	244.12 (50.16)	17502 (3980)	- 0.378 (0.037)	- 1242 (56.00)	16.56 (0.87)

TABLE 5.1.4

Monodisperse Non-Equilibrium Simulation Results

$N = 256;\ \rho^{\dagger} = 0.70$

$\frac{\dot{\gamma}}{\left[\frac{E_o}{m\sigma^2}\right]^{\frac{1}{2}}}$	$\frac{\phi}{E_o}$	$\frac{U}{E_o}$	$\frac{PV}{N E_o}$	$\frac{P_{xy}(K)}{\left[\frac{E_o}{\sigma^3}\right]}$	$\frac{P_{xy}(\phi)}{\left[\frac{E_o}{\sigma^3}\right]}$	$\frac{\eta}{\left[\frac{(mE_o)^{\frac{1}{2}}}{\sigma^2}\right]}$
0	0.274 (0.005)	1.774 (0.005)	12.57 (0.21)	-	-	-
0.5	0.305 (0.006)	1.805 (0.006)	13.89 (0.27)	- 0.032 (0.009)	- 1.789 (0.145)	3.642 (0.209)
1.0	0.343 (0.008)	1.843 (0.008)	15.50 (0.34)	- 0.069 (0.009)	- 3.153 (0.210)	3.222 (0.205)
2.0	0.404 (0.028)	1.904 (0.028)	18.29 (1.24)	- 0.125 (0.011)	- 5.157 (0.659)	2.641 (0.332)
5.0	0.319 (0.008)	1.819 (0.008)	14.97 (0.38)	- 0.208 (0.027)	- 3.487 (0.169)	0.739 (0.036)
10.0	0.637 (0.048)	2.137 (0.048)	29.58 (2.20)	- 0.324 (0.027)	- 7.218 (0.651)	0.754 (0.066)
20.0	0.834 (0.063)	2.334 (0.063)	39.70 (3.02)	- 0.268 (0.019)	- 7.183 (0.431)	0.373 (0.022)
50.0	1.095 (0.087)	2.595 (0.087)	53.52 (4.11)	- 0.190 (0.045)	- 5.947 (0.389)	0.123 (0.008)
100.0	1.641 (0.134)	3.141 (0.134)	81.83 (7.08)	- 0.111 (0.036)	- 5.392 (0.055)	0.055 (0.010)

TABLE 5.1.5

Monodisperse Non-Equilibrium Simulation Results

$N = 864;\ \rho^{+} = 0.70$

$\dfrac{\dot{\gamma}}{\left[\frac{E_o}{m\sigma^2}\right]^{\frac{1}{2}}}$	$\dfrac{\phi}{E_o}$	$\dfrac{U}{E_o}$	$\dfrac{PV}{N\,E_o}$	$\dfrac{P_{xy}(K)}{\left[\frac{E_o}{\sigma^3}\right]}$	$\dfrac{P_{xy}(\phi)}{\left[\frac{E_o}{\sigma^3}\right]}$	$\dfrac{\eta}{\left[\frac{(mE_o)^{\frac{1}{2}}}{\sigma^2}\right]}$
0.0	0.273 (0.003)	1.773 (0.003)	12.51 (0.13)	-	-	-
0.5	0.300 (0.006)	1.800 (0.006)	13.69 (0.25)	- 0.330 (0.010)	- 1.726 (0.104)	4.112 (0.214)
1.0	0.341 (0.006)	1.841 (0.006)	15.44 (0.26)	- 0.698 (0.010)	- 3.182 (0.125)	3.880 (0.135)
2.0	0.435 (0.016)	1.935 (0.016)	19.64 (0.69)	- 0.126 (0.010)	- 5.787 (0.296)	2.957 (0.150)
5.0	0.317 (0.008)	1.817 (0.008)	14.67 (0.36)	- 0.136 (0.007)	- 3.168 (0.066)	0.661 (0.014)
10.0	0.350 (0.010)	1.850 (0.010)	16.38 (0.45)	- 0.148 (0.023)	- 3.409 (0.133)	0.356 (0.015)
20.0	0.491 (0.032)	1.991 (0.032)	23.11 (1.47)	- 0.116 (0.024)	- 3.678 (0.238)	0.190 (0.012)
50.0	565.4 (93.8)	566.9 (93.8)	43307 (7723)	- 0.358 (0.046)	- 13724 (3093)	274.5 (61.8)

TABLE 5.2.1

5% Polydisperse Non-Equilibrium Simulation Results

N = 500

$\frac{\dot{\gamma}}{\left[\frac{E_o}{m\bar{\sigma}^2}\right]^{\frac{1}{2}}}$	$\frac{\phi}{E_o}$	$\frac{U}{E_o}$	$\frac{PV}{N E_o}$	$\frac{P_{xy}(K)}{\left[\frac{E_o}{\bar{\sigma}^3}\right]}$	$\frac{P_{xy}(\phi)}{\left[\frac{E_o}{\bar{\sigma}^3}\right]}$	$\frac{\eta}{\left[\frac{(mE_o)^{\frac{1}{2}}}{\bar{\sigma}^2}\right]}$
0.0	0.274 (0.010)	1.774 (0.010)	12.61 (0.16)	-	-	-
1.0	0.336 (0.016)	1.836 (0.016)	15.26 (0.67)	- 0.072 (0.011)	- 3.049 (0.278)	3.121 (0.277)
2.0	0.434 (0.023)	1.934 (0.023)	19.34 (0.23)	- 0.118 (0.015)	- 5.939 (0.564)	3.029 (0.284)
3.0	0.594 (0.033)	2.094 (0.033)	26.86 (1.47)	- 0.167 (0.024)	- 9.073 (0.708)	3.080 (0.236)
4.0	0.374 (0.044)	1.874 (0.044)	18.45 (0.74)	- 0.174 (0.027)	- 4.843 (0.299(	1.254 (0.076)
5.0	0.408 (0.011)	1.908 (0.011)	18.88 (0.49)	- 0.236 (0.023)	- 4.984 (0.232)	1.044 (0.049)
6.0	0.430 (0.008)	1.930 (0.008)	20.04 (0.38)	- 0.277 (0.016)	- 5.371 (0.170)	0.941 (0.030)
8.0	0.487 (0.012)	1.987 (0.012)	23.11 (1.36)	- 0.320 (0.017)	- 6.239 (0.221)	0.820 (0.028)
10.0	0.537 (0.010)	2.037 (0.010)	25.53 (0.47)	- 0.341 (0.013)	- 7.086 (0.200)	0.743 (0.021)
12.5	0.612 (0.009)	2.112 (0.009)	29.39 (0.45)	- 0.345 (0.007)	- 7.924 (0.147)	0.662 (0.012)
15.0	0.681 (0.011)	2.181 (0.011)	32.96 (0.54)	- 0.350 (0.011)	- 8.629 (0.217)	0.599 (0.015)
17.5	0.751 (0.018)	2.251 (0.018)	36.67 (0.92)	- 0.353 (0.014)	- 9.344 (0.333)	0.554 (0.019)

continued ......

TABLE 5.2.1 continued ......

$\dfrac{\dot{\gamma}}{\left[\dfrac{E_o}{m\bar{\sigma}^2}\right]^{\frac{1}{2}}}$	$\dfrac{\phi}{E_o}$	$\dfrac{U}{E_o}$	$\dfrac{PV}{N\,E_o}$	$\dfrac{P_{xy}(K)}{\left[\dfrac{E_o}{\bar{\sigma}^3}\right]}$	$\dfrac{P_{xy}(\phi)}{\left[\dfrac{E_o}{\bar{\sigma}^3}\right]}$	$\dfrac{\eta}{\left[\dfrac{(mE_o)^{\frac{1}{2}}}{\bar{\sigma}^2}\right]}$
20.0	0.847 (0.024)	2.347 (0.024)	41.59 (1.20)	- 0.332 (0.012)	- 9.989 (0.346)	0.516 (0.017)
25.0	1.009 (0.023)	2.509 (0.023)	50.30 (1.16)	- 0.324 (0.015)	-11.400 (0.253)	0.469 (0.010)
30.0	1.212 (0.054)	2.712 (0.054)	67.23 (2.81)	- 0.316 (0.016)	-12.672 (0.721)	0.433 (0.023)
35.0	1.454 (0.062)	2.954 (0.062)	73.50 (3.37)	- 0.290 (0.014)	-13.710 (0.839)	0.400 (0.024)
40.0	1.887 (0.062)	3.387 (0.062)	95.87 (3.32)	- 0.264 (0.013)	-15.541 (0.505)	0.395 (0.013)
45.0	2.331 (0.162)	3.831 (0.162)	118.96 (9.12)	- 0.248 (0.028)	-17.368 (2.133)	0.391 (0.048)
50.0	2.816 (0.309)	4.316 (0.309)	145.31 (18.14)	- 0.218 (0.039)	-19.719 (3.803)	0.399 (0.076)
55.0	3.520 (0.414)	5.020 (0.414)	184.20 (23.24)	- 0.204 (0.038)	-23.121 (3.596)	0.424 (0.066)
60.0	154.5 (33.9)	156.0 (33.9)	10907 (2611)	- 0.269 (0.038)	- 2430 (703)	40.50 (11.73)

TABLE 5.2.2

10% Polydisperse Non-Equilibrium Simulation Results

N = 500

$\dfrac{\dot{\gamma}}{\left[\dfrac{E_o}{m\bar{\sigma}^2}\right]^{\frac{1}{2}}}$	$\dfrac{\phi}{E_o}$	$\dfrac{U}{E_o}$	$\dfrac{PV}{N\,E_o}$	$\dfrac{P_{xy}(K)}{\left[\dfrac{E_o}{\bar{\sigma}^3}\right]}$	$\dfrac{P_{xy}(\phi)}{\left[\dfrac{E_o}{\bar{\sigma}^3}\right]}$	$\dfrac{\eta}{\left[\dfrac{(mE_o)^{\frac{1}{2}}}{\bar{\sigma}^2}\right]}$
0.0	0.273 (0.008)	1.773 (0.008)	12.57 (0.20)	-	-	-
1.0	0.331 (0.013)	1.831 (0.013)	15.151 (0.576)	- 0.066 (0.014)	- 3.049 (0.260)	3.115 (0.271)
2.0	0.426 (0.025)	1.926 (0.025)	19.428 (1.129)	- 0.128 (0.027)	- 5.871 (0.522)	3.000 (0.261)
3.0	0.551 (0.045)	2.051 (0.045)	25.093 (2.039)	- 0.170 (0.021)	- 8.369 (0.926)	2.846 (0.308)
4.0	0.719 (0.045)	2.219 (0.045)	32.885 (2.107)	- 0.203 (0.016)	-10.998 (0.812)	2.800 (0.204)
5.0	0.551 (0.027)	2.051 (0.027)	25.60 (1.24)	- 0.239 (0.020)	- 8.284 (0.594)	1.705 (0.118)
6.0	0.578 (0.036)	2.078 (0.036)	27.16 (1.64)	- 0.269 (0.015)	- 8.336 (0.519)	1.434 (0.087)
8.0	0.631 (0.037)	2.131 (0.037)	29.99 (1.76)	- 0.298 (0.014)	- 9.009 (0.526)	1.163 (0.066)
10.0	0.760 (0.039)	2.260 (0.039)	36.60 (1.88)	- 0.325 (0.017)	-10.739 (0.469)	1.106 (0.047)
12.5	1.101 (0.054)	2.601 (0.054)	33.66 (2.72)	- 0.343 (0.009)	-14.946 (0.724)	1.223 (0.058)
15.0	2.077 (0.189)	3.577 (0.189)	104.18 (10.23)	- 0.343 (0.016)	-27.252 (2.635)	1.840 (0.176)
17.5	3.837 (0.513)	5.337 (0.513)	200.16 (28.45)	- 0.322 (0.020)	-49.841 (2.869)	2.866 (0.412)

CHAPTER 6

SUMMARY, MAIN CONCLUSIONS AND RECOMMENDATIONS FOR FUTURE STUDIES

CHAPTER 6

SUMMARY, MAIN CONCLUSIONS AND RECOMMENDATIONS FOR FUTURE STUDIES

The research reported in the preceding chapters of this thesis has been aimed at the investigation of the properties of dense solid/liquid suspensions. Of particular interest is the behaviour under the effects of a velocity gradient, i.e. the rheological properties of these systems. The technological importance of dense suspensions, coupled with the great wealth of commonly encountered behaviour has led to a sustained research effort spanning many decades. A brief summary of some of the more important milestones in the development of experimental rheology has been presented in Section 1.2. Despite this immense research effort, experimental investigations have not, as yet been able to provide a full explanation for the plethora of experimentally observed suspension rheology. A completely different approach has been adopted in the present study, however. Rheological properties of simplified model systems embodying the essential features of solid/liquid suspensions have been studied through the use of computational particulate dynamics simulation techniques. These techniques are based upon molecular dynamics simulations, whose popularity has increased dramatically in recent years as a means of investigating experimentally inaccessible phenomena. A survey of the relevant molecular dynamics literature comprises Section 1.3. The basic strategy underlying all the simulations described herein has been to restrict the complexity of the model systems as far as possible. A study of the properties of these simplified systems has been shown to provide a unique insight into the corresponding behaviour of experimental systems.

Initial studies focussed upon systems of particles interacting through the classical hard-sphere potential. The shear rate dependent behaviour under conditions of constant kinetic energy has been studied using the discontinuous peculiar velocity rescaling technique originally described by Erpenbeck(68). New data is presented for hard-sphere systems over the reduced density range $\rho^{+} = 0.80 - 1.10$, corresponding to either side of order-disorder phase transition. At low shear rates the viscosity of the isokinetic hard-sphere systems at densities corresponding to the fluid side of the phase transition ($\rho^{+} = 0.80, 0.90$) are shown to obey a square root shear rate relationship. Estimates of the zero shear viscosity at these densities, obtained through the extrapolation of this square root relationship are found to be in excellent agreement with the previously published data of Alder, Gass and Wainwright(55). At higher densities, the viscosity is observed to increase rapidly at vanishing shear rate, reminiscent of a solid-like response to a small shear stress.

At higher shear rates the isokinetic hard-sphere model has been observed to exhibit strongly non-linear behaviour. Similar non-linear behaviour exhibited by the sheared isokinetic soft-sphere model(4) has been explained in terms of a shear-induced perturbation of the equilibrium phase behaviour. Resolution of the kinetic energy, diffusivity and pressure of the sheared isokinetic hard-sphere model into orthogonal contributions reveals large normal differences in these system properties. Further evidence of this shear-induced anisotropy is presented in the form of snapshot configurational plots as viewed from mutually perpendicular viewpoints. The sheared system is clearly shown to have adopted a structured arrangement. In order to facilitate the imposed shear gradient, particles are arranged in strings parallel to the direction of flow. Diffusivity normal to the direction of flow is reduced drastically in this regime.

The kinetic energy shear-rate scaling behaviour of the isokinetic hard-sphere model is used in order to make qualitative predictions concerning the shear rate dependent behaviour of the model hard-sphere suspension. An important consequence of this scaling behaviour is that the high shear rate behaviour of the isokinetic hard-sphere system maps onto the low shear rate region of the model hard-sphere suspension and vice versa. Consequently, the non-linear behaviour observed in this and other isokinetic studies(4,77) corresponds to the shear thickening transition commonly exhibited by dense suspensions at high shear rates(119).

Further studies have focussed upon a system of particles interacting through a novel interparticle potential comprising a repulsive skin originating at the surface of a hard-spherical core. This repulsive skin is meant to represent the slightly soft interactions resulting from diffuse, solvated or stabilizer layers found at the surface of real colloidal particles. When expressed as a function of 'effective hard-sphere density' to allow for the density contribution from the repulsive skin, the fluid branch of this 'colloidal-sphere' model equilibrium behaviour is accurately represented by that of the hard-sphere model. A simple expression relating adjustable parameters in the colloidal-sphere model to an effective hard-sphere diameter is presented. Use of this expression allows the equilibrium behaviour of variations upon the studied model to be predicted through the algebraic manipulation of the currently available simulation results.

A study into the effects of incorporating a narrow distribution of particle sizes into the simulations has shown that this inevitable feature of experimental systems appreciably affects equilibrium properties of dense suspensions. In agreement with the previous findings of Dickinson and co-workers(46-49), a small degree of polydispersity results in a lowering of the osmotic pressure of the disordered phase and an increase in the osmotic pressure of the ordered phase. Clearly the equation of state transition width decreases with increasing polydispersity.

A series of non-equilibrium simulations have studied the shear behaviour of the isokinetic colloidal-sphere model over the reduced density range $\rho^{\dagger} = 0.60 - 0.80$. Qualitatively, the shear-rate dependent behaviour has been observed to resemble that of the sheared isokinetic hard-sphere model. Further non-equilibrium studies have examined the behaviour of the colloidal-sphere model with 5% and 10% polydispersity. At these relatively low degrees of polydispersity, the viscosity of the isokinetic colloidal-sphere system in the high shear rate region is shown to increase when compared to a monodisperse system at equivalent packing fraction. The viscosity increase may be explained in terms of the inability of mildly polydisperse systems to pack efficiently into the streamlined particle 'strings' associated with this flow regime.

A similar kinetic energy shear rate scaling procedure to that used for the hard-sphere case has been used in order to make a 'first attempt' prediction of the flow properties of the model colloidal-sphere suspension. In broad agreement with the predicted properties of the model hard-sphere suspension, the observed non-linear behaviour is shown to correspond to the high shear rate 'shear thickening' region of the model colloidal-sphere suspension flow curve. The inability to scale the present results onto experiment arises from the lack of a knowledge of the value of an 'effective friction constant' representing the hydrodynamic drag forces opposing particle translation. An estimate of this parameter requires a knowledge of the suspension medium viscosity whilst contained in the interstices between suspended particles. In concentrated suspensions the dimensions of these interstices will be very small indeed, and the relevant viscosity value will differ significantly from that of the bulk viscosity.

Armed with the qualitative predictions concerning the shear behaviour of experimentally inaccessible properties of particulate suspensions, it is now possible to postulate a plausible explanation for the form of the generalised dense suspension flow curve. A useful concept upon which it is possible to base the timescale required for structural changes in any system is that of the relaxation time of the constituent particles. In the present context this relaxation time may be conveniently envisaged as the average time taken for a particle to diffuse a distance equivalent to its own diameter. Predictions of the properties of the model hard-sphere suspension presented in Chapter 3.5 have shown particle diffusivity to decrease rapidly with decreasing shear-rate. Ever-lengthening relaxation times consequently prevail as the shear-rate approaches zero. Indeed, in this extremely low shear rate regime, Brownian motion must be solely responsible for preventing relaxation times from taking on an infinite value. Times required for the establishment of steady state conditions in this low shear-rate long relaxation time regime will often be well outside the time allowed by the experimental rheologist. Actual equilibration times will be dependent upon several factors, including particle diameter, suspension medium viscosity, packing fraction of the suspended particles and the original state of the sample. The low shear-rate behaviour frequently observed experimentally may consequently be attributed to metastability. Only at higher shear rates, when relaxation times have been reduced dramatically, are steady state conditions allowed to prevail. Little wonder, then that experimental flow curves have been observed to be non-reproducible, or that the rheological behaviour of certain systems described as 'shear history dependent'.

At intermediate shear rates the dense suspension takes on a sheared crystalline structure, sometimes referred to as the 'string phase'. Evidence for transitions between sheared crystalline configurations are presented in the current work, but may well be strongly influenced by system size (rheometer gap width) effects. The shear thickening transition commonly observed for dense suspensions at high shear rates corresponds to a shear induced perturbation of the equilibrium phase behaviour, which has been observed at low shear rates for isokinetic systems. Experimentally this transition is often accompanied by shear dilatancy, which is manifested as an increase in osmotic pressure in constant volume simulations.

The potential value of particulate dynamics simulations as a complement to experimental techniques in order to elucidate the experimental behaviour exhibited by dense suspensions, has hopefully been demonstrated by the present work. Ultimately however, computer simulation studies should be able to provide a quantitative description of experimental behaviour. Progress towards this objective will be achieved through advances on both the experimental as well as the simulation front. An obvious experimental requirement is the ability to produce 'well-characterised' suspensions of monodisperse particles of the desired diameter. The production of 'nearly monodisperse' systems with particle diameters of several microns is currently possible. In order to prepare systems in which the particle relaxation times are short enough to allow the attainment of steady state conditions in a reasonably short time, particle diameters are required to be smaller than this, ideally 1 micron or less. At present the production of particles in this smaller size range inevitably leads to increased variation in both particle shape and size.

Characterisation of the equilibrium properties of these systems, for example the osmotic pressure-concentration relationship over the entire concentration range would constitute an important advance in the study of colloidal suspensions. Given this data it may then be possible to tailor the form of the inter-particle interaction through the modification of adjustable parameters in the effective pair-potential.

Brownian motion has been incorporated into computer simulation studies of solid/liquid suspensions by several workers(99,101). It's incorporation into a Mean-Field Stokesian Dynamics(94) simulation however, where the effective hydrodynamic friction constant controlling the damping of particle velocities is maintained at a constant, shear rate independent value would presumably allow the study of the low shear-rate region of the dense suspension flow curve.

A recent 'granular dynamics' approach(120) aimed at the study of the flow of dry powders explores the use of a restitution coefficient to constrain the system kinetic energy. Collisions between real suspended particles are undoubtedly inelastic. Incorporation of such a kinetic energy constraint into the simulation of a sheared suspension could consequently prove to be a worthwhile avenue to explore.

REFERENCES

REFERENCES

1. Harris, J. (1970), Rheology and Non-Newtonian Flow, London, Longman.

2. Cheng, D.C.H. (1983), Further Observations on the Rheological Behaviour of Dense Suspensions, International Symposium preprint - The role of particle interactions in powder mechanics, Eindhoven, August 29th-31st 1983, EFCE publication Series No. 28, 242.

3. Alder, B. J. and Wainwright, T. E. (1959), Studies in Molecular Dynamics, I, General Method, J. Chem. Phys., 31, 459.

4. Woodcock, L. V. (1984), Origins of Shear Dilatancy and Shear Thickening Phenomena, Chem. Phys. Lett., 111, 455.

5. Pusey, P. N. and van Megen, W. (1986), The Behaviour of Concentrated Suspensions of Nearly Hard Colloidal Spheres, Nature 320, 340.

6. Markovitz, H. (1968), The Emergence of Rheology, Physics Today, 21, 4, 23.

7. Shortley, G. and Williams, D. (1953), Elements of Physics, 5th Edition, Volume 1, New Jersey, Prentice-Hall Inc.

8. Newton, I., (1966), Mathematical Principles of Natural Philosophy, translated from the Latin by Motte, A. and Cagon, F., University of California Press.

9. Coulson, J. M. and Richardson, J. F. (1977), Chemical Engineering, Volume 1, 3rd Edition, Pergamon Press, p. 52.

10. Mallock, A. (1888), Proc. Roy. Soc., 45, 126.

11. Mallock, A. (1888), Proc. Roy. Soc. A157.

12. Couette, M. (1890), Ann. Chim. Phys., 21, A description of Couette flow appears in Walters, K. (1975), Rheometry, London, Chapman and Hall, p. 53.

13. Weber, W. (1841), Ann. Phys. Chem., 54, 1.

14. Stein, H. N. (1987), Rheological Behaviour of Suspensions, in Encyclopaedia of Fluid Mechanics. Ed. N. D. Cheremisinoff, Gulf Publishing Co., Houston, Texas.

15. Reynolds, O. (1886), Experiments showing dilatancy, a property of granular material, possibly connected with gravitation. The Royal Institution Library of Science, ed. Bragg, W. L. and Porter, G. P. (1970), Elsevier.

16. Einstein, A., Brownian Motion, Dover Publications Inc. (1956).

17. Thomas, D. G. (1965), Transport Characteristics of Suspensions, J. Colloid Sci., 20, 267.

18. Reiner, M. (1949), Deformation and Flow, London, Lewis.

19. Bingham, E. C. (1922), Fluidity and Plasticity, New York, McGraw-Hill.

20. Freundlich, H. and Röder, H. L. (1938), Dilatancy and its relation to thixotropy, Trans. Faraday Soc., 34, 308.

21. Casson, N. (1959), A flow equation for pigment-oil suspensions of the printing ink type, in Rheology of disperse systems, ed. C. C. Mill, London, Pergamon Press.

22. Batchelor, G. K. (1970), The stress-system in a suspension of force free particles, J. Fluid Mech. 41, 545.

23. Bogue, C. D. and White, J. L. (1970), Engineering analysis of non-Newtonian fluids, London, Technical Editing and Reproduction Ltd.

24. Leighton, D. and Acrivos, A. (1987), The shear induced migration of particles in concentrated suspensions. J. Fl. Mechanics, 181, 415,25,177,109.

25. Leighton, D. and Acrivos, A. (1987), Measurement of shear induced self diffusion in concentrated suspensions of spheres. J. Fl. Mech. 177.

26. Woodcock, L. V. (1986), Osmotic pressure effects in dispersion rheometry, J. non-Newtonian Fluid Mech. 19, 349.

27. Goodwin, J. (1987), The rheology of colloidal dispersions, in solid-liquid dispersions, ed. T.H.F. Tadros, Academic Press

28. Piirma, I., (1982), Emulsion Polymerization, London, Academic Press.

29. Shih, W. Y., Aksay, L. A. and Kikuchi, R. (1987), Phase diagrams of charged colloidal particles, J. Chem. Phys., 86, 9, 5127.

30. Hoffman, R. L. (1972), Discontinuous and dilatant viscosity behaviour in concentrated suspensions, Trans. Soc. Rheol., 16, 155.

31. Krieger, I. M. (1972), Rheology of monodisperse latices, Adv. Coll. Int. Sci., 3, 111.

32. Barnes, H. A. (1980), A survey of industrial problems and academic progress. Dipsersion Rheology. R.I.C. Industrial Division Report.

33. Hansen, J. P. and McDonald, I. R. (1976), Theory of simple liquids, London, Academic Press.

34. Metropolis, N. Rosenbluth, A. W., Rosenbluth, M. N., Teller, A. H. and Teller, E. (1953), Equation of state calculations by fast computing machines, J. Chem. Phys., 21, 1087.

35. Wood, W. W. and Parker, R. (1957), Monte Carlo equation of state of molecules interacting with the Lennard-Jones potential I. A supercritical isotherm at about twice the critical temperature; J. Chem. Phys., 27, 720.

36. Alder, B. J. and Wainwright, T. E. (1957), Phase transition of a hard-sphere system, J. Chem. Phys., 27, 1208.

37. Woodcock, L. V. (1981), Glass transition in the hard-sphere model and Kauzmann's paradox, Ann. N. Y. Acad. Sci., 371, 274.

38. Woodcock, L. V. and Angell, C. A. (1981), Diffusivity of the hard-sphere model in the region of fluid metastability. Phys. Rev. Lett. 47, 16, 1129.

39. Speedy, R. J. (1987), Diffusion in the hard-sphere fluid, Mol. Phys. 62, 2, 509.

40. Speedy, R. J. (1986), Hard-spheres and instabilities, Ann. N. Y. Acad. Sci., 484, 214.

41. Rahman, A. (1964), Correlations in the motion of atoms in liquid Argon, Phys. Rev. 136, 2A, 405.

42. Verlet, L. (1967), Computer 'experiments' on classical fluids, I. Thermodynamical properties of Lennard-Jones molecules, Phys. Rev. 159, 98.

43. Fincham, D. and Heyes, D. M. (1983), Comparisons between experimental Argon and Lennard-Jones 12:6 shear viscosities, Chem. Phys., 78, 425.

44. Abraham, F. F. (1986), Computational statistical mechanics. Methodology, applications and supercomputing, Adv. Phys., 35, 1.

45. Hoover, W. G., Ross, M., Johnson, K. W., Henderson, D., Barker, J. A. and Brown, B. C. (1970), Soft sphere equation of state, J. Chem. Phys. 52, 4931.

46. Dickinson, E. (1979), Polydispersity and osmotic pressure of stable ordered colloidal dispersions, J.C. S. Faraday II, 75, 466.

47. Dickinson, E. (1983), Symmetry aspects of phase separation in polydisperse systems, Chem. Phys. Lett., 101, 6, 562.

48. Dickinson, E. (1980), Statistical thermodynamics of fluid phase equilibrium in a conformal polydisperse system, J.C.S. Faraday II, 76, 1458.

49. Dickinson, E., Parker, R. and Lal, M. (1981), Polydispersity and the colloidal order-disorder transition, Chem. Phys. Lett., 79, 3, 578.

50. Dickinson, E. and Parker, R. (1985), Polydispersity and the fluid-crystalline phase transition, J. Physique Lett., 46, 229.

51. Salacuse, J. J. and Stell, G. (1982), Polydisperse systems: statistical thermodynamics, with applications to several models including hard and permeable spheres, J. Chem. Phys., 77, 7, 3714.

52. Hansen, J. P., Reatto, L., Tau, M. and Victor, J. H. (1985), Validity of the high temperature approximation and influence of polydispersity on the phase separation in charged colloidal dispersions, Mol. Phys. 56, 2, 385.

53. Green, M. S. (1954), Markoff random processes and the statistical mechanics of time dependent phenomena II. Irreversible processes in fluids, J. Chem. Phys. 22, 398.

54. Allen, M. P. and Tildesley, D. J. (1987), Computer simulation of liquids, Oxford, Clarendon Press.

55. Alder, B. J., Gass, D. M. and Wainwright, T. E. (1970), Studies in molecular dynamics VIII. The transport coefficients for a hard-sphere fluid. J. Chem. Phys., 53, 3813.

56. Levesque, D., Verlet, L. (1973), Computer experiments on classical fluids IV. Transport properties and time correlation functions of the Lennard-Jones liquid near its triple point, Phys. Rev. A7, 1690.

57. Rekhson, S. M., Heyes, D. M., Montrose, C. J. and Litovitz, T. A. (1980), J. Non-Crystalline Solids, 38 & 39, 403.

58. Levesque, D. and Verlet, L. (1987), Molecular dynamics calculations of transport coefficients, Mol. Phys., 61, 1, 143.

59. Schoen, M. and Hoheisel, C. (1985), The shear viscosity of a Lennard-Jones fluid calculated by equilibrium molecular dynamics, Mol. Phys. 56, 3, 653.

60. Gosling, E. M., McDonald, I. R. and Singer, K. (1973), on the calculation by molecular dynamics of the shear viscosity of a simple fluid, Mol. Phys., 26, 1475.

61. Ashurst, W. T. and Hoover, W. G. (1973), Argon shear viscosity via a Lennard-Jones potential with equilibrium and non-equilibrium molecular dynamics, Phys. Rev. Lett., 31, 206.

62. Lees, A. W. and Edwards, S. F. (1972), The computer study of transport processes under extreme conditions, J. Phys., C5, 1921.

63. Ashurst, W. T. and Hoover, W. G. (1975), Dense fluid shear viscosity via non-equilibrium molecular dynamics, Phys. Rev. A11, 658.

64. Ashurst, W. T. and Hoover, W. G. (1975), Shear viscosity and thermal conductivity - the excess, A.I.Chem.E. Journal, 21, 410.

65. Woodcock, L. V. (1988), Predicting the rheology of complex fluids, Proceedings of the SERC-CCPS conference on Industrial Applications of Molecular Simulations, University of London, January 6th-8th, 1988 (for special issue of 'Molecular Simulation' journal).

66. Naitoh, T. and Ono, S. (1976), The shear viscosity of hard-sphere fluid via non-equilibrium molecular dynamics, Phys. Lett., 57A, 448.

67. Naitoh, T. and Ono, S. (1979), The shear viscosity of a hard-sphere fluid via non-equilibrium molecular dynamics, J. Chem. Phys., 70, 4515.

68. Erpenbeck, J. J. (1983), Non-equilibrium molecular dynamics calculations of the shear viscosity of hard-spheres. Physica, 118A, 144.

69. Erpenbeck, J. J. (1984), Shear viscosity of the hard-sphere fluid via non-equilibrium molecular dynamics, Phys. Rev. Lett., 52, 1333.

70. Evans, D. J. (1979), The frequency dependent shear viscosity of methane, Mol. Phys. 37, 1745.

71. Heyes, D. M., Kim, J. J., Montrose, C. J. and Litovitz, T. A. (1980), Time dependent non-linear shear stress effects in simple liquids: a molecular dynamics study, J. Chem. Phys., 73, 3987.

72. Evans, D. J. and Morriss, G. P. (1984), Non-linear response theory for steady planar Couette flow, Phys. Rev. A30, 1528.

73. Hoover, W. G., Evans, D. J., Hickmann, R. B., Ladd, A.J.C., Ashurst, W. T. and Moran, B. (1980), Lennard-Jones triple-point bulk and shear viscosities. Green-Kubo theory, Hamiltonian mechanics, and non-equilibrium molecular dynamics, Phys. Rev. A22, 1690.

74. Heyes, D. M. and Montrose, C. J. (1980), Non-linear shear-stress and thermal effects in fully flooded elastohydrodynamic line contacts, ASME Journal of Lubrication Technology, 102, 465.

75. Heyes, D. M., Montrose, C. J. and Litovitz, T. A. (1983), Viscoelastic shear thinning of liquids: a molecular dynamics study, J.C.S. Faraday II, 79, 611.

76. Heyes, D. M. (1986), Tensile viscosities of the Lennard-Jones, Phys. Lett. A, 115, 1, 2, 42.

77. Heyes, D. M. (1986), Shear thinning and thickening of the Lennard-Jones fluid, J. Chem. Soc. Faraday Trans. 2, 82, 1365.

78. Heyes, D. M. (1986), The nature of extreme shear thinning in simple liquids, Mol. Phys., 57, 6, 1265.

79. Heyes, D. M. (1986), Non-Newtonian behaviour of simple liquids, J. Non-newtonian Fluid Mechanics, 21, 137.

80. Heyes, D. M. (1987), Viscosity and self-diffusion of simple liquids, J. Chem. Soc. Faraday Trns. II, 83, 11, 1985.

81. Heyes, D. M. (1987), Transport coefficients of the Lennard-Jones fluid: Analysis of molecular dynamics data, Physica 146A, 341.

82. Ciccotti, G. and Jaccucci, G. (1975), Direct computation of dynamical response by molecular dynamics: the mobility of a charged Lennard-Jones particle, Phys. Rev. Lett., 35, 789.

83. Anderson, H. C. (1980), Molecular dynamics simulations at constant pressure and/or temperature, J. Chem. Phys., 72, 2, 384.

84. Andrea, T. A., Swope, W. C. and Anderson, H. C. (1983), The role of long ranged forces in determining the structure and properties of liquid water, J. Chem. Phys., 79, 4576.

85. Nosé, S. (1984), A molecular dynamics method for simulations in the canonical ensemble, Mol. Phys., 52, 255.

86. Woodcock, L. V. (1971), Isothermal molecular dynamics calculations for liquid salts, Chem. Phys. Lett., 10, 257.

87. Evans, D. J. and Morriss, G. P. (1983), Isothermal isobaric molecular dynamics, Chem. Phys., 77, 63.

88. Berendsen, H.J.C., Postma, J.P.M., van Gunsteren, W. F., Di Nola, A. and Haak, J. R. (1984), Molecular dynamics with coupling to an external bath, J. Chem. Phys., 81, 3684.

89. Brown, D. and Clarke, J.H.R. (1984), A comparison of constant energy, constant temperature and constant pressure ensembles in molecular dynamics simulations of atomic liquids, Mol. Phys., 51, 1243.

90. Woodcock, L. V. (1987), Some "ad hoc" notes on isokinetic and (N,V,T) dynamics, CCP5 Information Quarterly (March 1987).

91. Koplik, J., Banavar, J. R., Willensen, J. (1988), Molecular dynamics simulations of immiscible fluid flow, preprint from 4th EPS Liquid State Conference - Hydrodynamics of dispersed media - May 24th-27th, Arcachon, France.

92. Woodcock, L. V. (1985), Origins of thixotropy, Phys. Rev. Lett., 54, 1513.

93. Barnes, H. A., Edwards, M. F. and Woodcock, L. V. (1987), Applications of computer simulations to dense suspension rheology, Chem. Eng. Sci., 42, 4, 591.

94. Woodcock, L. V. (1987), Mean field Stokesian dynamics - CCPS Information Quarterly (December 1987).

95. Whittle, M. and Clarke, J.H.R. (1983), Shear viscosity in diatomic fluids, Mol. Phys., 49, 5, 1199.

96. Marechal, G. and Ryckaert, J. P. (1983), Atomic versus molecular description of transport properties in polyatomic fluids: n-butane as an example, Chem. Phys. Lett. 101, 548.

97. Edberg, R., Morriss, G. P. and Evans, D. J. (1987), Rheology of n-alkanes by non-equilibrium molecular dynamics, J. Chem. Phys., 86, 8, 4555.

98. Brown, D. and Clarke, J.H.R. (1986), Molecular dynamics computer simulation of polymer fibre microstructure, J. Chem. Phys., 84, 5, 2858.

99. Ermak, D. L. and McCammon, J. A. (1978), Brownian dynamics with hydrodynamic interactions, J. Chem. Phys., 69, 1352.

100. Bacon, J., Dickinson, E. and Porter, R. (1983), Farad. Disc. Chem. Soc., 76, 165.

101. Bossis, G. and Brady, J. F. (1987), Self diffusion of Brownian particles in concentrated suspensions under shear, J. Chem. Phys., 87, 9, 5437.

102. NAG (1984) Routine G05DDF. NAG FORTRAN Library Manual Vol. 4, Mark 9.

103. Van Megen, W. and Snook, I. (1976), Statistical mechanical approaches to phase transitions in hydrophobic colloids, I. Effects of electrolyte concentration, J. Colloid Interface Sci., 57, 40.

104. Van Megen, W. and Snook, I. (1975), A hard-sphere model for order-disorder transitions in colloidal dispersions, Chem. Phys. Lett., 35, 399.

105. Van Megen, W. and Snook, I. (1983), Diffusion in concentrated monodisperse colloidal solutions, Farad. Discuss. Chem. Soc., 76.

106. Dickinson, E. (1983), Royal Society of Chemistry, Annual Reports C.

107. Barker, J.A. and Henderson, D. (1976), What is "liquid"? Understanding the state of matter, Rev. Mod. Phys., 48, 4, 587.

108. Dickinson, E. (1978), Equations of state of polydisperse hard-disc and hard-sphere systems, Chem. Phys. Lett., 57, 1, 148.

109. Pusey, P.N. (1987), The effect of polydispersity on the crystallization of hard spherical colloids, Physics Abstracts - preprint.

110. Ottewill, R. and Richardson, R. (1982), Studies of particle-particle interactions using polystyrene latices and time-average light scattering, Coll. Polym. Sci., 260, 7, 708.

111. Percus, J.K. and Yevick, G.J. (1958), Analysis of classical statistical mechanics by means of collective co-ordinates, Phys. Rev., 110, 1.

112. Carnahan, N.F. and Starling, K.E. (1969), Equation of state for non-attracting rigid spheres, J. Chem. Phys., 51, 635.

113. Vrij, A., Jansen, W., Dhont, J.K.G., Pathmamanoharan, C., Kops-Werkhoven, M.M. and Fijnaut, H.M. (1983), Farad. Discus. Chem. Soc., 76.

114. Evans, R. and Napper, D.H. (1978), Disjoining pressures in colloidal dispersions, J. Coll. Int. Sci., 63, 43.

115. Parker, R. (1984), Computer simulation of colloidal dispersions, Ph.D. thesis, University of Leeds.

116. Chapman, S. and Cowling, T.G. (1960), Mathematical theory of non-uniform gases, Cambridge University Press, 4th edition.

117. Enskog, D. (1922), Kinetic theory of thermal conduction, viscosity and self-diffusion in certain dense gases and liquids, Svensk. Akad. Handl., 63, 4. A description of Enskog's work may also be found in reference (116).

118. Ree, Ree and Eyring (1958), Relaxation theory of transport problems in condensed systems, Ind. Eng. Chem. 50, 1036.

119. Barnes, H.A., Shear thickening ("dilatancy") in suspensions of non-aggregating solid particles dispersed in Newtonian liquids: a review and practical guide - in press.

120. Woodcock, LV. and Turner, M.C. (1988), I.F.P.R.I. Report.